UNIVERSITÉ DE GENÈVE
Département de physique nucléaire et corpusculaire

FACULTÉ DES SCIENCES
Professeur Philippe Mermod

Searches for Magnetic Monopoles and Highly Ionising Particles at $\sqrt{s} = 8$ TeV at the LHC

THÈSE

présentée à la Faculté des sciences de l'Université de Genève
pour obtenir le grade de Docteur ès sciences, mention physique

par

Akshay Katre

d'Inde

Thèse N° XXXX

GENÈVE
Atelier d'impression ReproMail
2016

Le modèle standard de la physique des particules décrit remarquablement bien les données expérimentales recueillies à ce jour. Les physiciens pensent cependant que cette théorie ne fournit pas une description complète de la réalité. Quelle est l'origine de la matière noire ? Comment expliquer la hiérarchie entre les masses des particules dites élémentaires ? Est-il possible de décrire toutes les interactions de manière cohérente au sein d'une même théorie ? Ce sont quelques-unes des questions fondamentales laissées sans réponse par le modèle standard. Beaucoup de nouvelles théories physiques, comme la supersymétrie, ont été proposées pour répondre à ces questions, mais elles ont grand besoin de vérification expérimentale.

Construit dans un tunnel de 27 km au CERN près de Genève, le grand collisionneur de hadrons (LHC) a accéléré et collisionné des faisceaux de protons à une énergie de centre de masse de 7 et 8 TeV entre 2010 et 2012 et a atteint 13 TeV en 2015, accédant à ce régime d'énergie pour la première fois en laboratoire. Les collisions à haute énergie permettent d'étudier la structure de la matière à son niveau le plus fondamental. En particulier, elles permettent la production de nouvelles particules massives qui étaient inaccessibles aux machines précédentes.

Dans cette thèse, les données des détecteurs ATLAS et MoEDAL au LHC sont exploitées pour rechercher une certaine classe de particules dont l'existence est prédite par certaines théories : les particules massives stables hautement ionisantes (HIPs), c'est à dire des particules chargées dont la durée de vie est suffisamment longue pour laisser une trace dans le détecteur le long de leur trajectoire. Bien que cette recherche soit conçue pour être sensible à différents types de HIPs d'une manière générique, la découverte ou l'exclusion de particules qui portent une charge magnétique fondamentale, appelés monopôles magnétiques, est l'objectif majeur de cette thèse. Le monopôle magnétique a été postulé par Paul Dirac en 1931 comme une manière élégante d'expliquer quantification de la charge électrique, entre autres vertus. L'un des résultats des calculs de Dirac est que l'unité fondamentale de charge magnétique doit correspondre à de nombreuses unités de charge électrique ; la signature attendue d'un monopôle dans un détecteur est donc une perte d'énergie par ionisation très élevée le long de sa trajectoire. La présence de monopôles est scrutinée à chaque fois qu'un nouveau collisionneur de particules est construit. Avec le LHC, nous avons l'occasion d'explorer le régime d'énergie des multi-TeV pour la première fois.

Dans cette thèse, de nouvelles simulations ont été développées pour émuler et comprendre la réponse du détecteur aux particules hautement ionisantes, et deux méthodes complémentaires ont été employées pour distinguer des signaux de nouvelle physique au LHC : l'identification de HIPs dans le détecteur à tâches multiples ATLAS avec notamment le développement d'un nouveau déclencheur d'événements ; et le piège de monopôles magnétiques avec l'expérience MoEDAL.

Avec ATLAS, une stratégie a été optimisée pour sélectionner des événements intéressants parmi les milliards de collisions enregistrées et minimiser le taux d'événements indésirables qui miment les nouvelles particules. Pour ce faire, nous utilisons une signature spécifique d'arrêt des HIPs dans le calorimètre électromagnétique d'ATLAS. Dans son mode de fonctionnement initial, le détecteur ATLAS ne pouvait pas déclencher sur les particules qui s'arrêtent avant de pénétrer profondément dans le calorimètre, comme le feraient une grande partie des monopôles produits lors des collisions. Par conséquent, le travail effectué comprend une extension du système de déclenchement d'ATLAS utilisant le détecteur de traces pour identifier les HIPs. Le nouveau déclencheur a été mis en place en 2012 et a accumulé une quantité importante de données à 8 TeV qui ont servi de base à ce travail de thèse. Le travail comprend également l'analyse détaillée des données, avec notamment l'estimation des bruits et des erreurs systématiques. Les résultats pour les monopôles portant la charge de Dirac surpassent largement ceux obtenus précédemment aux collisionneurs.

Avec MoEDAL, un concept inédit, le piège à monopôles, a été employé pour chercher spécifiquement les monopôles magnétiques produits dans les collisions du LHC. L'idée est peu conventionnelle, mais très simple : des barres d'aluminium placées proches d'un point d'interaction du LHC (dans la caverne de l'expérience LHCb) sont exposées aux produits de collisions avant d'être transportées à un laboratoire à Zurich pour détecter la présence de charges magnétiques piégées à l'aide d'un magnétomètre supra-conducteur. Les résultats obtenus avec une exposition à des collisions à 8 TeV en 2012 permettent d'exclure des domaines jusqu'ici inexplorés de haute masses et hautes charges magnétiques. Cela ouvre la voie à de nouvelles recherches avec les collisions à 13 TeV à partir de 2015. De manière incomparable, un monopôle piégé serait transportable et ses propriétés uniques pourraient être étudiées dans leurs moindres détails.

CONTENTS

1 INTRODUCTION

1.1 MAGNETIC MONOPOLES

The dynamics of electrically charged particles and electromagnetic fields are described by the classical theory of electromagnetism. These are contained in Maxwell's equations,

$$\vec{\nabla} \cdot \vec{E} = \frac{\rho_e}{\epsilon}, \quad \vec{\nabla} \times \vec{E} = -\frac{\partial \vec{B}}{\partial t}, \tag{1}$$

that determine the electric field ($\vec{E}$) generated by a source with charge density ρ_e. It states that electric fields *diverge away from* a (positive) charge, i.e. electric field lines originate on positive charges and terminate on negative ones. Similarly magnetic fields are described by,

$$\vec{\nabla} \cdot \vec{B} = 0, \quad \vec{\nabla} \times \vec{B} = \mu_0 \epsilon_0 \frac{\partial \vec{E}}{\partial t} + \mu_0 \vec{j_e} \tag{2}$$

where the magnetic field is determined by the electric current density $\vec{j_e}$. The magnetostatic equations state that the magnetic field *curls around a current* and does not *diverge* i.e. magnetic field lines do not begin or end anywhere. The zero divergence of the magnetic field ($\vec{\nabla} \cdot \vec{B} = 0$; Gauss' law for magnetism) implies the absence of the magnetic analogue to electric charges.

The theory incorporates the results of observations where no magnetic charges or magnetic currents are seen, with only the electric charge and current densities as the source of electric and magnetic fields.

If the magnetic analogue of electric charges (magnetic monopoles) were to exist, then these charges would have magnetic current and charge density. This leads to modifications in Maxwell's equations which would observe a symmetry in the descriptions of the magnetic and electric fields,

$$\vec{\nabla} \cdot \vec{B} = \mu_0 \rho_m, \quad \vec{\nabla} \times \vec{E} = -\frac{\partial \vec{B}}{\partial t} - \mu_0 \vec{j_m}, \tag{3}$$

with the magnetic charge ρ_m and current density $\vec{j_m}$. The magnetic charge of the monopoles g, would then be the integral of the magnetic charge density ρ_m over a region of space.

With the introduction of the magnetic monopoles, Maxwell's equations are symmetric under a duality transformation which mixes the electric and magnetic fields,

$$\begin{pmatrix} \vec{E} \\ c\,\vec{B} \end{pmatrix} = \begin{pmatrix} \cos\xi & \sin\xi \\ -\sin\xi & \cos\xi \end{pmatrix} \begin{pmatrix} \vec{E}' \\ c\vec{B}' \end{pmatrix},$$
$$\begin{pmatrix} c\rho_e \\ \rho_m \end{pmatrix} = \begin{pmatrix} \cos\xi & \sin\xi \\ -\sin\xi & \cos\xi \end{pmatrix} \begin{pmatrix} c\rho'_e \\ rho'_m \end{pmatrix} \tag{4}$$

with c the speed of light and ξ the transformation parameter. With these symmetries to the Maxwell's equations, possible only by the inclusion of magnetic monopoles, the magnetic and electric fields in Nature can be considered as simple transformations of one another. These transformations lead to $\vec{E} \rightarrow \vec{B}$ and $\vec{B} \rightarrow -\vec{E}$ for transforms between the fields, and $c\rho_e \rightarrow \rho_m$ and $\rho_m \rightarrow -c\rho_e$, for $\xi = \pi/2$ for the transforms of their sources.

1.1.1 *Dirac monopoles*

The isolated magnetic point charge *g* would then have an associated Coulomb field,

$$\vec{B}(\vec{r}) = \frac{g}{4\pi}\frac{\vec{r}}{r^3}. \tag{5}$$

A vector potential $\vec{A}$ is introduced by the description of the electromagnetic field, which is related to the magnetic field $\vec{B}$ by,

$$\vec{B} = \vec{\nabla} \times \vec{A} = \frac{\mu_0 g}{4\pi r^2}\hat{r}. \tag{6}$$

The absence of monopoles would imply a smooth vector potential $\vec{A}$, resulting in a sourceless magnetic field, $\vec{\nabla} \cdot \vec{B} = 0$. In 1931, Dirac proposed that the vector potential $\vec{A}$ was not an observable quantity and thus need not be smooth [1]. The solution proposed by Dirac was to consider the vector potential of an infinitely thin solenoid extending from $-\infty$ to the origin. This potential given by,

$$\vec{A}(\vec{r}) = \frac{\mu_0 g(1-\cos(\theta))}{4\pi r \sin\theta}\hat{\phi} \tag{7}$$

could be defined everywhere except at $\theta = \pi$. This singularity, known as the *Dirac string*, is invisible since the actual observable in classical electrodynamics is $\vec{B}$, and the curl of the vector potential gives a field of the same form as Eq. 6.

The presence of the vector potential from the Dirac string must be experienced by an electrically charged particle, analogous to the Aharonov-Bohm effect [2] where an electromagnetic vector (or scalar) potential is experienced. Thus the Dirac string describing an infinitesimally small loop will cause a change in the wave function's phase of a point like particle with electric charge q going around it, described as,

$$\Delta\phi = \frac{q}{\hbar}\int \vec{A}\cdot d\vec{l} = \lim_{\theta\to\pi}\frac{q}{\hbar}\frac{\mu_0 g(1-\cos\theta)}{4\pi r\sin\theta}\int_0^{2\pi} r\sin\theta d\phi = \frac{\mu_0 qg}{\hbar}. \quad (8)$$

This implies that the Dirac string, in principle, could be detectable. However, if the phase change would be a multiple of 2π, the string would be undetectable, as expected from a point like particle with magnetic charge. This leads to a significant conclusion of the Dirac quantisation condition [3] that states: the presence of magnetic monopoles leads to the requirement that charge is quantised, expressed as,

$$gq = \frac{nh}{\mu_0} \quad (9)$$

where n is a non-negative integer.

It is interesting to note that the quantisation condition can be reached via several other scenarios as described in [4, 5], which only reinforces the importance of this result.

The electric charge is indeed observed to be quantised in Nature in units of the lowest absolute non-zero electric charge, the electric charge of the electron, e [6]. To obtain the elementary magnetic charge, known as the Dirac charge g_D, Eq. 9 is rewritten in terms of e, the fine structure constant $\alpha = \frac{\mu_0 e^2 c}{2h}$, and assuming $n = 1$,

$$g = \frac{n}{2\alpha}(ce) \xrightarrow{n=1} g_D = \frac{ce}{2\alpha}. \quad (10)$$

Using natural units such that c=1, the lowest magnetic Dirac charge g_D is roughly equivalent to 68.5 times the elementary electric charge e.

1.1.2 *The Schwinger Monopole*

A few decades later, Julian Schwinger extended Dirac's theory predicting monopoles to study its relativistic invariance [7]. Consequently he found the vector potential that would represent a solution for a magnetic monopole field to be described by,

$$\vec{A}(\vec{r}) = \frac{\mu_0 g}{4\pi r}\cot\theta\hat{\phi}. \quad (11)$$

Which eventually leads to a different quantisation condition compared to the one proposed by Dirac,

$$gq = \frac{2nh}{\mu_0}. \quad (12)$$

This implies that the minimum magnetic monopole charge should be twice the Dirac charge which also has an impact on the magnitude of the monopole coupling. Schwinger's work also generalised the quantisation condition to describe dyons, particles that carry both electric and magnetic charges [8],

$$q_1 g_1 - q_2 g_2 = \frac{2n\hbar}{\mu_0} \tag{13}$$

where q_1, g_1 and q_2, g_2 are the electric and magnetic charges of the two dyons.

1.1.3 *Monopole-photon coupling*

The electron-photon coupling is given by the fine structure constant, α, which can be used as the premise to analogously define the monopole-photon coupling via a magnetic coupling constant, α_m. This strength of the coupling of magnetic monopole to photons can be defined by substituting $g^2 = (ng_D/c)^2$ for e, which leads to,

$$\alpha = \frac{\mu_0 e^2 c}{4\pi\hbar} \quad \xrightarrow{e \to g = ng_D/c} \quad \alpha_m = \frac{\mu_0 g_D^2}{4\pi\hbar c} n^2 \tag{14}$$

Taking into account Eq. 10, it implies that the strength of the monopole-photon coupling is at least four orders of magnitude greater than that of the electron-photon coupling. Considering $n = 1$, the magnetic coupling is $\alpha_m \approx 34.24$, which is a large coupling value that has strong implications in the understanding of the production of monopoles and their interactions with matter.

1.1.4 *Monopoles in Grand Unified Theories*

Both t'Hooft [9] and Polyakov [10], independently showed that grand unified theories (GUTs) in which the $U(1)$ group of electromagnetism is embedded in a larger compact non-Abelian group, predict the existence of magnetic monopoles.

The minimum of the scalar potential is degenerate in the GUT models and the symmetry of the vacuum is broken when the vacuum state assumes a specific direction. A solution known as the hedgehog configuration arises in GUT models, where the scalar field is coupled to a spatial direction,

$$\phi^a = v\frac{r^a}{r}, \quad a = 1, 2, 3. \tag{15}$$

While not corresponding to the absolute minimum of the scalar potential, the solution is nonetheless topologically stable [9]. Eq. 15 leads to a solution of the non-Abelian electromagnetic gauge potential, which represents the Coulomb-like non-Abelian field of a point like particle from which the Dirac string vector potential can be extracted [11].

The charge quantisation condition in the GUT models arise if the $U(1)$ group of electromagnetism is embedded into a semi-simple non-Abelian group of higher rank. This is similar to Dirac's theory where the quantisation was a consequence of the existence of magnetic monopoles. The GUT models that undergo a spontaneous symmetry breaking do predict monopole solutions. The non-Abelian analogue of Dirac's charge quantisation condition reads just as Eq. 9 in the GUT models and thus the minimum magnetic charge of the GUT monopole is twice the Dirac charge, $2.0g_D$.

Unlike the Dirac theory of magnetic monopoles, GUT models actually make predictions on the mass of the monopole to be approximately, $M \approx 137m_X$, where m_X is the mass of the vector boson of the model [11]. In GUT models, the mass of the vector boson is of the same order as the unification scale (10^{16} GeV) [12], thereby resulting in a prediction of the monopole mass of the order of 10^{18} GeV, beyond the reach of present particle colliders.

1.1.5 *Magnetic monopoles in electroweak models*

While monopoles are not believed to exist within the framework of the Standard Model (SM) [13, 14], it has been proposed that monopole-like solutions are possible in the SM electroweak sector [15]. Known as electroweak monopoles, these solutions obey Schwinger's charge quantisation condition and therefore have a minimum magnetic charge of $2g_D$. Recent developments in the theory have predicted monopole masses within the range of 4 - 10 TeV [16, 17], which are only just within the limit of the hadron colliders, such as the Large Hadron Collider (LHC) and possible Future Circular Colliders (FFC).

1.2 MATTER INTERACTIONS

The monopole interaction with electromagnetic fields is similar to that of electrically charged particles. A particle with electric and magnetic charge experiences a force in the presence of an electromagnetic field which is described by the Lorentz force,

$$\vec{F} = q\left(\vec{E} + \vec{v} \times \vec{B}\right) + g\left(\vec{B} - \vec{v} \times \frac{\vec{E}}{c^2}\right), \tag{16}$$

with q and g the electric and magnetic charges respectively. The interactions of a magnetic monopole with the electric field is at least an order of magnitude stronger than that of an electrically charged particle, since the Dirac charge is equivalent to $68.5e$. Conversely, the magnetic field from a moving monopole of charge g influences an electron in an atomic orbital with a strength βg, where β is the monopole velocity relative to the speed of light. Thus, both monopoles and highly electrically charged objects (HECOs), that are probed in this analysis, would appear as highly ionising particles (HIPs) in detectors.

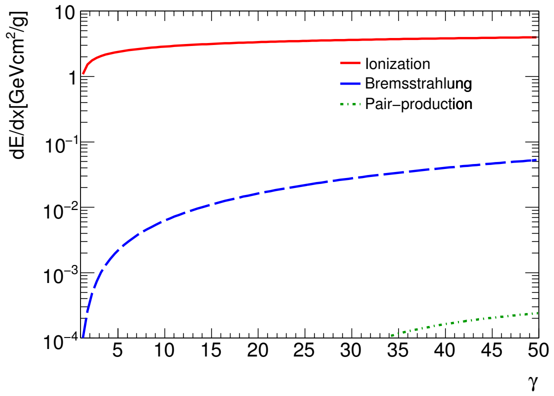

Figure 1: Electromagnetic energy deposition by ionisation (solid red line), Bremsstrahlung (blue dashed line) and pair-production (dashed-dotted green line) for a mass 1000 GeV $|g| = 1.0 g_D$ magnetic monopole in Argon as a function of the monopole relativistic γ factor [18, 19].

For most HIPs, the most distinguishable parameter is its measured energy loss in matter, dE/dx. For both, electrically and magnetically charged particles, the energy loss is carried out via three mechanisms, ionisation of the medium, pair-production and bremsstrahlung. A comparison of the energy loss of a monopole of mass 1000 GeV and charge $|g| = 1.0 g_D$ in argon via the three different mechanisms is shown in Fig. 1. The energy losses from bremsstrahlung and pair-production in the range $\gamma < 10$ are negligible. With the dominant energy loss process of a monopole at a particle collider being ionisation, it is the only process that is described in detail in this section.

1.2.1 *Energy loss via ionisation*

As *electrically* charged particles traverse through a medium, they lose energy by either interacting with atomic electrons or by collisions with the atomic nuclei. The interactions with electrons results in the liberation of electrons from the atoms in the material (ionisation), while the collisions with the nuclei displace the atom from the lattice causing a Non-Ionising Energy Loss (NIEL). In practical particle detectors, the energy loss via ionisation is far greater than that via NIEL and hence is the only one considered here.

The mean ionisation energy loss (or stopping power) for electrically charged particles (HECOs in this case) is described by the Bethe-Bloch formula:

$$-\frac{dE}{dx} = K\frac{Z}{A}\frac{z^2}{\beta^2}\left[\ln\frac{2m_e c^2\beta^2\gamma^2}{I} - \beta^2 - \frac{\delta}{2}\right] \tag{17}$$

where z is the charge of the projectile particle in units of e and βc its velocity, $m_e c^2$ the electron rest mass, I is the mean ionisation energy of the material, and δ is the density effect correction that becomes relevant for ultra-relativistic particles.

For magnetic monopoles that ionise the medium that they traverse, large energy depositions are expected due to the strength of the interaction of orbiting electrons with the magnetic field of monopoles. To study the interaction of monopoles with matter, the Eq. 17 can be modified by substituting βg for ze.

The energy losses of monopoles consist of two regimes, namely, a high-momentum transfer or close-interaction regime and a low-momentum transfer or distant-interaction regime. The former is modelled by Kazama, Yang and Goldhaber (KYG) who solved the Dirac's equation of an electron in the magnetic field of a monopole [20]. While the latter is modelled using the dipole approximation. An energy loss formula based on the first order Born approximation which takes into account the close- and distant-interaction regimes with an accuracy of about 3% for monopoles with $\beta \geqslant 0.2$ and $\gamma \leqslant 100$ was developed by Ahlen [21]. The energy loss formula was given by,

$$-\frac{dE}{dx} = K\frac{Z}{A}g^2\left[\ln\frac{2m_e c^2\beta^2\gamma^2}{I} + \frac{k(g)}{2} - \frac{1}{2} - \frac{\delta}{2} - B(g)\right] \tag{18}$$

here, $g = ng_D$ is the magnetic charge, βc is the monopole speed. $k(g)$ is the KYG correction:

$$k(g) = \begin{cases} 0.406, & |n| \leqslant 1 \\ 0.346, & |n| \geqslant 1.5, \end{cases} \tag{19}$$

which arises from the relativistic cross section calculated in Ref. [20]. $B(g)$ is the Bloch correction:

$$B(g) = \begin{cases} 0.248, & |n| \leqslant 1 \\ 0.672, & |n| \geqslant 1.5 \end{cases} \tag{20}$$

which accounts for higher order effects for low-energy collisions in which the monopole velocity approaches the orbital velocity of the electron. For $\gamma > 100$ spin effects and contributions from the internal structure of the nuclei become important and the above energy loss equation does not hold.

For very low velocities ($\beta < 0.01$), the energy loss of monopoles in silicon is described by [22, 23],

$$-\frac{dE}{dx} = (45\mathrm{GeV cm}^{-1})n^2\beta, \tag{21}$$

with $n = g/g_D$. Since the interactions with the electron spin are not modelled, this formula gives a lower limit on the energy losses. The intermediate velocity range of $0.01 < \beta < 0.1$ is where shell effects might play a small role and the energy loss is modelled by interpolating between the predictions of Eq. 18 and Eq. 21.

No spin dependence is assumed in the energy loss by ionisation of monopoles since the spin-flip transitions are negligible in the ranges

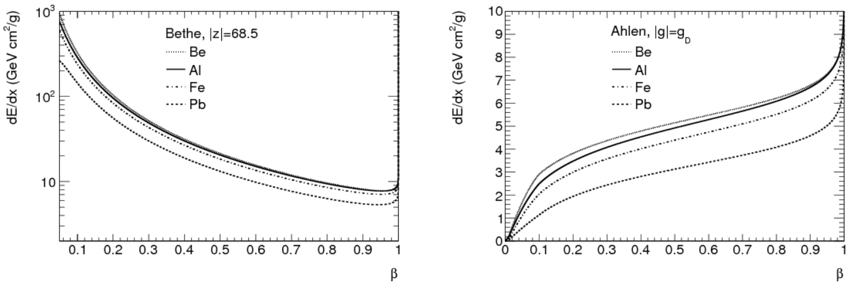

Figure 2: Energy loss per unit length, dE/dx, by an electrically charged particle with $|z| = 68.5e$ (left) and a magnetic monopole of charge $|g| = 1.0g_D$ (right) as a function of the particle velocity, β, for different materials [24].

considered. Only at very low velocities does the monopole spin become important, at which point the ionisation has ceased due to the β dependence of the magnetic field that the electron experiences [21].

On comparing equations 17 and 18, it can be seen that the energy loss by ionisation of a magnetic monopole of charge $|g| = 1.0g_D$ is four orders of magnitude greater than those of electrically charged particles with $|z| = 1.0e$. With no velocity dependence for the monopole energy loss in Eq. 18 the magnetically charged particles tend to deposit lesser of their kinetic energy at lower velocities compared to the electrically charged particles. Correspondingly, the electrically charged particles deposit most of their kinetic energies at low velocities, known as Bragg peak, towards the energy of their trajectory. The energy loss via ionisation by an electrically charged particle of charge $|z| = 68.5e$ and a magnetically charged particle of charge $|g| = 1.0g_D$ as a function of the particle velocity β for different materials is shown in Fig. 2.

1.3 DETECTION TECHNIQUES

A vast number of experiments have been carried out through the years to search for magnetic monopoles, using direct and indirect methods of detection. These experiments implement various techniques and technologies that exploit the large ionisation signature of monopoles as they traverse through matter. With the advent of particle detectors with precision tracking measurements, the monopoles accelerated in a magnetic field could be searched for as anomalous tracks. For monopoles trapped in matter, the simplest yet surest way of detecting monopoles is by detecting a divergence in the magnetic flux.

1.3.1 *High ionisation active detection*

As described in Sec. 1.2, monopoles are highly ionising particles with energy losses that are orders of magnitude larger than those of electrically charged particles. While most particle detectors are calibrated for minimum ionising particles (MIPs), their technologies do allow

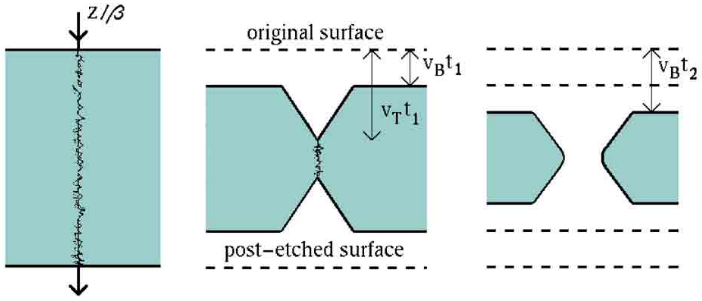

Figure 3: Schematic depictions of the formation of a damage zone by a highly ionising particle (left), the formation of an etch pit (middle) and the enlarging of an etch pit with continued etching (right) [31].

detection of δ-electrons[1] from the distinct monopole signature. For example, while scintillator detectors and the Transition Radiation Tracker (TRT), of ATLAS (A Toroidal LHC ApparatuS), are capable of detection both MIPs and HIPs, the design of the silicon and pixel trackers at ATLAS would reach a peak plateau value and give an ambiguous response. Therefore, depending on the detection technique, the charge collected or light produced, would generally give a good distinction between monopoles and MIPs. For slow moving monopoles however, the energy losses are not very well understood and it is expected that they bind to the atomic nuclei.

While the ionisation technique does help identify monopoles, it does not help distinguish between similar signature objects, such as HECOs and dyons.

1.3.2 *Heavily etched nuclear track detectors*

Nuclear track detectors (NTDs) are plastic foils that are used to identify HIPs produced in both cosmic ray experiments [25, 26, 27, 28] and particle colliders [29, 30]. The passage of HIPs through these foils creates damage at the level of polymeric bounds along their trajectory. The extent of the damage is dependent on the charge and velocity of the incident particle.

An etching process is followed, that causes etch-pits in the foil which are detectable under an optical microscope (see Fig. 3). The size and shape of these etches give information about the charge, energy and direction of motion of the incident highly-ionising particle.

1.3.3 *Tracks in magnetic fields*

Monopoles are accelerated along the magnetic field, unlike electric charges that experience a force in a plane perpendicular to the direction of the field. Standard track algorithms in particle detectors are built to reconstruct tracks of electrically charged particles, with the curvature of the track in the $r - \phi$ plane helping in determining the

1 These are electrons that have been knocked off their atomic orbitals by energetic particles that traverse through the medium.

particle momentum. These algorithms can be reconfigured to detect monopoles, that in the presence of a magnetic field are accelerated in the field, producing straight tracks in the $r - \phi$ plane, but follow a near parabolic trajectory in the $r - z$ plane.

Such techniques have been used at the CLEO [32] and TASSO [33] collaborations, that implement parametrisations of the expected trajectory to help identify monopole tracks. It is noteworthy that the large amount of δ-rays produced along the monopole's trajectory can cause the tracking algorithms to have difficulties in identifying monopole-like particles in high granularity detectors.

1.3.4 *Time of flight detection*

Some experiments rely on the fact that monopoles are expected to be heavy fundamental particles. Time-of-flight (TOF) detection techniques are used to measure the time a particle takes to traverse through a select region of the detector (for example, between two scintillator detector planes), with heavier particles tending to take longer times. This helps reduce cosmic backgrounds [32, 33] but can also be combined efficiently into triggering algorithms to select particles at colliders [34].

1.3.5 *Cherenkov radiation*

Cherenkov radiation is electromagnetic radiation that is produced when a charged particle traverses a dielectric medium faster than the speed of light in that medium. For cosmic monopoles moving with high velocities, the amount of Cherenkov radiation produced can be a strong identification factor [35]. Additionally, even slow moving monopoles that produce copious amounts of energetic δ-rays, which themselves produce Cherenkov radiation, can be distinguished from backgrounds [36].

1.3.6 *Nuclear emulsions*

Nuclear emulsion plates are photographic plates with particularly thick emulsion layers that are capable of recording tracks of charged particles that pass through. The tracks can be analysed in detail after developing the plates (much like old-school photographs). By measuring track lengths and the ionisation in the emulsion, monopoles can be detected by comparing to tracks to those of known particles [37].

1.3.7 *Monopoles trapped in matter*

Monopoles produced in the early universe might be trapped in matter, bound to nuclei of materials with binding energies of the order of 100 keV [38]. To detect such monopoles that are bound in matter, be it meteorites, moon rocks or in the Earth's crust, different techniques than the ones discussed so far need to be implemented.

In addition to early universe monopoles bound to planetary matter, those produced at particle accelerators can also be analysed. Monopoles produced in high-energy collisions at colliders travel through layers of inactive medium before reaching sub-detector systems that are used to identify them. Therefore it is possible that monopoles stop and are trapped in the inactive detector material. In the case of experiments housed at the LHC, material close to the interaction points (for example, beam pipe surrounding the interaction points) are generally a source for looking for trapped monopoles [24].

Extraction technique

The monopoles that are trapped in matter can be extracted by applying a strong magnetic field (5 T or higher) to pull monopoles out of a solid sample surface [39, 40, 41, 42, 43]. Additionally, the sample can also be heated and evaporated before extracting the monopole with the magnetic field [44]. The magnetic field applied would accelerate the extracted monopole to an appropriate velocity and before being identified using an array made of say, scintillators or nuclear-track detectors. Thus the experiments that use this method generally implement it in three steps, (1) extraction, (2) acceleration and (3) detection, with uncertainties associated to each step of the process. The efficiencies generally depend on the assumed monopole mass and charge and drop to zero above a certain mass value [45].

Induction technique

With the development of the superconducting magnetometers, the extraction technique was gradually abandoned in favour of the more beneficial induction technique. The induction technique reduces the number of steps required to analyse a sample (no extraction nor acceleration steps required), the large solid samples can be analysed faster and the measurement is directly sensitive to the magnetic charge with no dependence on the monopole mass.

The technique involves passing the samples through a superconducting coil and measuring the change in the induced currents (*persistent current*). This persistent current is directly proportional to the charge of the monopole with the indisputable signature of a monopole provided by consistent non-zero persistent current measurements via multiple passes of the sample through the coils. The MoEDAL (Monopole and Exotics Detector at the Large Hadron Collider) experiment search carried out in this thesis (see Chapter 4) uses the induction technique to search for trapped monopoles in the MoEDAL Magnetic Monopole Trapper samples [29] as well as the beam pipe from the CMS (Compact Muon Solenoid) experiment [46].

1.4 OBSERVATIONS OF MONOPOLE-LIKE EVENTS

A host of searches for magnetic monopoles produced at accelerators, in cosmic rays or bound in matter have been performed with no reproducible evidence for its existence. However, through the course of time, there have been certain experiments that claimed apparent observations which briefly caused great excitement in this field. The interpretations of these results have either been re-evaluated or in some cases, deemed to be inconclusive to claim the existence of a magnetic monopole.

In 1975, a balloon-borne experiment claimed that it observed a downward-pointing track that strongly supported the observation of a $2g_D$ monopole with a mass of over 200 GeV [47]. The experiment consisted of layers of NTD foils that were complemented with a layer of nuclear emulsion and a layer of Cherenkov radiator coupled to a fast film. Later reassessment of the data showed the track to be inconsistent with that of a monopole and with only a single event, the actual identity of the particle could not be established [26].

A series of experiments in the 1980s also showed observations of magnetic monopoles. The first of which was performed by Cabrera in 1982, where a four-turn loop of 5 cm diameter was connected to a superconducting input coil of a SQUID (Superconducting Quantum Interference Device) magnetometer [48]. The passage of a Dirac monopole through the loops results in a flux change of $8\phi_0$ - a factor of 4 from the turns in the pickup loop and of 2 from the monopole itself. In its 151 days of data-taking period, a single large event was recorded on 14^{th} February, 1982, which was consistent with the signal of a single Dirac charge monopole. While this is the best observation of a magnetic monopole to date, the observation comes with some caveats. First, the observation being caused by instrumental effects could not be ruled out. Second, the monopole flux calculations were inconsistent with results from other cosmic ray facilities [27].

Another experiment in 1983, placed nuclear emulsion plates contained in a lead-mercury shield in the Homestake gold mine at a depth of 1370 m for 250 days. While the shielding eliminates local radioactivity affecting the plates, the deep underground location eradicates essentially all cosmic ray background. After the exposure, the volume was scanned for all visible tracks, with all but seven tracks attributed to α particles (based on track lengths). Six of those seven tracks were further analysed and found to be protons due to reactions of thorium decay α's [37]. The seventh track, however, is attributed to either ternary fission reaction which has a probability of occurrence in this experiment of 0.01 or, to the more exotic hypothesis that suggests a monopole-induced ternary-fission, i.e. a monopole creates intense fields that distorts the nucleus to which it is bound to sufficiently induce a fission reaction.

A dedicated magnetic monopole detector deployed in 1986 made an observation of an unexplained event. The experimental setup was based on the induction technique and the 0.18 m^2 detector had an effective observation time of 8242 hours. The expected total magnetic flux is 2 ϕ_0 from a Dirac monopole and this experiment recorded an event with a total flux of 0.83 ϕ_0 on August 11^{th} 1985. The authors wrote a detailed paper [49] highlighting all the plausible reasons for the event, with none of them seeming likely, making the event yet another possible monopole candidate.

1.5 SEARCHES FOR COSMOLOGICAL MONOPOLES

Monopoles are shown to be a general consequence of the unification of the fundamental interactions [50, 9, 10]. However, this in itself is not reason enough to guarantee an observation. If the masses of monopoles are indeed 10^{16} GeV, then given the technology at the current accelerator experiments, there is no possibility of producing these monopoles.

However, in the phase transitions during the very early stages of the universe, monopole production would have been possible. Being stable particles, the monopole density could only be diminished by annihilation of monopole-antimonopole pairs. With the rapidly expanding universe however, these pairs might have a harder time 'finding' each other, and therefore an appreciable density of monopoles might have persisted. These GUT models do lead to the *cosmological monopole problem*, which predicts the monopole density to be comparable to that of the baryon density, giving rise to a contradiction between GUT and cosmological models. This problem is avoided by considering the inflationary universe model which, apart from providing other cosmological problems, reduces the monopole abundance to an acceptably small level. With multiple scenarios in which monopoles can be produced [50], searches for cosmological monopoles attract an active interest amongst experimentalists, the only "problem" being that these cosmological models make no definitive predictions on the monopole abundance.

A stringent limit on the flux of the monopoles is obtained from the Parker limit [51]. It observes that magnetic monopoles are accelerated by the magnetic field of the Milky Way galaxy whose energy density is dissipated at a rate proportional to the monopole density. A flux bound for magnetic monopoles of $10^{-16} cm^{-2} s^{-1} sr^{-1}$ is obtained by requiring that the magnetic field energy is not substantially depleted within a time period of the order of 10^8 years. This rate of dissipation of the magnetic field energy exhibits a mass dependence, thereby altering the flux limit for monopoles with mass $\geqslant 10^{20}$ GeV to $10^{-13} cm^{-2} s^{-1} sr^{-1}$.

The velocities of the heavy cosmological monopoles are affected by gravitational and magnetic fields. Independent of its mass, a cosmological monopole would acquire a galactic in-fall velocity of $10^{-3}c$ from gravitational fields alone. The effect of the galactic magnetic field of strength $B \approx 3 \times 10^{-10}$ T, on a cosmological monopole of Dirac charge over the coherence length of about $L \approx 10^{19}$ m results in a velocity of

$$v = \left(\frac{2g_D BL}{m}\right) \approx 10^{-2}c. \tag{22}$$

Monopoles travelling at such low velocities are highly penetrative, such that a monopole with mass 10^{16} GeV would penetrate 10^{11} cm of rock - essentially passing through the Earth without slowing down. Therefore, a combination of various detector techniques are applied in experiments searching for cosmological monopoles to be sensitive to a large range of monopoles masses[2].

The Laboratori Nazionali del Gran Sasso hosted the Monopole Astrophysics and Cosmic Ray Observatory (**MACRO**) [52] which is a large multipurpose underground detector. The detector collected data from 1989 to 2000, and was sensitive to GUT monopoles with velocity $\beta \geqslant 4 \times 10^{-5}$. Using a combination of layers of liquid scintillator, streamer tubes filled with a helium-n-pentane gas mixture and nuclear track detectors (NTDs), MACRO was able to set a flux limit of $1.4 \times 10^{-16} \mathrm{cm}^{-2}\mathrm{s}^{-1}\mathrm{sr}^{-1}$ for $\beta \geqslant 4 \times 10^{-5}$ [27].

The Radio Ice Cherenkov Experiment (**RICE, 2008**) located at the South Pole was well suited to search for intermediate-mass monopoles ($10^7 \leqslant \gamma \leqslant 10^{12}$) [35]. This is attributed to its large effective volume and its ability to clearly distinguish between a monopole that drastically loses energy in the ice as opposed to a neutrino event. The experiment was sensitive to relativistic ($\gamma \geqslant 10^6$) intermediate-mass monopoles, i.e. monopoles with mass significantly less than the conventional GUT energy [53]. With no observed monopole-like events, RICE was able to set an upper limit on the monopole flux of the order of $10^{-18} \mathrm{cm}^{-2}\mathrm{s}^{-1}\mathrm{sr}^{-1}$. While the β range covered by RICE is fairly limited compared to previous searches, the limits established for intermediate-mass monopoles exceeded those from MACRO by two order of magnitudes.

A balloon-borne experiment called **ANITA-II** (Antarctic Impulsive Transient Apparatus) accumulated data for 31 days between December 2008 and January 2009 [54]. The experiment was designed to detect Cherenkov radiation produced in ice, with the capabilities of detecting ultra-relativistic monopoles. In the absence of any monopole-like events, ANITA-II set an upper limit on the monopole flux to $10^{-19} \mathrm{cm}^{-2}\mathrm{s}^{-1}\mathrm{sr}^{-1}$ within the kinematic range of $\gamma \geqslant 10^9$.

The **ANTARES** (Astronomy with a Neutrino Telescope and Abyss environmental RESearch) experiment is an underwater telescope based in the Western Mediterranean Sea [55]. It is deployed at a depth of 2467 m with modules consisting of photomultiplier tubes that detect Cherenkov radiation from the ionisation of the sea water. Fast monopoles ($\beta \geqslant 0.51$) of charge $1.0 g_D$ are expected to produce 8550 times more Cherenkov photons than muons of the same velocity [36]. ANTARES took data for 116 days (in 2007-2008) and with different analysis selections applied to different monopole β bins in the range $0.55 \leqslant \beta \leqslant 0.995$. One single event was observed in the range, $0.675 \leqslant \beta \leqslant 0.725$, which was consistent with the expected atmospheric muon and neutrino background. A 90% Confidence Limit (C.L.) upper limit on the monopole flux is set in the

2 In a sense, the induction method which is solely dependent on the magnetic flux produced by a monopole, it is capable of detecting monopoles of all masses and velocities.

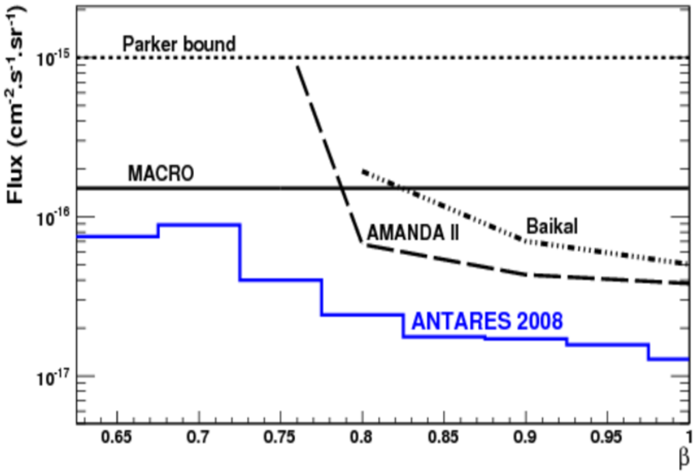

Figure 4: The ANTARES 90 % C.L. upper limit on an upgoing magnetic monopole flux for relativistic velocities $0.625 \leqslant \beta \leqslant 0.995$ obtained in this analysis, compared to the theoretical Parker bound [51], the published upper limits obtained by MACRO [27] for an isotropic flux of monopoles as well as the upper limits from Baikal [56] and AMANDA [57] for upgoing monopoles [36].

range 1.3×10^{-17} and $8.9 \times 10^{-17} \mathrm{cm}^{-2}\mathrm{s}^{-1}\mathrm{sr}^{-1}$ for monopoles in the range $0.625 \leqslant \beta \leqslant 0.995$, as shown in Fig. 4.

Located at the South Pole, the **IceCube** experiment consists of 86 strings with 60 digital optical modules (DOMs) each [58]. These consist of photomultiplier tubes to detect Cherenkov radiation and are deployed at a depth of 1450 - 2450 m and cover a total volume of one cubic kilo-meter. Using the data collected in 2008-09 and 2011-12, searches for relativistic ($\beta \geqslant 0.76$) and mildly relativistic ($\beta \geqslant 0.51$) monopoles were made. No candidates for monopoles were found and a monopole flux limit was constrained down to a level of $1.55 \times 10^{-18} \mathrm{cm}^{-2}\mathrm{s}^{-1}\mathrm{sr}^{-1}$ [36].

The **SLIM** (Search for LIght Monopoles) experiment located at the Chacaltaya high altitude Laboratory (5230 m) consisted of an array of a large NTDs [25]. The detector was sensitive to intermediate monopole mass in the range $10^5 < M < 10^{12}$ GeV. It had a β-dependent charge sensitivity, with sensitivity to charge $2g_D$ in the range $4 \times 10^{-5} < \beta < 1$ and to charge $1g_D$ in the range $\beta > 10^{-3}$. With no candidates found in the NTDs, a 90% C.L. upper limit of $1.3 \times 10^{-15} \mathrm{cm}^{-2}\mathrm{s}^{-1}\mathrm{sr}^{-1}$ was set [28].

The **Super-Kamiokande** [59] experiment sets a stringent limit on the monopole flux ranging from 6×10^{-28} to $7 \times 10^{-20} \mathrm{cm}^{-2}\mathrm{s}^{-1}\mathrm{sr}^{-1}$ for monopoles with mass $m > 10^{17}$ GeV. This limit was set using 2853 days of data taken over a decade (from Apr. 1996 - Aug 2008) through three upgrade cycles of the Super-K [60]. The approach at Super-K was to detect an excess of neutrinos from the sun with an energy of 29.79 MeV which are produced when monopoles accumulate and catalyse proton decays.

The searches for monopoles trapped in matter provide a complimentary alternative to collider searches and searches in cosmic rays. The experiments that search for trapped monopoles are sensitive to low mass monopoles that may be a result of secondary production in collisions between high-energy cosmic rays and astronomical bodies. In addition, they are also sensitive to high mass monopoles that may have been formed in the early universe (during the Big Bang nucleosynthesis) and may be trapped in the core of planetary bodies, known as *stellar monopoles*. A small summary of such searches is provided below. For a comprehensive description see [45] .

Atmospheric monopoles

Monopoles in the atmosphere can be gathered through a detector using a stronger field of a large magnet (depending on the polarity of the monopole). Such an approach was used over an effective collecting area of 24,000 m^2 and a 90% C.L. limit of $4.4 \times 10^{-16} cm^{-2} sr^{-2} s^1$ was set on the monopole flux of incoming positively charged monopoles for a wide range of masses (up to 10^7 GeV), charge (1.0-12.0g_D) and energies ($10^2 - 10^{11}$ GeV) [61].

If monopoles thermalise in the atmosphere, the surface of magnetite outcrops which act as attraction sites is a possible location to detect them. Using a portable extraction device, 1000 m^2 of a site in the Adirondack Mountains was scanned for positively charged monopoles. With no monopoles being found, a limit on the monopole flux of about $1.6 \times 10^{-14} cm^{-2} sr^{-1} s^1$ for monopoles with charge above 1.0g_D and mass below 10 GeV [39].

Ocean searches

Monopoles can accumulate in deep-ocean deposits if they are thermalised by either the atmosphere or in ocean water [40, 41, 42]. The large exposure time (of the order of a million years) is the main advantage of such searches, which is also sensitive to higher masses and energies (given the depth of the ocean) compared to above sea-level experiments.

The most stringent limit from the ocean searches resulted from the combination of three different searches. These were performed on 1600 kg of sediments from deeper ocean (4.4 km depth on average), 8 kg of 2.5-cm-thick ferromanganese crust from the Mid-Atlantic ridge and four manganese nodules collected from the floor of the Drake Passage using the extraction technique. A combined upper limit of $4.8 \times 10^{-19} cm^{-2} sr^{-1} s^{-1}$ was set for cosmic monopoles with magnetic charge of magnitude 1.0-60.0g_D, with masses below 130 GeV, stopping in the atmosphere or ocean.

Searches in moon rocks

Using the induction technique, Moon rock samples that were collected during the Apollo missions (19.8 kg in total) were analysed for magnetic monopoles in the early 1970s. These samples have an expected exposure time of about 500 million years. A flux limit of $6.4 \times 10^{-19} cm^{-2} sr^{-1} s^{-1}$ was set for cosmic monopoles that would stop within a 4 m depth of the Moon's surface [62, 63].

Polar volcanic rocks

Monopoles created in the early universe and bound to the planetary cores could resurface by being bound to polar rocks. A search conducted in 2013, used 23.4 kg of volcanic rocks from a large variety of locations in arctic and Antarctic areas and analysed them using the induction technique. The search resulted in a limit of $1.6 \times 10^{-5}/gm$ at 90% confidence limit on the stellar monopole density in the Solar System. In addition, this search was extended to interpret cosmic monopoles within an energy and mass range that were likely to stop inside the Earth, yielding a limit of $2.2 \times 10^{-14} cm^{-2} sr^{-1} s^{-1}$ [64].

1.7 SEARCHES FOR MONOPOLES AT COLLIDERS

Indirect searches

The **L3** experiment at LEP searched for indirect monopole signatures by looking for the process $Z \to \gamma\gamma\gamma$ [65]. The process which is highly suppressed in the Standard Model has its cross section enhanced by the existence of monopoles that would couple to the Z boson. The analysis found the results consistent with Quantum Electrodynamics (QED) background expectations which lead to setting a branching ratio limit $BR(Z \to \gamma\gamma\gamma) < 0.8 \times 10^{-5}$, with a lower limit on the mass of the monopole at 520 GeV.

At Tevatron, the **DØ** experiment performed another indirect search at $\sqrt{s}$ = 1.8 TeV [66]. The search focused on the high monopole-photon coupling, which is orders of magnitude higher than the photon coupling to the electric charge. The analysis expected virtual monopoles to give rise to photon-photon re-scattering as described in [67, 68]. With no excess of events observed over the background, lower 95% C.L. limits of 610, 970, *or* 1580 GeV on the mass of spin-0, ½ and 1 Dirac monopole is set.

Searches at e^+e^- colliders

The **MODAL** (Monopole detector at LEP) experiment (the predecessor of MoEDAL), was a dedicated monopole experiment at the e^+e^- LEP collider operated at $\sqrt{s}$ = 91.1 GeV [30]. The MODAL experiment placed NTD foils around the I5 interaction point at LEP, with monopoles expected to have distinct tracks of highly ionising particles through the foil. With no candidates for monopoles found during two exposure periods in 1990 and 1991, MODAL set cross section limits of 70 pb assuming the Drell-Yan mechanism. A similar attempt using NTD foils wound around the beam pipe and other parts of the **OPAL** (Omni-Purpose Apparatus at LEP) detector produced cross section limits of 0.3 pb, assuming the Drell-Yan mechanism [69]. With a centre-of-mass energy of 90 GeV at LEP, both these experiments were able to probe masses up to only 45 GeV, for charges up to $2.0g_D$.

The results from a search at **OPAL** at LEP2 with data collected at $\sqrt{s}$ = 206.3 GeV improved on those from LEP. The search focused on monopole signatures of high ionisation in the jet chambers of OPAL and bent tracks in the plane parallel to its solenoid magnetic field. With zero events observed, the upper limits on the production cross section of Drell-Yan produced monopoles of charge $1.0g_D$ in the mass range of 45-102 GeV, was set to 0.05 pb.

Searches at HERA

The beam pipe from the **H1** experiment at the e^+p HERA collider running at $\sqrt{s}$ = 300 GeV, was used to search for monopoles using the induction technique [70]. With no events consistent with monopole signal detected, upper limits varying from 0.06 pb to 2 pb (for charges 1.0-6.0g_D) in the mass range 5-140 GeV were set. It should be noted that this search assumed a pair-production of monopoles through photon-photon interactions, since Drell-Yan production does not occur in e^+p collisions. The model considered in this search considered monopoles of spin-0 produced in elastic collisions and those of spin-½ monopoles produced in inelastic collisions.

Searches at Tevatron

Three independent analyses were carried out at Tevatron for the direct search of magnetic monopoles. The first used the induction technique on detector samples of the DØ and **CDF** (Collider Detector at Fermilab) detectors that were exposed to collisions at $\sqrt{s}$ = 1.8 TeV [71]. The search assumed a Drell-Yan production mechanism and set upper limits on the production cross sections at 0.6, 0.2, 0.07 and 0.2 pb for charges 1.0, 2.0, 3.0 and 6.0g_D respectively. Correspondingly lower mass limits were set at 265, 355, 410 and 375 GeV respectively. In addition to the induction search, the CDF experiment used collision data with $\sqrt{s}$ = 1.96 TeV to search for monopoles with a dedicated time-of-flight trigger that is sensitive to monopoles with $\beta > 0.2$ [34]. The analysis relied on the monopole signature of high ionisation associated with a track consistent with a magnetically charged particle. With no events observed after the analysis selections, an upper limit on the production cross section of 10^{-2} pb, assuming the Drell-Yan production mechanism for monopoles of charge $|g|$ = 1.0g_D is set, with a lower mass limit set to 476 GeV.

Searches at LHC

The most recent collider search for magnetic monopoles comes from the **ATLAS** experiment with data from 7 TeV pp collisions [72]. The search used a combination of the Transition Radiation Tracker (TRT) and the Electromagnetic (EM) Calorimeter to identify signatures of monopoles of masses ranging from 200 to 1500 GeV. The analysis selections found no monopole events compatible with those of an expected monopole signature. A model independent limit using fiducial regions of high and uniform selection efficiency (see subsection 3.4.7 for details for a similar procedure adopted for the analysis described in this dissertation) was used to set a limit of about 2 fb on the production cross section of monopoles of charge 1.0g_D and with masses ranging from 200 to 1500 GeV. Additionally, the analysis also considered a Drell-Yan production mechanism to set the cross section limit that ranged from 0.2 to 0.02 pb for masses between 200 to 1200 GeV. The lower mass limit of 862 GeV was obtained for a Drell-Yan produced monopole.

The ATLAS analysis carried out at $\sqrt{s}$ = 7 TeV, is the inspiration for the work that is presented in this dissertation which performed a similar search at the increased centre-of-mass energy in 2012. In this work, a new trigger was developed that allowed ATLAS to probe magnetic monopoles with charges greater than 1.0g_D, for the first time. In addition, the trigger could also select events with lower energies, thereby significantly improving the overall signal efficiency of the analysis. This work also documents an analysis that was performed with the Magnetic Monopole Trapper (MMT) prototype of the MoEDAL experiment. The MoEDAL experiment is sensitive to

Experiment	Type of search	$\sqrt{s}$	σ_{limit}	Mass limit [GeV]
L3	Indirect	91.1 GeV	0.8×10^{-5} [3]	520
DØ	Indirect	1.8 TeV	-	610
MODAL	Direct	91.1 GeV	70 pb	45
OPAL (LEP)	Direct	91.1 GeV	0.3 pb	45
OPAL (LEP2)	Direct	206.3 GeV	0.05 pb	45-102
H1	Direct	300 GeV	0.06 pb	5-140
DØ, CDF Detector material	Direct	1.8 TeV	0.6 pb	265
CDF	Direct	1.96 TeV	0.01 pb	476
ATLAS	Direct	7 TeV	0.2 - 0.02 pb	200 - 1200

Table 1: A summary of the previous experimental searches for magnetic monopoles with 1.0 g_D Dirac charge at colliders.

probe much higher charges of magnetic monopoles (up to $g = 6.0g_D$) and provides a complementary analysis to the ATLAS searches.

3 This indirect search set limits on the branching fraction as described in the text

2

THE LARGE HADRON COLLIDER, ATLAS AND MOEDAL

2.1 THE LARGE HADRON COLLIDER

The CERN accelerator complex (see Fig. 5) is a series of machines that progressively increases the energy of the proton beams in each machine before the next in series takes over. The LHC is the last element of this chain, where protons are accelerated up to the record energy of 7 TeV [73].

In the Linear Accelerator (LINAC 2), the protons are sourced from a hydrogen gas bottle by stripping the gas of its electrons on passage through an electric field. At the end of LINAC 2, protons reach an energy of 50 MeV and enter the Proton Synchrotron Booster (PSB) [1]. The beams are passed on from PSB to the Proton Synchrotron (PS) and then to the Super Proton Synchrotron (SPS). At the end of each synchrotron the protons are accelerated gradually from 1.4 GeV to 25 GeV and finally to 450 GeV. They are then transferred to the LHC (in both directions of the LHC ring, the fill time is 4′20″ per LHC ring) where they are accelerated to their nominal energy of 7 TeV. Under normal operating conditions, beams could circulate in the LHC approximately 15 hours [73].

The Large Hadron Collider (LHC) is a two-ring-superconducting-hadron accelerator and collider that is installed in the 26.7 km tunnel, which was formerly occupied by the Large Electron-Positron (LEP)

1 marked as only BOOSTER in Fig. 5

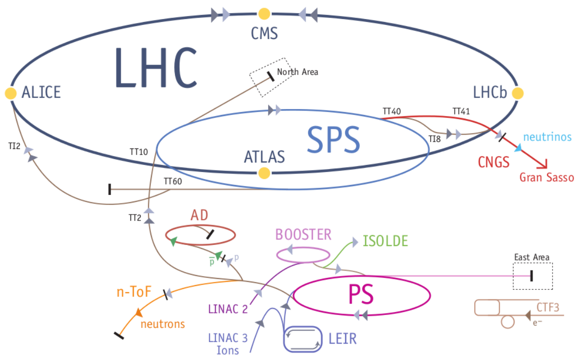

Figure 5: The CERN accelerator complex with the LHC forming the largest and the final element in a series of machines used to boost the energy of the particle beams. Taken from Ref. [74].

Parameter	2010	2011	2012	Design Value
Beam energy	3.5	3.5	4	7
Bunch spacing [ns]	150	75/50	50	25
Maximum number of bunches	368	1380	1380	2808
Maximum bunch intensity (protons per bunch)	1.2×10^{11}	1.45×10^{11}	1.7×10^{11}	1.15×10^{11}
Peak luminosity [$cm^{-2}s^{-1}$]	2.1×10^{32}	3.7×10^{33}	7.7×10^{33}	1×10^{34}
Maximum mean number of events per bunch crossing	4	17	37	19

Table 2: The table highlights a few important parameters of the LHC. The table is taken from [75].

collider. The tunnel lies between 45 m and 170 m underground on a plane inclined at 1.4% sloping towards the *Leman* lake.

In the LHC, particles circulate in a vacuum tube and are manipulated using electromagnetic devices. Dipole magnets help keep the particles in near circular orbits, quadrupole magnets focus the beam and accelerating cavities are electromagnetic resonators that accelerate particles.

The protons are circulated around the LHC ring in 2808 bunches, with each bunch consisting of about 10^{11} protons. The LHC is designed to operate with a bunch spacing of 25 ns, however during the 2012 data taking period, the bunch spacing was 50 ns. Tab. 2 lists the important parameters of the LHC.

One of the goals of the LHC is to probe the physics beyond the SM with a centre-of-mass collision energies of up to 14 TeV. For a given process, the number of events generated per second in the LHC collisions is given by:

$$N_{event} = L\sigma \tag{23}$$

where σ is the cross section of the process of interest and L the machine luminosity. The luminosity depends on different beam parameters which can be described for a Gaussian beam distribution by:

$$L = \frac{N_b^2 n_b f_{rev} \gamma_r}{4\pi\epsilon_n \beta*} F \tag{24}$$

where N_b is the number of particles per bunch, n_b the number of bunches per beam, f_{rev} the revolution frequency, γ_r the relativistic gamma factor, ϵ_n the normalised transverse beam emittance and $\beta*$ the beta function at the collision point. The geometric luminosity reduction factor F takes into account that the beams collide under a small crossing angle.

The cross sections have by definition the dimension of an area which are denoted in units of barn (1 barn = 10^{-28} m^2). Different physics processes have different cross sections associated to them, with rarer processes (possibly even the production of monopoles) having very low cross sections. In order to observe such processes one must make sure to have sufficiently large number of collisions (luminosity) within a reasonable time.

The absence of the observation of beyond the SM physics is results in setting a *cross section limit* for a given process. These limits describe the constraint on the production cross section of a physics process which can be easily compared across various experiments.

There are four interaction points of the LHC where the two proton beams cross each other. At each interaction point a detector is located to study the interactions as seen in Fig. 5. ATLAS and CMS are two high luminosity experiments that are designed to run at a peak luminosity of $L = 10^{34}$ $cm^{-2}s^{-1}$ for proton collisions. The dedicated B-physics detector, LHCb, is a low luminosity precision experiment with a typical peak luminosity of $L = 10^{32}$ $cm^{-2}s^{-1}$. The LHC will also operate with heavy ion beams for ALICE (A Large Ion Collider Experiment) which intends to study the quark-gluon plasma and will have a peak luminosity of $L = 10^{27}$ $cm^{-2}s^{-1}$ for nominal lead-lead ion operations. The LHC can deliver a maximum total integrated luminosity per year of 80 - 120 fb^{-1}, depending on the average turnaround time of the machine during operation [73].

During the 2012 data taking period the maximum centre-of-mass energy reached was 8 TeV while the 13 TeV collisions began only in 2015.

2.2 THE ATLAS DETECTOR

The ATLAS detector is the largest detector at the LHC and like CMS is a multi-purpose detector, designed to perform precision Standard Model (SM) experiments as well as probe for new physics phenomena. Weighing about 7000 tonnes, the detector provides hermetic coverage and is made of several sub-detector components that perform precision tracking, particle identification and measure a range of particle energies.

Fig. 6 shows a schematic diagram of the ATLAS detector with its sub-detector components marked out. The Inner Detector (ID) is encompassed in a 2 T solenoid field.

The significant energy loss of electrically charged particles at lower β compared to magnetically charged objects means that monopoles are likely to penetrate further into the detector as compared to HECOs. This is reflected in the Fig. 7 which shows the minimum kinetic energy required by electrically (left) and magnetically (right) charged objects to reach the EM calorimeters in ATLAS (and other detectors).

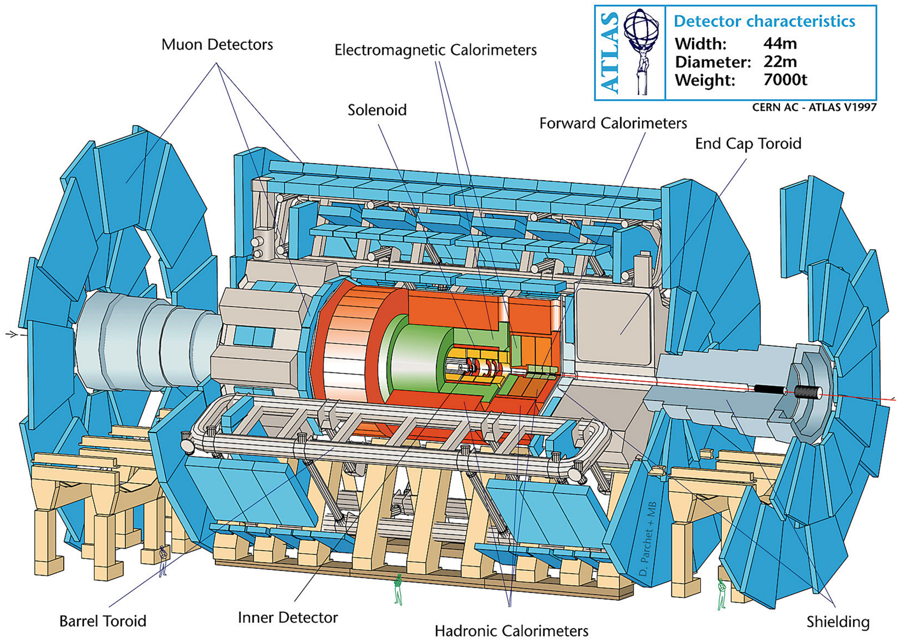

Figure 6: A cut-away view of the ATLAS detector [76].

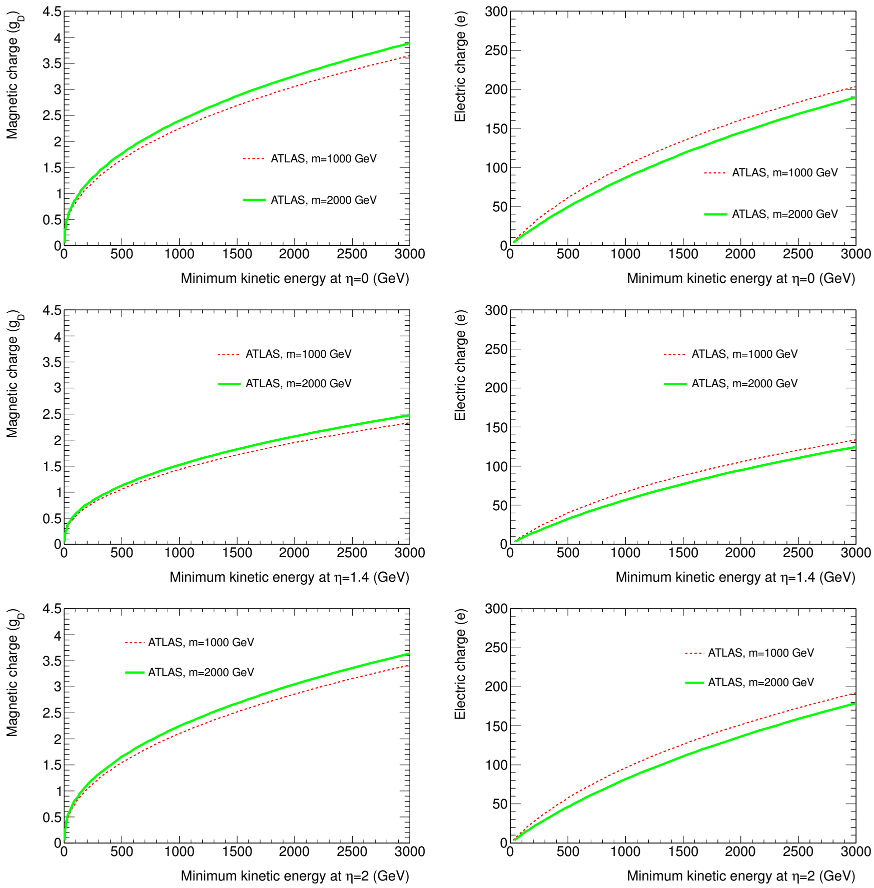

Figure 7: The minimum kinetic energy required by HIPs to reach the calorimeter of the ATLAS detector, as a function of the magnetic charge (left) and electric charge (right). The curves are shown for 1000 GeV and 2000 GeV masses at angles corresponding to η~0 (top), η~1.4 (middle) and η~2.0 (bottom) [24].

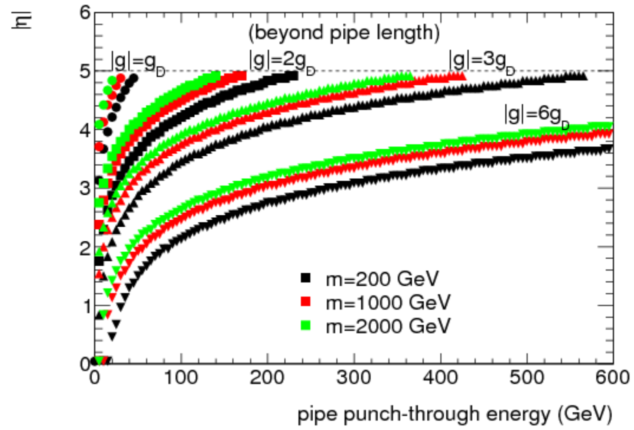

Figure 8: The energy below which magnetically charged particles stop in the ATLAS or CMS beam pipe as a function of pseudo-rapidity for various magnetic charges and masses [24].

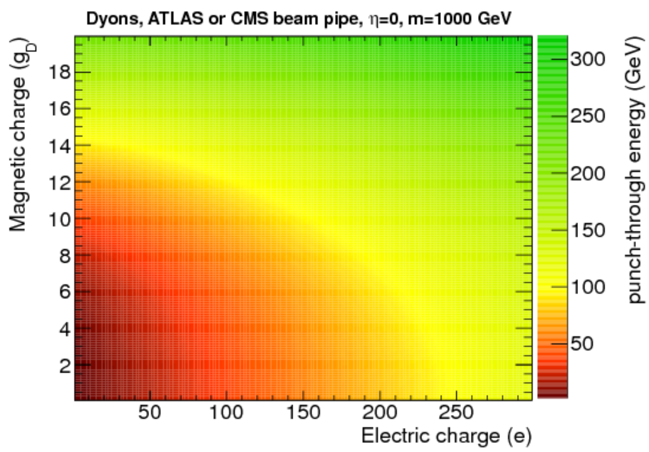

Figure 9: The energy below which magnetically and electrically charged dyons with $m = 1000$ GeV and $\eta = 0$ stop in the ATLAS or CMS beam pipe as a function of their magnetic and electric charges [24].

2.2.1 *The beam pipe*

Particles from collisions at ATLAS need to penetrate through the beryllium beam pipe before entering the ID. The relatively high density of beryllium is capable of stopping low energy and high mass HIP candidates as seen in Fig. 8. Fig. 8 shows that low energy monopoles do not punch through the beam pipe at low $|\eta|$. Similarly, the punch through energy for dyons (particles with both electric and magnetic charge) with η =0 and m=1000 GeV, is shown Fig. 9.

2.2.2 *The ATLAS Inner Detector*

Submerged within the large solenoid is the optimised, multi-technology ID [77] used as the central tracking detector. Within $|\eta| <$ 2.5 the ID is designed to provide excellent momentum and track resolution of charged particles from both primary and secondary vertexes, above a given p_T threshold (nominally 0.5 GeV) [76]. In addition,

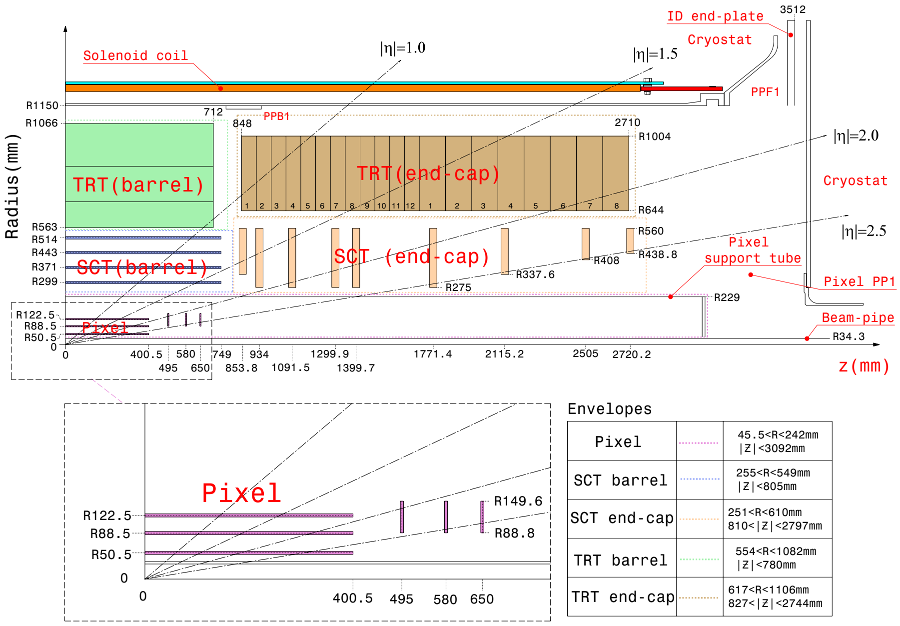

Figure 10: Plan view of the quarter-section of the ATLAS inner detector showing each of the major detector elements with its active dimensions and envelopes [76].

it also provides electron identification over $|\eta| < 2.0$ and an energy range extending from 0.5 GeV to 150 GeV.

The cylindrical ID has a length of ± 3512 mm (about the origin on the z-axis) and a radius of 1150 mm. Three independent but complementary sub-detectors constitute the ID, with the envelopes of each sub-detector shown in Fig. 10, the details of which can be found in [76]. The silicon pixel and micro-strip layers provide precise and discrete space points that allow for high-resolution track pattern recognition. These layers are surrounded by the TRT that comprise many layers of gaseous straw tube elements interleaved with transition radiation material. The TRT provides continuous tracking to enhance the pattern recognition and improve momentum resolution within $|\eta| < 2.0$.

Fig. 11 and 12 show the sensors and the structural elements that are traversed by 10 GeV tracks in the barrel and end-cap regions respectively.

The different components of the ID respond differently to the high ionisation of traversing HIPs.

The **Pixel detector** consists of 1744 silicon pixel modules [78] arranged in three concentric layers in the barrel and three disks in each end-cap. It covers the radial distances from 50.5 mm to 150 mm. Each module consists of 47,232 pixels, with each pixel of about 50µm $\times$ 400 µm. The distance between adjacent pixels (or strips) is known as *pitch*. The direction of the shorter pitch on the pixel modules helps define the local x and y coordinates giving the precision measurement in the R-ϕ plane [79]. The y-coordinate is given by the longer pitch which is oriented approximately along the z-axis in the barrel and along the R in the end-cap. Each module consists of 16 radiation-hard front-end chips [80] and a total of ~80.4 million readout channels for the pixel

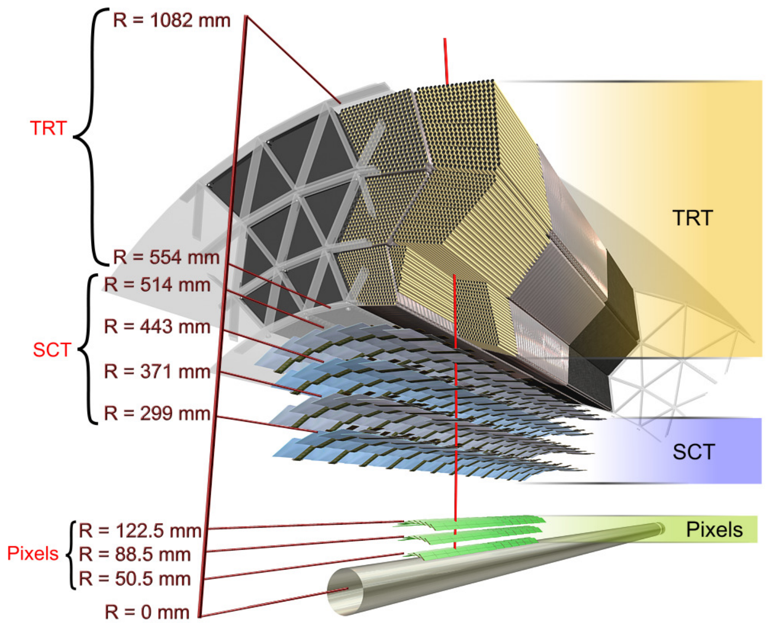

Figure 11: A schematic drawing showing the sensors and structural elements traversed by a charged track of 10 GeV p_T in the barrel inner detector (η=0.3). The track traverses through the beryllium beam pipe, three cylindrical silicon-pixel layers, four cylindrical double layers of barrel silicon-microstrip sensors and approximately 36 axial straws in the barrel TRT modules [76].

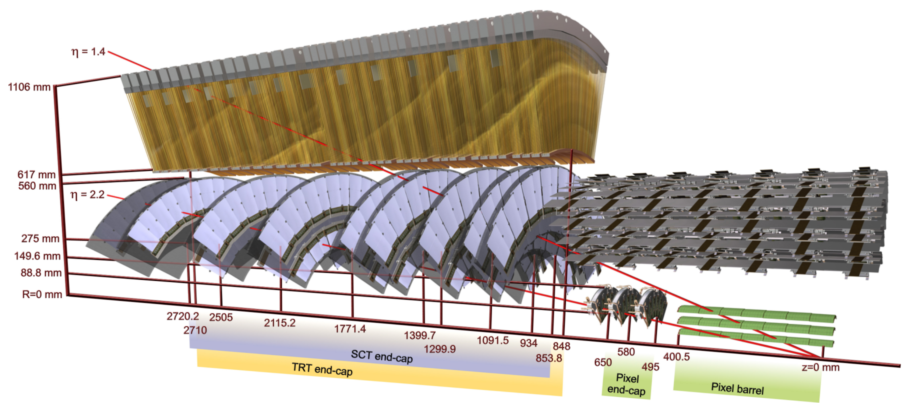

Figure 12: Drawing showing the sensors and structural elements traversed by two charged tracks of 10GeV p_T in the end-cap inner detector (η=1.4 and 2.2). The end-cap track at η=1.4 traverses successively the beryllium beam pipe, the three cylindrical silicon-pixel layers, four of the disks with double layers of end-cap silicon-microstrip sensors (SCT), and approximately 40 straws contained in the end-cap TRT wheels. In contrast, the end-cap track at η=2.2 traverses successively the beryllium beam pipe, only the first of the cylindrical silicon-pixel layers, two end-cap pixel disks and the last four disks of the end-cap SCT. The coverage of the end-cap TRT does not extend beyond $|\eta|$=2 [76].

detector. For particles originating from the interaction point, the pixel layer provides three measurement points.

HIPs traversing through pixel

The charge delivered on each sensor is amplified by an analogue block and compared to a programmable threshold (3.5 keV in the case of ATLAS) using a comparator [81]. The Time-over-Threshold (ToT) is calculated by subtracting the Trailing Edge (TE) time stamp from the Leading-Edge (LE) time stamp. The calibration results in a ToT count of 30 for a minimum ionising particle that is incident normally on the 250 μm thick sensor [82]. The hit information is deleted if the hit time exceeds the latency of the L1 trigger (approximately 3.2 μs), corresponding to a ToT overflow at 255. The high ionisation of the traversing HIPs causes a large ToT resulting in the loss of signal from the pixel.

The **SemiConductor Tracker** (SCT) detector system is composed of 4088 modules of silicon-strip detectors spanning radially from 299 mm to 560 mm. In the barrel, the modules are arranged in 4 concentric layers around the interaction point, parallel to the solenoid with a constant pitch of 80 μm. In each end-cap region the modules are placed on 9 disks perpendicular to the z-axis with variable pitch. Most SCT modules consist of four silicon-strip sensors - two on each face of the module. A hybrid readout channel is placed between these sensors which has a binary output that registers a hit if the pulse height in a channel exceeds a preset threshold; normally corresponding to a charge of 1 fC.

HIPs traversing through SCT

The SCT readout architecture is binary, in which each channel holds information that conveys if the pulse-height from the hit is above the preset threshold or not. No further information about the size of the pulse is recovered later. The calibration of these thresholds is therefore central to the detector operation to ensure uniform, good efficiency while maintaining the noise occupancy at a low level. Unlike the pixel though, there is no loss of signal for a HIP traversing the SCT. However, its high ionisation generates high activity in the SCT - with large number of hits produced by the HIP and associated δ-electrons.

The **Transition Radiation Tracker** detector is a straw tracker composed of 298304 carbon-fibre reinforced Kapton straws 4 mm in diameter held at a potential of -1530 V with respect to a 31 μm diameter gold-plated tungsten wire at the centre referenced to ground [83]. It covers radial distances from 563 mm to 1066 mm. It is arranged in three cylindrical layers in the barrel with 32 modules in each layer and readouts at either ends. The end-cap modules are radially arranged in 80 wheel-like structures.

The TRT operates as a drift chamber, such that the base gas is ionised by the traversing charged particle creating about 5-6 primary ionisation clusters per mm of path length. A detectable signal is produced by the drifting electrons that reach the wire and cascade in the strong electric field. The signal on each wire is amplified, shaped and discriminated against an adjustable threshold [84]. The gas mixture used in the TRT is of 70% Xenon, 27% Carbon-dioxide and 3% Oxygen. Xenon gas has a high efficiency to absorb transition radiation photons, which is required for particle identification capabilities of the TRT [85, 86].

The custom-designed Application Specific Integrated Circuit (ASIC) is built for analog readout and performs Amplification, Shaping, Discrimination, and Base-Line Restoration (ASDBLR). A second ASIC, the Drift Time Measuring Read Out Chip (DTMROC) samples the results from ASDBLR and makes time measurement of the signals and provides a digitised result to off-detector electronics for up to 16 straw channels [84].

The TRT, is capable of registering a hit-type information regardless of the magnitude of the energy deposit. The average energy deposit by a minimum ionising particle is 2.3 keV, producing a low-threshold (LT) TRT hit[2]. The much higher energy from transition photons deposit about 6-15 keV and are detected by a second, higher threshold (HT) discriminator.

The basic operational mode of the TRT is the detection of avalanche currents on the anode wire initiated by the clusters of primary ionisation electrons from a track. For the avalanche currents above the threshold, the ASDBLR sends a pulse to the DTMROC where the LE - marked by the first transition bit - corresponds to the distance of closest approach. While the TE corresponding to the maximum drift time is, roughly, fixed to 2 mm. The TRT reads out data in three time periods, each of 25 ns, for any triggered event. Each of the 25 ns time periods is divided into eight time bins of 3.12 ns by the DTMROC, where the information about whether the low threshold is exceeded is recorded for every time bin. The high threshold hit information is registered separately over the entire 25 ns time period. If any of the time periods registers a HT bit, the hit is said to be a HT hit. When the Level-1 accept signal is received from the central ATLAS trigger system, the DTMROC ships 27 bits (24 bits for tracking and 3 bits of high threshold information for 3×25 ns periods) to the Back End RODs where it is assembled into events for Level 2 and later processing. The maximum drift time in the magnetic field is approximately 60 ns, which motivates the choice of sending three crossing times' worth of data. Fig. 13 shows an illustration of the readout from the DTMROC.

A HIP traversing the TRT will heavily ionise and produce a large number of δ-electrons. It is these δ-electrons that arrive simultaneously at the TRT straws that collectively cross the high threshold limit. Thus the distinct signature of HIPs traversing the TRT, is the large fraction of localised HT TRT hits. The average number of HT TRT hits for HIPs along its trajectory is over 60%.

The Fig. 14 shows the simulation of a charge $1.0 g_D$ monopole sample traversing through the ATLAS detector.

The **Beam Conditions Monitor** (BCM) monitors the background particles rate protects the silicon trackers from instantaneous high radiation doses caused by the LHC beam incidents. It consists of forward and background stations, each with with four modules located

2 The low threshold is set at about 300 eV [84]

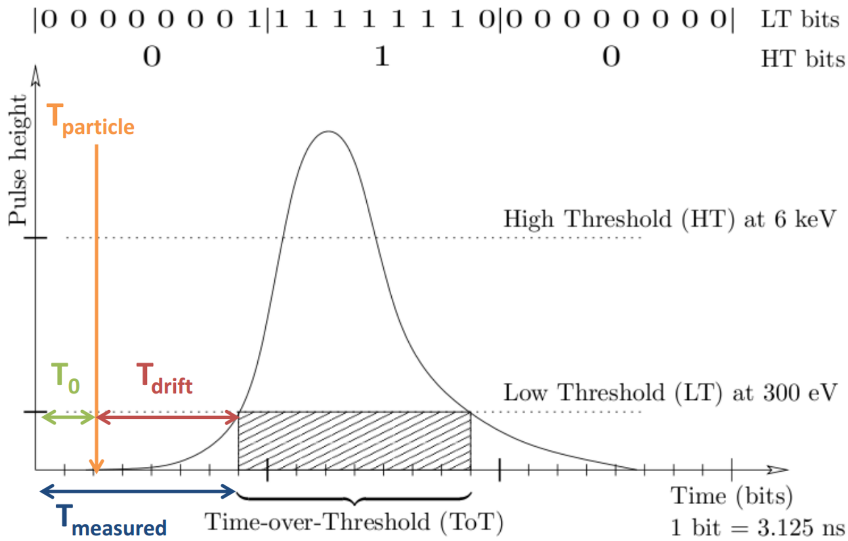

Figure 13: The TRT signal pulse in a 75 ns read-out window. The values of the low- and high-threshold bits are shown for the example pulse, with each low-threshold bit corresponding to a time bin of 3.12 ns and each high-threshold bit corresponding to a 25 ns time bin [87].

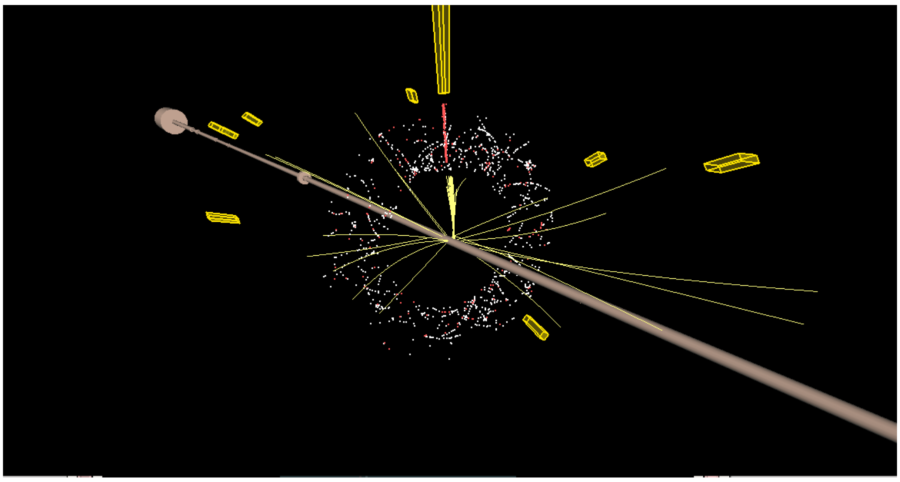

Figure 14: A simulated event of a $1.0g_D$ monopole of mass 1000 GeV in the ATLAS detector. The diagonal brown cylinder represents the beam pipe. The thin lighter yellow lines represent the inner detector tracks generated in the event. The darker yellow towers illustrates the electromagnetic deposits in the calorimeter. The white and red points represent the low and high threshold hits in the TRT. The trajectory of the monopole is demonstrated by the large number of tracks associated to the high density of high threshold TRT hits aligned with the calorimeter cluster (traversing vertically upwards in this figure).

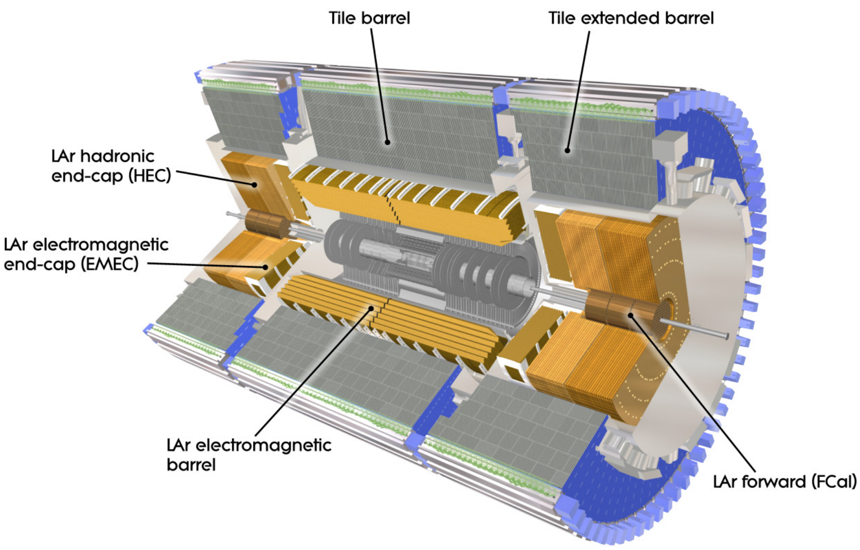

Figure 15: Cut-away view of the ATLAS calorimeter system [76].

at a radius of 5.5 cm at a distance of ± 1.84 m from the interaction point. The BCM signal provides trigger information as well as an instantaneous hit-rate used as input to the beam-abort signal.

2.2.3 *The ATLAS Calorimeters*

The ATLAS calorimeters comprise different sample detectors that provide full ϕ-symmetry and coverage around the beam pipe, as shown in Fig. 15 [76]. They cover the range of $|\eta| < 4.9$ and use techniques to satisfy the various requirements of different physics processes of interest as well as to match the radiation environment over this large η-range. The EM calorimeter provides fine granularity, in the η region that matches the inner detector, and is ideal for precision measurements of electrons and photons. While the rest of the calorimeter has coarser granularity which is sufficient for the physics requirements for jet reconstruction and missing transverse energy, E_T^{miss} measurements.

The calorimeters close to the beam pipe are housed in three cryostats, one barrel and two end-caps. The EM barrel calorimeter is placed in the barrel cryostat, while each end-cap cryostat contains an EM end-cap calorimeter (EMEC), followed by a hadronic end-cap calorimeter (HEC) and a forward calorimeter (FCal). The active detector medium of all these calorimeters is liquid argon (LAr), which is chosen for its intrinsic linear behaviour, radiation-hardness and stable response over time.

The main function of the calorimeters is to contain all the electromagnetic and hadronic particle showers and reduce limit punch-through into the muon system. Therefore, the calorimeter depth is an important design consideration. The EM calorimeter thickness is > 22 radiation lengths (X_0) in the barrel and > 24 X_0 in the end-caps. Good resolution of high energy jets is due to the approximately 9.7

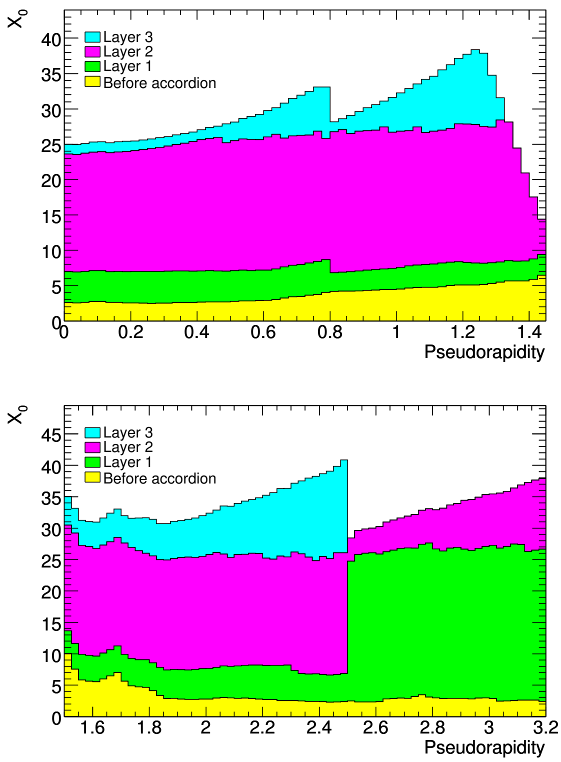

Figure 16: The cumulative amounts of material in units of radiation length X_0 and as a function of $|\eta|$ in front of the and in the electromagnetic calorimeters. The plots show for barrel (top) and end-cap (bottom) the thickness of each accordion layer as well as the amount of material in front of the accordion [76].

(10) interaction lengths (λ) of active calorimeter material in the barrel (end-caps). Combined with the 1.3 λ from the outer support the total thickness at $\eta = 0$ is shown to be sufficient to reduce punch-through well below the irreducible level of prompt or decay muons, in both measurements and simulations. With the large η coverage, this thickness ensures a good E_T^{miss} measurement that is essential for many physics signatures and in particular for SUperSYmmetric (SUSY) particle searches. Fig. 16 shows the material budget of the EM calorimeters in units of X_0.

The EM Calorimeter

Positioned right after the central solenoid system, the electromagnetic calorimeter (ECAL) consists of a barrel component ($|\eta| <1.475$) and two end-cap components ($1.375 < |\eta| < 3.2$). The barrel calorimeter is split into two identical halves, with a separation distance of 4 mm, at z = 0. The end-cap calorimeters is divided into two coaxial wheels, an outer wheel that covers the region $1.375 < |\eta < 2.5$ and an inner wheel covering $2.5 < |\eta| < 3.2$. An accordion geometry that provides complete ϕ symmetry without azimuthal cracks is used for Kapton electrodes and lead absorbed plates (see Fig. 17). The thickness of the lead absorber plates is optimised as a function of η in terms of the EM calorimeter performance in energy resolution. A presampler (at

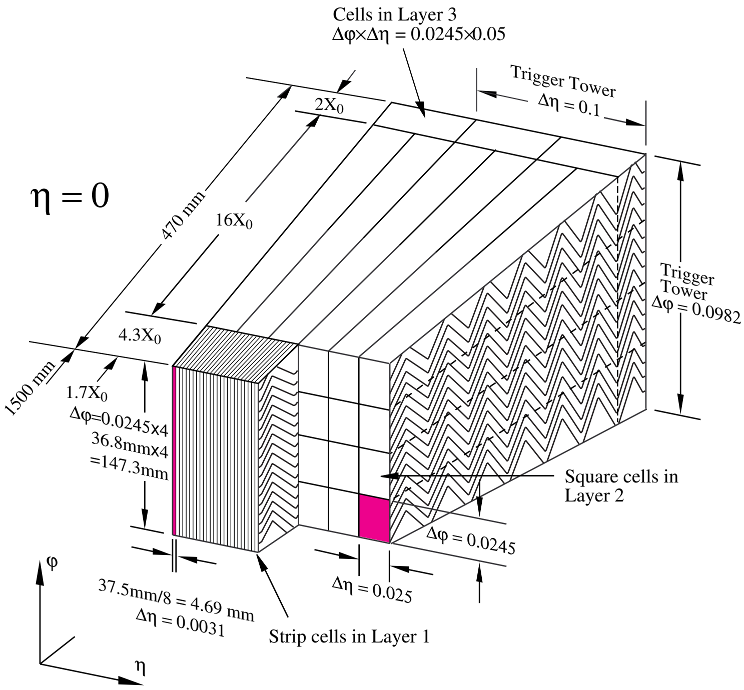

Figure 17: Sketch of a the barrel module showing the different layers of the EM calorimeter. The granularity in η and ϕ of the cells of each of the three layers and of the trigger towers is also shown [76].

$|\eta$ <1.8) is used to correct for energy lost by electrons and photons upstream of the calorimeter, which consists of an active LAr layer of 1.1 cm (0.5 cm) thickness in the barrel (end-cap) region.

Fig. 17 depicts an ECAL barrel module that has three layers - EM1, EM2 and EM3 with variable granularity. As can be seen, the EM1 is finely segmented along η, which gets coarser at the edge zones of the barrel and end-caps, the complete details can be found in [76]. The largest fraction of electromagnetic shower energies is collected in the deep EM2 layer. While the tails of the electromagnetic shower is collected in EM3 and is therefore less segmented in η.

A separate thin liquid-argon layer (11 mm in depth) called the **presampler** provides shower sampling in from of the active ECAL. In the barrel, the presampler is made up of 32 identical azimuthal sectors (there are two barrel regions, analogous to the rest of the ECAL) with the dimensions of each sector covering the half-barrel length and providing a coverage in $\Delta\eta \times \Delta\phi$ of 1.52×0.2. Each sector is composed of eight modules, with the length of the modules increasing with $|\eta|$ such that a constant η-granularity of $\Delta\eta = 0.2$ is obtained for each module, with the exception of the module at the end of the barrel, for which the η-coverage is reduced to 0.12.

The Hadronic calorimeters

Directly outside the ECAL envelope the **Tile calorimeter** is placed. It consists of the barrel region ($|\eta| < 1.0$) and two extended barrel regions ($0.8 < |eta| < 1.7$). The active material in these calorimeters are scintillating tiles and it uses steel as the absorber. Both regions are divided azimuthally into 64 modules and the total radial range of the Tile calorimeter region extends from an inner radius of 2.28 m to 4.25 m outer radius. Analogous to the ECAL, it is segmented in three layers with approximately 1.5, 4.1 and 1.8 λ thick for the barrel and 1.5, 2.6 and 3.3 λ for the extended barrel. At η=0, the total detector thickness at the outer edge of the tile region is 9.7 λ.

The **Hadronic End-cap Calorimeter** is located directly behind the end-cap electromagnetic calorimeter and consists of two independent wheels per end-cap. The HEC provides a transitional layer between the end-cap and the forward calorimeters and has a range of 1.5 $\leqslant |\eta| \leqslant$ 3.2. Each wheel comprises of 32 identical wedge-shaped modules and is divided into tow segments in depth, for a total of four layers per end-cap.

The **Forward Calorimeter** provides uniform calorimeteric coverage of up to $|\eta| \leqslant 4.9$ as well as reduces the radiation background levels in the muon spectrometer. The FCAL is made up of three modules in each end-cap and the first of which is made of copper that provides electromagnetic measurements; while the remaining two are made of tungsten that predominantly measure the energy of hadronic interactions.

2.2.4 *The Muon system*

The charged particles that exit the barrel and end-cap calorimeters are detected using the muon spectrometer. The spectrometer triggers on muon-like events and provides charged particle tracking within the $|\eta| < 2.7$ region. The bending of the muon tracks is facilitated by large barrel toroid in the $|\eta| < 1.4$ region and by two end-cap inserted into both ends of the barrel toroid over the range $1.4 < |\eta| < 1.6$. The Resistive Plate Chambers and Thin-Gap Chambers form a part of the muon trigger system. While the Monitored Drift Tubes and Cathode Strip Chambers provide precision measurements. The conceptual layout of the muon spectrometer is shown in Fig. 18.

2.2.5 *Overview of the ATLAS Trigger System*

The collision rate at the LHC is 40 MHz for a bunch spacing of 25 ns, which at nominal luminosity of L = 10^{34} cm^{-2}s^{-1} has around 23 pile-up events in addition to the signal event per bunch crossing. The incoming event rate is far too high to be written directly to the mass storage systems and events are stored based on selections performed by a three level trigger system.

The first of these is the hardware Level-1 (L1) trigger based on coarse calorimeter [88] and muon information. Raw event fragments from the different sub-detectors are read out in parallel in pipeline memories. The latency offered by Level-1 is 2.5 μs and it needs to reduce the bunch crossing rate of 40 MHz to 75 kHz (approximately selecting 1% of total collisions). The Level-1 readout data is added

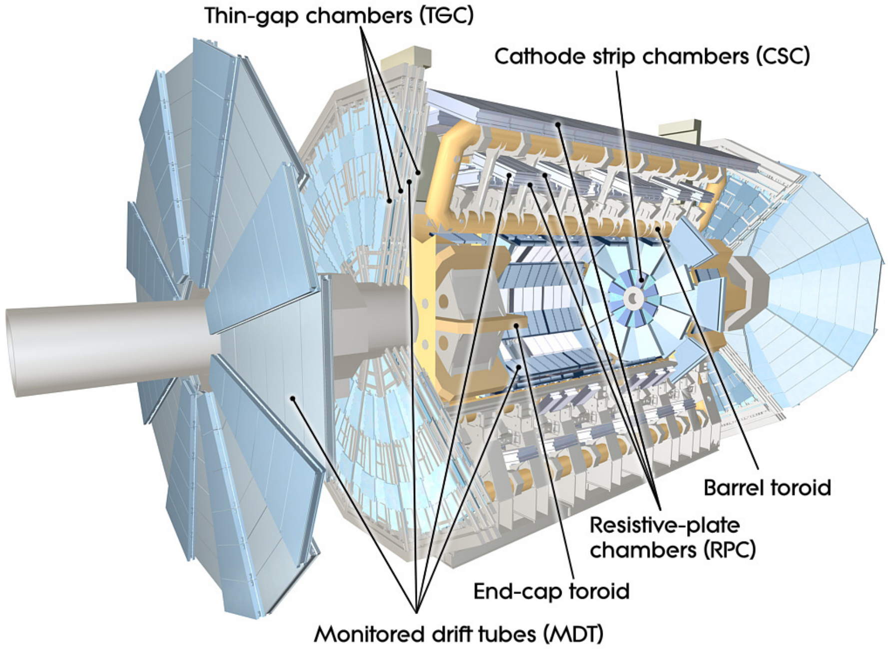

Figure 18: Cut-away view of the ATLAS muon system [76].

to the readout stream via a dedicated Read-out-driver (ROD), if the event is accepted.

The Level-1 trigger identifies Regions of Interest (RoI), which are considered for processing in the latter stages of the trigger system. The information of the RoI coordinates, energy and type of signature is passed onto the Level-2 of the trigger [89].

The e/γ Level-1 requires transverse isolation and that showers do not penetrate to the hadronic calorimeters. Trigger towers are constructed of fixed $\Delta\eta \times \Delta\phi$ sizes which measure the transverse energy within them. Fig. 19 shows a 2×2 trigger-tower region at the centre of a 4×4 trigger-tower window [76]. For the ECAL, for each of the four possible 1×2 and 2×1 pairs within the region, the transverse energy E_T values are summed, in order to find relatively narrow showers. In the case of the e/γ algorithm at least one of the four sums is required to pass the programmable threshold in E_T. For this analysis, the Level-1 threshold was η dependent with a minimum requirement of 18 GeV. Each of the four EM 1×2 and 2×1 pairs is added to the sum of 2×2 'core' towers in the hadronic calorimeter, and at least one of the four sums is required to pass the threshold. To ensure that the e/γ shower is contained in the EM calorimeter, the sum of the core 2×2 hadronic region must be less than the programmed hadronic veto threshold - 1 GeV in the case of this analysis.

The software based triggers are the Level-2 (L2) and the Event Filter (EF) that are collectively the High Level Trigger, or simply, HLT. At Level-2 the entire event granularity within the RoI is available and the data is retrieved from the read-out-buffers (ROB). Unpacking relevant data from only relevant regions of the detector saves time, especially in data preparation and reconstruction algorithms. The Event Filter and the Level-2 work similarly with different time latencies -

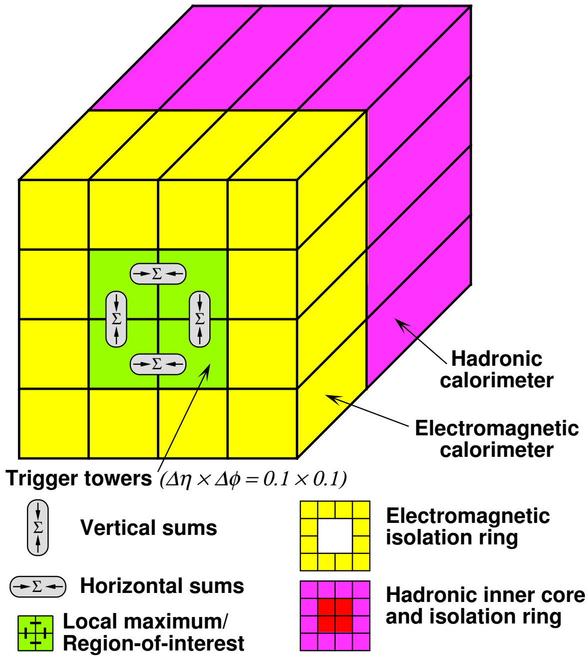

Figure 19: Building blocks of the electron/photon and tau algorithms with the sums to be compared to programmable thresholds [76].

the Event Filter being afforded more time. The HLT as a whole is responsible for reconstructing physics processes and optimising the system performance.

The HLT strategy is to reject 'uninteresting' events as quickly as possible and maximise the computing resources on the important events. To this effect, a *seeded* and *stepwise* reconstruction approach has been selected at ATLAS. "Seeded" implies that successive levels of the triggers are seeded by the previous ones. "Stepwise" means that reconstruction of particles takes place in steps and are rejected as soon as they fail some selection at any given step, freeing up resources for the next RoI or event.

Signatures of each physics process is represented by a *trigger chain* at each trigger level. Each trigger chain is an item in the *trigger menu* that is compiled to reconstruct the various processes. For the reconstruction of basic trigger objects (electrons, photons etc) fast *feature extraction algorithms* (FEX) are used that are interleaved with *hypothesis algorithms*. Each trigger chain is composed of at least one FEX and hypothesis algorithms collectively known as a *sequence*. Fig. 20 shows a schematic diagram of a trigger chain.

One or more FEX algorithms can be used per step and apart from the basic reconstruction, these algorithms generate detector features that are analysed and converted into trigger quantities. These quantities are used by the hypothesis algorithms which apply cuts on them and decide if the candidate is still 'good' or not. The chain is immediately terminated if at any step the hypothesis algorithm rejects the RoI, and moves onto the next one. The trigger chain is said to have passed if all the criteria of all the sequences are met.

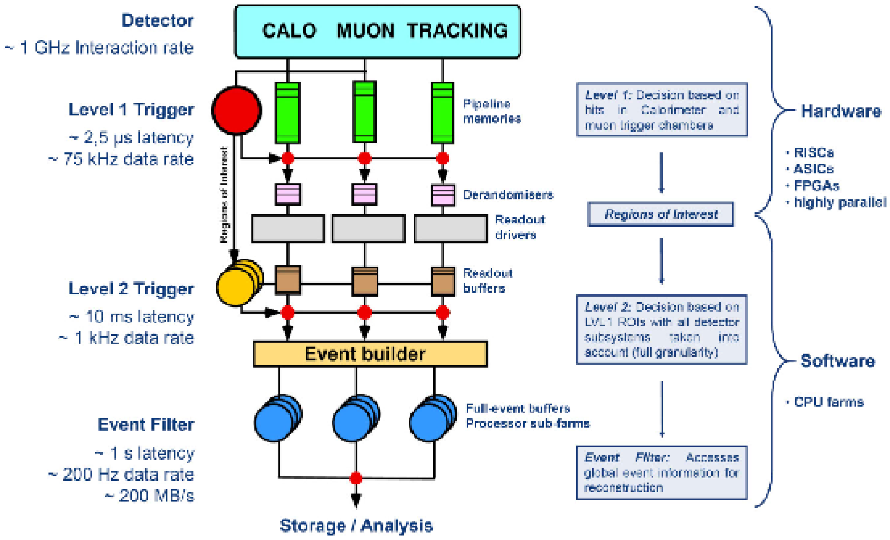

Figure 20: Illustration of a sequence in the ATLAS trigger system [88].

2.3 THE MOEDAL DETECTOR

The Monopole & Exotics Detector at the LHC (MoEDAL) experiment is a dedicated experiment designed to enhance, in a complementary way, the physics reach of the LHC. The primary objectives of MoEDAL is to directly search for the Magnetic Monopole or Dyon and other highly ionising Stable (or meta- stable) Massive Particles (SMPs) at the LHC.

The MoEDAL experiment [90] is located at Interaction Point 8 (IP8) along with the single arm forward LHCb detector. Deployed around the LHCb experiment's Vertex Locator (VELO) vacuum vessel, it is a unique and largely passive LHC detector that comprises four sub-detector systems - two Nuclear Track-Detectors (NTDs), a TimePix pixel device sub-system and the Magnetic Monopole Trapper (MMT) sub-detector. The NTDs and MMTs are two complementary passive sub-detector systems designed to search for highly ionising particles. Stacks of NTDs placed around the interaction point are used to trace the passage of highly ionising particles, optimised to probe a range of particle charges. The MMTs consist of roughly 800 kg of aluminium samples are capable of slowing and eventually trapping the highly ionising particles; providing samples that are used for direct detection and measurement of magnetic charges by a superconducting magnetometer. The TimePix pixel detector array monitors the radiation environment in the MoEDAL cavern.

The advantage of using passive detection techniques is that MoEDAL is not dependent on model assumptions or restrictions from any electronic triggers or any limitations from electronic readouts. The rear side of IP8, provides a relatively open and low material budget environment for the passage of highly ionising particles. A noticeable feature of MoEDAL is the absence of backgrounds - while Standard Model particles might fog the NTD plates, they are highly unlikely to mimic the signal of new physics. Similarly for MMTs, it is

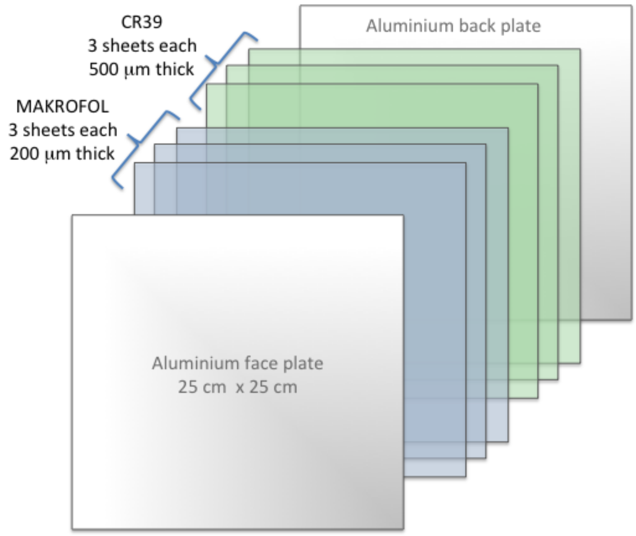

Figure 21: The composition of a MoEDAL NTD stack, the lexan sheets are not shown [91].

next to impossible for Standard Model particles to produce signals of trapped monopoles.

2.3.1 *Nuclear track detectors*

The NTDs consist of nine plastic sheets comprising of 3 sheets of CR39, 3 sheets of MAKROFOL and 3 Lexan sheets that form the first, middle and end sheets of the stack [91, 92, 90]. A depiction of the basic MoEDAL NTD stack is given in Fig. 21. Highly ionising particles that might be produced in collisions would pass through the plastic detector whose trajectory is marked by damages to the NTD stack. The damage zones are revealed as cone-shaped etch-pits by using a hot sodium hydroxide solution on the plastic detector. The etching process is followed by scanning the plastic sheets using manually controlled and/ or computer controlled optical scanners. The holes left by the etching process are detected by the scanners to an accuracy better than ~ 50 μm in the multi-layered NTD stack. The base areas of the etch-pit cones increase with increasing ion charges and the trajectories of each highly ionising particles are reconstructed by tracking the etch cones successively through the stack.

In 2015, a novel high-threshold NTD array ($Z/\beta \sim 50$). the Very High Charge Catcher (VHCC) was installed in the forward acceptance region of the LHCb detector. Placed between the LHCb RICH1 detector and the Trigger Tracker (TT), the VHCC consists of two flexible low-mass stacks of MAKROFOL in an aluminium foil envelope. It is the only part of the MoEDAL detector in the forward region of the LHCb and it enhances considerable the overall geometrical acceptance of the MoEDAL NTDs.

Figure 22: Left: Photograph of the 2012 MMT test array placed downstream of the LHCb stacked under the beam pipe 1.8 m away from the interaction point along the back of the VELO vacuum vessel.

2.3.2 *TimePix*

To measure the radiation levels in the cavern, TimePix pixel device arrays (256 × 256 square pixels with a pitch of 55 µm) are used. The TimePix provides a real-time radiation monitoring system of highly-ionising beam-related backgrounds. The TimePix chip consists of a preamplifier, a discriminator with threshold adjustment, synchronisation logic and a 14-bit counter. These TimePix devices are used by MoEDAL in Time-over-Threshold modes where each pixel acts as an analog-to-digital converter for energy measurement. In other words, the devices act as tiny electronic bubble-chambers providing a real-time measurement of the energy deposition of the backgrounds in the cavern [91, 93].

2.3.3 *MMT sub-detector system*

Before the deployment of the full 800 kg of MMT detector in 2015, a prototype of the sub-system was installed in 2012. The trapping prototype consisted of 160 kg of aluminium rods of 60 cm length with a diameter of 2.5 cm, placed in 11 boxes that were stacked as close to the LHCb interaction point as permissible (see. Fig. 22). Aluminium is a good choice for the trapping volume material three important reasons. First, the large magnetic moment of the aluminium nucleus means that it will strongly bind a trapped monopole [38]. Second, aluminium does not present a problem with respect to activation. Lastly, with aluminium being non-magnetic, it favours the stability of the SQUID magnetometer during measurements. In addition to the above, aluminium is cost-effective and readily available.

The 11 boxes comprising the trapping material were stacked in two columns, that were numbered 1 to 11 starting from the bottom, with the eleventh box centred on top of the two columns. The boxes were placed downstream of the LHCb detector, immediately in front of the

LHCb VELO vacuum vessel, covering 1.3% of the total solid angle (Fig. 22). In the LHCb coordinate system[3] the position of the centre of the top box was $(x, y, z) = (0, -45\text{cm}, -150\text{cm})$ with an uncertainty of 1 cm for each coordinate. A summary of the sub-detector geometry and its surroundings along with a quantification of the amount of material in radiation lengths (X_0) present in the installation is shown in Fig. 23. With an average of 1.4 X_0, the material budget between the interaction point and the trapping detector varies from 0.1 to 8 X_0.

Several components within the VELO vacuum vessel and on its outer wall along with various flanges, a vacuum pump and a vacuum manifold attached to the VELO vessel contribute significantly to the material budget. These components are implemented in the geometry simulations that is built on the LHCb geometry model. To model cables and small pipes, the approximation of a grid of material was used, with 101 vertical steel rods of radius 0.3 cm spaced out by 1 cm at z = -115 cm - representing an average of 2.3% of the total X_0. The uncertainty on the material budget is modelled by using two different sets of material geometries that are conservative estimates of the maximum and minimum amount of material that could be plausibly unaccounted for. The implementation of these geometries was done by changing the grid rod radius to 0.01 cm (minimum extra material) and 0.5 cm (maximum extra material), respectively. Simulations of monopoles propagating through the different geometries (using the GEANT4 toolkit) are used to determine the effect of this systematic uncertainty in the detector acceptance.

In September 2012, this initial MMT prototype was installed and exposed to 0.75 ± 0.03 $\text{fb}^{-1}$of 8 TeV proton-proton collisions. The rods were retrieved in 2013, and cut into samples of 20 cm length[4] with a non-ferromagnetic saw, for a total of 606 samples.

3 A right-handed coordinate system in which the z-axis points along the beam in the direction of the LHCb detectors, y is the vertical direction and x is the horizontal direction is used

4 Box 11 was an exception for the sample lengths, where the rods from this box were cut into a mix of 10, 15, 20 and 30 cm samples to study the dependence of the sample size on the magnetometer response

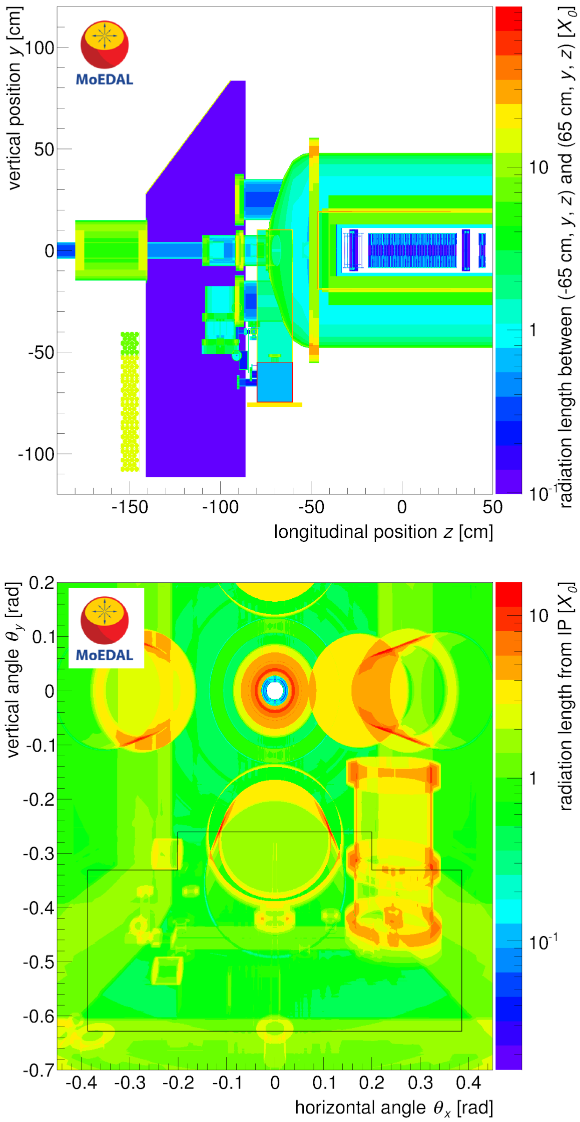

Figure 23: Material budget in radiation length in the yz plane for $|x| < 65$ cm (top) and in the $\theta_x\theta_y$ plane for $z = -145$ cm (bottom). In the bottom figure, the outline corresponding to the trapping detector position is indicated in black. The grid used as an approximation to model cables and pipes is not included in these figures [29].

3 SEARCHES IN ATLAS

3.1 SIMULATIONS OF MONOPOLES AND HECOS

To study the interactions of monopoles and HECOs with the ATLAS detector, simulations are developed based on the GEANT-4 software. The simulations take account of the equations of motion and the model of production of δ-rays by highly ionising particles. Simulations of the energy deposits are digitised and physics objects are reconstructed using the ATHENA software package.

The simulation process involves a series of steps called the **Full Chain** of Monte Carlo production that range from generating physics events to reconstructing detector processes. Fig. 24 shows the schematic representation of the full chain required for producing simulated samples. While most ATLAS analyses are performed on Analysis Object Data (AOD), this HIP analysis requires detailed information from the TRT which is available only in the Event Summary Data (ESD) data format.

Simulations of physics processes are handled by the ATLAS Production Group that produces centrally the simulated samples for all physics analyses groups. Large production campaigns through the year enable all the analysis at ATLAS to have simulated samples with the same geometry and physics conditions. The simulated samples for this analysis were produced in the MC12c campaign with the ATLAS-GEO-21-02-02 version of the simulated detector geometry implemented in GEANT-4 [94], the conditions tag OFLCOND-MC12-SIM-00 [95] which contains information relevant to the detector running conditions and the GEANT-4 physics list QGSP_BERT [96].

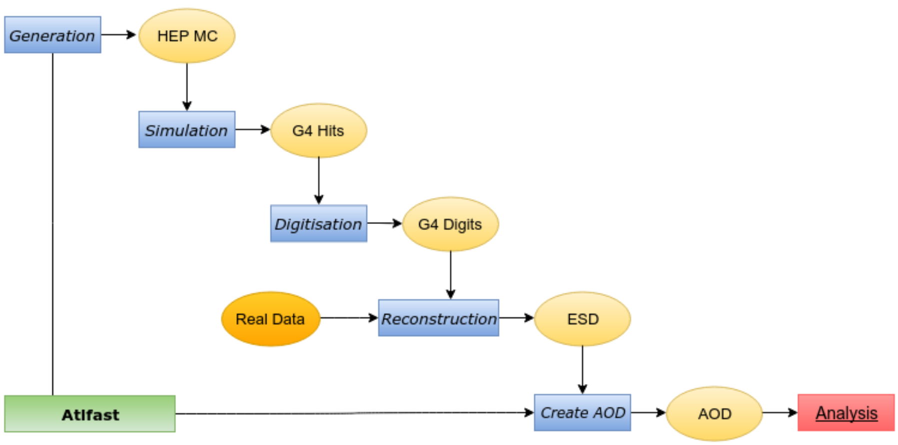

Figure 24: The full chain process used to generate simulated events in the ATLAS detector. The processes from the reconstruction step onwards are common to both simulated and real data events.

In the MC12c production campaign, the digitisation and reconstruction were performed using a single transform (step), DigiMReco_trf. It takes as input the GEANT-4 detector geometry, the offline conditions tag, the ATLAS software database (DBRelease-26.9.1), pile-up profile distribution and trigger menu database configuration (MC_pp_v4_tight_prescales) to produce simulations of HIPs through the ATLAS detector.

3.1.1 *Event generation*

The event generation step produces the primary final state particles for specified physics processes - in this case magnetic monopoles and HECOs. Different event generators are used to generate different types of physics processes; for example, Alpgen [97], AcerMC [98] and MadGraph [99] are tree level matrix element generators specialised on simulation of hard scattering processes via pertubative Quantum Chromodynamics (QCD). Full event generators such as PYTHIA [100], Herwig++ [101] and SHERPA [102] simulate the non-pertubative parton showering, hadronisation and underlying event. The matrix element generators can be interfaced with full event generators which is fed into the detector simulations.

From Ref. [24] the charge and mass reach of ATLAS at 8 TeV collisions is established. Two types of samples are simulated: first, single monopole events to obtain model-independent interpretations using the single particle generator [103] and second, spin-½ pair-produced monopoles assuming the Drell-Yan mechanism using the MadGraph5 generator.

Including both types of samples in total, 96 signal samples were fully simulated in which six mass points (200, 500, 1000, 1500, 2000 and 2500 GeV) were considered for four charges of both monopoles (0.5, 1.0, 1.5 and 2.0g_D) and HECOs (10, 20, 40 and 60e).

A large number of mass points are selected since no mass constraints are placed across various theories and to better study the model-independent results. The array of charge points selected are theoretically motivated, from monopole of charge g_D as predicted by Dirac, to 2.0g_D as predicted by Schwinger. Fractional magnetic charges are not predicted by theories, however this is no motivation not to search for them and historically they have been included in previous searches.

The output from the event generators are stored as a HepMC (high-energy physics Monte Carlo), a graph of particles and vertexes that is fed into the simulation step of the **Full chain**. The particles simulated in the event generation step are also known as the *truth particles*[1] and different from *reconstructed* particles which are created in the reconstruction stage.

1 The variables of interest associated with these objects, such as energy, pseudo-rapidity etc, bear the word *truth/ true* as a prefix to that variable name.

Single particle samples

The single particle generator can be conceptualised as a "Particle Gun" that fires a single monopole (or HECO) that is uniformly distributed in η, ϕ and E^{kin} through the detector. Therefore, no production mechanism is assumed for HIPs and cross section limits can be set assuming no specific production model. These model-independent cross section limit obtained with single particle samples serve as a crucial result for this analysis.

The ranges of these parameters in this analysis were: 10 GeV $< E^{kin} <$ 3000 GeV, $-\pi < \phi < \pi$ and -3 $< \eta <$ 3. For each mass and charge points sets of 50,000 event samples were generated with equal number of monopoles (HECOs) and anti-monopoles (anti-HECOs).

Drell-Yan samples

Simulations of pair-produced spin-½ monopoles in proton-proton collisions at a centre-of-mass energy of 8 TeV were made using the Monte Carlo leading-order matrix element generator MadGraph5 [99]. The parton distribution function (PDF) CTEQ6LI [104] is used with the AU2 [105] tune. Generated four-vectors are processed by the PYTHIA8 [100] generator that adds parton shower, hadronisation effects and decays of the by-products of the simulated proton-proton collisions. The generated particles are processed by PYTHIA until 20,000 events have been successfully simulated.

To optimise for computational usage, a requirement on the minimum transverse momentum, p_T, of the generated particles was imposed to ensure that only those HIPs that are energetic enough to reach the EM calorimeter are simulated [72]. This requirement was mass and charge dependent and was obtained by finding the transverse momentum at which the L1 trigger efficiency was non-zero. The obtained minimum p_T was chosen about 50-100 GeV below the turn-on, in order to remain conservative.

Dirac's theory [106] has no restrictions on the spin of the monopoles and thus the search is extended to include spin-0 magnetic monopoles as well as HECOs. Generator-level samples of Drell-Yan pair-produced spin-0 HIPs were used to infer their reconstruction efficiency as described in [107]. The full simulation of spin-0 events was avoided since the interaction of HIPs with the ATLAS detector is spin-independent and the spin-dependent differences in efficiency can be quantified at the generator level using the production kinematic distributions alone.

For determining the systematic uncertainties, various 5000 event samples were at times re-simulated, see Sec. 3.6 for all details.

3.1.2 *Simulation*

In this step the event-generated HIPs are passed through a GEANT-4 simulation of the ATLAS detector to record the trajectories and energy depositions as GEANT-4 **hits**. The ATLAS-GEO-21-02-02 version of the ATLAS geometry is implemented in the simulation.

The passage of magnetic monopoles through the GEANT-4 simulation of the ATLAS detector is not implemented by default. A custom simulation package, SIMULATION/G4EXTENSIONS/MONOPOLE/, was developed that correctly sets the equations of motion for magnetically charged particles in electromagnetic fields (Eq. 16). In addition, the package computes the energy loss for fractional and integer magnetic charged (using Eq. 18) in units of g_D while taking into account the generation of δ-rays as well as the propagation of the monopole through the detector. The simulation package is an extension of the one developed for the 2011 monopole search [72].

The following sub-sections highlight the features implemented via the monopole simulation package in GEANT-4.

Energy deposition by HIPs

Ionisation, pair-production and bremsstrahlung are the three primary energy loss mechanisms by which electromagnetically charged particles interact with matter [108, 21, 109]. As seen in Fig. 1 shows the energy loss in Argon of a mass 1000 GeV and charge $1.0g_D$ monopole is dominated by ionisation mechanism [110, 19]. The pair-production and bremsstrahlung mechanisms are thus neglected for monopoles and HECOs.

The energy loss for HECOs given by Eq. 17 is implemented in the G4HIONISATION [111] class of GEANT-4 [112, 113], which simulates their continuous energy loss.

For monopoles, the energy loss by ionisation given by Eq. 18 is implemented in the monopole simulation package. Eq. 18 predicts the energy loss to be proportional to g^2, as seen in Fig. 25 which shows the energy loss of monopoles as a function of speed-of-light fraction β. However, the inverse β-dependence in Eq. 17 for the energy loss of HECOs means that they lose more energy as they slow down unlike monopoles that ionise more when travelling with higher β.

The energy loss equations for monopoles along with the KYG (Eq. 19) and B (Eq. 20) corrections for fractional and multiple charged monopoles are implemented in G4MPLATLASIONISATIONWITHDELTAMODEL class.

Effect of the magnetic field

The Inner Detector of ATLAS is encompassed by a solenoid magnet that produces a 2 T field parallel to the beam axis (as described in Sec. 2.2). The HECO simulations use the known laws of motion in a magnetic field such that they bend in the r-ϕ plane that is perpendicular to the magnetic field. This can be illustrated by plotting the difference between the ϕ position of the reconstructed HECO clusters and their truth values, as seen in Fig. 26.

However, the electrically neutral magnetic monopoles are accelerated (decelerated) along the direction of the magnetic field in the r-z

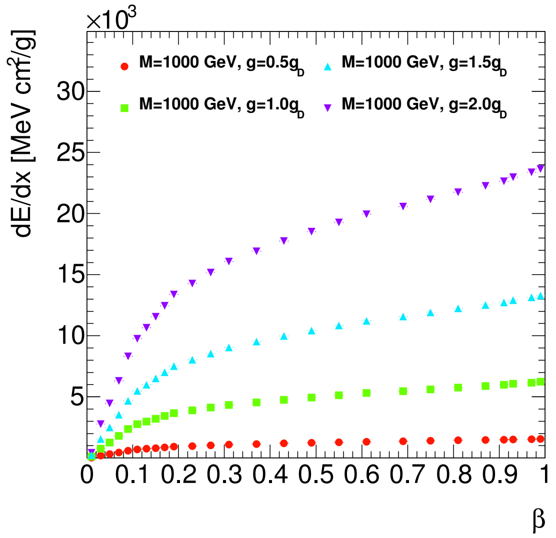

Figure 25: The energy loss via ionisation of the magnetic monopole for charges $0.5g_D$, $1.0g_D$, $1.5g_D$, $2.0g_D$ of mass 1000 GeV as a function of the monopole speed-of-light fraction β [114].

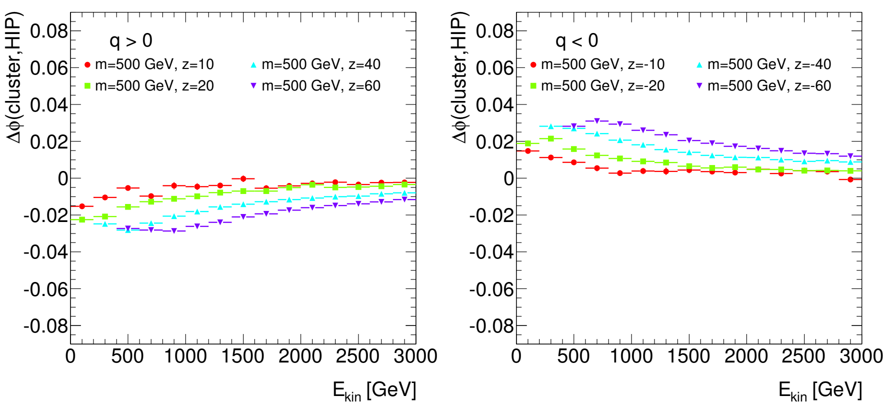

Figure 26: Profile histograms of the difference between the EM cluster ϕ and the HECO truth ϕ as a function of HECO truth kinetic energy. The plots are for HECOs with a mass 500 GeV and charges $|z| = 10e$, 20e, 40e and 60e. HECOs with electric charge $z > 0$ are plotted on the left and with electric charge $z < 0$ on the right. High-charge HECOs lack entries at the lower E_{kin} values because they need higher energies to penetrate through the detector up to the EM calorimeter [114].

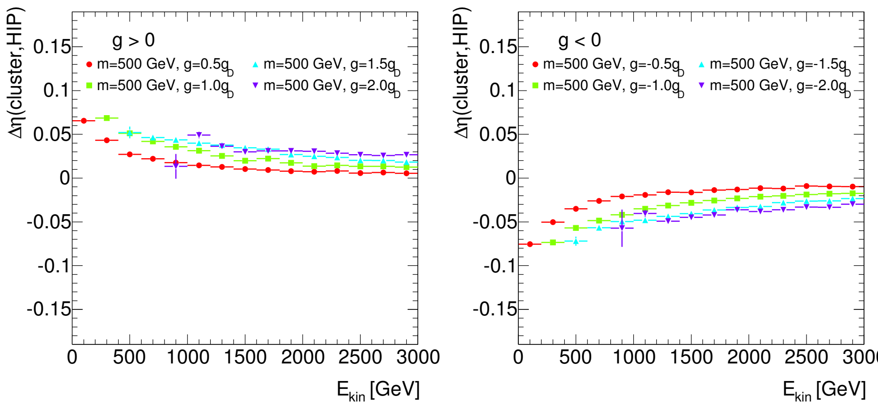

Figure 27: Profile histograms of the difference between the EM cluster pseudo-rapidity η and the monopole truth pseudo-rapidity as a function of monopole truth kinetic energy. The plots are for monopoles with a mass of 500 GeV and charges $|g| = 0.5g_D$, $1.0g_D$, $1.5g_D$ and $2.0g_D$. Monopoles with magnetic charge $g > 0$ are plotted on the left and with magnetic charge $g < 0$ on the right. High-charge monopoles lack entries at the lower E_{kin} values because they need higher energies to penetrate through the detector up to the EM calorimeter [114].

plane. Thus clusters reconstructed in simulation are misaligned in η with respect to their truth counterparts as seen in Fig. 27.

As expected, the positively charged monopoles and HECOs bend in the opposite direction with respect to their negative analogues. The extent of bending is proportional to the charge of the HIP.

Monopole timing

The acceleration of monopoles in the magnetic field requires integrating the monopole equation of motion over the changing velocity at each step of its propagation. Otherwise, the time propagation parameter of the monopole is set to zero. A new class, G4MplEquationSetup, was developed that correctly instantiates the monopole equations of motion when simulating its propagation through the detector.

Modifications to the monopole simulation package are validated in the TRT and the calorimeter. Fig. 28 shows the distance of the TRT hit from the interaction point as a function of time for several monopole tracks in the detector. Each dotted line represents a pair-produced spin-½ monopole; there are in total 10 monopoles in the figure. The effect of acceleration of different monopoles in the magnetic field can be seen in this figure.

The calorimeter cluster times[2] for the different mass and charge combinations are shown in Fig. 29. As expected, heavier monopoles record higher cluster times in the calorimeter since they travel, on

2 In the calorimeter, the cluster time is computed as the weighted average of the arrival time on each calorimeter cell, by using the square of the cell energy as weights; all calorimeter cells belonging to the cluster are used, except those from the presampler layer. For clusters with cells only in the presampler have the timing information set to zero.

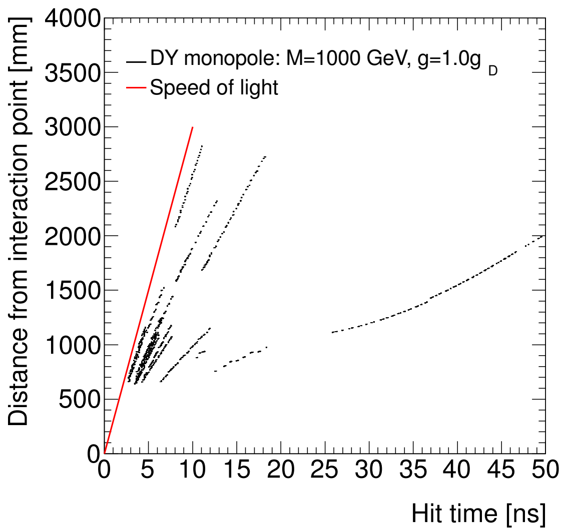

Figure 28: TRT hit distance from the interaction point as a function of time for magnetic monopoles of mass 1000 GeV and charge $|g| = 1.0g_D$ from 10 events chosen randomly in a simulated sample. The red line shows the hit distance vs time expected for a particle travelling at the speed of light [114].

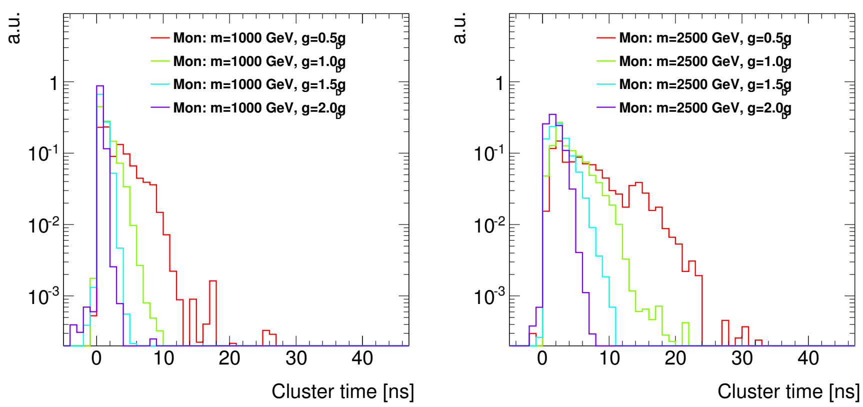

(a) (b)

Figure 29: Cluster times for single monopoles of mass 1000 GeV (left) and 2500 GeV (right) for various charge combinations [114].

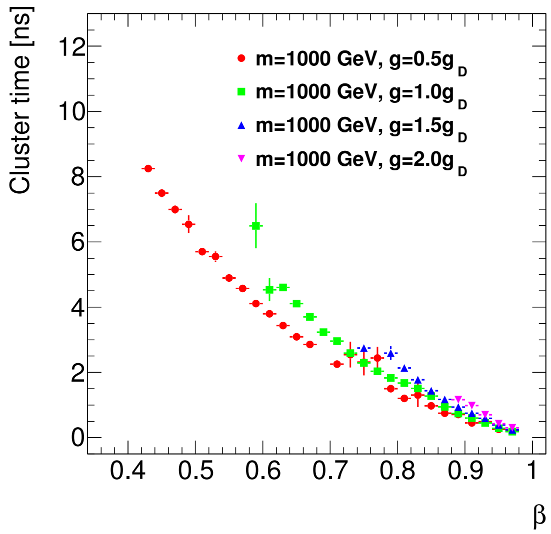

Figure 30: Average cluster time for single monopoles generated in $|\eta| < 0.3$ of various mass and charge combinations as a function of monopole speed β [114].

average, at lower speeds than lighter monopoles. The range in β for different charges vary. Lower charge monopoles have a broader β spectrum due to their lower energy loss enabling them to penetrate further into the detector and form clusters even for lower initial energies. The average calorimeter cluster timing as a function of the monopole's generated β is shown in Fig. 30. Only monopoles generated centrally ($|\eta| < 0.3$) are considered in Fig. 30 to eliminate geometrical dependence. The arrival time of low charge monopoles is lesser, on average, than those of higher charge monopoles, which only reach the calorimeter if they have sufficiently high β to reach the calorimeter.

The geometrical dependence of the calorimeter cluster timing is seen in Fig. 31 which shows the profile distribution of the cluster timing as a function of η for single monopoles of different masses and charges. An η dependence based on the charge of the monopole is observed. It should be noted that since the lower charge monopoles have a broader β spectrum, they are more likely to reflect the amount of material traversed before reaching the calorimeter.

δ-ray production

HIPs ionise the ATLAS detector material through which they traverse, producing a large number of δ-rays [108, 21, 109]. These δ-rays have significantly higher energies that is carried away from the core of the HIP trajectory and sufficient to further ionise the medium. The production of δ-rays is modelled in [109] and is implemented in the G4eIonisation class of the simulation package, which include the secondary δ-ray and Bremsstrahlung production.

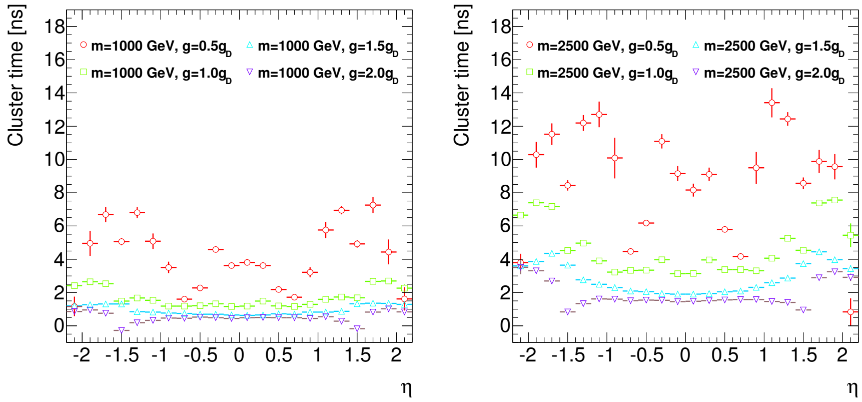

(a) (b)

Figure 31: Average cluster time for single monopoles of mass 1000 GeV (left) and 2500 GeV (right) for various charge combinations as a function of η [114]. The lower mass monopoles record smaller cluster times compared to their heavier counterparts of the same charge.

Recombination effects in Liquid Argon

The charge collected by each cell of the calorimeter from the ionisation of the Liquid Argon determines the energy deposited in the ECAL. The ionisation density is high in the case of monopoles and HECOs, which allow electron-ion pairs to recombine before the charge is collected by calorimeter cells, thus resulting in a lower recorded energy and underestimating the deposited energy.

This phenomenon described by Birk's Law [115, 116, 117, 118] was implemented in the ATLAS simulation since April 2010 in the form:

$$E_{vis} = E_0 \frac{1 + A' \frac{k}{E_D}}{1 + \frac{k}{(\rho E_D)} \frac{dE}{dx}}, \tag{25}$$

where E_0 and E_{vis} are the true deposited and visible energy respectively. The energy deposited per unit length is given by $\frac{dE}{dx}$ and ρ is the LAr density. E_D is the drift electric field assumed to be uniform 10 kV/cm.

The Birks' constant, k, was measured by the ICARUS TPC collaboration [119] to be 0.0486 (kV/cm)(g/cm^2)(1/MeV) by using cosmic ray muons and protons. The normalisation parameter, A', is set to 1.51 [120].

Using heavy-ion data to describe the recombination effects for very high dE/dx values, a correction to the Birks' law was developed [121]. The ICARUS measurement only described well the recombination effects by particles with single electric charge. Fig. 32 shows the correction implemented in the ATLAS simulation, while Fig. 33 summarises the resulting improvement. The value of the correction is taken as a constant for dE/dx > 12,000 MeV/cm due to lack of available data [121].

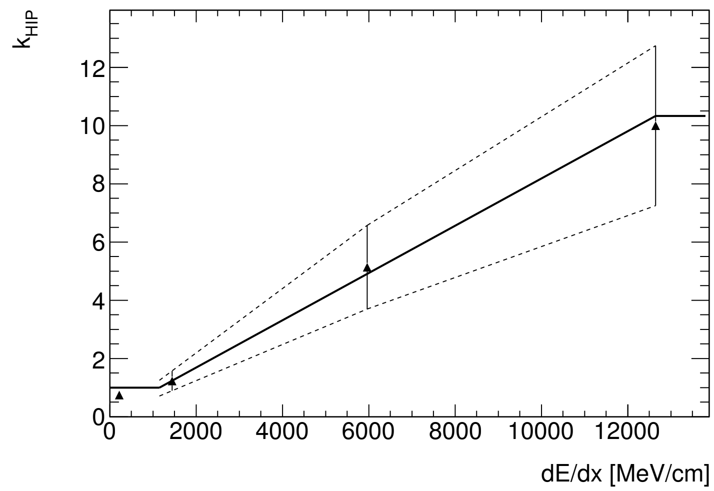

Figure 32: HIP correction to Birks' Law as a function of dE/dx for various heavy ions for $E_D = 7$ kV/cm [114].

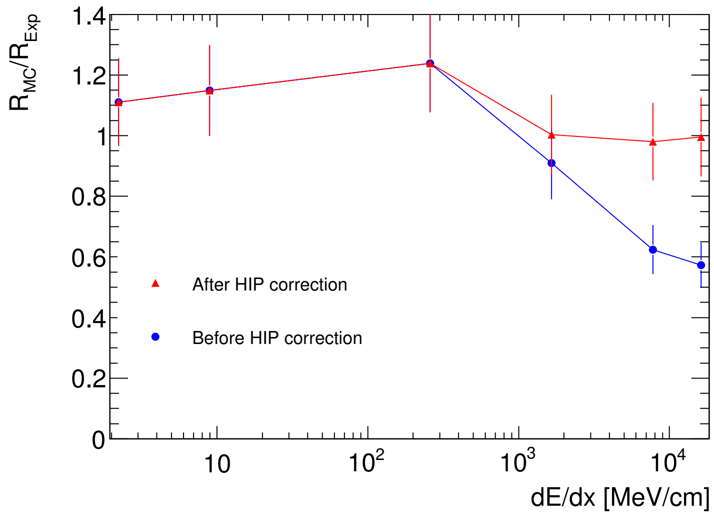

Figure 33: Performance R_{MC}/R_{Exp} of the ATLAS implementation of Birks' Law as a function of dE/dx for various heavy ions for $E_D = 7$ kV/cm (see Ref. [121] for details). The blue circles show the performance before the HIP correction. The red triangles show the improved performance after the application of the HIP correction [114].

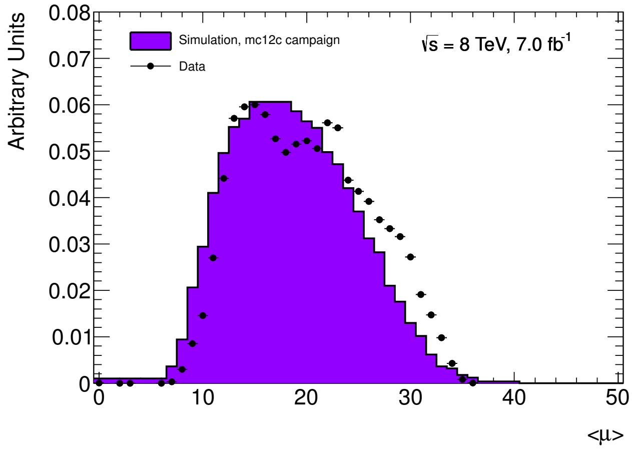

Figure 34: The pile-up distributions for the dataset used in this search and for the MC12c production campaign used for HIP simulations.

3.1.3 *Digitisation of simulated samples*

The digitisation step uses the GEANT4 **Hits** from the simulation step and *digitises* them to the response of the detector to produce **Digits**, such as times and voltages. These responses would be similar to those expected from the Raw Data[3] from the real detector. The digitisation of the simulated samples is done using the ATHENA software.

In the digitisation step, the pile-up conditions of the collected data are simulated by overlaying digits from additional collisions. The production campaigns determine the pile-up profiles based on the data collected at the time of the campaign. A pile-up re-weighting is performed at the analysis level to account for any differences between the pile-up profiles in simulation and in data. Pile-up profiles can be classified as: (a) in-time pile-up: for all collisions in the same bunch crossing and (b) out-of-time pile-up: for collisions from neighbouring bunch crossings.

The average number of interactions per bunch crossing ($\langle\mu\rangle$) accounts for both types of pile-up and its distribution is shown in Fig. 34. The differences between the pile-up distributions of simulation and data in this plot are observed because only a fraction of the 2012 data was used in this analysis (see Sec. 3.3 for details)

Monopole samples of charge $2.0g_D$ required high amounts of computational resources during the digitisation and reconstruction stages, causing memory limitations problems. Despite access to high-memory queues, it was not possible to digitise and reconstruct this set of sample completely. No obvious bias was introduced to the samples that succeeded since the issue was related to the conditions of the machines to which the jobs were assigned. These samples however have a pile-up profile that is truncated at $\langle\mu\rangle$=18.

3 The data from collisions that passes through the detector is colloquially referred to as Raw Data.

3.1.4 *Reconstruction of digitised events*

With the digitised samples from either simulated samples or data, the raw **Digits** are reconstructed into tracks and energy deposits that are stored in the ESD format. The reconstruction process carries out particle identification, and building physics objects (such as calorimeter jets and electrons) as well as the running of the entire trigger menu. The following sub-sections describe the most important reconstruction aspects for this analysis.

Trigger reconstruction

The ATLAS trigger menu is an amalgamation of a multitude of triggers from Level-1 through to the HLT, dedicated to select events with interesting physics processes. The trigger reconstruction process uses the trigger menu and applies the different trigger algorithms on the reconstructed physics objects either in simulation and on data[4].

The reconstruction step is crucial to the testing and deployment of new trigger algorithms, such as the HIP trigger that was developed for this search. The HIP trigger is included in the ATLAS trigger menu since September 2012, and was included in ATHENA 17.2.11.2.1 and its subsequent releases.

Simulations of signal and background samples were done with releases that included the HIP trigger in the trigger menu.

TRT hits and drift circles

Each TRT straw returns a 24-bit signal giving the drift time information over three bunch crossings spanning 75 ns - giving 8 bits per 25 ns for each straw (see Sec. 2.2.2 for details). Each bit represents a time window of 3.125 ns and holds a binary bit value which is set to 1 if the low threshold discriminator is on during the corresponding time bin.

The first non-zero bit (known as the Leading Edge) in the TRT readout is used to reconstruct TRT *drift circles* [122] from the drift time of the electrons produced in the cluster of closest approach to the wire. To reject hits from previous bunch crossings, hits with the first bit equal to 1 are rejected. The last non-zero bit, known as the Trailing Edge, is produced by electrons drifting from clusters that are produced far away from the wire. Additional three bits are assigned to each 25 ns window to distinguish between high and low threshold TRT hits. The collection of drift circles is stored as objects of the TRT_DriftCircleContainer class in ATHENA.

Analyses that build tracks using tracking algorithms require precision measurements from the TRT drift circles. For this analysis however, the position of the straw and the TRT bit value associated with the HT discriminator are sufficient.

4 In data, the trigger algorithms are applied in a sequential manner. Meaning, trigger menus in subsequent levels are applied only on events that pass the previous ones.

Topological calorimeter clusters

ATLAS uses two main clustering algorithms, the first is the *sliding window* algorithm which clusters calorimeter cells within a fixed-size rectangles and is used for electron, photon and tau lepton identification. The second is the *topological* algorithm that selects neighbouring cells that have significant energies compared to the expected noise thus generating clusters with a variable number of cells. The topological clusters are used in this analysis and its implementation consists of two steps, the *cluster maker* and the *cluster splitter* [123].

The growth of the cluster starts at the seed cells, found by the **cluster maker**, which pass large signal to noise thresholds. Medium thresholds are used to determine if neighbouring cells[5] can serve as additional seeds to expand the cluster; while low threshold cells ensures that the tails of the showers are not disregarded by including all direct neighbour cells on the outer perimeter. The expected noise is η-dependent to which contributions from pile-up are added in quadrature.

The cluster maker step is sufficient to build isolated calorimeter clusters. However, the events in ATLAS are far from such ideal conditions where clusters could cover large areas of the detector if sufficient energy is present between incident particles. The **cluster splitter** algorithm is designed to distinguish overlapping clusters that are sufficiently apart. A local maximum forms a cluster if it has at least 4 cells that have energies higher than their neighbouring cells and a minimum of 500 MeV. Shared cells between overlapping clusters are weighted and assigned to either of the clusters, thereby avoiding double counting of cells.

The topological clusters thus represent a three dimensional energy blob in the calorimeter that sometimes share cells on the border between them.

3.1.5 *Simulated background samples*

The time line of this analysis did not sync with the general 2012 production campaigns of the simulation group and thus the HIP trigger algorithm was not included in their trigger menu. To study the effects of backgrounds from Standard Model processes, simulations of these samples needed to be reprocessed with the HIP trigger algorithm present in the ATLAS trigger menu. Due to the limited computational resources available, only a few Standard Model processes samples were reprocessed.

The main backgrounds in this analysis are high-energy electrons and high-p_T QCD processes with high threshold TRT hit combinatorial. For a qualitative background study a few samples of Drell-Yan

5 Neighbouring cells are defined (usually) as eight surrounding cells within the same calorimeter layer. The set of neighbours can also include cells overlapping partially in η and ϕ in adjacent layers, giving typically 10 neighbours for a calorimeter with identical geometry. In ATLAS, this number can be higher as the granularity varies between different calorimeter layers.

JZXW	Leading TruthJet pT range [GeV]
JZ0W	0-20
JZ1W	20-80
JZ2W	80- 200
JZ3W	200-500
JZ4W	500-1000
JZ5W	1000-1500
JZ6W	1500-2000
JZ7W	2000+

Table 3: Jet p_T slices defined on the basis of the p_T of the truth leading jet in the sample.

produced electron-positron pairs, W decays into electron (positron) and anti-neutrino (neutrino) and high-p_T di-jet events were simulated. Low p_T QCD events also form a significant part of the backgrounds that pass the analysis selections in data. However, the probability for such events to pass the HIP trigger is very low and thus would require a large number of events to be simulated. The simulated background samples are thus of limited quantitative use and the background estimates in this search are made by fully data-driven methods.

The samples were reprocessed via the official production chain by including the HIP trigger in the trigger menu and the storage of events was limited to only those that passed the Derived-ESD (dESD)[6] filter. The limited computational resources restricted the reprocessing of low-p_T QCD samples.

The Drell-Yan produced electron-positron pairs are generated and stored in mass bins ranging from 20 GeV to 3000 GeV. The di-jet events are generated and stored in p_T bins, where the binning is determined as shown in Tab. 3. The file list of the background samples used in this analysis are given in Ref. [124].

3.2 DEDICATED TRIGGER FOR HIGHLY IONISING PARTICLES

Monopoles and highly ionising particles have distinct signatures in general purpose experiments such as ATLAS, as described in Chapter 1. In ATLAS, subsystems such as the TRT detector can help identify these signatures and distinguish them from SM background processes.

The following section describes the highly ionising trigger that was developed to identify the signatures of HIPs. Subsequently this trigger was used in the analysis detailed in this dissertation.

6 The dESD storage format in the ATLAS framework was chosen as this stores TRT hit information that is crucial to this analysis.

3.2.1 *Motivation for a dedicated HIP trigger*

In the previous search for magnetic monopoles at ATLAS [72] candidates were triggered by an unprescaled standard electron and photon EF triggers with relatively high thresholds, resulting in relatively low signal efficiency. The maximum signal efficiency[7] obtained was 14.53% for a 1000 GeV charge $1.0g_D$ monopole sample produced with Drell-Yan process. HIPs with low energy would range out and stop before they can penetrate deep into the detector, failing to satisfy the increasing energy thresholds. In addition, HIPs with higher charge, which have correspondingly higher dE/dx, predominantly stop in the first layers of the ECAL and are missed by standard electron/photon triggers. This is because of an inherent requirement of these triggers that the candidate must deposit energy in the second layer of the ECAL.

The motivation for developing an independent trigger for HIP searches was to probe HIPs with lower energies and/or with higher charges, which would otherwise be missed by the previously used triggers. The requirement of depositing energy in the second layer of the ECAL is dropped in this trigger, which means HIPs that stop in the first layers of the calorimeter will also be captured as candidates by the trigger. In addition, the new trigger does not impose high transverse energy requirements as photon triggers do, thus further increasing the efficiency for HIP signals.

3.2.2 *The HIP trigger*

The trigger uses high ionisation hits in the TRT to select events which have the signature of at least one HIP. From the software development aspect the trigger is divided into two parts, the Feature Extraction (FEX) and the hypothesis (hypo). The FEX, reconstructs "physics" features within an RoI and creates feature objects. The hypothesis is an algorithm that uses these reconstructed physics features and applies some selection cuts on, for example, the number and fraction of high threshold TRT hits etc. Thus the hypothesis also verifies trigger conditions and, in addition, particle candidates can be created [125]. To maintain homogeneity with the code designed for the trigger, its description is outlined over the next two sub-sections.

3.2.3 *The Feature Extraction Algorithm*

The L2 HIP trigger is seeded by the lowest unprescaled L1 seed, i.e. EM18VH[8] (EM30 was also considered, only as backup). The trigger

7 The number of simulated signal events that would pass the trigger selection.

8 The trigger name indicates which sub-detector it functions in along with the energy threshold and any additional cuts. The EM18VH trigger is ECAL trigger with 18 GeV energy threshold requirement i.e. the energy deposited by a particle must be at least 18 GeV. However the *V* in the name stands for *varied threshold* and implies that the energy threshold is η-dependent. For EM18VH the energy thresholds varied from 18-20 GeV depending on the η. The *H* in the name denotes a hadronic veto which

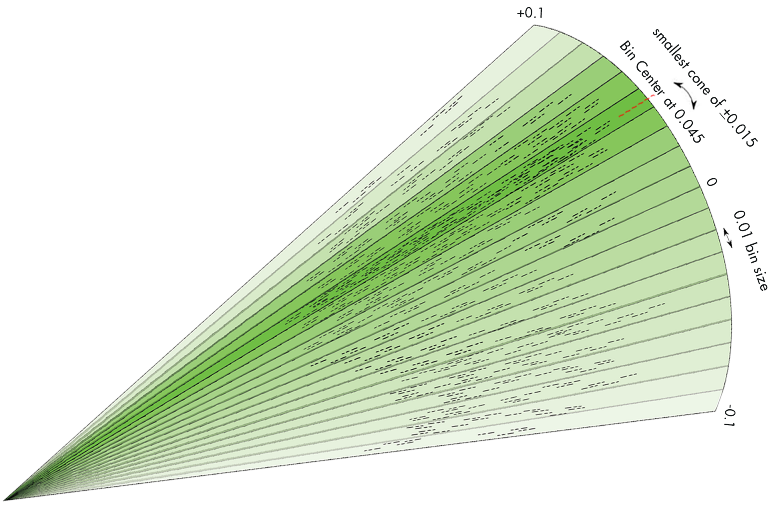

Figure 35: Illustrative diagram of the wedge constructed by the trigger centred around the RoI (zeroth ϕ position) with 10 bins on either side. Each bin has a width of $\Delta\phi$=0.01. Each small black line represents a single high threshold TRT hit in the bin, with the colour gradient highlighting its density - the darker the gradient, the higher the density. *Image credit: Abhay Katre*

EM18VH has an implicit hadronic veto. This has a negligible impact on the signal, since most of the HIP candidates with 1.0g_D or higher would range out before entering the hadronic calorimeter (assuming the Drell-Yan pair-production model).

The L1 trigger identifies the positions (η-ϕ information) of the RoI for event in the detector using set energy thresholds and other hardware based requirements. The signature of HIPs corresponds to a large number of TRT hits in a localised region (where the HIP has traversed through). A wedge of ± 0.1 rad in ϕ[9] is built around the RoI, and is binned in 20 bins each of 0.01 rad in ϕ. For each of these bins in ϕ, the number of TRT hits as well as High Threshold (HT) TRT hits are counted. An illustration of the binning in ϕ around an RoI is shown in Fig 35, where the zeroth position corresponds to the position of the RoI in ϕ.

Comprehensively, a loop over all the TRT hits in the event is run where these hits are binned according to their ϕ position in the wedge and a loose η matching[10]. Hits whose ϕ position is not within the wedge are not considered further. The total number of TRT hits and HT TRT hits are computed in each bin of the wedge and the bin with the maximum number of HT TRT hits is considered as the central bin - through which the HIP has most likely traversed.

implied that candidates with more than 1 GeV in the hadronic calorimeter would be vetoed [126].

9 Monopoles are expected to have a straight trajectory in ϕ. The trigger was initially developed considering only the monopole efficiency. However when extending this search to HECOs, which bend in ϕ, their overall efficiency was found to be reasonably high

10 A simple requirement is made such that the TRT hit η and the RoI-η are on the same side of the detector

The central bin, along with two adjacent bins (one on either side) now corresponds to a wedge size of ± 0.015 in ϕ and is the wedge of main interest in the trigger- where the number and fraction of HT TRT hits serve as the trigger handles. In cases where the maximum hits in the wedge are at the extremes, only two bins are selected. As a safety measure, wedges corresponding to ± 0.025, ± 0.035, ± 0.045 and ± 0.055 were also created for which the number and fraction of HT TRT hits were also read out. Larger wedge sizes are more likely to contain TRT hits that did not originate from HIPs; having a larger number of low threshold hits in the wedge decreases the fraction trigger handle increasing the likelihood of missing the event. Smaller wedge sizes provide more robust signal selections in high pile-up environment albeit, a wedge too narrow could miss the HIP candidates altogether.

The FEX output was a vector capable of storing 5 elements, with each element corresponding to a particular bin size (in increasing order from ± 0.015 to 0.055). Each element of the vector is a float, where the integer part corresponds to the number of HT TRT hits (N_{HT}^{trig}in the wedge of the corresponding wedge size), and the decimal part corresponds to the fraction of HT TRT hits (f_{HT}^{trig}) in the same wedge.

3.2.4 *The Hypothesis*

The FEX output is accessed by the trigger hypothesis, where the cuts on the trigger handles are enabled. Fig. 36a, 36b show the distributions and the discriminating strength of the two trigger handles for data and simulated background and signal samples. Fig. 37, shows the dependence of the two trigger handles (extracted from an emulation of the trigger) for a single run in data and a simulated signal sample. This helps identify suitable cut values for the trigger handles.

The final selections were made with a view to achieve a minimum trigger rate (See Sec. 3.2.7) while keeping the signal efficiency mostly intact. An emulation of the trigger was used to determine the final selections, as shown in Fig. 38. The signal efficiency is computed as the ratio of the number of events that pass the trigger selection cuts to the total number of events in the signal sample. The DY samples have an inherent cut on the truth p_T at the event generation stage to not simulate particles that would not reach the calorimeter and the total number of events is thus scaled accordingly [72] (also see Appendix E).

The fraction of HT TRT hits is a strong discriminant against background processes and thus a stronger cut on the fraction allows for a looser cut on the number of HT TRT hits. The lower cut on the number enables probing of lower charged HIPs, which would still yield a high fraction. Tab. 4 shows the final selection cuts that were applied for the trigger handles to ensure a higher signal efficiency of the HIP signals in a broad range of charges while maintaining a low background rate.

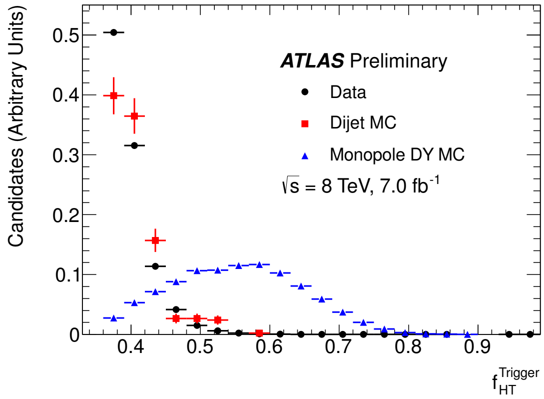

(a)

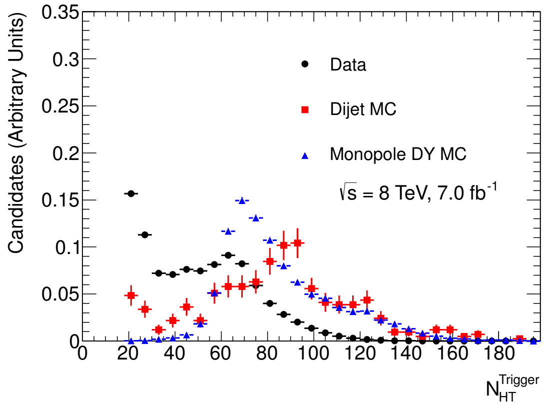

(b)

Figure 36: (a) Fraction of TRT HT hits from the HIP trigger (for candidates with $N_{HT}^{trig} > 20$); (b) Number of TRT HT hits from the HIP trigger (for candidates with $f_{HT}^{trig} > 0.37$). The data distributions shown are made using only 10% of data. In addition MC samples were used to generate expected distributions from expected QCD processes (JZ5W), and Drell-Yan MC monopoles with mass 1000 GeV and charge $|g| = 1.0 g_D$. The distributions are normalised to the same number of candidates.

Feature object	Selection cut
Fraction of HT TRT	0.37
Number of HT TRT	20

Table 4: Selection cuts of the trigger objects in the wedge around the RoI.

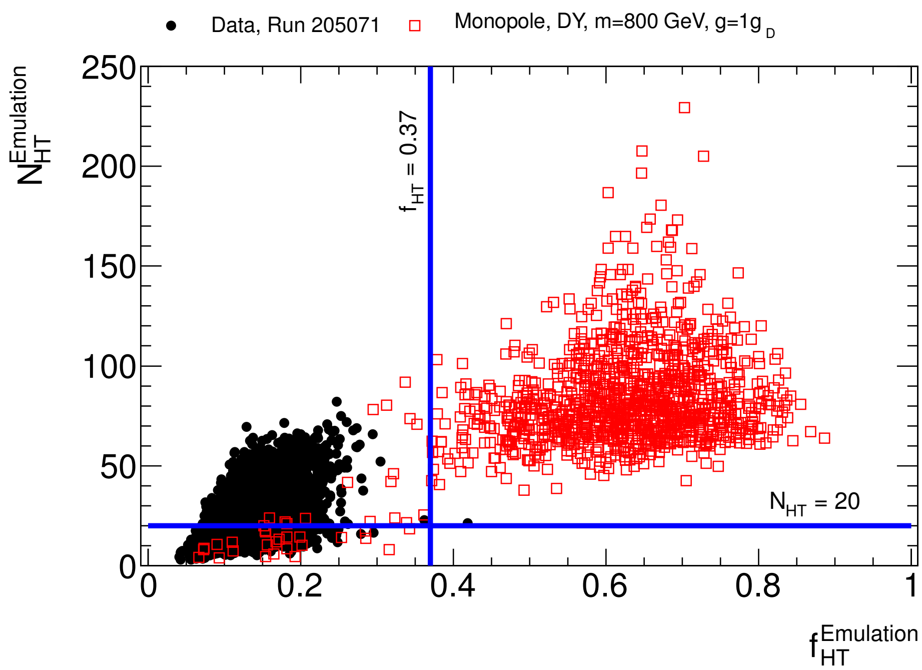

Figure 37: Number of HT TRT hits versus the fraction of HT TRT hits over total TRT hits for data and Signal MC. The solid black circles represent the data that was collected from Run 205071 that fired the trigger emulation and the red full circles represent the candidates from signal MC.

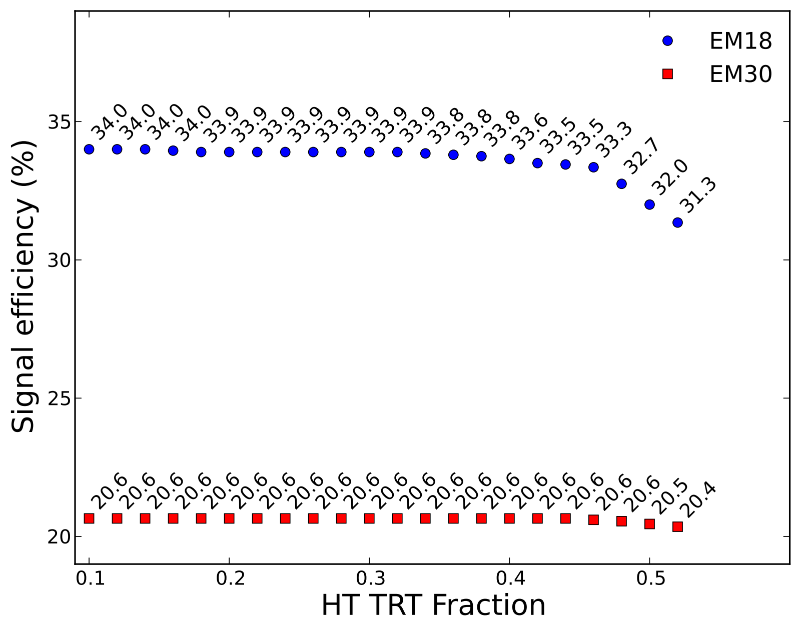

Figure 38: Signal efficiency for a DY produced monopole of mass 800 GeV and charge $1.0g_D$ using an emulated trigger as a function of the cut in the fraction of HT TRT hits in the smallest wedge size and a cut of 20 HT TRT hits.

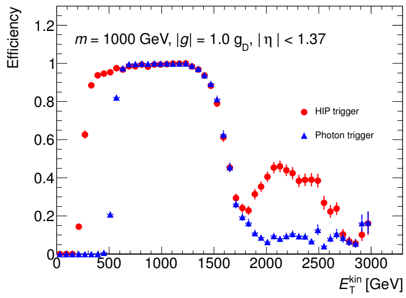

(a)

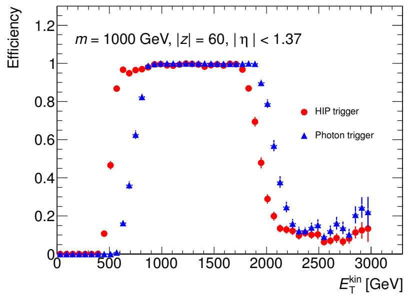

(b)

Figure 39: The HIP trigger efficiency as a function of the transverse kinetic energy for single (a) monopole ($g = g_D$) and (b) HECO ($|z| = 60e$) samples. The efficiency is plotted for the central region of the detector, i.e. for the $|\eta| < 1.37$ region.

3.2.5 *HIP Trigger Performance: Signal Efficiency*

The HIP trigger was used at ATLAS to probe new mass and charge points for HIPs that were previously inaccessible at ATLAS using standard triggers. While the optimisations of the trigger were made with a specific charge and mass point of monopoles, the HIP trigger is able to trigger on 96 different mass and charge points for monopoles and HECOs.

Fig. 39a and 39b show the efficiency of the HIP trigger as a function of the initial *truth* kinetic energy for single monopoles and HECOs respectively. In addition, to compare the lowest threshold trigger in the absence tracking requirements, i.e. the 120 GeV photon trigger, which would be used without the HIP trigger. Fig. 39a shows that the low energy monopoles are picked up by the HIP trigger to which the standard triggers would not be sensitive. There is a drop in efficiency at high (> 1500 GeV) energies in both triggers, this is attributed to an implicit hadronic veto that exists[11]. A rise in efficiency is seen for the HIP trigger at even higher kinetic energies, this is discussed in some detail in Appendix C.1. For the HECOs, the HIP trigger does pick out candidates at lower energies, however the drop in efficiency is earlier for the HIP trigger than the photon trigger. This issue is again discussed in Appendix C.2.

The HIP trigger efficiencies with respect to the L1 trigger for all mass and charge points are summarised in Fig. 40. The ionisation in the TRT is directly proportional to the square of the charge, and thus higher charged samples tend to have higher relative efficiencies. A small mass dependence is observed for DY produced samples, this is attributed to the higher mass samples being produced more centrally, given that the TRT acceptance ($\eta < 2$) is narrower than the calorimeter acceptance. The relative HIP trigger efficiency with respect to L1 is $\epsilon > 50\%$.

11 While in the HIP trigger a hadronic veto exists in L1, the standard photon triggers apply a hadronic veto at EF level. This EF veto cuts on the ratio of the energy deposited by the candidate in the Tile calorimeter to the energy deposited in the ECAL [127].

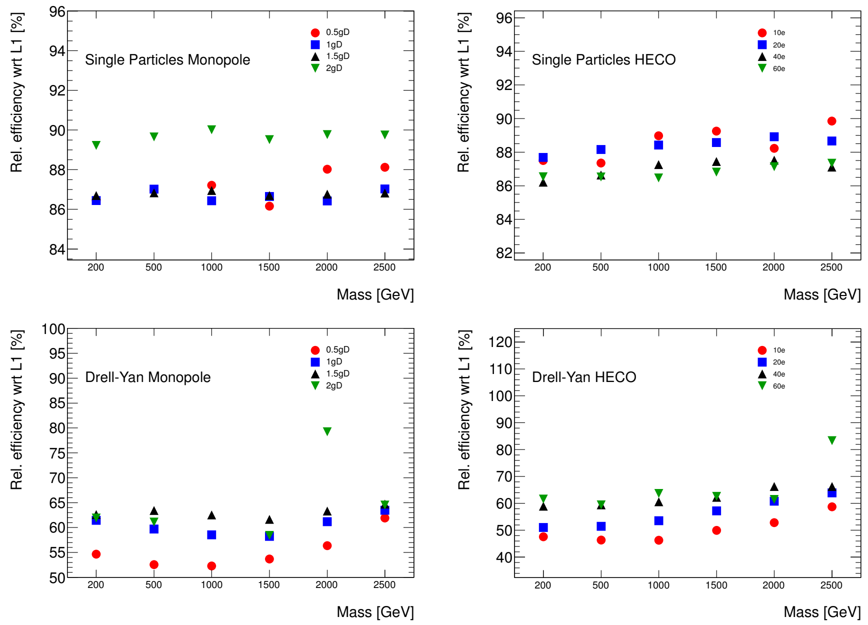

Figure 40: HIP trigger efficiency with respect to the L1 trigger for all mass and charge points, in single-particle (top) and DY (bottom) monopoles (left) and HECOs (right) samples. To avoid overcrowding in these plots, the errors bars are not shown. The DY monopole with charge 2.0g_D outlier, at 2000 GeV, is due to low statistics in the sample with large uncertainties associated to the value.

The L1 trigger efficiencies[12] for all mass and charge points are summarised in Fig. 41. There are two factors that contribute to the L1 efficiency, namely, (a) the ability to deposit at least 18 GeV E_T in the electromagnetic calorimeter, and (b) not penetrate to the hadronic calorimeter and deposit more than 1 GeV E_T.

The L1 efficiency is entirely dependent on the production model, as it requires that the HIP possesses the right amount of energy to stop in the ECAL and also the right angle to be within the ECAL acceptance. Single particles are produced with a flat distribution in η and energy that have arbitrary bounds. While the absolute values of the total L1 efficiencies from the single HIPs are solely dependent on the arbitrary choice of energy and η limits, their relative charge and mass dependence can be discussed.

Single monopoles of lower charges tend to penetrate through to the Tile calorimeter and hence are vetoed by the L1, thereby resulting in lower efficiencies (0.5g_D in particular). The higher charge monopoles tend to ionise more[13], and with increasing mass the monopoles traverse the detector more slowly. Thus monopoles of higher masses tend to penetrate further through the detector to reach the EM calorimeter, thereby showing an increase in efficiency as a function of mass for higher charges. The DY HIP efficiencies are affected by the kinematics of the production model. The high mass candidates are more centrally produced than the lower mass ones. However, the

12 Can be regarded as acceptance in this case
13 The dE/dx for monopoles is directly proportional to the square of its charge

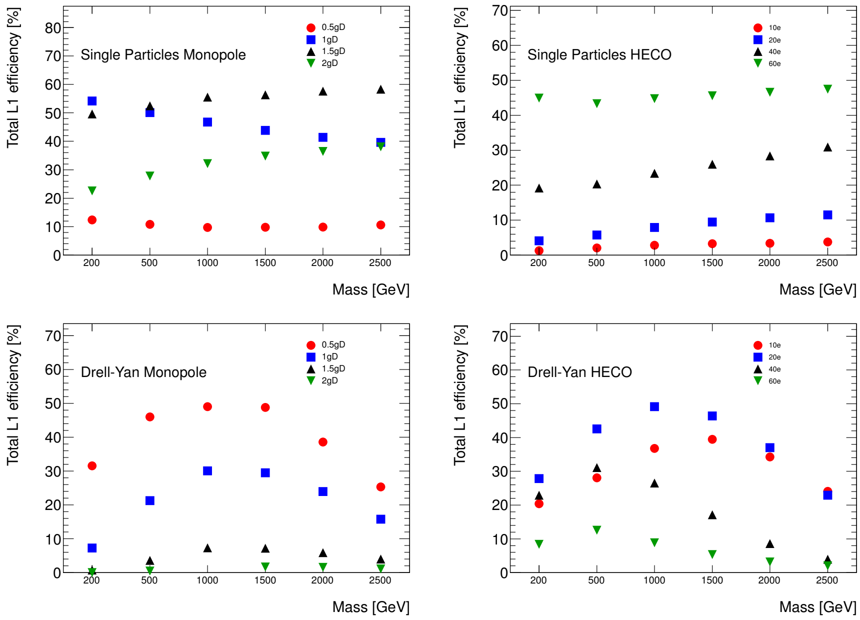

Figure 41: L1 trigger efficiency for all mass and charge points for single-particle (top) and DY (bottom) monopoles (left) and HECOs (right).

higher mass samples also tend to have lower kinetic energies, thereby stopping before reaching the calorimeter. Therefore an inverted bowl shaped dependence is observed in the efficiency as a function of mass. As the ionisation of monopoles depends on their squared charge, the lower charge - but now model dependent - monopoles, tend to stop in the calorimeter, whereas, the higher charged monopoles tend not to reach the calorimeter at all.

The energy loss in HECOs is proportional to its charge squared and it increases with decreasing velocity. The increase in efficiency with the increase in mass for **single HECOs** is due to the large ionisation energy loss for slower moving HECOs that inevitably stop in the electromagnetic calorimeter. In principle, the increase in efficiency should be more significant as a function of mass, however due to simulation issues (as discussed in Appendix C.2) the rise in efficiency is not so drastic. The charge dependence, is as expected, with HECOs of lower charge penetrating through to the Tile calorimeter and triggering the L1 veto, while the higher charge HECOs stop in the calorimeter. The efficiency behaviour of DY HECOs is similar to that of monopoles with respect to the mass dependence. There is a charge dependence that is observed, however, the lower efficiency for 10e samples occurs because these samples penetrate through to the Tile calorimeter and trigger the L1 veto.

3.2.6 *HIP Trigger Performance: Pile-up dependence*

The performance of the trigger in different pile-up conditions and regions of the detector is tested using signal MC samples. Fig. 42

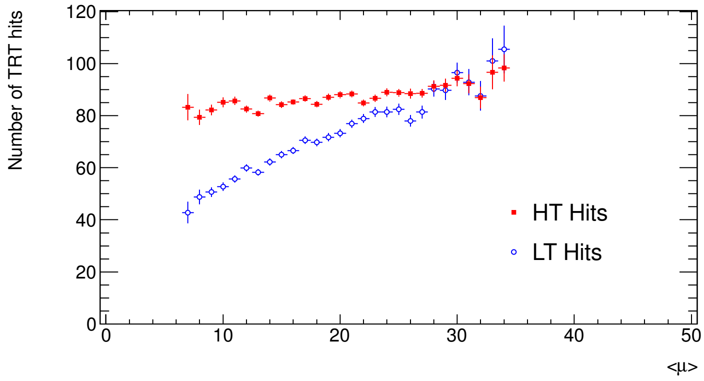

Figure 42: The profile distribution of the number of TRT hits in the trigger wedge around the RoI as a function of pile-up for a DY produced monopole of charge $1.0g_D$ and mass 1000 GeV. The distribution shows the pile-up dependence for the two types of TRT hits. As expected from pile-up, the number of low threshold hits increases with the increase in pile-up.

shows the profile of the number of TRT hits as function of $\langle\mu\rangle$ for both, low and high threshold hits for a typical monopole sample.

The number of HT TRT hits originating from a signal sample is fairly constant as a function of pile-up. The number of LT TRT hits, as expected, increases as a function of pile-up. This *feature* of the trigger helps maintain a low rate in higher pile-up conditions; thereby never surpassing the 1 Hz bandwidth allotted to the HIP trigger. The pile-up conditions correspond to the 2012 data-taking period.

In future runs of the LHC the pile-up conditions is expected increase. The HIP trigger would in these situations be unable to deliver similar efficiencies as in 2012 without modifications.

To study the effect of pile-up on the signal efficiency, a simulated sample was generated with $\langle\mu\rangle = 60$[14], to correspond to higher luminosity conditions[15]. The trigger handles along with the simulated signal efficiencies were compared for this sample with those corresponding to the 2012 running conditions (with maximum $\langle\mu\rangle = 40$). The distributions of the different trigger handles are shown in Fig. 43, 44 where higher shifts for the higher pile-up conditions are as expected (except the fraction of HT TRT hits, which correspondingly decreases).

The distributions of the number of TRT hits are all shifted to higher values, and the distribution of the LT TRT hits does not only shift considerably but also exhibits a long tail compared the $\langle\mu\rangle$=40, as expected. Fig. 43a shows that the HIP trigger at higher pile-up conditions will give lower fraction values for the same algorithm. Fig. 44 shows the trigger efficiency as a function of the truth kinetic energy of the candidates, for samples with two different pile-up profiles. The

14 The notation here is slightly misleading. $\langle\mu\rangle$=60 implies that the maximum pile-up value for the sample is 60. It does not refer to the peak value of the pile-up distribution

15 All other running conditions - trigger menu, detector geometry, centre-of-mass energy etc were kept the same as in 2012

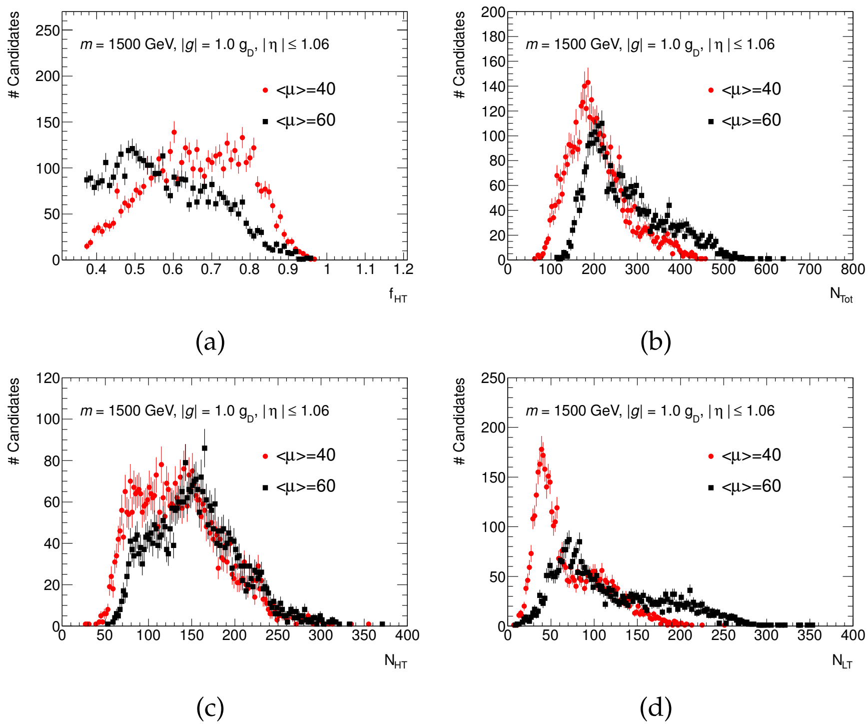

Figure 43: A comparison of the different pile-up conditions simulated to study the effect of the HIP trigger performance. The plots show (a) the fraction, (b) the total, (c) the high threshold and (d) the low threshold of TRT hits as seen by the HIP trigger under different pile-up conditions.

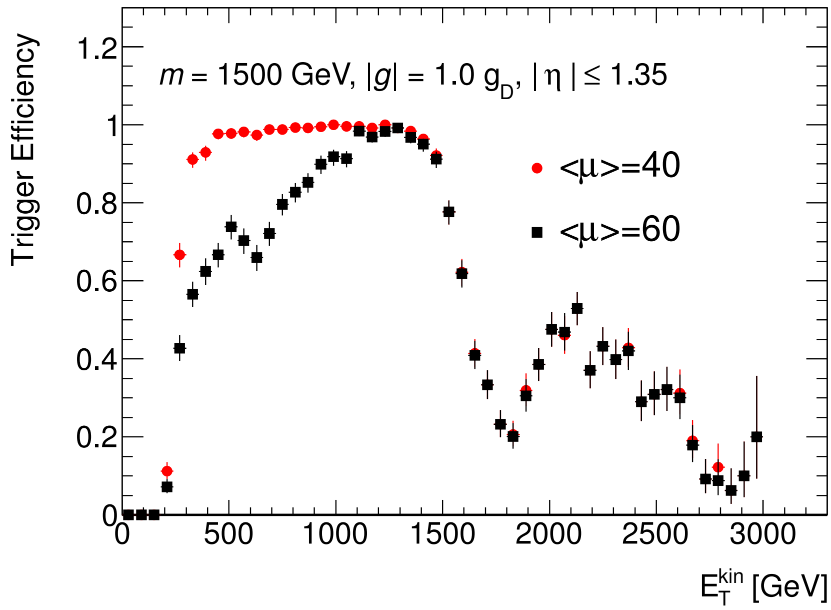

Figure 44: The HIP trigger efficiency for simulated different pile-up conditions shows a loss of efficiency at low E_T^{kin} values for higher pile-up conditions. Modifications in the trigger algorithm are required to improve the efficiency of monopoles at lower E_T^{kin}.

sample with $\langle\mu\rangle$=40 corresponds to 2012 running conditions, while the $\langle\mu\rangle$=60 corresponds to the higher pile-up conditions expected in future runs of the LHC. The loss in signal efficiency as observed in Fig. 44 for higher pile-up conditions is due to lower energetic monopoles that with $\langle\mu\rangle$=60 give considerably lower fractions. This motivates the need for a modified algorithm to cope with higher pile-up conditions.

3.2.7 *HIP Trigger Performance: In data*

Before a trigger is deployed at Tier-0, it is put through a rigorous validation procedure to ensure the software releases are extremely robust and stable. A *nightly version* of the software release is set for tests every night that test various software aspects by running on input files with few events. Once the trigger is deployed and successfully passes the nightly tests, it is collected for further *CAF HLT* tests that are conducted on a weekly basis. These tests maintain the same software releases and conditions as at Tier-0, and are run on a larger event samples. The CAF HLT tests also provide rough initial estimates on the rate of the trigger and predicted a rate of 0.32 Hz for the HIP trigger. The HIP trigger was deployed at Tier-0 from the end of Sept., 2012 until the end of the Run-1. The trigger ran at Tier-0 with a rate between 0.4–0.6 Hz, well below the allocated bandwidth of 1 Hz for data taking.

Fig. 45 shows the rate of the HIP trigger as a function of the instantaneous luminosity for the run 212815, on Oct 17, 2012. The negative

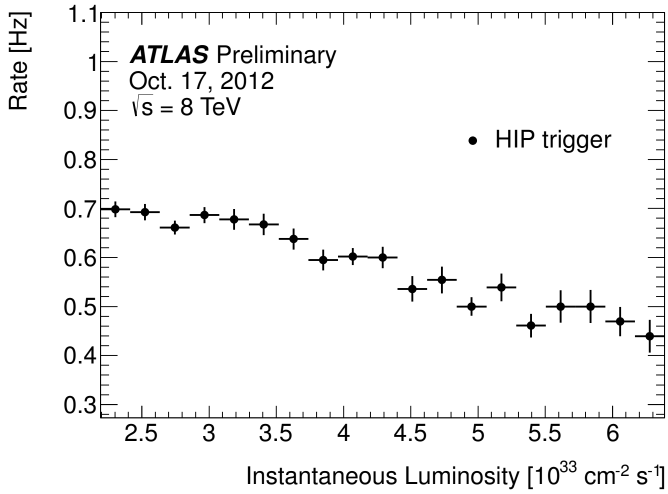

Figure 45: Instantaneous rate of the monopole trigger in run 212815.

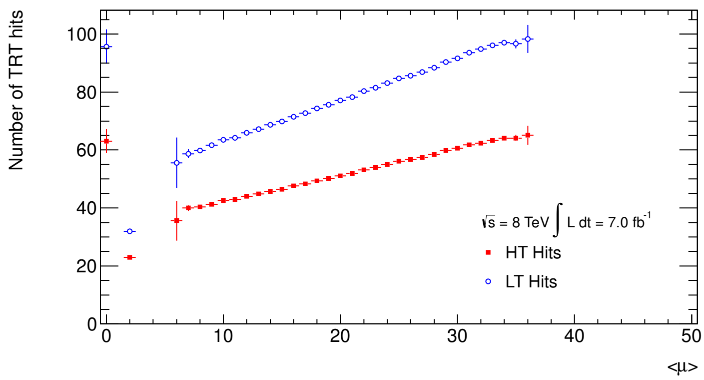

Figure 46: The profile distributions showing the dependence of the number of TRT hits of both types LT and HT on the pile-up of the events. The distribution shows that as the pile-up is increased, the number of TRT hits also to be larger. Fig. 48a and Fig. 48b confirm this feature as the number of TRT hits is in general larger for high pile-up conditions.

correlation between the rate of the HIP trigger and the instantaneous luminosity can be explained by the pile-up dependence of the trigger variables. Fig. 46 highlights the pile-up dependence of the TRT trigger variables in data. It shows that both the number of HT and LT hits increase as pile-up increases, with the number of LT hits increasing faster. The ϕ-wedge is contaminated by a large number of low threshold hits at high pile-up, in turn lowering the f_{HT} value of the trigger variable. Thus the HIP trigger at high instantaneous luminosities has a lower rate. As the run progresses, the luminosity and the pile-up drop, thereby having candidates with nominal f_{HT} that pass the trigger thresholds. However the overall rate of the trigger is maintained at under 1 Hz.

Fig. 47 shows the distribution of the number of HT TRT hits in the barrel and the end-caps, which exhibit a double peak structure albeit with a larger second peak in the end-caps. The first peak at approximately 20 HT TRT hits can be attributed to isolated particles

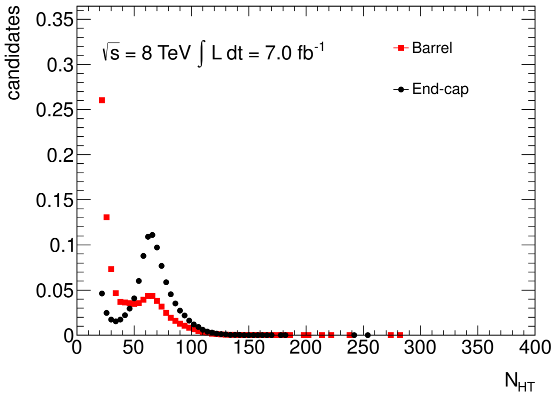

Figure 47: The distribution of the number of HT TRT hits in the trigger in data. The two histograms show the distributions of the number of HT TRT hits in barrel and end-cap separately. The second peak in the distribution is predominantly from the end-caps and these are contributions from high-p_T jets. The distribution starts at $N_{HT} >$ 20 and also has the implicit cut requiring, f_{HT} >0.37 since only triggered events are selected in data.

with sufficiently high-p_T. The second peak with approximately 60 HT TRT hits, can be attributed to jets. The TRT hits associated to each EM cluster are possibly overlapped by hits from several particles in the jet. The L1 hadronic veto is ineffective beyond $|\eta| > 1.7$ and thus several high-p_T jets produce a large number of HT TRT hits and a sufficient fraction to pass the HIP trigger in the end-caps.

Fig. 48a shows the distributions of the number of HT TRT hits for low ($\langle\mu\rangle \leqslant 22$) and high ($\langle\mu\rangle > 22$) pile-up conditions. The two peaks are prevalent in both, the high and low pile-up distributions. Similarly Fig. 48b shows the distributions of the number of LT TRT hits for different pile-up conditions. The features in Fig. 48a and Fig. 48b are similar, however, the second peak is more shifted to towards high number of LT TRT hits for the high pile-up scenario, as expected.

3.3 ATLAS DATASET

As described in Sec. 3.2, the HIP trigger was deployed during the last 3 months of the Run-1 campaign. During this time, the HIP trigger collected data in periods G, H, I, J and L, which was filtered using the recommended ATLAS good run list [16]. The luminosity calculator tool provided by ATLAS shows that the data collected by HIP trigger in 2012 corresponds to 7.0 fb^{-1}.

The data collected from the trigger is stored in the ESD format, which is further processed using a HIP filter algorithm that creates a new storage format, the dESD. The HIP dESD filter algorithm, selects events that fired the HIP trigger as well as events that pass the standard photon (of threshold 120 GeV) or electron (of threshold 60 GeV)

16 The ATLAS good run list checks the stability of the LHC beams and quality flags for all ATLAS sub-detector systems for each event. At the end of 2012, a complete list was drawn by the ATLAS collaboration called, PHYS_Standard_All_Good

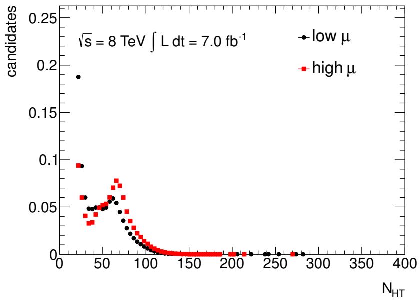

(a)

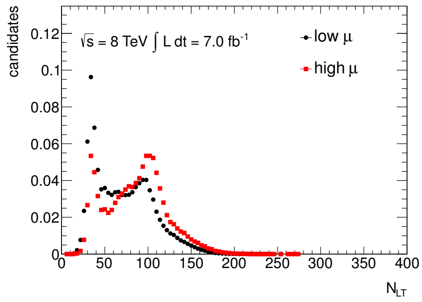

(b)

Figure 48: (a) The distribution of the number of HT TRT hits in the trigger wedge in data. (b) The distribution of the number of LT TRT in the trigger wedge in data. These distribution in data has the implicit cuts of $N_{HT} > 20$ and $f_{HT} > 0.37$ since only triggered events are selected in data. The distribution is plotted separately for low ($\langle\mu\rangle \leqslant 22$) and high ($\langle\mu\rangle > 22$) pile-up conditions to understand its effect on the triggered variable. The distributions are as expected with the high μ distribution shifted to higher values. The double peak structure is explained in text.

triggers and satisfy criteria that are outlined in [128]. Two other filters from separate analyses also contributed to the final dESD. Fig. 49 shows the breakdown of the percentage of events from the different triggers that constitute the final dataset that was considered for this analysis.

3.3.1 *Run condition stability*

To ensure that the run conditions are similar between different runs in the data sample, the number of events fired by the HIP trigger in a given run over the total integrated luminosity of the run is plotted. With similar conditions across all runs within the dataset, this should yield a relatively flat distribution. Fig. 50 shows the ratio of the number of events fired by a standard photon trigger and the integrated luminosity of each run within the dataset which is fairly constant.

A similar ratio is plotted for events fired by the HIP trigger in Fig. 51. The number of events fired by the HIP trigger in the entire dataset corresponding to 7.0 fb^{-1} is 876895. Thus about 125270 events per fb^{-1} (represented by the dotted line) are expected. As seen in Sec. 3.2.6, the HIP trigger is pile-up dependent and has a lower rate at higher luminosities, where fatter bunches produce higher pile-up. Fig. 52 shows the dependence of the ratio of the number of events fired by the HIP trigger to the integrated luminosity of the run against the average pile-up of the run. A negative correlation between the quantities is observed, as expected from the HIP trigger's design. Fig. 52 can thus be adequately used to describe stable conditions between different runs used in the dataset.

There are two outliers in Fig. 52, which were separately studied to understand the large deviation from the expected value. The run

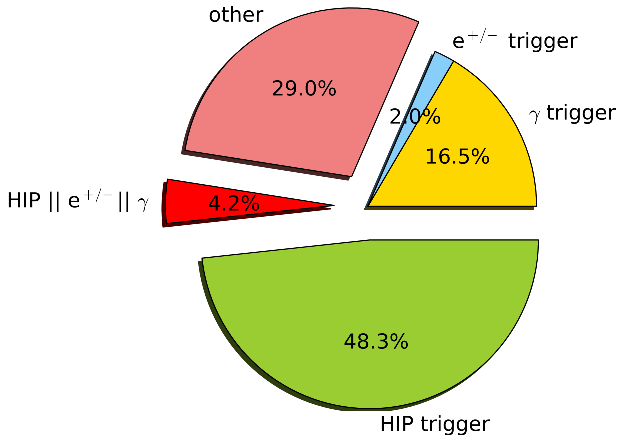

Figure 49: The percentage of events in the ATLAS dESD considered in this analysis triggered by the different EF triggers.

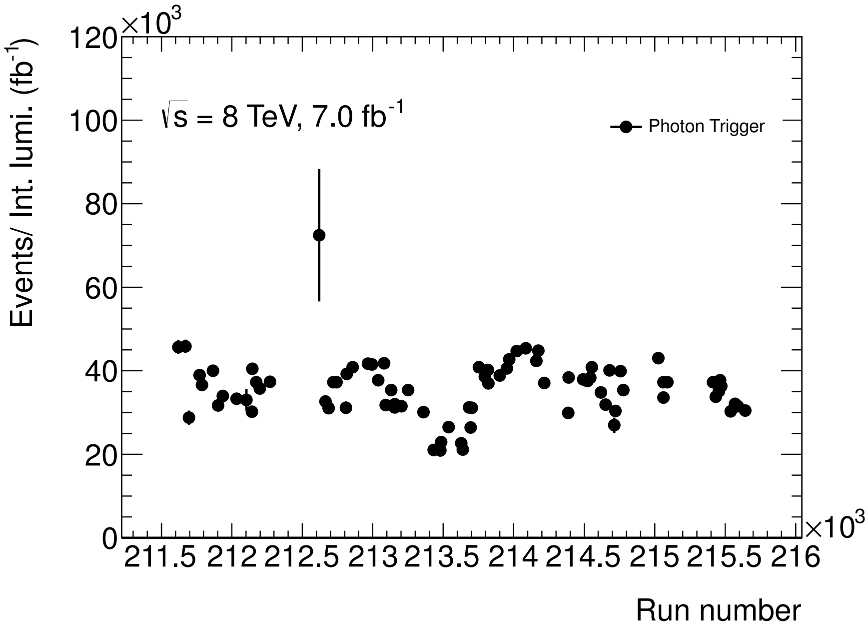

Figure 50: The ratio of the number of events fired by the single photon trigger with an energy threshold of 120 GeV in a run to the integrated luminosity of the run for the entire dataset corresponding to 7.0 fb^{-1}. The errors shown are estimated only on the number of events fired by the trigger in each run.

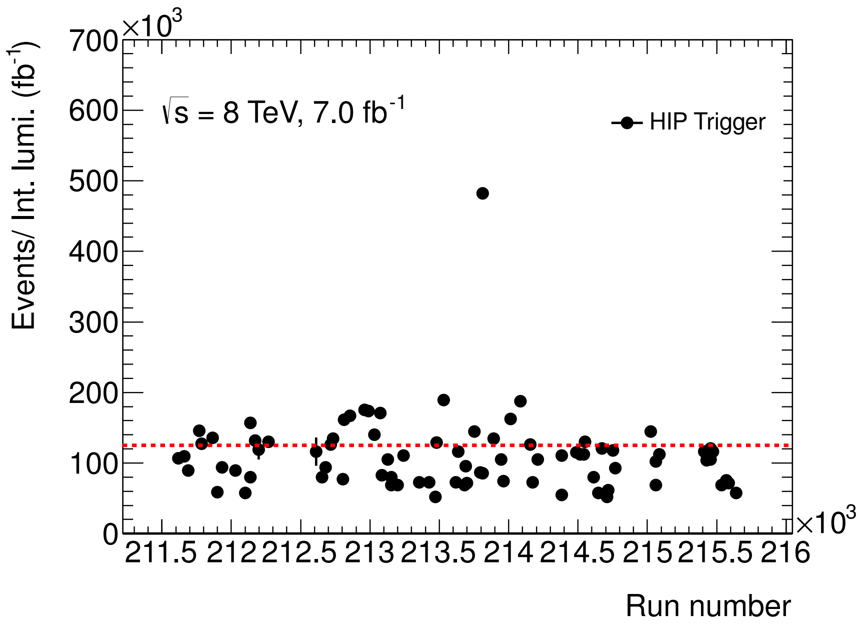

Figure 51: The ratio of the number of events fired by the HIP trigger in a run to the integrated luminosity of the run for the entire dESD dataset corresponding to 7.0 fb^{-1}. The errors shown are estimated only on the number of events fired by the trigger in each run.

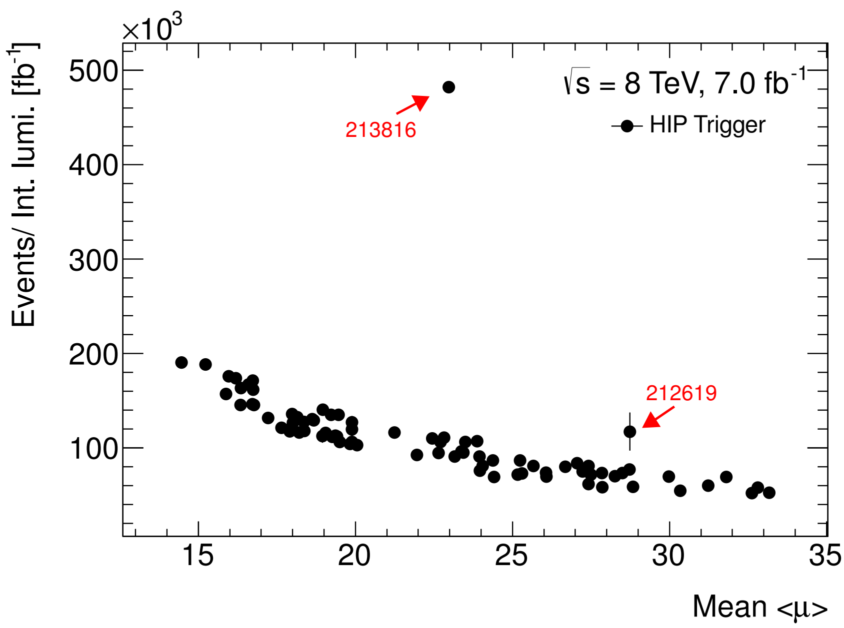

Figure 52: A scatter plot of the average pile-up of a run against the ratio of the number of events fired by the HIP trigger in a run to the integrated luminosity of the run. The errors shown are estimated only on the number of events fired by the trigger in each run.

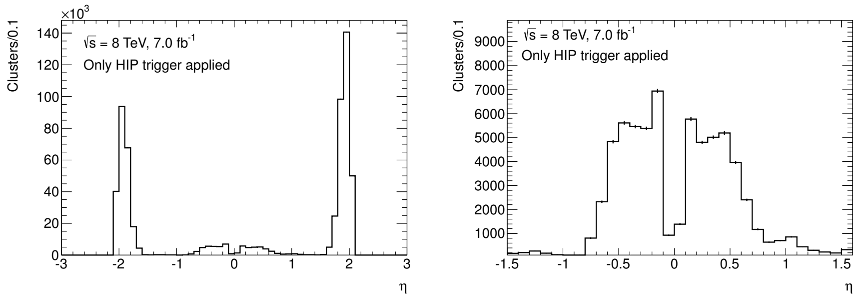

Figure 53: The pseudo-rapidity distributions of the cluster that fired the HIP trigger in the ATLAS dataset. This distributions are shown for the entire pseudo-rapidity range (left) and only for the barrel region (right).

number 213816, which expects $\approx$ 490000 events per fb^{-1}, was known to have TRT gas problems before the run. The same run was reported by the Data Acquisition Quality (DAQ) shifter to have "TRT turned yellow due to high threshold hits occupancy in end-cap having a spike". The second run , #212619, is a run with significantly fewer events (34 events) compared to the other runs, as can be seen by the larger error bars in the figures. The luminosity for this run was 0.00029 fb^{-1}. The low statistics contribute significantly to the large deviation from the expected values.

Run 213816, with the total integrated luminosity of 0.0472 fb^{-1}, is disregarded from the analysis. The total error on the luminosity is 2.8%, thus quoting an integrated luminosity value of 7.0 fb^{-1} with the removal of the run 213816 is still well within the uncertainties on the luminosity.

Fig. 53 shows the cluster pseudo-rapidity for events that fired the HIP trigger in the entire ATLAS dataset. An asymmetry is observed in this distribution which is further discussed in Appendix D.

3.4 ANALYSIS STRATEGY

The strategy to select signal-like candidates with high efficiency and to reject the bulk of background-like processes involves a series of selections. In terms of its software implementation, this is achieved in two steps. The first set of selections, called *preselections*, is applied in the analysis framework which saves all relevant information for all the interesting events in a data format referred to as nTuples. The second set of selections is called *offline selections* which imposes criteria based on the information stored in the nTuples. The following subsections chronologically describe the selections applied starting from the cuts in the analysis framework to the offline selections.

It is important to note that ESDs from data that are used as inputs in the analysis framework tool are already filtered using the dESD filter. Therefore, events that remain in data ESDs are either triggered by the HIP trigger or have passed another analysis filter. In the case of MC signal samples no such filter is applied.

At the stage of the analysis framework, a set of 'preselection' cuts are applied to limit the information to only the interesting candidates. The clusters formed by the CaloCalTopoCluster algorithm (see Sec. 3.1.4) are considered as calorimeter cluster candidates in this analysis. To match the L1 trigger requirements, a cut is placed at 16 GeV on the transverse energy E_T of the calorimeter cluster. While this threshold value is lower than that in the L1 trigger, it helps eliminate the other candidates in the event that were not triggered by the HIP trigger.

To identify HIP-like candidates, an algorithm, similar to the HIP trigger algorithm (see Sec. 3.2), is developed to select candidates based on the fraction and number of HT TRT hits associated with an EM cluster candidate. The algorithm builds a wedge of size $\Delta\phi = \pm 0.05$ in the TRT that is centred around the azimuthal angle of the cluster, $\phi_{cluster}$. A $(\phi)_{max}$ is identified as the azimuthal angle where the maximum density of HT TRT hits lie in the $\Delta\phi = \pm 0.05$ wedge[17]. The average ϕ_{HT}^{avg} of all the HT TRT hits in a narrower wedge of size $\Delta\phi = \pm 0.01$ centred around $(\phi)_{max}$ is then computed.

A rectangular road of width $\pm$4mm centred around ϕ_{HT}^{avg} is built in the TRT barrel. This road is wide enough to include two TRT straws (a TRT straw is 4 mm in diameter). In the TRT end-cap, which provides only the z and ϕ information, a wedge-shaped road of size $\Delta\phi = \pm 0.006$ centred around ϕ_{HT}^{avg} is defined. The angular width is chosen such that it is $\pm$4 mm at the inner radius of the TRT end-cap wheels. Fig. 54 shows an example of the $\pm$4 mm road constructed in the TRT barrel along the monopole trajectory.

The TRT hits contained in the roads defined above are computed with loose η requirements, owing to the TRT geometry. The loose η requirement was such that, a TRT hit was considered to be a part of the road centred around ϕ_{HT}^{avg}, if the TRT hit and the cluster were on the same side of the detector, by asserting $\eta_{TRT} \times \eta_{cluster} > 0$. Additionally, in the central region with $|\eta| < 0.1$, no η requirements are placed since the precise η information is not available.

Two parameters are constructed from the TRT hit information in the roads, namely, the number of HT TRT hits (N_{HT}^{presel}) and the fraction of HT TRT hits (f_{HT}^{presel}). These two parameters help identify HIP-like candidates which satisfy the requirement, $N_{HT}^{presel} > 10$ and $f_{HT}^{presel} > 0.4$, in the TRT region associated to a cluster candidate. The f_{HT}^{presel} parameter is improved further when building the final discriminant as detailed in Sec. 3.4.3. Fig. 55 shows the distributions of the two constructed parameters for simulations of a single particle monopole with a mass of 1000 GeV and charge $1.0g_D$ along with simulations of electrons from the $Z \to e^+e^-$ process. The double peak structure in the monopole distribution is attributed to the different number of hits in the barrel (first peak) and end-cap (second peak) regions.

17 This is computed by taking the maximum of the $|\phi_{HT} - \phi_{clust}|$ distribution.

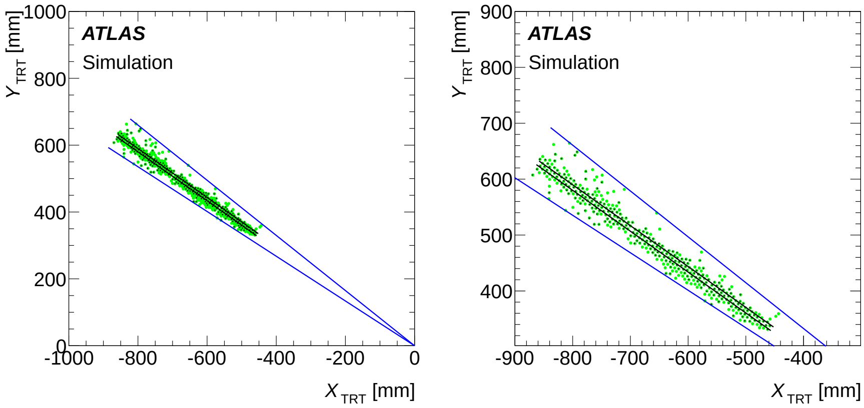

Figure 54: An example of a simulated monopole trajectory in the r-ϕ plane, showing the barrel TRT hits in a wedge of $\Delta\phi = \pm 0.05$ rad around the EM cluster. The black and green points are the high-threshold and low-threshold hits, respectively. Overlaid is the ± 4 mm rectangular road.

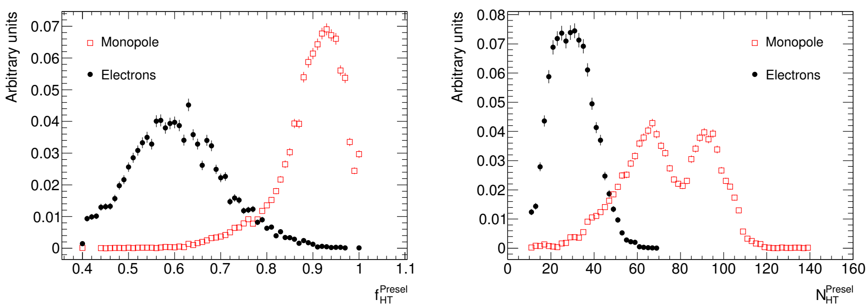

Figure 55: The distributions of the constructed preselection variables N_{HT}^{presel} and f_{HT}^{presel} for simulated single particle monopoles of mass 1000 GeV and charge $1.0 g_D$ and electrons from the $Z \to e^+e^-$ processes. The preselected variables are required to have $N_{HT}^{presel} > 10$ and $f_{HT}^{presel} > 0.4$. The two peaks in the N_{HT}^{presel} distribution are due to the different number of HT TRT hits in the barrel (first peak) and end-cap (second peak) regions.

The detailed information of candidates that satisfy the criteria described thus far are written into nTuples that are analysed further as described in the following subsection.

3.4.2 *Offline selections*

The nTuples produced by the analysis framework are used for the final analysis of data and signal samples. The second set of selections applied use the relevant information stored in the nTuples to select signal-like candidates per event. The cuts are described below in the order they are applied:

- Overlap removal: Signatures of highly ionising particles require a region of high-f_{HT} in the TRT associated to a narrow cluster in the ECAL. It is found that several preselected EM clusters can be matched to the same high fraction TRT region, which is undesirable. Fig. 56 shows the number of preselected candidates for a single monopole of mass 1000 GeV and various charges, where only one preselected candidate per event is expected. The additional preselected candidates observed in Fig. 56 is not attributed to pile-up events, since the distribution of the average number of preselected candidates is uniform across all $\langle\mu\rangle$ values in the samples. Thus the cause of the additional preselected candidates is attributed to the clustering algorithm which in rare cases splits the topological clusters when its energy thresholds are crossed as described in Sec. 3.1.4.

  To identify the set of calorimeter clusters that are associated to the same TRT region, their η and ϕ information is used. A set of calorimeter clusters is built based on certain criteria: for all clusters whose standard deviations of η and ϕ satisfy, $\Delta(\eta_{cluster}) < 0.1$ and $\Delta(\phi_{cluster}) < 0.05$. To ensure that only one cluster is associated to the TRT hits, the candidate (from the defined set) with the highest summed energy in the presampler and the EM1 is selected. This is based on the expected signature of the monopole in the calorimeter, which must deposit a large fraction of its energy in the first layers of the calorimeter.

- HIP trigger: Only events that fire the HIP trigger are considered.

- Cluster energy: The summed cluster energy in all EM calorimeter layers $E_T^{EM} > 16$ GeV. This is a somewhat redundant cut with the $E_T > 16$ GeV already applied at preselection, but further reduces the candidates to those which triggered the event. The difference in this offline selection is that the transverse cluster energy is considered only for the ECAL (Presampler,EM1, EM2, EM3) as compared to the entire transverse cluster energy in the preselection.

- EM layer energies: It is required that the candidate deposits at least 5 GeV in the presampler or the EM1 of the ECAL. Background candidates that would start to shower and deposit the

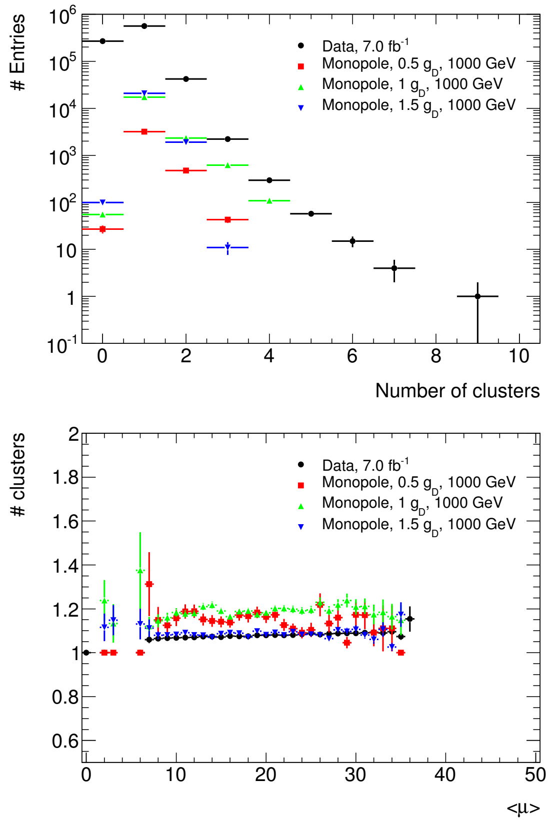

Figure 56: The distributions showing the number of preselected clusters (top) and the profile histogram of the number of preselected clusters as a function of pile-up $\langle\mu\rangle$ (bottom). The single particle monopole simulations are used for various charges of the same mass, 1000 GeV. For the profile distributions, it was required that the event has at least one preselected cluster candidate.

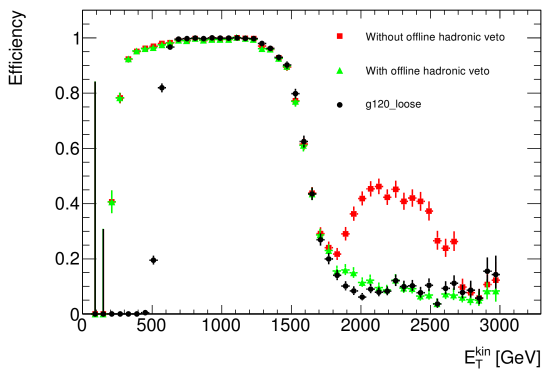

Figure 57: The HIP TRT trigger efficiency for single-monopoles with charge $|g| = 1.0g_D$ and mass 1000 GeV as a function of the initial transverse kinetic energy in the central region $|\eta| < 1.35$. The efficiency after the application of the offline veto is also shown.

energy in EM2 are rejected in such cases. The same requirement is also used in the definition of the w variable, as described in detail in Sec. 3.4.4.

- Pseudo-rapidity (η): Only candidates within $|\eta| < 1.375$ and $1.52 < |\eta| < 2.0$ are retained for further analysis. A strong correlation was observed between the final selection variables (described in the Appendix B) in the ECAL barrel and end-cap transition region i.e. $1.375 < |\eta| < 1.52$ and hence this region was disregarded. The TRT ends at $|\eta| = 2.0$ and therefore a cut is placed at this value to ensure the robustness of the f_{HT} variable.

- Offline hadronic veto: As described in Appendix C.1, an inefficiency was observed in the hadronic veto from Level-1 for the simulated HIP samples, resulting in an increase in the trigger efficiency for such samples. An offline hadronic veto is applied by summing up the cluster energy in barrel and extended barrel of the HCAL and rejecting events where $E_{Had} > 1$ GeV. The resulting efficiency as a function of E_T^{kin} is shown in Fig. 57.

- Single candidate: To allow for an event-based estimation of the background from data, it is preferable to have only one candidate per event. Therefore, if there are multiple candidates in the event after all the above selections are applied, the candidate with the highest f_{HT} value is selected as the final candidate considered in the analysis.

To distinguish the monopole/ HECO signal from background processes the analysis uses two powerful discriminating variables. The first of these variables (f_{HT}) is similar to the fraction of high-threshold TRT hits handle as described in the trigger section (3.2) and preselection.

The second variable describes the width of the cluster in the EM calorimeter and is hence called the w variable. Energy loss via Bremsstrahlung and pair-production are considered to be negligible

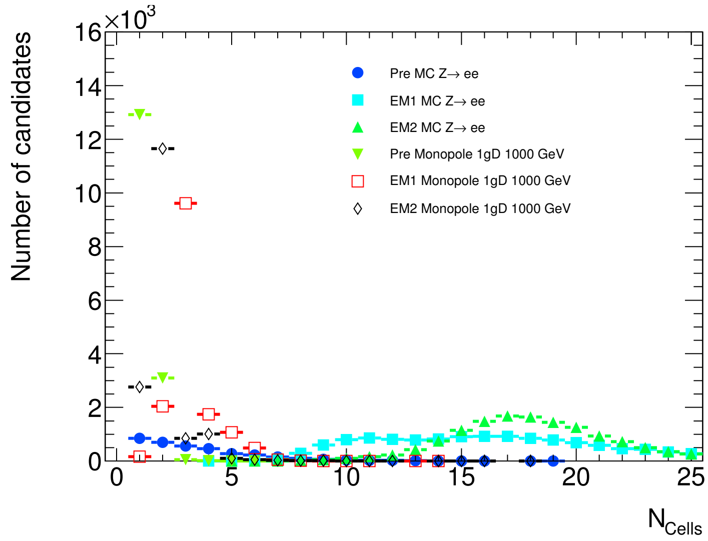

Figure 58: The distribution of the number of cells in a given layer that contains at least 95% of the energy in that layer. Highly ionising particles are expected to have narrow cluster signatures i.e. they deposit most of the energy in few cells. In the case of the backgrounds, such as $Z \to ee$, the cluster sizes are typically larger due to Bremsstrahlung. The distribution of N_{cells} for electrons extends to 50, but the plot is truncated to clearly show the distinction between signal and background-like processes.

and therefore most of the energy from highly ionising particles is deposited only in a few cells of the calorimeter as shown in Fig. 58.

These two variables were used in the previous monopole analysis at ATLAS [72]. However to adopt these into the present analysis, these variables were redefined and re-optimised, the details of which are covered in the following sub-sections.

3.4.3 *The f_{HT} variable*

The preselection f_{HT}^{presel} variable is further refined for final selections, to account for inefficiencies in its calculation in the central ($|\eta| < 0.1$) and transition ($0.77 < |\eta| \leqslant 1.37$) regions. In the central region, the f_{HT}^{presel} is computed using the hits from both barrels, which reduces the f_{HT}^{presel} of the signal samples in this region. A new method was proposed, whereby the fraction of HT TRT was computed separately in each barrel using the corresponding hits and compared to the original f_{HT}^{presel} associated with the cluster. For defining the fractions in each barrel region, the $N_{TRT}^{eachbarrel} > 10$ to avoid high fractions originating from low number of TRT hits. The largest fraction value is chosen as the new f_{HT} associated with the cluster.

Similarly, in the transition region, the hits are considered separately from barrel and end-caps and compared to the original fraction of HT TRT hits. To define the fraction in the barrel a requirement, $N_{TRT}^{barrel} > 10$ is placed and similarly, for the end-cap the requirement is, $N_{TRT}^{end-cap} > 20$. Fig. 59 shows the number of TRT hits belonging to

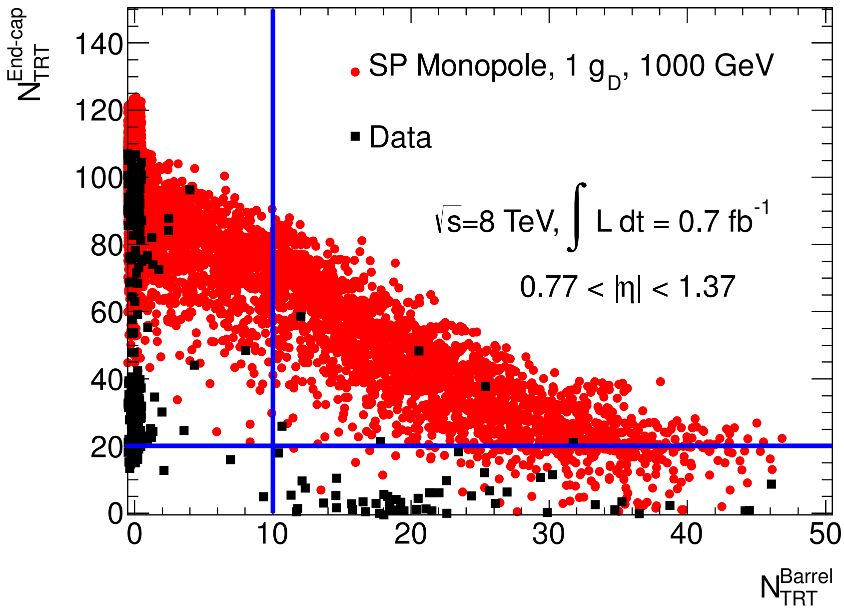

Figure 59: The number of TRT hits in the barrel and the end-cap from candidates in the transition region. The blue lines indicate the cuts placed on the number of hits required in the barrel and end-cap before defining a new fraction in the individual region.

the barrel and end-cap regions for an associated cluster candidate for both signal and data. Again, the largest fraction value among those observed when using the barrel only, the end-cap only, or both barrel and end-cap is chosen as the new f_{HT} associated with the cluster.

Fig. 60 shows the fraction of HT TRT hits for monopoles and data, with and without the recalculation method being applied. The peak at 1 for the monopole signal sample is increased with the use of the efficient recalculation method, while the distribution for the data remains unaffected. Fig. 61 shows the fraction of HT TRT hits in data and monopole signal sample as a function of η, showing the beneficial effect of the recalculation technique on the signal sample in the central η region (around η=0) and in the barrel-end-cap transition region (around $|\eta|$=1)..

The newly derived f_{HT} variable is used for the final selections of candidates.

3.4.4 *The w variable*

The w variable describes the width of the cluster in the EM calorimeter and is a powerful discriminant between signal and background processes. Formally, the w variable is defined in each layer as the fraction of energy deposited in n-cells of the layer over the total energy in the layer, Eq. 26.

$$w_i = \frac{E_i^n}{E_i} \tag{26}$$

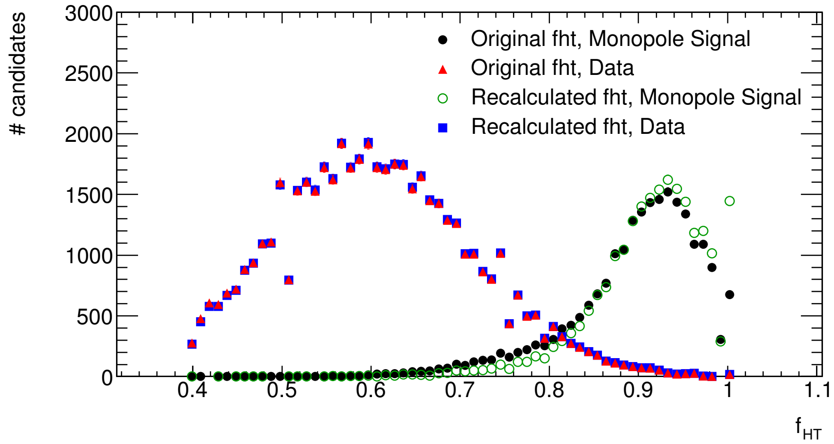

Figure 60: Distributions of the f_{HT} variable before and after applying the recalculation method in the central and transitions regions for a MC monopole sample and data. A considerable gain is observed for the signal sample with minimum impact on the backgrounds.

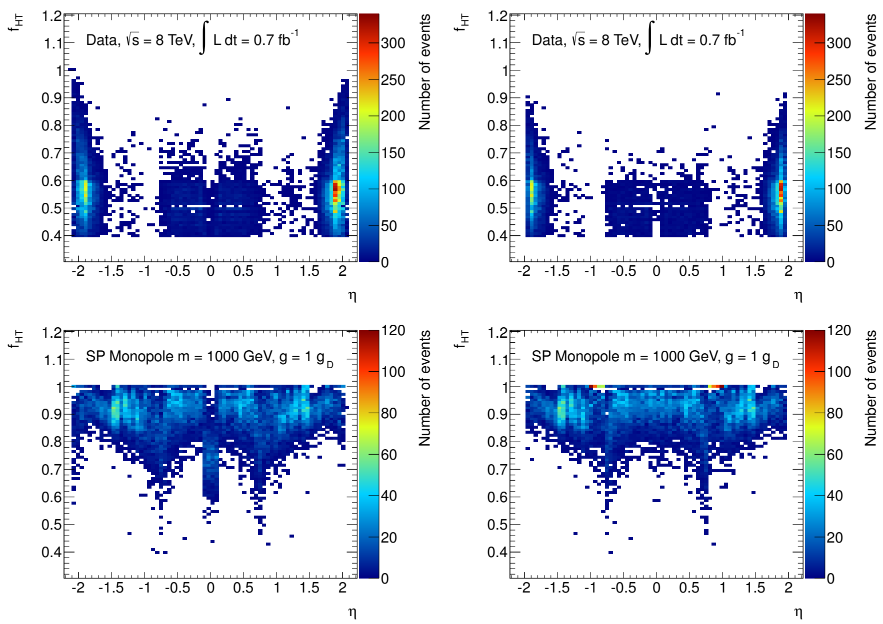

Figure 61: The distributions of f_{HT} as a function of η for data (top) and MC monopole sample (bottom). The distributions are shown for f_{HT} before (left) and after (right) applying the recalculation method. A considerable gain is seen for signal samples, with minimum impact on the data distributions.

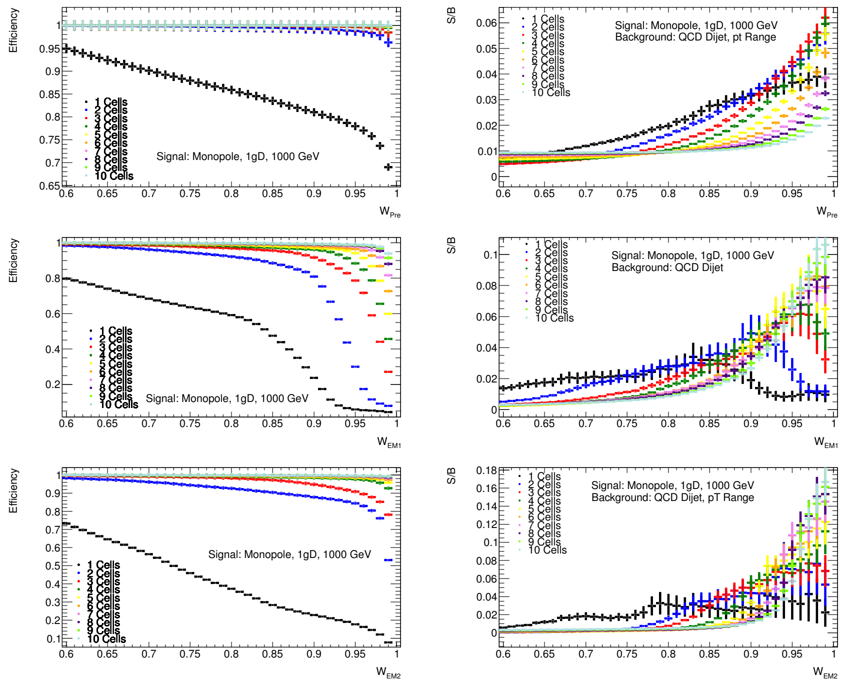

Figure 62: Selection of plots that were used to determine the number of cells for the w variables definition in the presampler (top), EM1 (middle) and EM2 (bottom) calorimeter layers. The plots on the left show the signal efficiency as a function of a cut in the w variable in each layer. The plots on the right show the signal over background ratio as a function of a cut in the w variable for a di-jet sample as background.

where, i refers to the calorimeter layer (Presampler, EM1 or EM2). n refers to the number of cells used in the i^{th} layer, which is 2 for Presampler, 4 for EM1 and 5 for EM2. E_i^n is the sum of the energy from n most energtic cells in the i^{th} layer, while E_i is the cluster energy contained in the i^{th} layer.

The number of cells (n) used in each layer is estimated by a rough optimisation process with the aim to maximise the signal efficiency and the discrimination power between HIPs and electron or jet backgrounds. Fig. 62 shows an example plot for one specific monopole sample that was used to optimise for the number of cells to be used in the w variable. All signal samples with different masses and charges were examined as well which gave similar conclusions. The number of cells for which the signal efficiency as well as the signal/ background ratio is maximised across all mass and charge points is chosen for a given layer. Through this process it was observed that the number of cells in the presampler, EM1 and EM2 should be 2, 4 and 5 respectively to describe the w_i.

In this analysis, the w variable is defined as a combination of the three w_i variables (i = Pre, EM1, EM2)[18]. To begin with, the w_i is defined in a given layer only if $E_i > 5$ GeV, to ensure that the en-

18 In Appendix A, the choice of combining the w variable is discussed. For simplicity, w refers to the combined average of w_i in the remainder of the text.

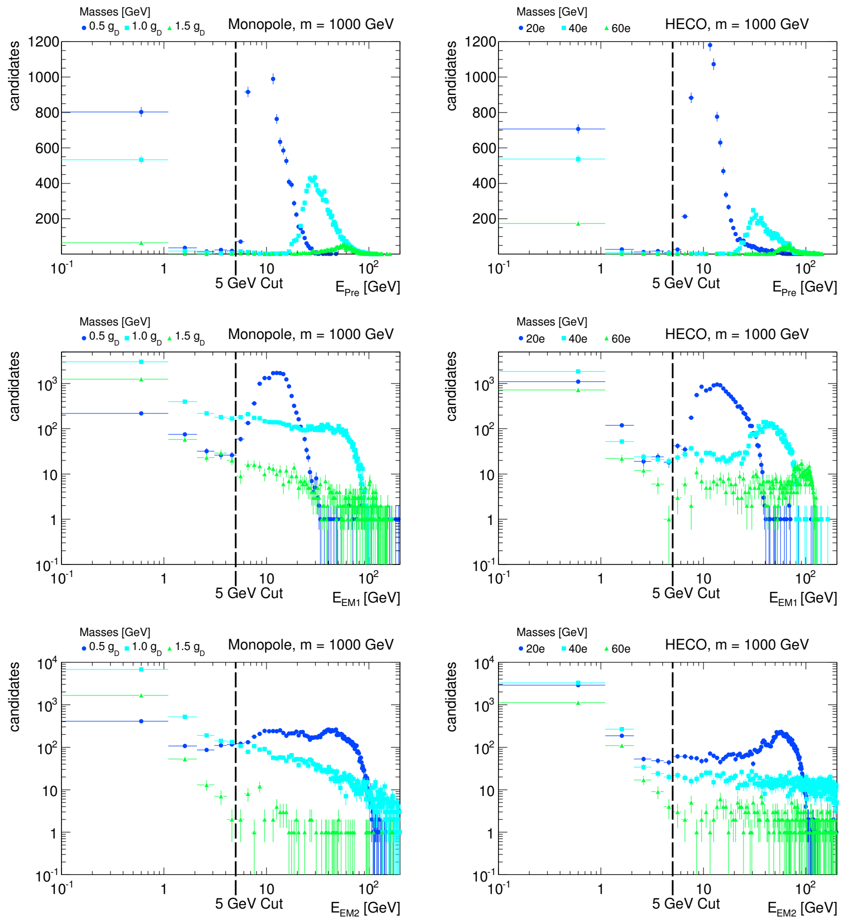

Figure 63: The energy distribution in each layer of the ECAL - Presampler (top), EM1 (middle) and EM2 (bottom) - for monopoles (left) and HECOs (right) with different charges. The distributions are plotted for DY produced HIPs having a mass of 1000 GeV. The x-axis is in log-scale to better highlight the effectiveness of the 5 GeV selection used to eliminate the noise in the definition of the w_i variable as described in the text.

ergy dispersion in the layer is due to the presence of a HIP and not noisy cells. Fig. 63 and 64 show the cluster energy distributions of typical HIP signals in the different layers of the calorimeter. As the HIP traverses through the detector, it deposits most of its energy in the presampler and the EM1. The zero energy deposition by candidates in the presampler is attributed to its limited pseudo-rapidity acceptance ($|\eta| < 1.8$). In subsequent layers, EM1 and EM2, the near-zero energy deposition shows candidates that have stopped in the previous layers with small residual energy that transmits to the current layer. The combined w variable is then defined as the average between all the w_i for which E_i exceeds a 5 GeV threshold. To further suppress backgrounds, candidates with only w_{EM2} defined are rejected, since HIPs that have penetrated through to the EM2 should also have energy deposits in at least one of the previous layers.

The distributions of individual w_i variable is shown in Fig. 65. The distributions peak close to one for signal samples while the back-

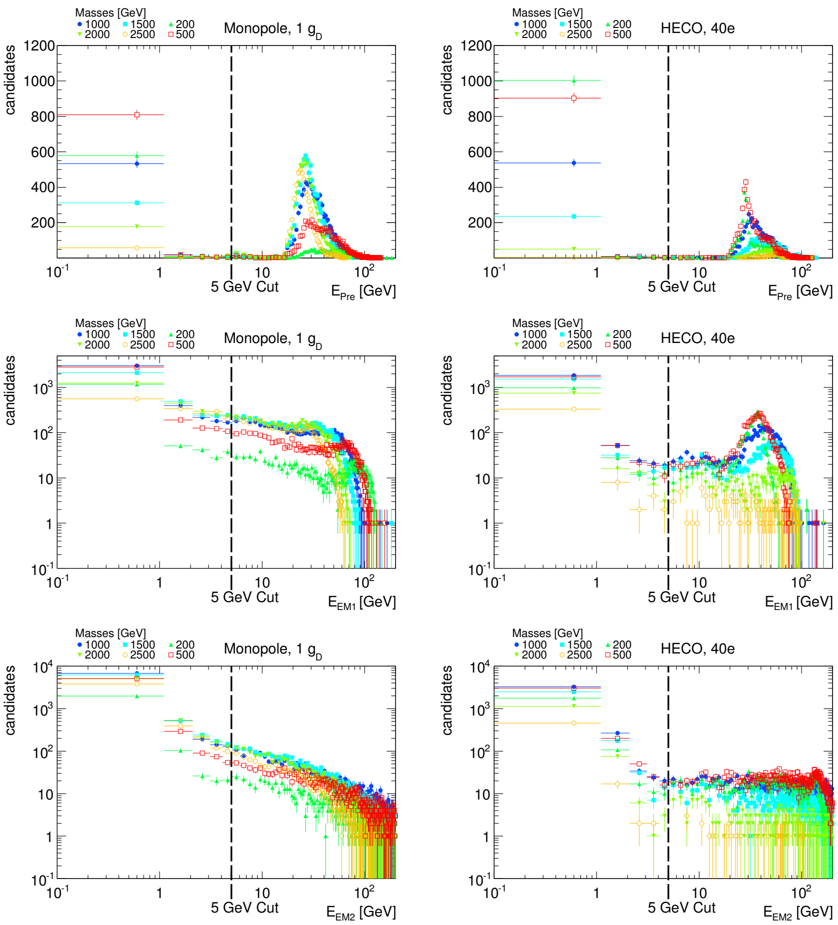

Figure 64: The energy distribution in each layer of the ECAL - Presampler (top), EM1 (middle) and EM2 (bottom) - for monopoles (left) and HECOs (right) with different masses. The distributions are plotted for DY produced HIPs having the charge of $1.0g_D$ for monopoles and $40e$ for HECOs. The x-axis (y-axis as well for EM1 and EM2) is in log-scale to better highlight the effectiveness of the 5 GeV selection used to eliminate the noise in the definition of the w_i as described in the text.

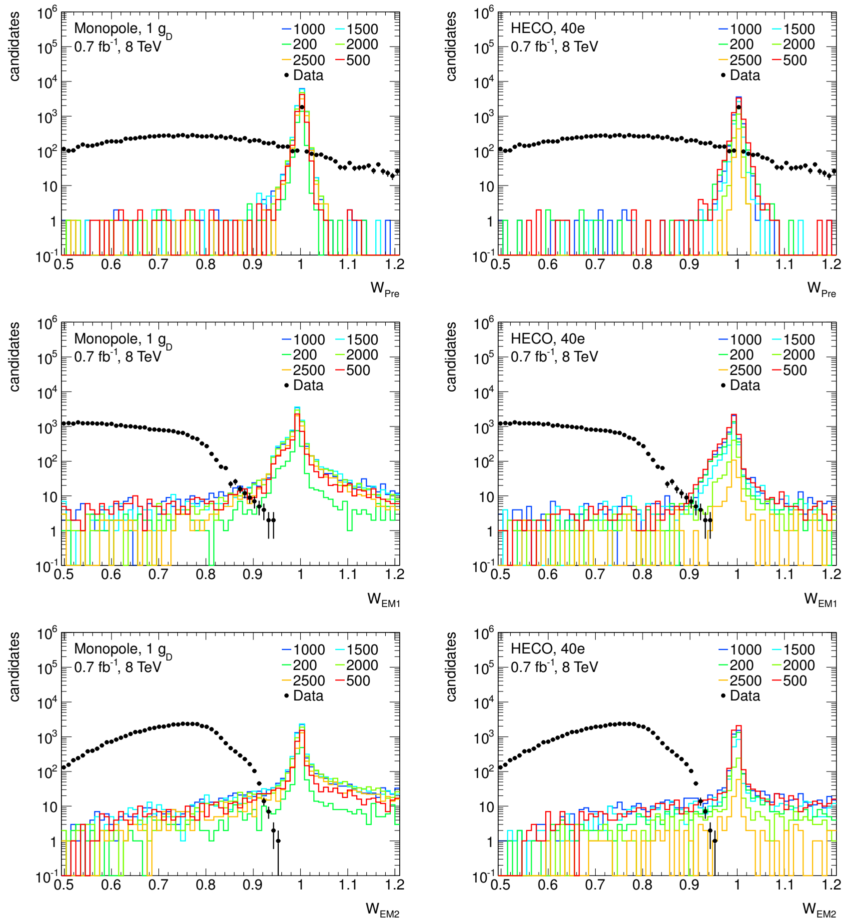

Figure 65: The individual w_i (i = Presampler (top), EM1 (middle), EM2 (bottom))distributions for $1.0 g_D$ monopoles (left) and $40e$ HECOs (right) in the different layers of the ECAL. The distribution of the w variable for data is also overlaid to highlight its discriminating power.

ground distributions peak at lower values. Due to the granularity of the presampler, the discriminating power of the w_{pre} variable is worse compared to the w_{EM1}, w_{EM2}. However, this has a negligible effect on the discriminating power of the combined w variable (see Fig. 104 in Appendix A).

The robustness of the final selection variables as a function of pile-up is crucial, keeping in mind the high instantaneous luminosity delivered by the LHC in 2012. Fig. 66 shows the dependence of the final selection variables on pile-up for monopoles and HECOs respectively.

A mass dependence of the w variable for monopoles can be observed in Fig. 66. The degradation of the w variable can be attributed to the bending of the HIPs in the magnetic field (in η for monopoles and in ϕ for HECOs). Lower mass HIPs tend to deviate from unity as the initial kinetic energy increases and the HIPs penetrate further into the calorimeter as shown in Fig. 67. Since their direction is not exactly aligned with the calorimeter cells (which point towards the interaction point) they deposit energy in a larger number of cells, thus degrading w variable. Fig. 68 shows the distributions of the w vari-

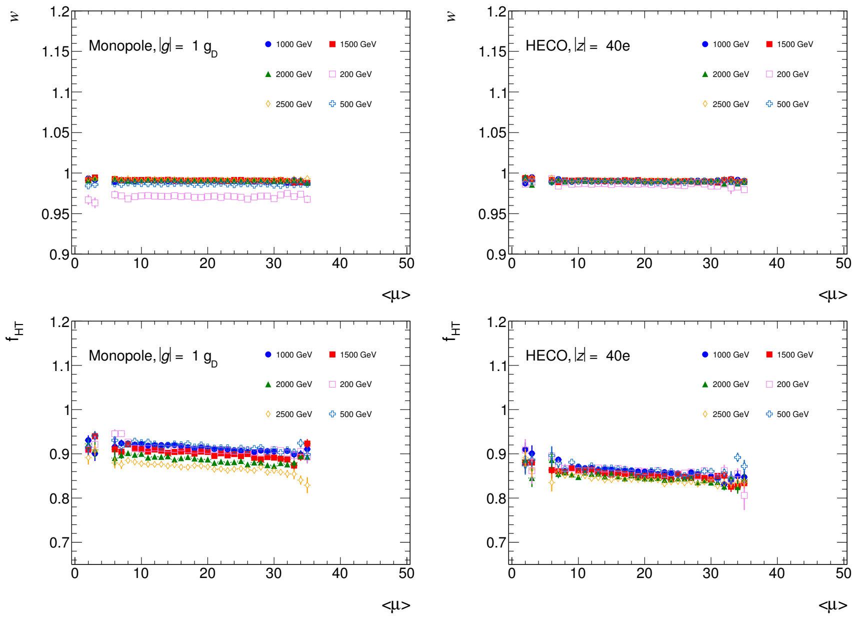

Figure 66: The profile distributions of the final selection variables, w and f_{HT} as a function of pile-up. A small but acceptable degradation with an increase in pile-up is seen for the f_{HT} variable. The w variable is very pile-up robust and is slightly mass dependent.

able for various HIP signals with varying masses and charges and for collision data.

One possible explanation can be attributed to the larger bending of low mass monopoles in the central-η region, whereby they penetrate through larger number of calorimeter cells. Fig. 69 shows the distribution of the number of cells in different layers of the ECAL that have non-zero energy deposits as a $1.0g_D$ monopole traverses through. Conversely, as seen in Fig. 70, the HECOs bend in ϕ where the calorimeter cells have a coarser segmentation, thereby traversing through a fairly constant number of cells and minimising mass dependence on the w variable.

Additionally, lower mass HIPs with high kinetic energy produce δ-rays which are energetic enough to propagate in the calorimeter and deposit their energy through bremsstrahlung. The δ-rays produced by low mass HIPs that reach the calorimeter cause a larger cascade that contributes to the degradation of w variable.

3.4.5 *Final selection variable cuts*

The selection criteria on the final variables were optimised using pseudo-data generated from the control region in data such that the low-f_{HT} region distribution was used to generate the w variable distribution and vice-versa). For each charge and mass point, the significance, defined as signal/$\sqrt{(\text{signal} + \text{background})}$, was determined as a function of the two selection variables. The resulting distributions are shown in Fig. 71 for HECO signal, where the choice of the final selection cut values for a given sample were determined by using the

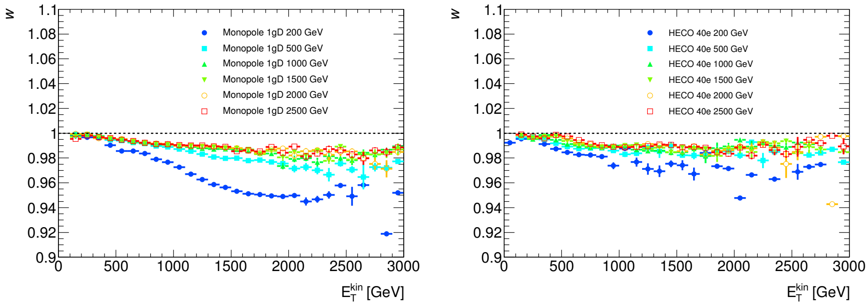

Figure 67: The profile of the w variable for all masses of a $1.0g_D$ monopole (left) and a charge $40e$ HECO (right) as a function of the truth HIP transverse kinetic energy. The w variable decreases with an increase in E_T^{kin} since HIPs with higher energies traverse further into the calorimeter and deposit energy in a larger number of cells, thereby reducing the value of the w variable. The degradation of the w variable for monopoles is larger than that of HECOs, this is attributed to the bending of the monopoles in η and is explained further in the text.

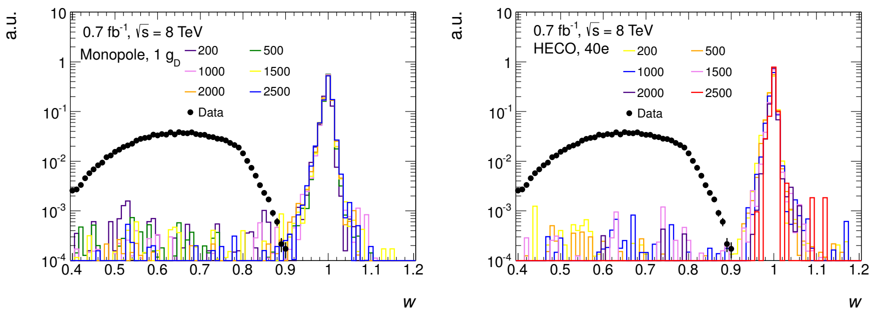

Figure 68: The discriminating power of the final selection variable w for Drell-Yan produced $1.0g_D$ monopoles (right) and $40e$ HECO (left) for various masses.

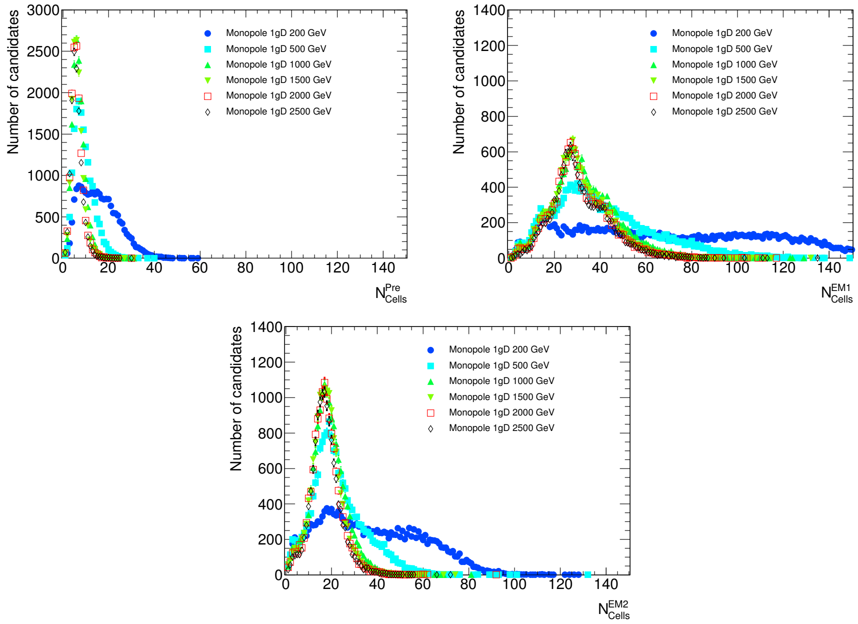

Figure 69: The number of cells in which a $1.0g_D$ monopole deposited non-zero energy in each layer. The low mass monopoles tend to deposit energy in more cells due to their bending in η where the granularity of the ECAL is very fine.

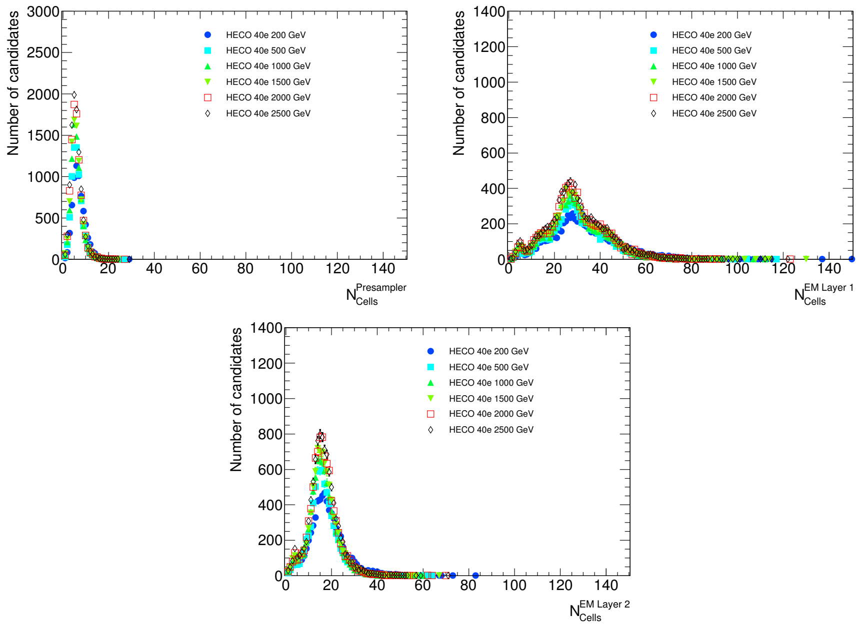

Figure 70: The number of cells in which a 40e HECO deposited non-zero energy in each layer. HECOs tend to bend in ϕ where the granularity of the ECAL is coarse, thereby the number of cells penetrated by all mass samples remains fairly constant.

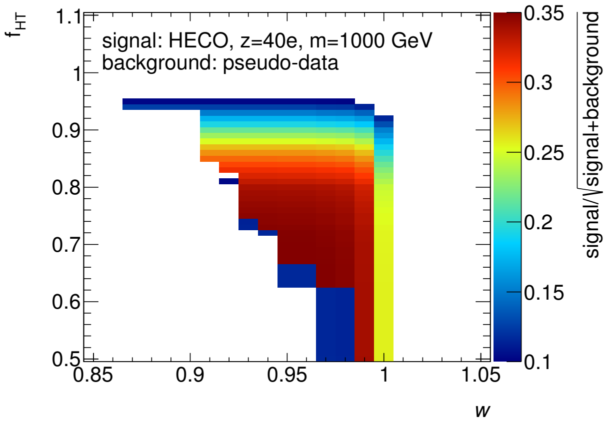

Figure 71: Illustration of the cut optimisation procedure. The number of signal and background events above the bin value on each axis is used to compute the quantity $\frac{\text{signal}}{\sqrt{\text{signal+background}}}$. The axes values for the bin which maximises the ratio is selected as the optimum cut value for the corresponding signal. The process is repeated for all signal samples and the final cut values are determined to accommodate (with least possible signal loss) all signal samples.

highest ratio bin. This optimisation method led to the cut values of $w \geqslant 0.96$ and $f_{HT} \geqslant 0.7$. However, for certain signal samples the peak of the w variable distribution lies very close to the cut value obtained, thereby making the signal efficiencies in these samples very sensitive to certain systematic uncertainties (for example, cross-talk). The cut on the w variable was therefore relaxed to $w \geqslant 0.94$.

3.4.6 *Selection efficiencies for Drell-Yan produced HIPs*

The main loss in efficiency for all samples considered in the analysis is caused by the acceptance of the L1 trigger, as discussed in Sec. 3.2.5. The final selection efficiencies for Drell Yan spin-½ and spin-0 [19] samples are summarised in Tab. 5 - 8. Only statistical uncertainties are quoted in the tables.

Tab. 9, 10 show the cut-flow for the Drell-Yan spin-½ Monopoles ($|g| = 1.0g_D$) and HECO ($|z| = 40e$) respectively.

The acceptance, at L1, for high charge monopoles is low as a large fraction of the Drell-Yan produced HIPs lose their energy and stop before they reach the calorimeter [24] (for example, $|g| = 2.0g_D$; acceptance $\mathcal{O}(0.01\%)$). For high charges in the Drell-Yan model, only the tails of the E_T^{kin} and E_L^{kin} distributions in Fig. 72 are accessible to the ATLAS calorimeter. Thus for such cases the monopole acceptance is highly dependent on the model of production. In the analysis, searches for Drell-Yan signals with less than 1% acceptances are not interpreted.

19 The samples are obtained using the procedure as described in [107].

	DY Spin-½ Monopole Selection Efficiencies [%]			
	Magnetic Charge			
Mass [GeV]	$\lvert g\rvert = 0.5g_D$	$\lvert g\rvert = 1.0g_D$	$\lvert g\rvert = 1.5g_D$	$\lvert g\rvert = 2.0g_D$
200	22.32 ± 0.29	3.51 ± 0.13	0.14 ± 0.03	0.001 ± 0.004
500	33.53 ± 0.33	14.86 ± 0.25	1.16 ± 0.09	0.02 ± 0.02
1000	27.83 ± 0.32	23.37 ± 0.30	3.65 ± 0.13	—
1500	23.66 ± 0.30	22.15 ± 0.29	3.53 ± 0.13	0.099 ± 0.033
2000	16.69 ± 0.26	16.53 ± 0.26	2.79 ± 0.12	0.055 ± 0.024
2500	9.796 ± 0.210	9.759 ± 0.216	1.61 ± 0.09	0.02 ± 0.01

Table 5: Drell-Yan spin-½ monopole selection efficiencies (in %). The uncertainties are statistical only.

	DY Spin-½ HECO Selection Efficiencies [%]			
	Electric Charge			
Mass [GeV]	$\lvert z\rvert = 10e$	$\lvert z\rvert = 20e$	$\lvert z\rvert = 40e$	$\lvert z\rvert = 60e$
200	3.79 ± 0.13	9.66 ± 0.21	11.89 ± 0.23	3.14 ± 0.12
500	6.714 ± 0.177	19.03 ± 0.28	20.00 ± 0.28	6.169 ± 0.170
1000	10.74 ± 0.22	24.61 ± 0.30	16.85 ± 0.26	3.80 ± 0.13
1500	13.83 ± 0.24	22.47 ± 0.30	9.966 ± 0.212	1.43 ± 0.09
2000	15.51 ± 0.26	17.47 ± 0.27	3.68 ± 0.13	0.24 ± 0.03
2500	12.25 ± 0.23	10.24 ± 0.21	1.05 ± 0.07	0.009 ± 0.007

Table 6: Drell-Yan spin-½ HECO selection efficiencies (in %). The uncertainties are statistical only.

	DY Spin-0 Monopole Selection Efficiencies [%]			
	Magnetic Charge			
Mass [GeV]	$\lvert g\rvert = 0.5g_D$	$\lvert g\rvert = 1.0g_D$	$\lvert g\rvert = 1.5g_D$	$\lvert g\rvert = 2.0g_D$
200	42.5 ± 0.3	10.0 ± 0.2	0.40 ± 0.04	0.01 ± 0.01
500	53.8 ± 0.3	34.8 ± 0.3	4.1 ± 0.1	0.11 ± 0.02
1000	44.3 ± 0.3	51.1 ± 0.3	11.4 ± 0.2	0.39 ± 0.04
1500	36.5 ± 0.3	49.7 ± 0.3	13.8 ± 0.2	0.43 ± 0.04
2000	30.9 ± 0.3	41.6 ± 0.3	10.9 ± 0.2	0.32 ± 0.04
2500	22.9 ± 0.3	30.8 ± 0.3	6.9 ± 0.2	0.12 ± 0.02

Table 7: Drell-Yan spin-0 monopole selection efficiencies (in %). The uncertainties are statistical only.

	DY Spin-0 HECO Selection Efficiencies [%]			
	Electric Charge			
Mass [GeV]	$\lvert z\rvert = 10e$	$\lvert z\rvert = 20e$	$\lvert z\rvert = 40e$	$\lvert z\rvert = 60e$
200	5.9 ± 0.2	28.0 ± 0.3	27.6 ± 0.3	8.2 ± 0.2
500	9.8 ± 0.2	35.3 ± 0.3	42.1 ± 0.3	15.1 ± 0.2
1000	15.1 ± 0.2	45.7 ± 0.3	37.5 ± 0.3	11.4 ± 0.2
1500	19.9 ± 0.3	47.7 ± 0.3	26.7 ± 0.3	4.8 ± 0.1
2000	25.5 ± 0.3	43.6 ± 0.3	13.2 ± 0.2	1.15 ± 0.07
2500	26.9 ± 0.3	31.7 ± 0.3	4.3 ± 0.1	0.18 ± 0.03

Table 8: Drell-Yan spin-0 HECO selection efficiencies (in %). The uncertainties are statistical only.

	Candidates			Events		
All Cuts	Total	Rel. eff.	Overall eff.	Total	Rel. eff.	Overall eff.
Total	–	–	–	26502	–	100.00
L1 trigger	–	–	–	7962	30.04	30.04
HIP trigger	–	–	–	6526	81.96	24.62
Preselection	11253	–	100	6503	99.65	24.54
Overlap removal	10877	96.66	96.66	6503	100	24.54
E_T^{EM}	10794	99.24	95.92	6503	100	24.54
EM Layers	10787	99.94	95.86	6503	100	24.54
Pseudorapidity	10310	95.58	91.62	6242	95.99	23.55
Hadronic veto	10286	99.77	91.41	6242	100	23.55
Single candidate	6242	60.68	55.47	6242	100	23.55
$W_{avg} \geqslant 0.94$	6224	99.71	55.31	6224	99.71	23.49
$f_{HT} \geqslant 0.70$	6195	99.53	55.05	6195	99.53	23.38

Table 9: Cut-flow table for a spin-½ monopole signal with mass 1000 GeV and charge $\lvert g\rvert = 1.0 g_D$ produced with the Drell-Yan model.

	Candidates			Events		
All Cuts	Total	Rel. eff.	Overall eff.	Total	Rel. eff.	Overall eff.
Total	–	–	–	23848	–	100.00
L1 trigger	–	–	–	6319	26.5	26.50
HIP trigger	–	–	–	4481	70.91	18.79
Preselection	6487	–	100	4432	98.91	18.58
Overlap removal	6262	96.53	96.53	4432	100	18.58
E_T^{EM}	6244	99.71	96.25	4431	99.98	18.58
EM Layers	6230	99.78	96.04	4421	99.77	18.54
Pseudorapidity	5800	93.1	89.41	4072	92.11	17.07
Hadronic veto	5782	99.69	89.13	4071	99.98	17.07
Single candidate	4071	70.41	62.76	4071	100	17.07
$W_{avg} \geqslant 0.94$	4065	99.85	62.66	4065	99.85	17.05
$f_{HT} \geqslant 0.70$	4018	98.84	61.94	4018	98.84	16.85

Table 10: Cut-flow table for a spin-½ HECO signal with mass 1000 GeV and charge $|z| = 40e$ produced with the Drell-Yan model.

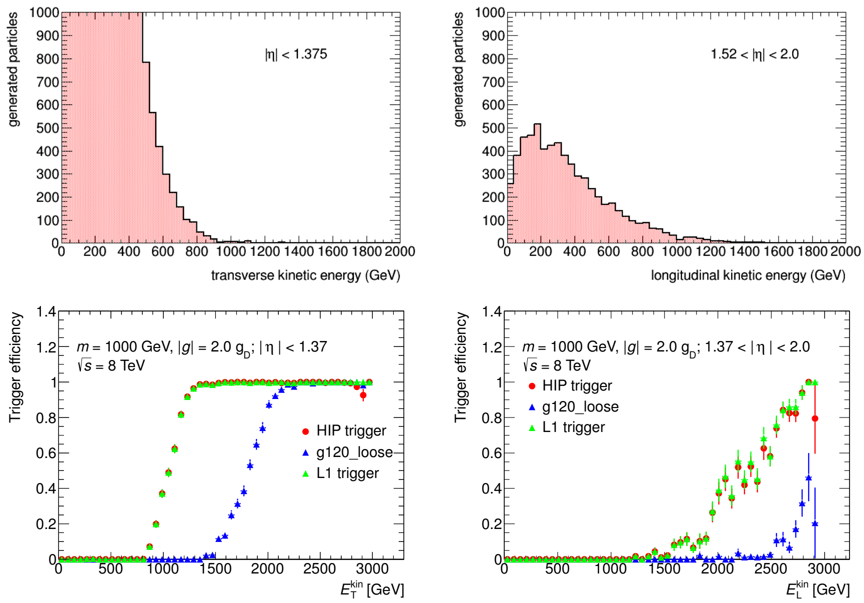

Figure 72: Distributions of the transverse kinetic energy in the barrel ($|\eta| < 1.375$, top-left) and longitudinal kinetic energy in the end-cap ($1.375 < |\eta| < 2.0$, top-right) for 8 TeV Drell-Yan HIPs with a mass 1000 GeV with the MadGraph generator. The distributions for the trigger efficiency (also showing the level-1 trigger) as a function of transverse kinetic energy in the barrel ($|\eta| < 1.375$, bottom-left) and longitudinal kinetic energy in the end-cap ($1.375 < |\eta| < 2.0$, bottom-right) for $2.0 g_D$ monopoles [114].

3.4.7 *Selection efficiencies for model independent samples*

Since there is no definitive production mechanisms of HIPs, model-independent results are derived for regions of kinematic parameter space which have high and uniform efficiencies, called fiducial regions. For this search, regions in the parameter space of kinetic energy and pseudo-rapidity of the HIPs where the uniform efficiency is above 90% are considered as the fiducial regions. These regions vary for each charge and mass point of HIPs and are determined individually for all of them. These results can in principle be used to interpret results in specific models by taking the kinematic distributions of the models into account.

The minimum kinetic energy of the HIP to which this search is sensitive depends on the amount of material the HIP needs to traverse before reaching the EM layer. The maximum kinetic energy depends on the ability of the HIP to traverse through the EM layer and into the HCAL to deposit 1 GeV of energy and provoke the L1 trigger veto. The amount of material in the detector is roughly proportional to ($\sin\theta^{-1}$) in the barrel region and to ($\cos\theta^{-1}$) in the end-cap. As in the case of determining p_T cuts (ref. Appendix E), the kinetic energy is defined in terms of the transverse kinetic energy ($E_T^{kin} = E_{kin}\sin\theta$) in the EM barrel region ($|\eta| < 1.475$) and the longitudinal kinetic energy ($E_L^{kin} = E_{kin}\cos\theta$) in the EM end-cap region.

The reconstruction efficiency was found to be symmetric in pseudo-rapidity within the statistical uncertainties. Therefore the $|\eta|$ vs $E_{T/L}^{kin}$ parameter space was considered to gain statistical precision.

An algorithm was developed to determine the fiducial regions for each of the mass and charge points. The algorithm builds efficiency maps in the given parameter space and determines the various fiducial regions with uniform efficiency. Only rectangular[20] fiducial regions that satisfy the efficiency condition within the parameter space were constructed by the algorithm. The bin size used in the efficiency maps was 25 GeV in kinetic energy and 0.05 in pseudo-rapidity.

The fiducial regions were found based on the following two conditions:

- $\mathrm{Eff}_{avg} > \mathrm{Eff}_{min} (= 90\%)$
- $\sigma_{\mathrm{Eff}} < 0.12$.

Where the Eff_{avg} is the average efficiency in the estimated fiducial region, defined as $\mathrm{Eff}_{avg} = \frac{1}{N}\sum_{i=1}^{N} x_i$, where x_i is the efficiency of the i^{th} bin. Eff_{min} is the minimum expected efficiency from the fiducial region, which is set to 90% for this search. σ_{Eff} is the standard deviation of the average efficiency that is maximised to secure the largest possible fiducial region with efficiency greater than E_{min}. It is defined as $\sigma_{\mathrm{Eff}} = \sqrt{\frac{1}{N}\sum_{i=1}^{N}(\mathrm{Eff}_i - \mathrm{Eff}_{avg})^2}$, where Eff_i is the efficiency of an individual i bin and the sum goes over all N bins

20 The choice of rectangular fiducial regions was motivated by the least complexity in developing the algorithm whilst also enabling a consistently shaped regions across all samples

The efficiency of each sample depends on the material distribution in the detector and hence varies as a function of pseudo-rapidity. Three regions in which the efficiency was significantly affected were identified. At $|\eta| \approx 1$ [21] there is a noticeable efficiency drop for HECOs and lower monopole charges. Another drop is noticed at $|\eta| \approx 1.5$, which is the transition region of the ECAL barrel and end-cap. In addition, the truncation of the maximum initial kinetic energy in the single-particle samples gives rise to a sharp sine shaped boundary to a region where there are no signal events. Thus the three regions in which the fiducial regions are independently identified are $0 < |\eta| < 1.0$ and $1.0 < |\eta| < 1.375$ for the EM barrel and $1.52 < |\eta| < 2.2$ for the EM end-caps.

The algorithm identifies a rectangular region which maximises the area described by $2 \cdot (|\eta_{max}| - |\eta_{min}|) \cdot (E^{kin}_{max} - E^{kin}_{min})$ while fulfilling the conditions stated above is selected as the final fiducial region for a given mass and charge point. Fig. 73 shows the different fiducial regions as determined by the algorithm for the $1.0g_D$ monopole and the 40e HECO samples of mass 1000 GeV.

If no fiducial region is found for a given mass or charge point, then no model-independent cross section limit is determined for that sample. For HIPs with low charge that do not fire the L1 trigger this is a common phenomenon. Therefore, no fiducial regions were found for HECOs of charge $|z| = 10e$ nor for monopoles with higher masses (1500 - 2000 GeV) and a charge of $|g| = 0.5g_D$. Since the fiducial regions are determined independently in the three η regions, there are certain cases where the fiducial regions are not defined for all three. For instance, for monopoles of charge $|g| = 2.0g_D$ and mass = 200 GeV, for example, no fiducial regions are found in the forward η range. The very high ionisation energy loss of this monopole requires it to have a very high kinetic energy to reach the end-cap calorimeter.

The boundaries in $E^{kin}_{T/L}$ and $|\eta|$ as identified by the algorithm are summarised in the plots shown in Fig. 74. Fig. 74a summarises the fiducial regions in $|\eta|$, in each independent η-range, for all mass and charge points. Fig. 74b, 74c and 74d summarise the range in kinetic energy for all samples. The $E_{T/L}$ regions in these plots can be combined with corresponding η-ranges for the same sample in Fig. 74a which will reconstruct the fiducial region rectangle for that η-range. Missing lines indicate that no fiducial regions were found for that region of parameter space.

3.5 Background estimation using the ABCD method

A data-driven methods is used to estimate the backgrounds in the signal region. The *ABCD method* is used, in which two *uncorrelated* observables are divided into four regions in their two-dimensional phase space. The regions are constructed such that only one of the regions is dominated by the signal and the information from the three background dominated control regions helps estimate the back-

21 The TRT barrel and end-cap transition region occurs at this η value

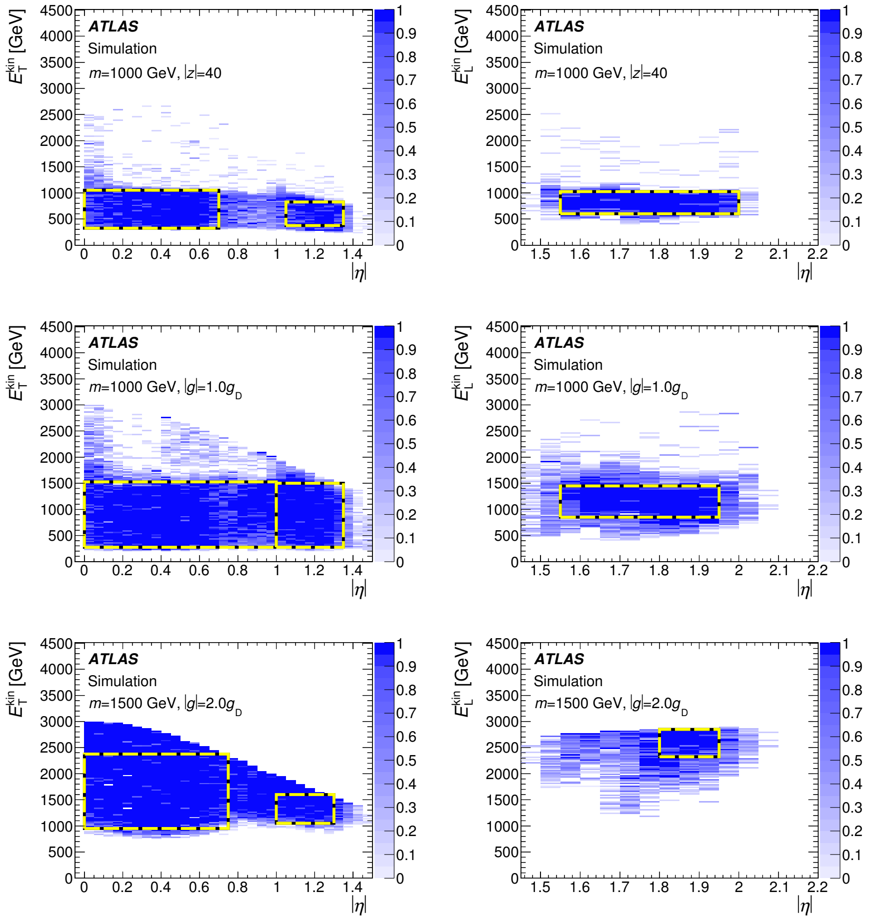

Figure 73: Total selection efficiency as a function of transverse kinetic energy (left) or longitudinal kinetic energy (right) and pseudo-rapidity, for HIPs with mass 1000 GeV and charge $|z| = 40e$ (top), mass 1000 GeV and charge $|g| = 1.0g_D$ (middle) and mass 1500 GeV and charge $|g| = 2.0g_D$ (bottom). These plots are obtained using fully simulated single-particle samples with a uniform kinetic energy distribution between 0 and 3000 GeV. The fiducial regions (as defined in the text) are indicated by rectangular dashed lines [129].

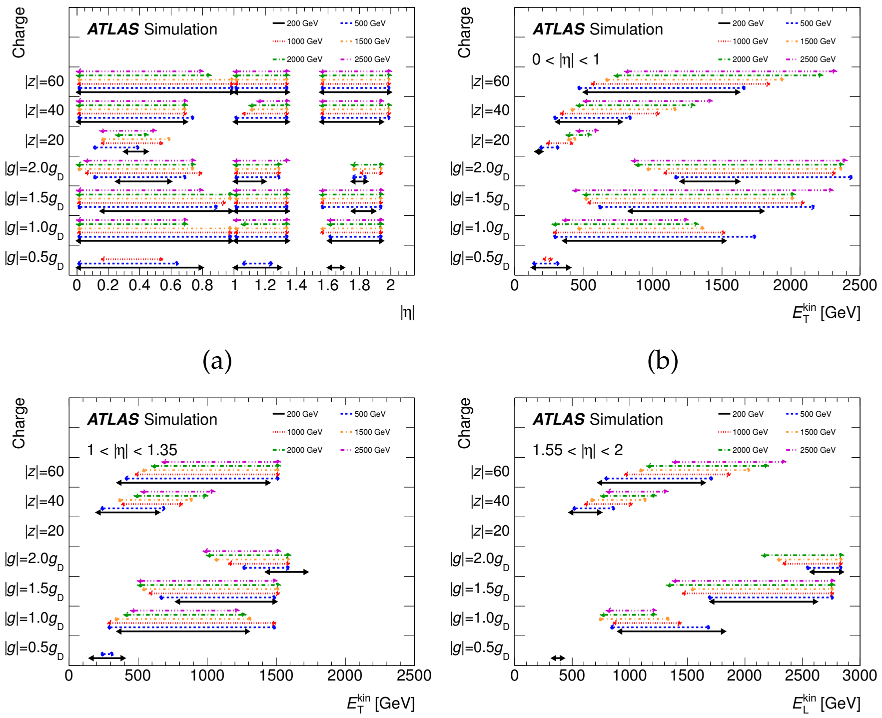

(a) (b)

(c) (d)

Figure 74: Fiducial regions for the HIP charges considered in the search. The various line styles correspond to different HIP masses. 74a show the $|\eta|$ acceptance ranges, while 74b- 74d shows the E^{kin} acceptance ranges corresponding to the three different $|\eta|$ ranges. Blank space indicate that no fiducial region of high efficiency is found for the corresponding mass and charge.

Sample	A	B	C	D
Data	0	618	3	4539

Table 11: The observed number of events in data in each of the regions of the ABCD method.

ground contribution in the signal region. In this analysis, the region dominated by the signal is region-A, while regions-B,C and D are background control regions as described by the cuts below,

$$\begin{array}{llll} A: & f_{HT} > 0.7 & w > 0.94 & \text{Signal region} \\ B: & f_{HT} > 0.7 & 0.84 < w \leqslant 0.94 & \text{Calorimeter sideband} \\ C: & f_{HT} \leqslant 0.7 & w > 0.94 & \text{TRT sideband} \\ D: & f_{HT} \leqslant 0.7 & 0.84 < w \leqslant 0.94 & \text{Background region} \end{array}$$

If the two observables are truly independent and regions-B,C and D have no signal contamination, then the ratio of the number of events in A and C should be equal to B and D. Thus, the number of expected background events in the signal region is:

$$A = \frac{B \cdot C}{D} \tag{27}$$

which gives the number of background events expected in the signal region.

The two observables considered in this analysis are the w variable and the f_{HT}, where the region of high-w and high-f_{HT} (region-A) is dominated by the HIP signal, as displayed in Fig. 75. The regions-B,C and D correspond to the regions that are dominated by backgrounds. Lower limits on the regions-B and D at $w > 0.84$, are placed as larger correlations observed in data for lower w and f_{HT} values (see Appendix B.1). A small correlation is observed in the ABCD regions, which is understood and treated as a systematic uncertainty as discussed in Appendix B.

Tab. 11 shows the observed number of events in each of the ABCD-regions in data. No events were observed in the signal Region-A. Region C has very few data events which has a large effect on the background estimation, especially given the possibility of leakage of signal events into this region as shown in Tab. 12 and 13.

The number of background events in the signal region is estimated by two separate methods. The first of these methods extrapolates the background distribution from region-D to the low-event region-C, with an aim to estimate the number of events in C more accurately. This number is then plugged into Eq. 27, from the background estimate in A can be precisely computed. The second method uses a likelihood function that is maximised using the RooStats package. The low statistics, signal leakages and the systematic uncertainties are taken into account by the likelihood.

Sample	B	C	D
$\lvert g\rvert = 0.5g_D$			
M = 200 GeV	1.6	2.3	0.0
M = 500 GeV	1.2	4.3	0.0
M = 1000 GeV	0.6	19.5	0.1
M = 1500 GeV	-	-	-
M = 2000 GeV	-	-	-
M = 2500 GeV	-	-	-
$\lvert g\rvert = 1.0g_D$			
M = 200 GeV	8.9	3.3	0.1
M = 500 GeV	0.7	1.6	0.0
M = 1000 GeV	0.2	0.8	0.0
M = 1500 GeV	0.1	0.9	0.0
M = 2000 GeV	0.1	1.4	0.0
M = 2500 GeV	0.1	1.9	0.0
$\lvert g\rvert = 1.5g_D$			
M = 200 GeV	8.0	2.6	0.1
M = 500 GeV	0.5	1.6	0.0
M = 1000 GeV	0.1	0.9	0.0
M = 1500 GeV	0.1	0.6	0.0
M = 2000 GeV	0.1	0.7	0.0
M = 2500 GeV	0.1	0.7	0.0
$\lvert g\rvert = 2.0g_D$			
M = 200 GeV	19.0	1.4	0.2
M = 500 GeV	0.4	1.6	0.0
M = 1000 GeV	0.1	0.6	0.0
M = 1500 GeV	0.1	0.3	0.0
M = 2000 GeV	0.1	0.4	0.0
M = 2500 GeV	0.0	0.5	0.0

Sample	B	C	D
$\lvert z\rvert = 10e$			
M = 200 GeV	-	-	-
M = 500 GeV	-	-	-
M = 1000 GeV	-	-	-
M = 1500 GeV	-	-	-
M = 2000 GeV	-	-	-
M = 2500 GeV	-	-	-
$\lvert z\rvert = 20e$			
M = 200 GeV	1.2	47.8	0.3
M = 500 GeV	0.6	36.2	0.2
M = 1000 GeV	0.4	34.9	0.2
M = 1500 GeV	0.2	37.2	0.1
M = 2000 GeV	0.2	36.8	0.2
M = 2500 GeV	0.5	36.0	0.1
$\lvert z\rvert = 40e$			
M = 200 GeV	0.4	4.3	0.0
M = 500 GeV	0.1	1.5	0.0
M = 1000 GeV	0.1	1.0	0.0
M = 1500 GeV	0.1	0.9	0.0
M = 2000 GeV	0.0	1.3	0.0
M = 2500 GeV	0.0	1.6	0.0
$\lvert z\rvert = 60e$			
M = 200 GeV	2.4	3.6	0.0
M = 500 GeV	0.3	2.1	0.0
M = 1000 GeV	0.1	1.1	0.0
M = 1500 GeV	0.1	1.0	0.0
M = 2000 GeV	0.1	0.8	0.0
M = 2500 GeV	0.1	0.6	0.0

Table 12: Leakages of the signal into the background control regions B–D in percentages, for single monopoles (left) and single HECOs (right).

Sample	B	C	D
$\|g\| = 0.5g_D$			
M = 200 GeV	-	-	-
M = 500 GeV	0.3	3.4	0.0
M = 1000 GeV	0.6	15.7	0.1
M = 1500 GeV	0.7	25.5	0.2
M = 2000 GeV	0.5	32.6	0.3
M = 2500 GeV	0.6	34.5	0.3
$\|g\| = 1.0g_D$			
M = 200 GeV	0.2	0.5	0.0
M = 500 GeV	0.2	0.1	0.0
M = 1000 GeV	0.1	0.4	0.0
M = 1500 GeV	0.3	1.7	0.0
M = 2000 GeV	0.3	4.7	0.0
M = 2500 GeV	0.1	10.8	0.0
$\|g\| = 1.5g_D$			
M = 200 GeV	0.5	1.4	0.5
M = 500 GeV	0.0	0.0	0.0
M = 1000 GeV	0.0	0.2	0.1
M = 1500 GeV	0.0	0.3	0.0
M = 2000 GeV	0.0	0.6	0.0
M = 2500 GeV	0.3	4.2	0.0
$\|g\| = 2.0g_D$			
M = 200 GeV	-	-	-
M = 500 GeV	-	-	-
M = 1000 GeV	-	-	-
M = 1500 GeV	-	-	-
M = 2000 GeV	-	-	-
M = 2500 GeV	-	-	-

Sample	B	C	D
$\|z\| = 10e$			
M = 200 GeV	2.3	70.1	1.6
M = 500 GeV	2.0	52.3	1.1
M = 1000 GeV	1.7	41.9	1.1
M = 1500 GeV	1.3	35.4	0.8
M = 2000 GeV	1.1	26.2	0.8
M = 2500 GeV	0.9	22.4	0.4
$\|z\| = 20e$			
M = 200 GeV	1.0	52.1	0.6
M = 500 GeV	0.5	25.3	0.1
M = 1000 GeV	0.3	21.3	0.1
M = 1500 GeV	0.1	21.4	0.1
M = 2000 GeV	0.2	21.5	0.1
M = 2500 GeV	0.0	24.9	0.1
$\|z\| = 40e$			
M = 200 GeV	0.1	6.1	0.0
M = 500 GeV	0.1	1.2	0.0
M = 1000 GeV	0.0	1.0	0.0
M = 1500 GeV	0.1	1.5	0.0
M = 2000 GeV	0.0	2.4	0.0
M = 2500 GeV	0.0	4.5	0.0
$\|z\| = 60e$			
M = 200 GeV	0.1	2.4	0.2
M = 500 GeV	0.1	1.1	0.0
M = 1000 GeV	0.1	0.8	0.0
M = 1500 GeV	0.2	0.5	0.0
M = 2000 GeV	0.0	0.0	1.3
M = 2500 GeV	-	-	-

Table 13: Leakages of the signal into the background control regions B–D in percentages, for Drell-Yan monopoles (left) and Drell-Yan HECOs (right).

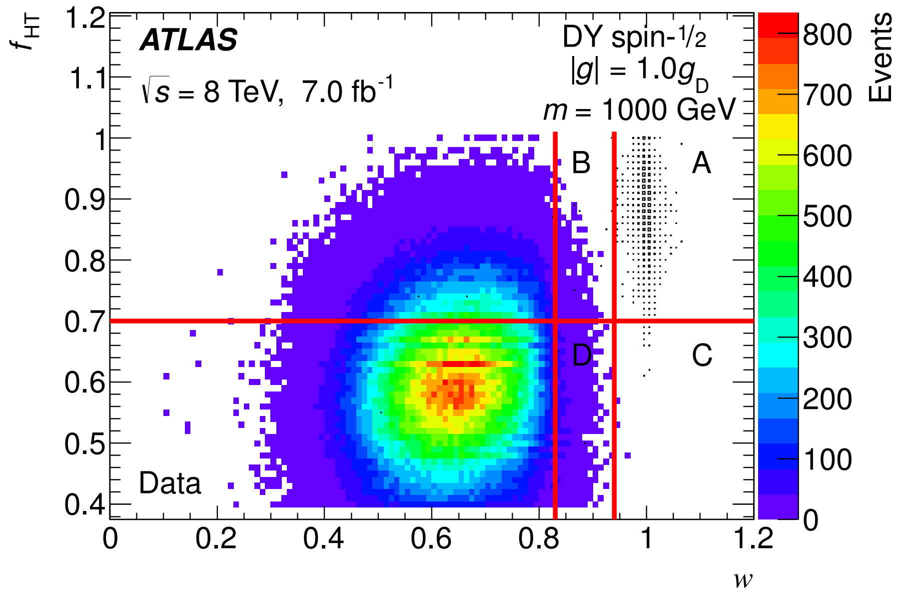

Figure 75: The distribution of the w variable as a function of f_{HT} for data and a selected simulated sample. The cuts used in the final selections are $0.94 \leqslant w$ and $0.7 \leqslant f_{HT}$. The colour scale is for data with the simulated signal sample represented by the black boxes. The regions for the ABCD method are also shown.

Fit function	Formula	Estimate	χ^2/n.d.f
power law	$a \times x^{-b}$	4.88	1.93
power law with exponential cut off	$a \times x^b \times \exp(x \times (-c))$	4.81	1.91
exponential	$a \times \exp(x * (-b))$	4.67	1.66
stretched exponential	$a \times \exp(-b \times x^c)$	0.78	0.54

Table 14: The number of events expected in region-C from the different fit functions used to parameterise the data.

3.5.1 *ABCD estimate using a fit to data*

The low number of events in region C results in a large statistical uncertainty in estimating the number of background events in region-A. Also, given the distribution of various signal samples it is possible to have significant signal leakage (candidates with high-w and low-f_{HT} values, as in the case of low charge HIPs) in this region.

The number of events in region-C (high-w and low-f_{HT}) can be estimated by extrapolating the number of events in region-D. This method helps reduce the large uncertainty associated with the number of events in region-C, thereby reducing the uncertainty in the overall background estimate.

A distribution of region-C and D are made by considering events with f_{HT} <0.7 and $0.84 < w \leqslant 0.94$ (for region-C) and $w > 0.94$ (for

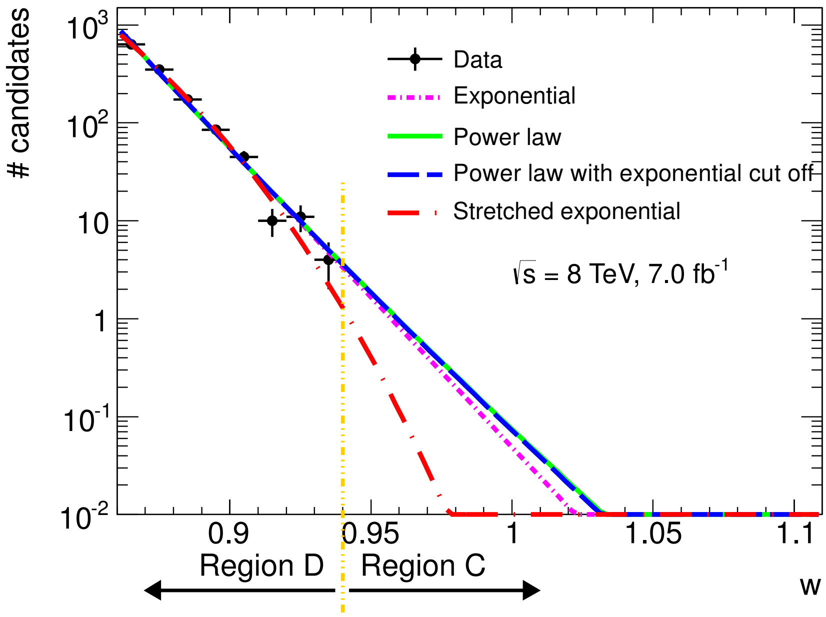

Figure 76: The different functions fitted to the data in the region-D to extrapolate the number of expected events in region-C. The region-C is kept blinded to avoid biases from the fits.

region-D). The events in region-C are kept blinded to not bias the extrapolation estimates made by fitting the data in region-D to region-C. Fig. 76 shows the different fitting functions that were used to parameterise the data, and the number of events estimated in region-C by each of the fitting functions are summarised in Tab. 14.

The exponential function (as described in Eq. 28) best describes the data based on the number of parameters and the χ^2/n.d.f of the fit. The parameters p_0 and p_1 are the normalisation and exponent factors of the fit, respectively.

$$f[X] = p_0 \cdot e^{X - p_1} \tag{28}$$

The **statistical uncertainties** on C_{est} are determined separately for each of the parameters in Eq. 28. The uncertainties are determined by keeping one of the parameters fixed and varying (adding and subtracting) the other by the uncertainty as determined by the fit. When determining the uncertainty due to the p_0 parameter, the p_1 parameter was kept fixed [22], while p_0 was varied such that χ^2/n.d.f. $\approx$5. Fig. 77 show the fits of the function when estimating the statistical uncertainty on C_{est}. The **systematic uncertainty** on the fit is determined by using the estimates from other two-parameter fit functions.

The number of estimated background events in region-C and region-A when using the exponential fit to the data are,

22 to the value as estimated by the original fit

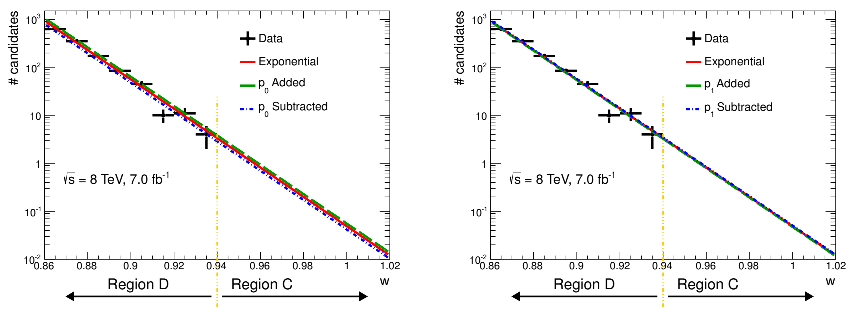

Figure 77: Estimation of the uncertainties arising from the parameters of the exponential function used to estimate the number of events in region-C.

$$\begin{aligned} C_{est} &= 4.67 \pm 0.67(\text{fit stat.}) \pm 0.70(\text{fit sys.}) \\ A_{est} &= 0.64 \pm 0.13(\text{fit stat. + sys.}) \pm 0.26(\text{sys.}). \end{aligned} \tag{29}$$

The estimate is compatible with that obtained from simple counting in B, C and D. The systematic uncertainty in the background estimate is dominated by the correlation, as described in Appendix B.3. This method is insensitive to signal leakages in region-C and supports the assumption that the simple BC/D estimate is not significantly biased by signal leakage.

3.5.2 *Background estimate using a likelihood*

A sophisticated method is also used to estimate the backgrounds in the signal region and set the cross section limits, that takes into account the signal leakages as well as the correlation corrections. A maximum-likelihood fit method is used to estimate the background in the RooStats framework as a part of the limit-setting procedure. The number of events in the regions-A,B,C and D are modelled as in Eq. 30- 33.

$$\mu_A = \sigma^{eff.}_{sig.}\mu + \mu^U \tag{30}$$

$$\mu_B = \sigma^{eff.}_{sig.}b\mu + \mu^U\tau_B \tag{31}$$

$$\mu_C = \sigma^{eff.}_{sig.}c\mu + \mu^U\tau_C \tag{32}$$

$$\mu_D = \sigma^{eff.}_{sig.}d\mu + \mu^U\tau_B\tau_C\rho \tag{33}$$

where μ and μ^U are the number of expected signal and background events in the signal region, $\sigma^{eff.}_{sig.}$ reflects the systematic uncertainty on the event selection efficiency for the signal, and the parameters b, c and d represent the signal leakages into the control regions B, C and D, respectively. The τ_B (τ_C) parameters are defined as the ratio of background events in control regions B (C) to the number of background events in the signal region. The correlation correction factor (see Appendix B.3 for details), ρ is introduced as a fixed parameter set to $\rho = 1.4$, the maximum upward variation - leading to more conservative limits. Nevertheless, the different choices of $\rho = 0.6$, $\rho = 1.0$ or $\rho = 1.4$ do not yield significant changes in the final results.

The free parameters of the fit μ, μ^{U}, τ_B, τ_C and $\sigma^{eff.}_{sig.}$ are determined by maximising the likelihood function as given in Eq. 34 with respect to the observed number of events N_A, N_B, N_C and N_D in regions-A,B,C and D respectively.

$$L(n_A, n_B, n_C, n_D \mid \mu, \mu^U, \tau_B, \tau_C) = \prod_{i=A,B,C,D} \frac{e^{-\mu_i} \mu_i^{n_i}}{n_i!}. \tag{34}$$

The model-independent background estimate using the observed number of events as shown in Tab. 11 is given by:

$$A_{est} = \frac{BC}{D} = 0.41 \pm 0.24(stat.) \pm 0.16(sys.) \tag{35}$$

The estimate in Eq. 35 assumes no leakage of signal into the background dominant regions and accounts for the correlations by adding a systematic uncertainty as described in Appendix B.3.

While in most cases the signal leakages into the control regions-B,C,D are negligible, for specific mass and charge points the leakage can be quite considerable $\mathcal{O}(40\%)$. Leakages into region-C are large when the discriminating power of f_{HT} is reduced due to lower ionisation produced by low charge HIPs. Moreover, heavier monopoles that traverse slowly through the detector produce reduced amounts of HT TRT hits, thereby having larger signal leakages.

Signal leakages into the region-B occur when fast, low-mass monopoles produce large amounts of energetic δ-rays that propagate and radiate in the EM calorimeter, thereby giving lower w values. The signal leakages into the regions-B,C,D are presented in Tab. 12 and 13.

3.6 SYSTEMATIC UNCERTAINTIES

Systematic uncertainties that affect the signal efficiency are studied and described in this section. The default settings of the ATLAS simulation software are treated as the nominal conditions. The effects of systematic uncertainties is studied by either resimulating the samples (for example to study the uncertainties in material density) or when possible, re-evaluated at the analysis level (for example, the uncertainty on the TRT occupancy). Systematics effects that require changes in the simulation, samples for all mass and charge points were generated with 5000 events and the efficiencies were re-evaluated to be compared to the nominal sample. Systematic uncertainties that did not require modifications to the simulations were implemented at the analysis level, allowing the use of the full statistics available in the nominal signal samples.

The following sub-sections describe the different systematic uncertainties that were considered in this analysis.

ATLAS material density

HIPs which stop before reaching the ECAL cause an important loss in efficiency which is sensitive to the amount of material upstream of the calorimeter. To understand the effect of this systematic, the GEANT4 ATLAS detector geometry (tag ATLAS-GEO-21-06-01) that is specifically designed for detector material studies is used to simulate 5000 events. The modified geometry provides an increase in the material budget compared to the nominal geometry used in standard Monte-Carlo productions. In the modified geometry tag, the inner detector has a material increase of 5% with respect to the default geometry tag and a 15% relative increases of Pixel and SCT services, i.e. 10% extra on top of the 5% in the whole inner detector.

The uncertainty arising from the material density in the ATLAS simulations is sub-dominant for the HIPs. The addition of material budget to the inner detector ionises the HIPs, resulting in the HIPs stopping earlier in the detector. This has a non-negligible effect on the low charge HIPs that tend to penetrate through to tile, triggering the hadronic-veto, but with the additional material budget more low charge HIPs tend to stop in the calorimeter itself. The uncertainty increases with mass for the HIPs since a larger number of heavier, slow moving HIPs traversing through the higher density detector tend to lose more energy and stop in the calorimeter.

Range cut for δ-rays in Geant4

To conserve computational resources, GEANT4 limits the propagation of low-energy δ-rays by not simulating the electrons below a kinetic energy threshold. The energy loss in such cases is added to the energy loss of the monopole continuously during the discrete steps in the trajectory propagation. This kinetic energy threshold is defined in GEANT4 as a distance parameter, which is internally converted to units of energy. Minimising this parameter helps achieve the best simulation precision as more low-energy δ-rays are explicitly simulated. The default parameter value used in the ATLAS TRT simulation is 50 μm which was lowered to 25 μm to measure this systematic. For each mass point, 5000 events were fully simulated using the reduced value of the parameter and the efficiencies were recomputed.

Uncertainty in the Birks' Law constant

The correction to the Birks' Law implemented in the ATLAS simulation due to the high ionisation density of the HIPs is described in Sec. 3.1.2. An uncertainty is associated to the precision of this correction derived from experimental heavy-ion data [121]. The dotted curves in Fig. 32 represent the upper (lower) uncertainties in the determination of the Birks' constant (k). Simulations are generated for 5000 events using the corrected values and upper (lower) uncertainty is established by comparing to the simulations generated with the nominal value of k (the solid black line) that was used in the analysis.

The effect of changing the visible energy is a dominant uncertainty for HIPs with low energy deposit energies in the calorimeter just below the selection thresholds. The HIPs produced with the DY production model have a energy distribution that peaks at lower energies that make low energy clusters in the calorimeter and are significantly affected by change in their visible energy. In addition, the energy loss is also dependent on the charge of the HIP, and therefore for monopoles the uncertainty from this systematic uncertainty increases with charge, while for HECOs it decreases with charge (see Sec. 1.2 for charge dependence on energy loss).

δ-ray production

The monopole energy loss and δ-ray production models used in Geant4 described by Eq. 18 in Sec. 1.1 has an associated uncertainty of about 3% [130, 21, 131]. Both the final selection variables are sensitive to the δ-ray production. While the monopoles use a custom GEANT4 code wherein the δ-ray production can be modified, the same is not possible for HECOs that are produced using the standard simulation procedures without creating a new physics list. The monopole samples were fully simulated by suppressing the δ-ray production by 3% for all monopole mass and charge points. The efficiencies were then recomputed and the uncertainties were estimated. The uncertainties for the HECOs were taken from those established for monopoles; for HECOs with $|z| \leqslant 40e$ the results of monopoles of charge $|g|$=0.5g_D were used, while for the uncertainties derived for $|g| = 1.0g_D$ were used for HECOs of charge $|z| = 60e$.

This uncertainty is sub-dominant and depends on the energy loss dependence of the HIPs. The energy loss is proportional to the charge of the HIP and suppressing the δ-ray production would result in a lower energy loss for high charge HIPs as they traverse towards the calorimeter. Thus for monopoles, this uncertainty increases with the monopole charge. The HECOs on the other hand have an additional β dependence on the energy loss as well. Similarly HIPs with low mass tend to penetrate futher into the Tile calorimeter, while those of high masses are able to reach the calorimeter.

TRT occupancy

The TRT occupancy is defined as the fraction of TRT channels that yield a signal, either from actual ionisation or noise in the event. The occupancy is thus dependent on the pile-up in the event and it is therefore crucial to have an accurate description of pile-up in the Monte Carlo simulations. Uncertainties in the occupancy measurement affect the fraction of TRT HT hits computed at various levels of the analysis and in turn also any efficiency estimates.

To study the occupancy in data, a dataset consisting of approximately 4 luminosity blocks from the dataset used in the search was used. The studies in simulations used a simulated sample of electrons from W decays was used. Both, the data and simulated samples were

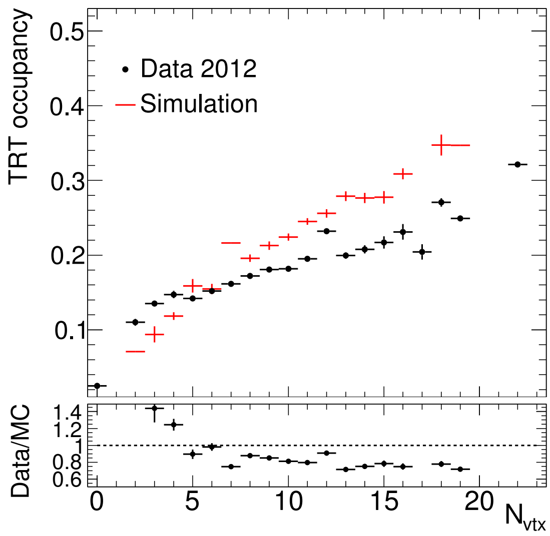

Figure 78: Comparison of the TRT occupancy as a function of the number of reconstructed vertexes for data and MC simulation [114].

processed through the dESD HIP filter, ensuring that events of similar characteristics were compared.

The TRT occupancy as a function of the number of reconstructed vertices for data and simulated sample is shown in Fig. 78 for data and simulation. The TRT occupancy in MC simulation is underestimated compared to that in data for low N_{vtx} values and overestimated for higher values. At the analysis level, the number of low threshold hits[23] was scaled by a factor dependent on the number of primary vertices. The factor was determined as the ratio between the TRT occupancy in data to that in simulation. The average factor of 0.92 was used for points that are not represented in Fig. 78. The event selection efficiencies were then recomputed and due to the overall overestimation of the TRT occupancy in the simulations, the resulting relative uncertainty yields a positive variation.

Variations of about 30% in the TRT occupancy, as shown in Fig. 78, could affect the efficiency of the HIP trigger as well. The increase in occupancy as a function of pile-up can be used to estimate the change in trigger efficiency due to a mismodelling of the TRT occupancy in simulation. Fig. 79 shows the HIP trigger efficiency as a function of pile-up, with the maximum variation for low charge HIPs - 40% in the case of monopoles of $|g|=0.5g_D$ and 50% for HECOs with $|z| = 60e$. Since this decrease assumes a change in TRT occupancy of 30%, these numbers represent a maximum estimate as the actual average mismodelling of the TRT occupancy is only 8%.

The number of TRT hits produced generally by HIPs is extremely high, generally very far from the trigger and analysis selection thresholds and thus this is an almost negligible systematic. A charge dependence is observed however, with this systematic being dominant for the low charge HIPs that produce TRT hits close to the thresholds

23 Those likely to come from pile-up as opposed to the HIP or associated δ-rays

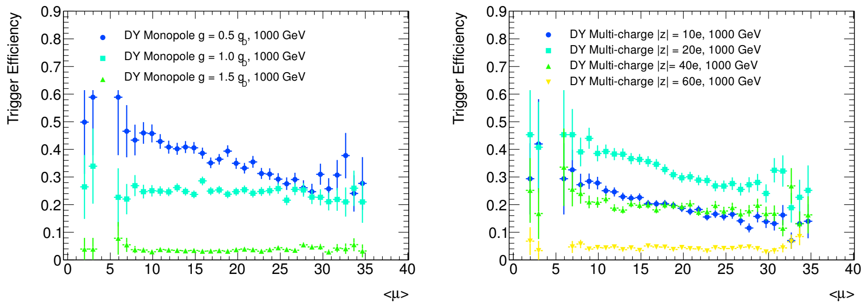

Figure 79: Profile distributions showing the trigger efficiency for different HIP samples as a function of pile-up $\langle\mu\rangle$. The trigger efficiency shows a pile-up dependence for low charge samples of both monopoles and HECOs.

used in the trigger and the selections. The mass dependence on this systematic is also negligible.

Liquid argon calorimeter cross-talk

One of the final discriminants in the search is the width of calorimeter cluster (w variable), which depends on the energy deposition in the electromagnetic calorimeter of ATLAS. The energy reconstruction in the ATLAS electromagnetic calorimeter is affected by the signal leakage from a cell recording a physical or calibrated signal to other cells, called cross-talk. The origin of the leakage could be on the electrodes or come through the electronic chain, resulting in three different types of cross-talk: capacitive, resistive and inductive [132]. Cross-talk in ϕ or η affects the determination of the width of calorimeter cluster.

The inductive cross-talk between the second and third layer cells as well as neighbouring cells of the second layer of the EM calorimeter have been previously studied and are summarised in [132]. The η cross-talk between neighbouring cells is 1.1% (in the barrel) and 0.6% (in the end-cap); while the cross-talk between the second and third layer cells is of the order of 0.9% (in the barrel) and 1.2% (in the end-cap). Resistive cross-talk exists between cells in the first and second layers and is of the order of 0.1% in both the barrel and end cap in η. Due to the high segmentation of the first layer, the capacitive cross-talk in η between the calorimeter cells is significant and of the order of 7.2% (in the barrel) and 6.3% (in the end-cap outer wheel). The η cross-talks are implemented by default in the ATLAS simulation.

The cross-talk in ϕ due to mutual inductance between the cells is not implemented in the ATLAS simulation. From [132], the mean cross-talk in ϕ is of the order of 1.8%. To evaluate the systematic uncertainty introduced by the cross-talk in ϕ, the cross-talk in the next-in-ϕ neighbour cell was assumed as 1.8% and the w variable was recomputed for the signal samples. The event selection efficiencies were then recomputed for the signal samples.

The uncertainty due to the ϕ cross-talk is observed to be very small with no strong charge or mass dependence. HIPs tend to deposit most of their energy in a very few cells and based on the definition of the w variable in each layer, the overall effect from this systematic is negligible.

Calorimeter arrival time

Inefficiencies in the Level-1 trigger arise for energy depositions recorded with delays of more than 10 ns, increasing the probability of assigning the deposition to the wrong bunch crossing. A delay of more than 10 ns correpsonds to $\beta > 0.37$ assuming the speed is constant. Given the array of charge and mass samples probed in this analysis, HIPs that reach the calorimeter have implicitly a $\beta > 0.37$ requirement. The β of the HIP reduces along its trajectory as it penetrates through the ATLAS detector, but this effect is too small to have any significant impact on the timing. The efficiency loss due to time delays of ECAL signals is therefore negligible and thus no systematic uncertainty is computed for this parameter.

Extrapolation method for spin-0 monopole efficiencies

The monopole efficiencies for the Drell-Yan spin-0 events are extrapolated using fine efficiency maps from single-particle samples folded with 22,000 generator-level Drell-Yan spin-0 events as explained in [107]. These results are compared to those of spin-½ monopoles samples that were fully simulated. Differences are assigned as an added systematic uncertainties to only the spin-0 Drell-Yan monopole efficiencies and the relative uncertainties are considered to be symmetric.

Luminosity measurement

The uncertainty due to the luminosity measurement is 2.8%. It is determined from a preliminary calibration of the luminosity scale from beam-separation scans performed in November 2012 as described in [133]. This is added in quadrature to the other uncertainties.

3.6.1 *Summary of systematic uncertainties*

Tab. 15- 18 summarise the relative uncertainties for the different components described in the previous sub-sections. These relative uncertainties are computed in the total signal efficiencies as the difference between the efficiencies obtained with the changed conditions with respect to the nominal sample for both spin-½ and spin-0 Drell-Yan produced signal samples.

To illustrate the mass dependence of the uncertainties representative charges of $1.0g_D$ and $40e$ are used in Tab. 15- 18. The charge dependence of the uncertainties are highlighted in the Tab. 19 and 20 that use the DY HIP samples for a representative mass of 1000 GeV HIPs.

The uncertainties measured in the single particle samples are derived only within the fiducial regions estimated for the samples in

Spin-½ $\lvert g\rvert = 1.0g_D$	Mass [GeV] 200	500	1000	1500	2000	2500
MC Stat.	±3.71	±1.69	±1.28	±1.33	±1.59	±2.21
Det. material	$\pm(2\pm3)$	$\pm(3\pm2)$	$\pm(4\pm2)$	$\pm(8\pm2)$	$\pm(3\pm3)$	$\pm(9\pm3)$
G4 range cut	$+(6\pm3)$	0 ± 2	$-(3\pm2)$	$-(2\pm2)$	$-(1\pm3)$	$-(10\pm3)$
Birks' high	$+(12\pm3)$	$+(3\pm2)$	$+(10\pm2)$	$+(13\pm2)$	$+(15\pm3)$	$+(9\pm4)$
Birks' low	$+(3\pm3)$	$-(7\pm2)$	$-(10\pm2)$	$-(9\pm2)$	$-(9\pm3)$	$-(17\pm3)$
$\delta-$ray	$\pm(7\pm3)$	$\pm(0\pm2)$	$\pm(2\pm2)$	$\pm(1\pm2)$	$\pm(3\pm3)$	$\pm(6\pm3)$
TRT Occ.	$+(1\pm2)$	0 ± 2	$-(1\pm1)$	$+(1\pm2)$	$+(2\pm2)$	$+(6\pm2)$
LAr xTalk	0 ± 2	$-(1\pm2)$	$-(3\pm1)$	$-(1\pm2)$	$-(3\pm2)$	$-(3\pm2)$
Total (UP)	$+16$	$+6$	$+12$	$+15$	$+16$	$+16$
Total (DOWN)	-9	-8	-12	-13	-11	-24

Table 15: Relative uncertainties on the signal efficiencies in percentages for Drell-Yan produced spin-½ monopoles of charge $\lvert g\rvert = 1.0g_D$. The errors on the uncertainties are statistical. The total relative uncertainties are calculated as quadratic sums of the individual relative uncertainties including the 2.8% uncertainty on the luminosity measurement. Note that the δ-ray and material density uncertainties are taken as symmetric, as described in the text.

Sec. 3.4.7. The relative uncertainties inside the fiducial regions with respect to the nominal sample for the single particle samples are shown in Tab. 21 and 22.

Depending on the systematic, a relative gain ('UP') or loss ('DOWN') in the efficiency is estimated which maybe asymmetric. For each systematic mentioned in the Tab. 15- 22 only the maximum uncertainty is given. The total uncertainty ('UP' or 'DOWN') is computed as the quadratic sum of the individual systematics.

3.7 RESULTS

With the observations of zero candidates that pass the HIP selections, the results are interpreted for model-independent as well as pair-produced monopoles via the Drell-Yan mechanism. Upper limits on the production cross section and lower mass limits are obtained for these models.

3.7.1 *Cross section limits*

The fiducial regions of uniform and high selection efficiency with $\epsilon \geqslant 90\%$ that were defined using single HIP samples were used to obtain model-independent production cross section limits. Upper limits on a simplified Drell-Yan pair-produced spin-½ monopoles were also set. In addition, by using the results from single particle monopoles and the systematic uncertainties on the event selection efficiency for the Drell-Yan spin-½ monopoles, the upper limits on the production cross section for pair-produced spin-0 monopoles were also produced. The

Spin-½ $\lvert z \rvert = 40e$	Mass [GeV] 200	500	1000	1500	2000	2500
MC Stat.	± 1.91	± 1.41	± 1.57	± 2.13	± 3.62	± 6.88
Det. material	$\pm(3 \pm 4)$	$\pm(2 \pm 3)$	$\pm(0 \pm 3)$	$\pm(6 \pm 4)$	$\pm(4 \pm 6)$	$\pm(11 \pm 9)$
G4 range cut	$+(4 \pm 4)$	0 ± 3	$+(2 \pm 3)$	$+(1 \pm 4)$	$+(2 \pm 6)$	$-(6 \pm 10)$
Birks' high	$+(8 \pm 4)$	$+(2 \pm 3)$	$+(4 \pm 3)$	$+(1 \pm 4)$	$+(1 \pm 6)$	$-(10 \pm 9)$
Birks' low	$+(1 \pm 4)$	$-(2 \pm 3)$	$-(1 \pm 3)$	$-(6 \pm 4)$	$-(2 \pm 6)$	$-(15 \pm 9)$
$\delta-$ray	$\pm(3 \pm 3)$	$\pm(4 \pm 2)$	$\pm(1 \pm 2)$	$\pm(8 \pm 2)$	$\pm(5 \pm 3)$	$\pm(10 \pm 4)$
TRT Occ.	$+(3 \pm 2)$	$+(1 \pm 2)$	0 ± 2	0 ± 2	$-(2 \pm 4)$	$-(1 \pm 6)$
LAr xTalk	$-(1 \pm 2)$	0 ± 2	$-(1 \pm 2)$	$-(2 \pm 2)$	$-(4 \pm 4)$	$-(6 \pm 6)$
Total (UP)	$+11$	$+6$	$+6$	$+10$	$+8$	$+17$
Total (DOWN)	-5	-6	-4	-12	-9	-26

Table 16: Relative uncertainties on the signal efficiencies in percentages for Drell-Yan produced spin-½ HECOs of charge $\lvert z \rvert = 40e$. The errors on the uncertainties are statistical. The total relative uncertainties are calculated as quadratic sums of the individual relative uncertainties including the 2.8% uncertainty on the luminosity measurement. Note that the δ-ray and material density uncertainties are taken as symmetric, as described in the text.

Spin-0 $\lvert g \rvert = 1.0 g_D$	Mass [GeV] 200	500	1000	1500	2000	2500
MC Stat.	± 2.02	± 0.92	± 0.66	± 0.68	± 0.80	± 1.01
Det. material	$\pm(2 \pm 3)$	$\pm(3 \pm 2)$	$\pm(4 \pm 2)$	$\pm(8 \pm 2)$	$\pm(3 \pm 3)$	$\pm(9 \pm 3)$
G4 range cut	$+(6 \pm 3)$	0 ± 2	$-(3 \pm 2)$	$-(2 \pm 2)$	$-(1 \pm 3)$	$-(10 \pm 3)$
Birks' high	$+(12 \pm 3)$	$+(3 \pm 2)$	$+(10 \pm 2)$	$+(13 \pm 2)$	$+(15 \pm 3)$	$+(9 \pm 4)$
Birks' low	$+(3 \pm 3)$	$-(7 \pm 2)$	$-(10 \pm 2)$	$-(10 \pm 2)$	$-(9 \pm 3)$	$-(17 \pm 3)$
$\delta-$ray	$\pm(7 \pm 3)$	$\pm(0 \pm 2)$	$\pm(2 \pm 2)$	$\pm(1 \pm 2)$	$\pm(3 \pm 3)$	$\pm(6 \pm 3)$
TRT Occ.	0 ± 2	0 ± 2	$-(1 \pm 1)$	$+(1 \pm 2)$	$+(2 \pm 2)$	$+(6 \pm 2)$
LAr xTalk	0 ± 2	$-(1 \pm 2)$	$-(3 \pm 1)$	$-(1 \pm 2)$	$-(3 \pm 2)$	$-(3 \pm 2)$
Extrapolation	-10	-9.5	-8.5	-7.5	-6.5	-5.5
Total (UP)	$+16$	$+6$	$+12$	$+15$	$+16$	$+15$
Total (DOWN)	-13	-12	-14	-15	-13	-24

Table 17: Relative uncertainties on the signal efficiencies in percentages for Drell-Yan produced spin-0 monopoles of charge $\lvert g \rvert = 1.0 g_D$. The errors on the uncertainties are statistical. The total relative uncertainties are calculated as quadratic sums of the individual relative uncertainties including the 2.8% uncertainty on the luminosity measurement. Note that the δ-ray and material density uncertainties are taken as symmetric, as described in the text.

Spin-0 $|z| = 40e$	Mass [GeV] 200	500	1000	1500	2000	2500
MC Stat.	± 1.09	± 0.79	± 0.87	± 1.12	± 1.73	± 3.17
Det. material	$\pm(3 \pm 4)$	$\pm(3 \pm 3)$	$\pm(0 \pm 3)$	$\pm(6 \pm 4)$	$\pm(4 \pm 6)$	$\pm(11 \pm 9)$
G4 range cut	$+(4 \pm 4)$	0 ± 3	$+(2 \pm 3)$	$+(1 \pm 4)$	$+(2 \pm 6)$	$-(7 \pm 10)$
Birks' high	$+(8 \pm 4)$	$+(2 \pm 3)$	$+(4 \pm 3)$	$+(1 \pm 4)$	$+(1 \pm 6)$	$-(10 \pm 9)$
Birks' low	$+(1 \pm 4)$	$-(3 \pm 3)$	$-(1 \pm 3)$	$-(6 \pm 4)$	$-(6 \pm 6)$	$-(15 \pm 9)$
$\delta-$ray	$\pm(3 \pm 3)$	$\pm(4 \pm 2)$	$\pm(1 \pm 2)$	$\pm(8 \pm 2)$	$\pm(5 \pm 3)$	$\pm(10 \pm 4)$
TRT Occ.	$+(3 \pm 2)$	$+(1 \pm 2)$	0 ± 2	0 ± 2	$-(2 \pm 4)$	$-(1 \pm 6)$
LAr xTalk	$-(1 \pm 2)$	0 ± 2	$-(1 \pm 2)$	$-(2 \pm 2)$	$-(4 \pm 4)$	$-(6 \pm 6)$
Extrapolation	-7	-1	$+0.3$	$+6$	$+9$	$+5$
Total (UP)	$+11$	$+6$	$+5$	$+12$	$+11$	$+17$
Total (DOWN)	-8	-6	-3	-12	-8	-26

Table 18: Relative uncertainties on the signal efficiencies in percentages for Drell-Yan produced spin-0 HECOs of charge $|z| = 40e$. The errors on the uncertainties are statistical. The total relative uncertainties are calculated as quadratic sums of the individual relative uncertainties including the 2.8% uncertainty on the luminosity measurement. Note that the δ-ray and material density uncertainties are taken as symmetric, as described in the text.

spin-½ Mass = 1000 GeV	Magnetic charge [g_D] 0.5	1.0	1.5
MC Stat.	± 2.48	± 1.28	± 3.65
Det. material	$\pm 9 \pm 8$	$\pm 4 \pm 2$	$\pm 8 \pm 5$
G4 range cut	-5 ± 8	$+3 \pm 2$	-4 ± 5
Birks' high	$+4 \pm 8$	$+10 \pm 2$	$+1 \pm 5$
Birks' low	$+4 \pm 8$	$+10 \pm 2$	-9 ± 4
$\delta-$ray	$\pm 1 \pm 8$	$\pm 2 \pm 2$	$\pm 5 \pm 5$
TRT Occ.	$+11 \pm 4$	-1 ± 2	3 ± 3
LAr xTalk	-4 ± 3	-3 ± 1	$+2 \pm 3$
Total (UP)	$+16$	$+12$	$+11$
Total (DOWN)	-10	-12	-14

Table 19: Relative uncertainties on the signal efficiencies in percentages for DY monopoles in fiducial regions. The total relative uncertainties are calculated as quadratic sums of the individual relative uncertainties including the 2.8% uncertainty on the luminosity measurement. Note that the δ-ray and material density uncertainties are taken as symmetric, as described in the text.

spin-½ Mass = 1000 GeV	Electric Charge [e] 20	40	60
MC Stat.	±1.24	±1.57	±3.57
Det. material	$\pm(3 \pm 2)$	$\pm0\pm3$	$\pm3\pm5.3$
G4 range cut	0 ± 2	$+2\pm3$	$+3\pm6$
Birks' high	$+5 \pm 3$	$+4\pm3$	$+3\pm6$
Birks' low	-7 ± 2	-1 ± 3	-0 ± 5
$\delta-$ray	$\pm1\pm2$	$\pm1\pm2$	$\pm2\pm2$
TRT Occ.	$+12 \pm 2$	0 ± 2	$+1\pm3$
LAr xTalk	-3 ± 2	-1 ± 2	0 ± 3
Total (UP)	$+13$	$+6$	$+7$
Total (DOWN)	-9	-4	-6

Table 20: Relative uncertainties on the signal efficiencies in percentages for DY HECOs in fiducial regions. The total relative uncertainties are calculated as quadratic sums of the individual relative uncertainties including the 2.8% uncertainty on the luminosity measurement. Note that the δ-ray and material density uncertainties are taken as symmetric, as described in the text.

Mass = 1000 GeV	Magnetic charge [g_D] 0.5	1.0	1.5	2.0
MC Stat.	±1.940	±0.289	±0.231	±0.431
Det. material	±3.58	±0.43	±0.24	±0.85
G4 range cut	-1.15	$+0.42$	$+0.27$	-0.36
Birks' high	-1.15	$+0.52$	$+0.42$	$+0.32$
Birks' low	-0.27	$+0.11$	-0.02	-0.78
$\delta-$ray	±0.35	±0.06	±0.33	±0.27
TRT Occ.	$+1.37$	$+0.67$	$+0.53$	$+0.46$
LAr xTalk	-1.58	-3.20	-2.56	-4.23
Total (UP)	$+5$	$+3$	$+3$	$+3$
Total (DOWN)	-5	-4	-4	-5

Table 21: Relative uncertainties on the signal efficiencies in percentages for single monopoles in fiducial regions. The total relative uncertainties are calculated as quadratic sums of the individual relative uncertainties including the 2.8% uncertainty on the luminosity measurement. Note that the δ-ray and material density uncertainties are taken as symmetric, as described in the text.

Mass = 1000 GeV	Electric Charge [e] 20	40	60
MC Stat.	±3.860	±0.435	±0.250
Det. material	±12.80	±0.076	±0.068
G4 range cut	-9.83	$+0.02$	$+0.18$
Birks' high	-6.65	-0.27	$+0.36$
Birks' low	-15.4	$+0.01$	-0.10
$\delta-$ray	±0.35	±0.35	±0.06
TRT Occ.	$+6.38$	$+0.74$	$+0.62$
LAr xTalk	-1.56	-0.87	-2.28
Total (UP)	$+15$	$+3$	$+3$
Total (DOWN)	-24	-3	-4

Table 22: Relative uncertainties on the signal efficiencies in percentages for single HECOs in fiducial regions. The total relative uncertainties are calculated as quadratic sums of the individual relative uncertainties including the 2.8% uncertainty on the luminosity measurement. Note that the δ-ray and material density uncertainties are taken as symmetric, as described in the text.

cross section limits were obtained using the CL_s method [134], using the RooStats framework [135].

The mass limits were attained by assuming the Drell-Yan production for spin-½ and spin-0 monopoles by comparing the observed limits on the production cross section with the theoretical predictions.

CL_s method

The frequentest CL_s method is useful in searches with low sensitivity that might be affected by fluctuations in the expected background. The method is a simple normalisation of the confidence level observed for the signal+background hypothesis, CL_{s+b}, to the confidence level observed for the background-only hypothesis, CL_b, defined as,

$$CL_s = \frac{CL_{s+b}}{CL_b}. \tag{36}$$

The confidence levels CL_{s+b} and the CL_b are defined as,

$$CL_{s+b} = P(q \geqslant q_{obs}|s+b) = \int_{q_{obs}}^{\infty} f(q|s+b), \tag{37}$$

$$CL_b = P(q \geqslant q_{obs}|b) = \int_{q_{obs}}^{\infty} f(q|b), \tag{38}$$

with $f(q|s+b)$, $f(q|b)$ are the probability distribution function of the test-statistic and q the observable, in this case, the number of observed signal events, μ. For a desired confidence level, for example, 95% (α = 0.95), the CL_s value is given by,

$$CL_s = 1 - \alpha = 0.05. \tag{39}$$

A logarithmic likelihood ratio [136] is used as test-statistic in this case,

$$-2\ln\lambda(\mu) = -2\ln(L(s+b)/L(b)), \tag{40}$$

with the likelihood functions $L(s+b)$ and $L(b)$ defined as in Eq. 34. The evidence of magnetic monopoles can only be observed as an increase in the number of events in the signal region over the background, i.e. the log likelihood is constructed for the case when $\mu \geqslant 0$. Three cases are then considered,

$$-2\ln\lambda(\mu) = \begin{cases} -2\ln\dfrac{L(\mu,\hat{\hat{\theta}}(\mu))}{L(0,\hat{\hat{\theta}}(0))} & \text{if } \hat{\mu} < 0, \\ -2\ln\dfrac{L(\mu,\hat{\hat{\theta}}(\mu))}{L(\hat{\mu},\hat{\theta})} & \text{if } 0 \leqslant \hat{\mu} \leqslant \mu, \\ 0 & \text{if } \hat{\mu} > 0, \end{cases} \tag{41}$$

where $\hat{\mu}$ and $\hat{\theta}$ are the maximum likelihood estimators of the maximised unconditional likelihood function. $\hat{\hat{\theta}}$ is the value of θ that maximises the likelihood for a given μ, meaning it is the conditional maximum likelihood estimator. The systematic uncertainties and signal leakages are represented by θ, which causes the probability distribution function of the log likelihood ratio to broaden with respect to a log likelihood ratio with fixed parameters. This is a consequence of the loss of information due to the systematic uncertainties on the event selection efficiency.

Model independent cross section limits

This monopole search can be interpreted for model-independent scenarios by using the defined fiducial regions of high and uniform selection efficiency for single monopoles. These fiducial regions are generated over uniform pseudo-rapidity, azimuthal angle and kinetic energy spectra, see Sec. 3.4.7 for details. The upper limits on the production cross section for single monopoles in the fiducial regions is obtained for an average selection efficiency of 90% in these regions, using the integrated luminosity of the analysed dataset, 7.0 fb^{-1}.

In the absence of any observed events in the signal regions, the upper limits on the number of signal events is taken as 3, from which the upper limits on the production cross section are computed and summarised in Tab. 23 and 24. The model independent upper limits on the production cross section was found to be 0.5 fb. Only results for mass and charge combinations for which fiducial regions were found

Single Monopole Mass [GeV]	LHC 8 TeV Limits on the cross section [fb]			
	$\lvert g \rvert = 0.5g_D$	$\lvert g \rvert = 1.0g_D$	$\lvert g \rvert = 1.5g_D$	$\lvert g \rvert = 2.0g_D$
200	0.47	0.48	0.48	0.49
500	0.48	0.48	0.49	0.47
1000	0.49	0.48	0.49	0.47
1500	-	0.47	0.48	0.47
2000	-	0.49	0.49	0.48
2500	-	0.48	0.48	0.48

Table 23: 95% CL upper limits on the production cross section of single monopoles in the fiducial regions. A dash indicates the absence of a cross section limit since no fiducial region of high efficiency was found for the given mass/charge point.

are presented. As discussed in Sec. 3.6, the systematic uncertainties were averaged over all the mass points for each charge. The minor differences between the mass/ charge combinations are therefore only due to the different leakages.

Cross section limits on pair-produced monopoles

This search considered, both, the Drell-Yan pair-produced monopoles of spin-½ and spin-0. A MC leading-order matrix element generator (MadGraph5 [99]) was used to generate the monopole events. Only leading-order calculations are used due to the large magnetic coupling to the photon, which makes the production process highly non-pertubative.

Spin-½ cross section limits

The upper limits on the number of signal events is taken to be 3 for all samples in the absence of any observed events in the signal region and the corresponding upper limits on the production cross section for the spin-½ DY monopoles are summarised in Tab. 25 and 26. Only results for mass and charge combinations for which the acceptance is greater than 1% are presented. The differences between the mass/ charge combinations are attributed to the different leakages.

Fig. 80 and 81 summarise the cross section limits as a function of the monopole and HECO mass respectively.

Spin-0 cross section limits

The upper limits on the production cross section of spin-0 pair-produced monopoles and HECOs assuming the DY mechanism is given in Tab. 27 and 28 respectively. The results are shown for mass

Single HECO Mass [GeV]	LHC 8 TeV Limits on the cross section [fb]			
	$\|z\| = 10e$	$\|z\| = 20e$	$\|z\| = 40e$	$\|z\| = 60e$
200	-	0.46	0.49	0.49
500	-	0.48	0.48	0.49
1000	-	0.48	0.47	0.48
1500	-	0.48	0.48	0.48
2000	-	0.49	0.48	0.5
2500	-	0.49	0.49	0.5

Table 24: 95% CL upper limits on the production cross section of single HECOs in the fiducial regions. A dash indicates the absence of a cross section limit since no fiducial region of high efficiency was found for the given mass/charge point.

DY Spin-½ Monopole Mass [GeV]	LHC 8 TeV Limits on the cross section [fb]			
	$\|g\| = 0.5g_D$	$\|g\| = 1.0g_D$	$\|g\| = 1.5g_D$	$\|g\| = 2.0g_D$
200	1.92	12.02	-	-
500	1.25	2.85	36.14	-
1000	1.58	1.75	11.28	-
1500	1.85	1.87	11.9	-
2000	2.62	2.61	14.31	-
2500	4.62	4.37	25.78	-

Table 25: 95% CL upper limits on the production cross section of Drell-Yan spin-½ monopoles. A dash indicates the absence of a cross section limit since the acceptance is lower than 1% for the given mass/charge point.

DY Spin-½ HECO Mass [GeV]	LHC 8 TeV Limits on the cross section [fb]			
	$\lvert z\rvert = 10e$	$\lvert z\rvert = 20e$	$\lvert z\rvert = 40e$	$\lvert z\rvert = 60e$
200	11.09	4.36	3.53	12.86
500	6.15	2.28	2.17	6.92
1000	4.11	1.79	2.53	11.73
1500	3.14	1.95	4.11	28.71
2000	2.8	2.52	11.79	194.9
2500	3.59	4.15	40.12	-

Table 26: 95% CL upper limits on the production cross section of Drell-Yan spin-½ HECOs. A dash indicates the absence of a cross section limit since the acceptance is lower than 1% for the given mass/charge point.

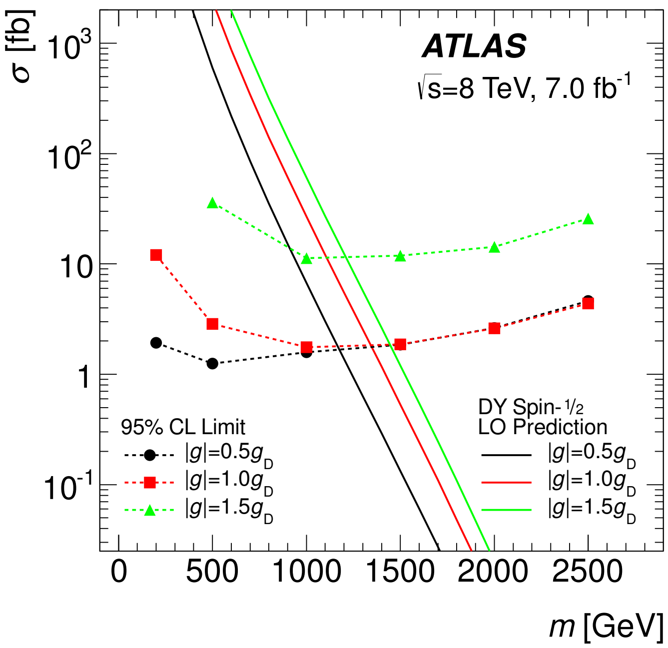

Figure 80: Observed 95% CL upper limits for Drell-Yan spin-½ monopoles as a function of HIP mass in various scenarios (dashed lines with markers). Overlaid on the plots are the theoretical cross sections (solid lines) [129].

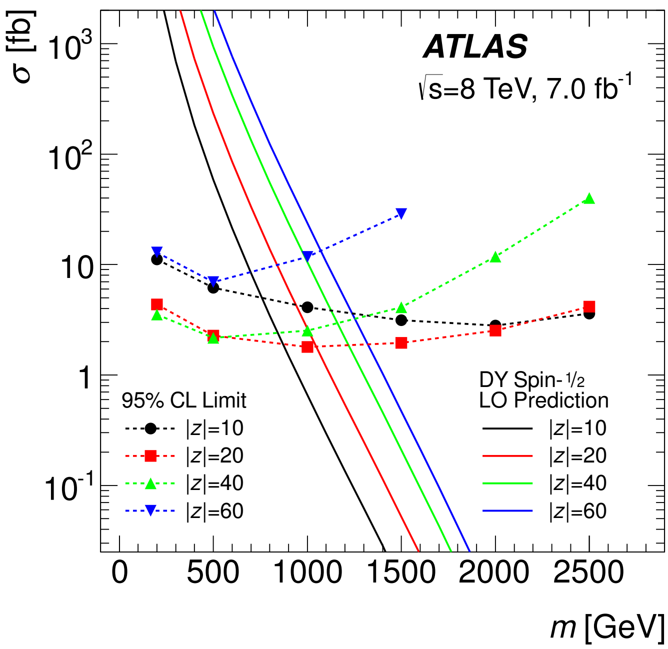

Figure 81: Observed 95% CL upper limits for Drell-Yan spin-½ HECOs as a function of HIP mass in various scenarios (dashed lines with markers). Overlaid on the plots are the theoretical cross sections (solid lines) [129].

and charge points which have an acceptance of greater than 1%. The event selection efficiencies were obtained by extrapolating results from single particle samples using only the generator level four-vectors for spin-0 DY monopoles, as discussed in [107]. The upper limits were set using the systematic uncertainties from the spin-½ DY produced monopoles as described in 3.6. Fig. 82 and 83 summarise the cross section limits as a function of the monopole and HECO mass respectively.

3.7.2 *Lower mass limits on DY produced monopoles*

The cross section exclusion limits obtained for the DY monopole models help set lower limits on the monopole mass. These limits were obtained by finding the mass for which the theoretical cross section prediction drops below the upper cross section limit.

These limits are only valid for the production model considered (DY spin-½ and spin-0) and are limited by the accuracy of the theoretical cross section predictions. However these limits provide a direct comparison to previous experimental searches which considered the same production mechanism. For example, the CDF experiment at Tevatron, set a lower mass limit of 476 GeV for spin-½ monopoles pair-produced via the DY mechanism of charge $1.0g_D$ [137]. While the previous ATLAS search at $\sqrt{s} = 7$TeV set a limit of 862 GeV for the spin-½ pair-produced monopoles of charge $1.0g_D$ produced via the DY mechanism [72]. This search sets limits of DY produced

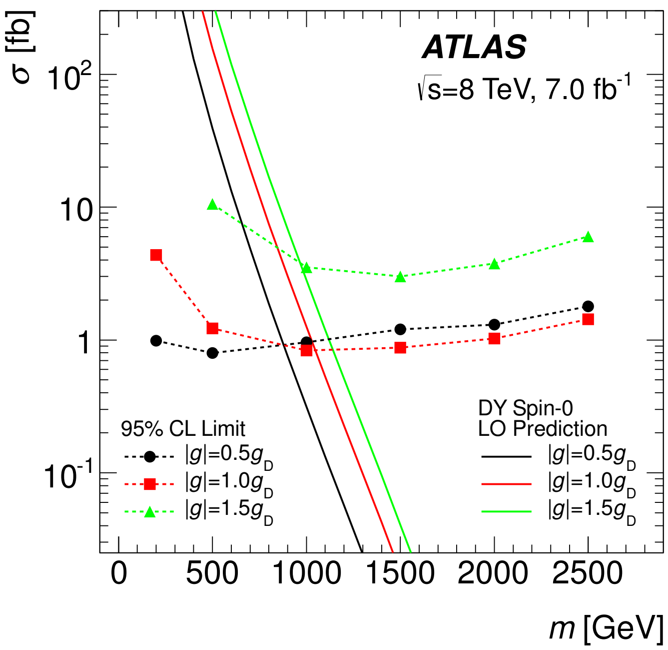

Figure 82: Observed 95% CL upper limits for Drell-Yan spin-0 monopoles as a function of HIP mass in various scenarios (dashed lines with markers). Overlaid on the plots are the theoretical cross sections (solid lines) [129].

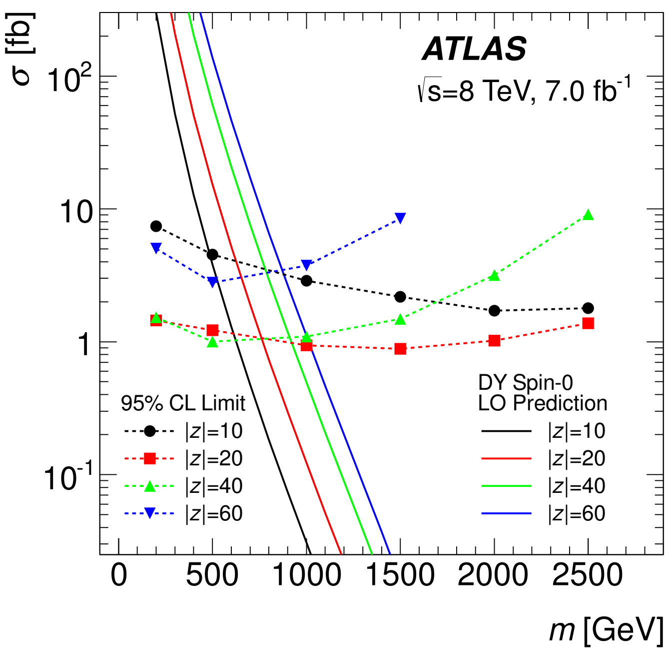

Figure 83: Observed 95% CL upper limits for Drell-Yan spin-0 HECOs as a function of HIP mass in various scenarios (dashed lines with markers). Overlaid on the plots are the theoretical cross sections (solid lines) [129].

DY Spin-0 Monopole Mass [GeV]	LHC 8 TeV Limits on the cross section [fb]			
	$\lvert g\rvert = 0.5g_D$	$\lvert g\rvert = 1.0g_D$	$\lvert g\rvert = 1.5g_D$	$\lvert g\rvert = 2.0g_D$
200	0.99	4.37	-	-
500	0.8	1.22	10.58	-
1000	0.96	0.83	3.52	-
1500	1.2	0.88	3.01	-
2000	1.3	1.02	3.76	-
2500	1.79	1.43	6.03	-

Table 27: 95% CL upper limits on the production cross section of Drell-Yan spin-0 monopoles. A dash indicates the absence of a cross section limit since the acceptance is lower than 1% for the given mass/charge point.

DY Spin-0 HECO Mass [GeV]	LHC 8 TeV Limits on the cross section [fb]			
	$\lvert z\rvert = 10e$	$\lvert z\rvert = 20e$	$\lvert z\rvert = 40e$	$\lvert z\rvert = 60e$
200	7.43	1.45	1.53	5.02
500	4.53	1.22	1	2.79
1000	2.87	0.94	1.09	3.73
1500	2.18	0.88	1.49	8.45
2000	1.71	1.02	3.18	37.66
2500	1.79	1.37	9.1	-

Table 28: 95% CL upper limits on the production cross section of Drell-Yan spin-0 HECOs. A dash indicates the absence of a cross section limit since the acceptance is lower than 1% for the given mass/charge point.

	$\lvert g\rvert = 0.5g_D$	$\lvert g\rvert = 1.0g_D$	$\lvert g\rvert = 1.5g_D$
spin-1/2 DY	1176	1340	1210
spin-0 DY	886	1047	968

Table 29: Mass limits (in GeV) in models of spin-1/2 (top) and spin-0 (bottom) DY monopole pair-production. These should not be taken at face value given the non-pertubative nature of the production mechanism, which makes cross section estimates highly speculative.

	$\lvert z\rvert = 10e$	$\lvert z\rvert = 20e$	$\lvert z\rvert = 40e$	$\lvert z\rvert = 60e$
spin-1/2 DY	775	1047	1162	1074
spin-0 DY	490	780	915	879

Table 30: Mass limits (in GeV) in models of spin-1/2 (top) and spin-0 (bottom) DY HECOs pair-production. These should not be taken at face value given the non-pertubative nature of the production mechanism, which makes cross section estimates highly speculative.

monopoles of spin-0 and spin-½ for charges up to $1.5g_D$ as shown in Tab. 29. In addition, Tab. 30 also shows the lower mass limits of HECOs.

4 SEARCHES IN MOEDAL

4.1 SIMULATIONS AT MOEDAL

Analogous to the simulations developed for the ATLAS experiment (see Sec. 3.1), samples are generated to give model-dependent and -independent results from the MoEDAL MMT prototype. The single particle samples for model-independent results, were produced using a particle gun with a flat kinetic energy distribution ranging from 0 to 10000 GeV. In accordance with the angular acceptance of the prototype, the polar (θ) and azimuthal (ϕ) angle distributions are flat in the range, 2.4 $< \theta <$ 3.0 rad and -2.7 $< \phi <$ -0.5 rad.

The pair-produced monopoles from initial pp states is modelled by a DY process, and implemented similarly as was done for ATLAS (see sub-section 3.1.1). Fig. 84 shows the distributions of the kinetic energy E^{kin} and θ. The DY kinematics produced by different spin models helps estimate the model dependence of the detector acceptance. Pythia6 is used for the initial-state QCD radiation and hadronisation of the underlying event.

The GEANT4 toolkit is used to perform the simulations of monopole propagation, energy loss and its eventual stopping [111, 112, 113].

Simulation samples were produced for a large array of mass (100 - 3500 GeV) and charge ($g = 1.0 - 6.0 g_D$) points, with 2 $\times 10^6$ events for each single monopole sample and 100,000 events in each DY sample.

4.1.1 *Simulating the energy loss of monopoles*

Simulations of the monopole energy loss along its trajectory through the LHCb VELO and its trapping by the MMTs is performed by the GEANT4 toolkit. The velocity-dependent energy loss formula modelled by the Bethe-Bloch formula is modified for monopoles [21, 138] as shown in Eq. 18.

For monopoles in the velocity range, $10^{-4} < \beta < 0.01$, an approximation for the energy loss given by Ahlen and Kinoshita [22, 138, 139] given by :

$$-\frac{1}{\rho}\frac{dE}{dx} = (f_n + f_c)\left(\frac{g}{g_D}\right)^2 \beta \frac{\text{GeV}}{\text{cm}^2 g} \qquad (42)$$

where, ρ is the density of the medium through which the monopole traverses. f_n and f_c are contributions from the non-conduction and conduction electrons respectively.

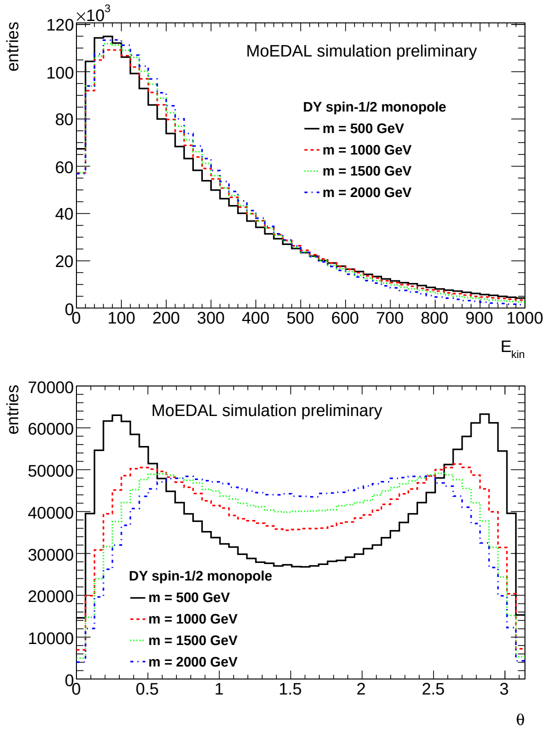

Figure 84: The kinematic distributions of spin-1/2 pair-produced monopoles considered for model-dependent results [29].

	f_n	f_c
Aluminium	13.7	80.0
Steel	18.9	28.4
Copper	19.5	14.5

Table 31: Contributions from non-conducting (f_n) and conducting (f_n) electrons for different materials.

Both, f_c and f_n are dependent on the material, and their values (shown in Tab. 31) are implemented in the GEANT4 framework for the three dominant materials in MoEDAL [23].

The $\frac{dE}{dx}$ for the intermediate β range, 0.01< β <0.1, were obtained using a linear interpolation method; other interpolation methods have shown to have a negligible impact on the acceptance of the trapping detector.

Owing to the large masses, the magnetic monopoles in this analysis are not highly relativistic, as can be seen in Fig. 85. For γ =100, the energy loss via bremsstrahlung contributes to approximately 5% of the total energy loss; this fraction scales linearly with $Z_2\gamma$ [131]. The energy losses via bremsstrahlung and pair-production, which are significant only for highly relativistic particles ($\beta > 0.9999$ or $\beta\gamma > 70$) [140], are negligible compared to ionisation and are not considered in the simulation. Additionally, the acceleration of monopoles along the magnetic field lines is irrelevant in the case of the MMTs which are located downstream of the LHCb, far from the experiment's dipole magnet. Therefore, while the magnetic field is simu-

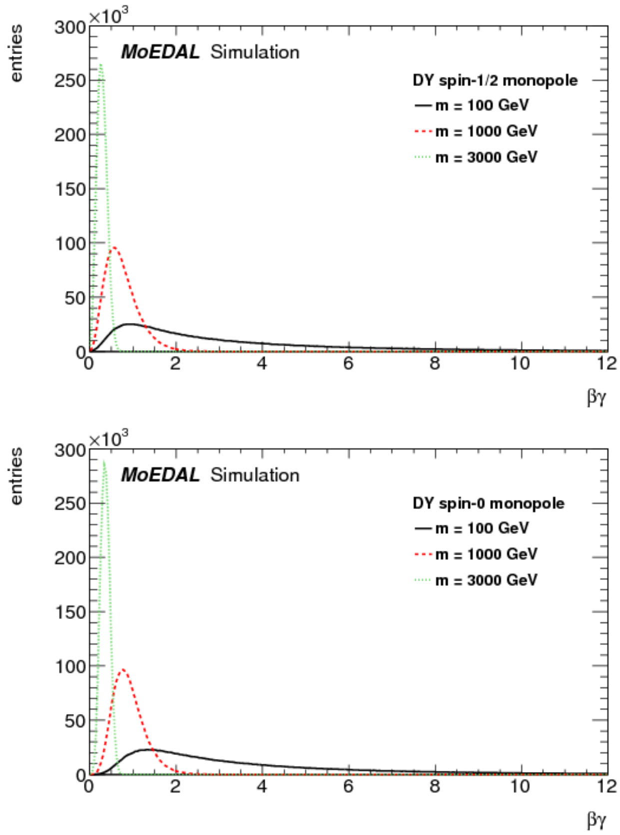

Figure 85: Initial $\beta\gamma$ distributions (with β=v/c and γ=$\frac{1}{\sqrt{1-\beta^2}}$) of spin-½ (top) and spin-0 (bottom) monopoles produced in the Drell-Yan model with masses in the range considered for this search. These distributions do not depend on the monopole charge [29].

lated in the Geant4 model, its effect is small and does not affect the monopole trapping or trajectories in any significant way.

4.1.2 *Simulation of trapping monopoles*

The Geant4 toolkit that simulates the propagation of monopoles produced in pp collisions is also capable of determining their stopping positions. In simulation, the monopoles are assumed to have stopped at a given position if their velocity falls to $\beta \leqslant 10^{-3}$. If the position of the stopped monopole is inside the prototype trapping volume, the monopole is considered to be trapped. It should be noted that the velocity criterion was changed to $\beta \leqslant 10^{-2}$ with no significant change in the results. In all models that predict the energy loss of monopoles, the velocity $\beta = 10^{-2}$ corresponds to a point where a monopole only travels a few mm in aluminium before it stops [23], as seen in Fig. 86.

4.2 TRAPPING ACCEPTANCE

The acceptance of the MMT prototype is defined for each event as the probability that at least one monopole, produced in the collision, stops inside one of the aluminium bars contained within the

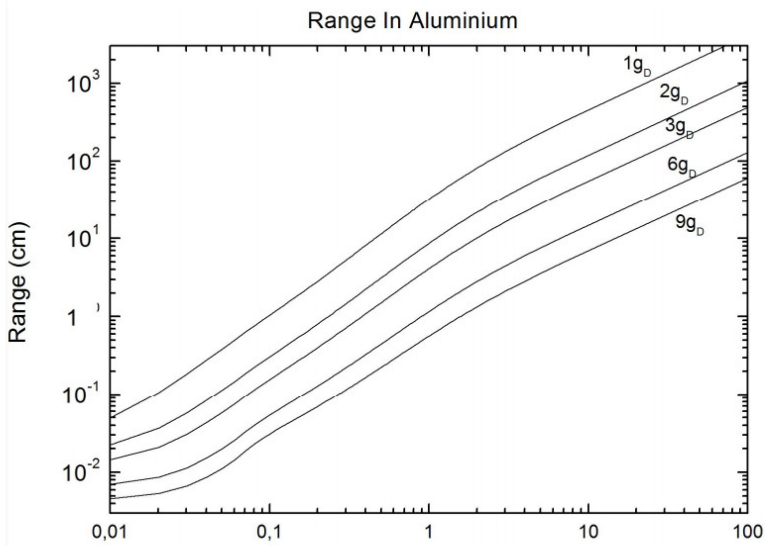

Figure 86: Range (in cm) versus β in aluminium for 1000 GeV monopoles of charge 1.0, 2.0, 3.0, 6.0 and 9.0g_D [23].

MMT. The acceptance is determined by simulating the propagation of monopoles with Geant4 through the geometry model that defines the prototype detector and the relevant material in its vicinity.

The acceptance of the MMT is highly dependent on the energy distribution of the monopole production model as well as the material budget between the production point and the trapping detector. Low charge and/or high energy monopoles tend to punch through the trapping material and are better captured in regions of the MMT that have higher material budget. On the other hand, high charge and/or low energy monopoles tend to stop before reaching the MMT and their acceptance is enhanced in regions with low material budget. For monopoles with the same charge and kinetic energy, the lower mass monopoles have higher velocity and correspondingly a higher dE/dx, and therefore tend to stop earlier. For instance, for a magnetic charge of $|g| = 2.0g_D$, a monopole of mass 100 GeV would need about 100 GeV more kinetic energy to reach the MMT prototype than a monopole with mass 1000 GeV.

4.2.1 *Model-independent analysis*

The acceptance of the MMT for a monopole of a given charge and mass can be defined in a unique way based on its energy and direction at the origin such that it is independent of the production model. Analogous to the definitions of the fiducial regions in ATLAS (see Sec. 3.4.7), the acceptance for the MMT can be described by using two kinematic variables in a model-independent manner, given that the collisions are symmetric with respect to the azimuthal angle, ϕ. The variables are the longitudinal kinetic energy E_z^{kin} and the polar angle θ. The acceptance for all mass and charge combinations was mapped using the particle gun Monte-Carlo samples as a function of the two kinematic variables (with -2.7 rad $< \phi <$ -0.5 rad, correspond-

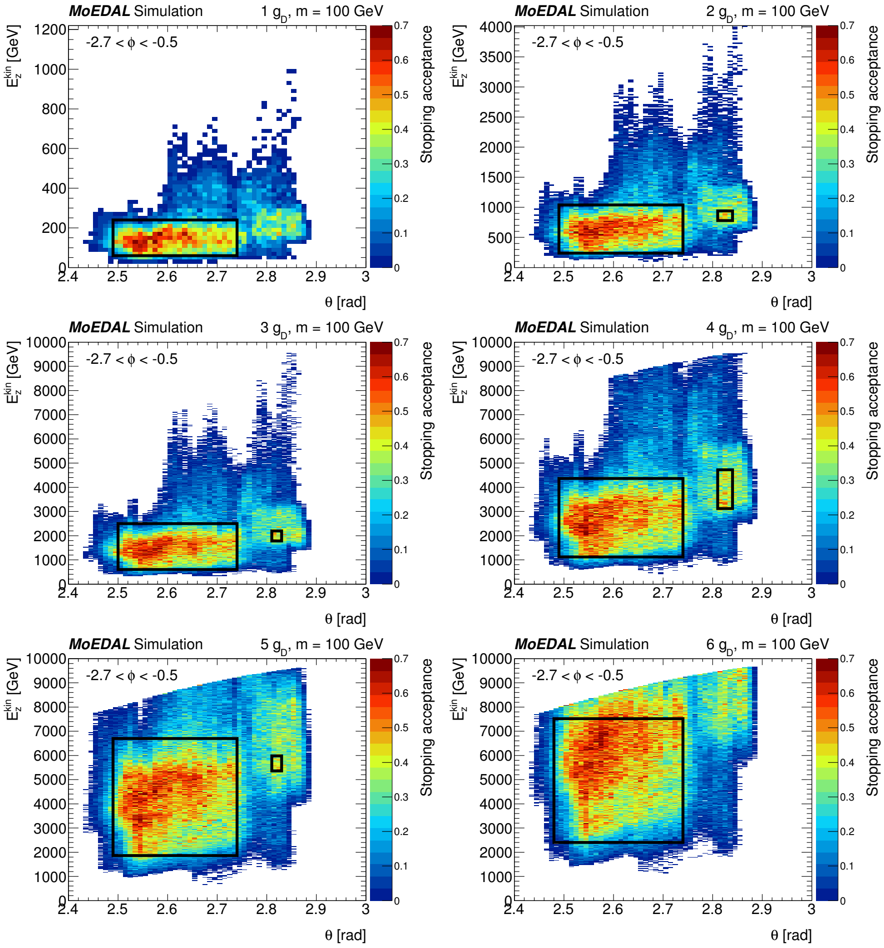

Figure 87: The acceptance of the MoEDAL test array in the kinetic energy and θ parameter space for monopole charges from 1.0 - 6.0g_D.

ing to the ϕ range of the MMT prototype). The acceptance maps are shown in Fig. 87 for monopoles with mass $m = 1000$ GeV.

The information contained in these two-dimensional acceptance maps is sufficient to obtain the acceptance for any given pair-production models to a good approximation. To present the data in a clear and simple manner, albeit at the cost of some precision and thereby ignoring low-acceptance regions, the information can be condensed by considering the so called fiducial regions, which provide reasonably high and uniform acceptance. To encompass a large region with uniform efficiency in the two-dimensional parameter space, an average efficiency of 40% is chosen for the fiducial region definition.

The algorithm defined in Sec. 3.4.7 was used to define the rectangular fiducial regions for all mass and charge combinations, requiring an average efficiency of 40% and a standard deviation of 15%. The acceptance is divided into two distinct regions in θ due to the presence of the vacuum pump in front of the upper part of the trapping volume and owing to the placement of the boxes that have only one box in the top row instead of two: low ($2.40 < \theta < 2.74$) and high ($2.75 < \theta < 2.96$) regions. For completeness, the maximum E_z^{kin} is allowed to exceed the beam energy of 4000 GeV minus the monopole

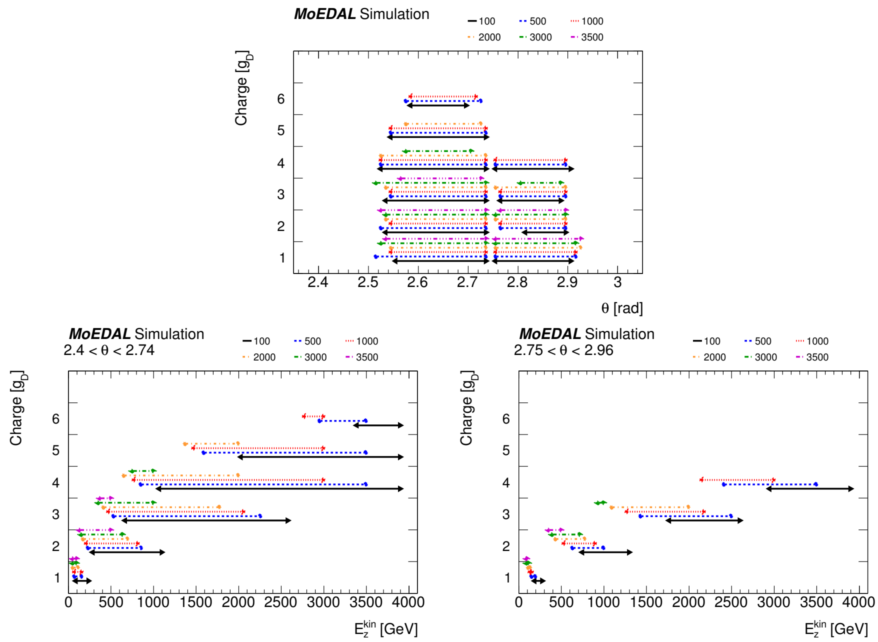

Figure 88: Graphical representation of the fiducial regions for various monopole charges and masses, defined as rectangles in the θ versus E_z^{kin} plane (with -2.7 rad $< \phi < -0.5$ rad) for which the average selection efficiency is larger than 40% with a standard deviation lower than 15%. The double arrows define the rectangle positions and dimensions, with various line styles corresponding to different monopole masses. The top plot shows the θ acceptance ranges, while the other plots show the E_z^{kin} acceptance ranges corresponding to the two different θ ranges. The relative uncertainty in the lower and upper E_z^{kin} bounds due to material and dE/dx uncertainties is $\pm 25\%$.

mass despite the fact that this can be non-physical for pair-produced monopoles. Fiducial regions are indicated as black rectangles for a selection of masses and charges in Fig. 87.

Fig. 88 graphically summarises the ranges of θ and E_z^{kin} that define the fiducial regions found by this algorithm for all mass and charge points considered in this search (blank spaces indicate that no fiducial region was found). The top plot shows the intervals in θ, the bottom left shows the interval in E_z^{kin} for the low-θ region, and the bottom right shows the intervals in the E_z^{kin} for the high-θ region.

4.2.2 *Acceptances for Drell-Yan produced monopoles*

The DY pair-produced monopoles are fully simulated in the geometry model with Geant4 to obtain the DY acceptances. The model kinematics as well as the mass and charge of the monopole contribute to its acceptance as summarised in Tab. 32 , with the highest acceptance for charge $2.0 g_D$ and intermediate masses.

The uncertainty on the estimated amount of material in the geometry description used by Geant4 is the dominant source of the systematic uncertainty. As described in Sec. 2.3.3, the precise mate-

m [GeV]	$\lvert g \rvert = 1.0 g_D$	$\lvert g \rvert = 2.0 g_D$	$\lvert g \rvert = 3.0 g_D$	$\lvert g \rvert = 4.0 g_D$
spin-1/2				
100	0.019±0.003	0.002±0.002	—	—
500	0.017±0.001	0.021±0.005	0.005±0.003	—
1000	0.014±0.001	0.022±0.004	0.008±0.004	0.002±0.001
2000	0.012±0.001	0.022±0.003	0.008±0.004	0.001±0.001
3000	0.016±0.001	0.013±0.004	0.002±0.002	—
3500	0.020±0.001	0.004±0.003	—	—
spin-0				
100	0.028±0.002	0.007±0.004	—	—
500	0.0082±0.0010	0.027±0.004	0.010±0.005	0.002±0.002
1000	0.0038±0.0007	0.022±0.002	0.011±0.004	0.003±0.002
2000	0.0020±0.0004	0.014±0.001	0.008±0.003	0.002±0.002
3000	0.0032±0.0007	0.008±0.002	0.002±0.002	—
3500	0.0069±0.0007	0.004±0.002	—	—

Table 32: Trapping acceptances for spin-1/2 (top) and spin-0 (bottom) monopoles with DY production kinematic distributions. The quoted uncertainties include both statistical and systematic uncertainties. Empty entries mean that the acceptance is lower than 0.1% [29].

rial description of cables and pipes present in the downstream of the VELO are not available and two different geometry models were used to help estimate the material uncertainty. An uncertainty of roughly 25% is associated to the E_z^{kin} boundaries of the fiducial regions used for the model-independent analysis. The uncertainty in the material maps also affects the DY trapping acceptance, with $\lvert g \rvert = 1.0 g_D$, resulting in an uncertainty of the order of 10%. For the charge $\lvert g \rvert = 2.0 g_D$ case, it is of the order of 10-20% for intermediate masses. The largest uncertainty is for the charge and mass combinations with the lowest acceptance, and exceeds 100% when the acceptance is below 0.1%.

The uncertainty associated with the position of the MMT is also estimated (1 cm on each axis). The range of the uncertainty is found to be between 1-17% and is taken into account in the total uncertainty. The uncertainty in the dE/dx in both the low and high β regimes results in a 1-10% uncertainty in the acceptance which is also included in the total uncertainty. A 1-9% uncertainty is estimated from the MC statistics and is always smaller than the total systematic uncertainty.

The DY acceptances including statistical and systematic uncertainty for the trapping detector is summarised in Tab. 32. The table excludes entries with acceptances lower than 0.1% for which the uncertainties exceed 100%, which is the case for all DY samples with $\lvert g \rvert > 4.0 g_D$.

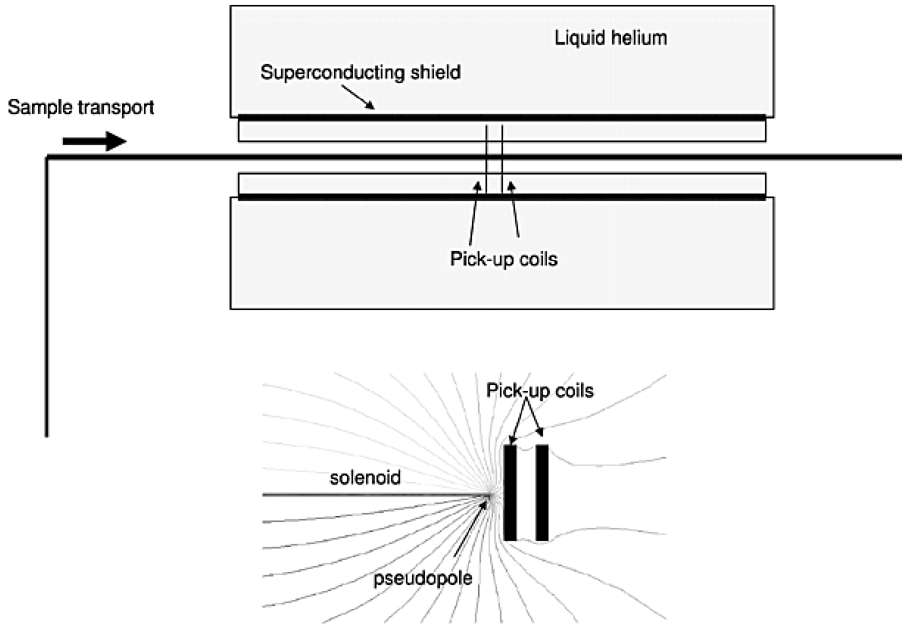

Figure 89: Top: schematic representation of the magnetometer used in this work. Bottom: magnetic field configuration of pseudopole near two superconducting pick-up coils [46].

4.3 MAGNETOMETER MEASUREMENTS

To detect the presence of monopoles trapped in material a 2G Enterprise DC-SQUID magnetometer is used to measure an induced non-decaying current from a transported monopole. The SQUID-based magnetometers provide a high precision to measure such a current but need to be calibrated to the response of monopole.

The magnetometer used in this search is housed at the laboratory maintained by the Earth and Planetary Magnetism group at the Department of Earth Sciences at the Swiss Federal Institute of Technology (ETH), Zurich. It consists of a flux sensing system comprising of two pick-up coils of 4 cm radius along the longitudinal z-axis of the magnetometer with the sensing region surrounded by superconducting shielding. The MMT samples are transported along the axis in the +z direction through an access shaft with diameter of about 4 cm. The magnetic flux from the MMT sample is sensed as a superconducting current in the pick-up coils.

A schematic outline of the magnetometer together with an illustration of the magnetic field configuration arising from a solenoid (one end of which is a pseudopole), near two superconducting pick-up coils is shown in Fig. 89.

4.3.1 *Calibration of magnetometer*

To calibrate the magnetometer, a needle of 14 mm in length and 1 mm diameter enclosed in a non-magnetic plastic holder is used. The dipole sample was made from floppy disk material and was subsequently magnetised such that the dipole moment, aligned along the longitudinal direction, is 3.02×10^{-6} A m^2. The uncertainty on the moment is less than 1% as assessed by comparing measurements with independent magnetometers at the ETH laboratory. The measurements of the calibration sample can be used to predict the magnetometer response to a monopole, using the convolution method described in Sec. 4.3.2.

4.3.2 *Expected magnetometer response to monopoles*

Two methods are employed to gauge the magnetometer response to a monopole, the first being the direct approach that uses a long solenoid and the other is the convolution method. Both these methods are described in detail in the next two subsections.

The direct approach using a long solenoid

To simulate the response from a monopole, a long solenoid is used since the magnetic field from one end of a semi-infinite solenoid follows an inverse square law [141]. Two thin solenoids (S_1 and S_2) wound with copper wire were used for this calibration. S_1 (S_2) is formed of two (three) layers of wound copper - similar techniques were used for a search with the H1 experiment as well [70]. The charge strength on the oppositely charged poles of the solenoids is given by :

$$q = \frac{I \cdot S \cdot n}{l}, \tag{43}$$

where, n is the number of turns on the solenoid. Its length and surface area are given by l and S respectively and I is the applied current. In units of Dirac charge g_D and the current flowing through the solenoids, the pseudopole strength is given as $32.4 g_D$ for S_1 and $41.4 g_D$ for S_2 per unit μA. Tab. 33 describes the different parameters of the two solenoids.

Highly magnetised materials can sometimes generate a fake monopole signal, leaving a residual current when the material is far from the pick-up coils, thus mimicking a monopole. To study and quantify this effect, ferromagnetic rock samples with dipole moments were used as described in the *Fake signals* sub-section below.

The convolution method

The other approach is to use the measurements of the current from the calibration sample. Fig. 90 shows these measurements as a function of the longitudinal position z of the sample. The measured current rises and reaches a peak value for a length that corresponds roughly to the longitudinal extent of the pick-up coil array (~4 cm) and eventually falls again. For this figure, the normalisation and calibration steps have been performed such that the value of the plateau region corresponds to the magnetic moment of the sample.

Calibration coil	1	2
Pseudopole strength/current (g D /μA)	32.4	41.4
Coil length l (mm)	250	250
Number of turns n	2750	7500
Wire diameter (mm)	0.18	0.1
Number of wire layers	2	3
Mean coil area S (mm2)	9.7	4.5
Uncertainty in area	6 %	10 %

Table 33: Description of the calibration solenoids [46].

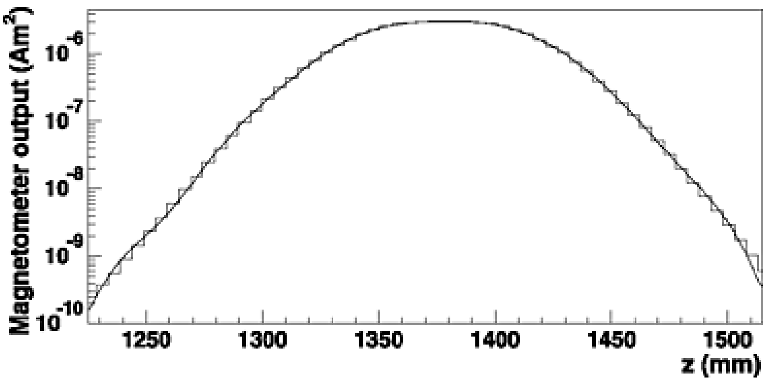

Figure 90: The measured current from the calibration sample as a function of z. A smoothed form of the spectrum is overlaid. The data are expressed in units of magnetic moment since the magnetometer calibration is such that the plateau value returns the value of the sample dipole moment [46].

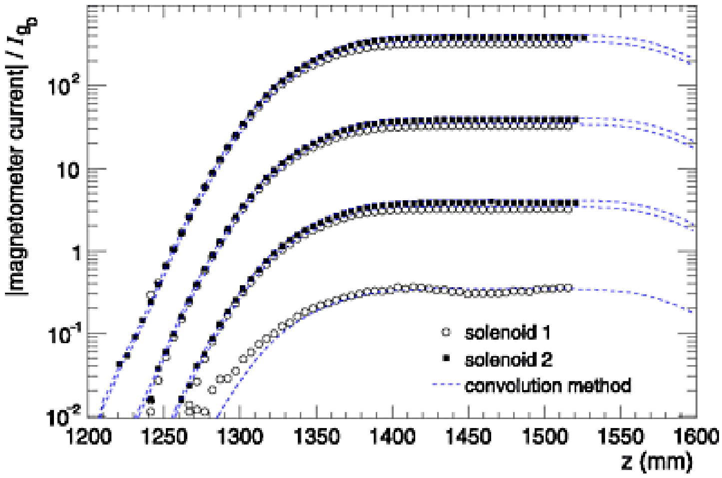

Figure 91: The dependence on z of the induced current for solenoids carrying a range of different currents. Also shown is the prediction of the convolution method (dashed lines) for a given solenoid carrying a certain value of current. Where two lines and two sets of data points are shown close together the upper line corresponds to the upper set of data points and vice versa. The unit of the y-axis is the current expected for a Dirac monopole (I_{g_D}), as estimated with the convolution method [46].

The superposition principle for magnetic fields implies that the field from a long thin magnet is equivalent to that of the sum of the individual dipole samples positioned alongside each other such that the total length would be that of the long magnet. Therefore the measurements shown in Fig. 90 can be used to predict the magnetometer response to a pseudopole by smoothing the distribution with a spline algorithm. Using the magnetometer response at 18 dipole positions, each 14 mm apart, the measurements are extracted and summed to give a response that corresponds to a long thin bar magnet possessing a pseudopole value of ~6500.0g_D. The sum is then scaled to correspond to the pseudopole charge associated with the solenoids for a range of currents that are derived using the solenoid properties in Tab. 33.

Fig. 91 shows the predicted induced current (dashed lines) for the solenoids carrying different currents. These distributions are made by subtracting the measured current at each position for a run with zero solenoid current from the finite current runs. The response rises and reaches a plateau before it begins to fall, as expected from a pseudopole. This corresponds to the solenoid moving towards, into and out of the pick-up coil array. The distributions are normalised such that the plateau value corresponds to the strength of the magnetic pseudopole at the end of the solenoid, which is directly proportional to the current in the solenoid. These distributions are expressed in units of I_{g_D}, which refers to the predicted induced current from a Dirac charge at the centre of the plateau region (z = 1470 mm). For S_2 the assumed current values were 0.01, 0.1, 1.0 and 10 μA, while those of S_1 were 7% higher than those of S_2.

Overall, the response is found to be linear and good agreement is observed between the two methods over several orders of magnitude (the studied range was $0.3g_D$ to $400.0g_D$) with a slight overestimation for the convolution method. The convolution method is able to make predictions for the magnetometer response at high z values that are not possible via the direct solenoid method due to the hardware limitations in the sample transport system. The magnetometer accuracy degrades for weak signals generated by low charge pseudopole (for instance, $0.3g_D$ in Fig. 91) which give small discrepancies at low z values.

The calibration of the magnetometer for the passage of a monopole with charge values between ~$0.3g_D$ and ~$400.0g_D$ is well determined by the two independent methods to an accuracy in reconstructed charge of around 10%. For a detailed discussion on the estimated uncertainties in the two methods, refer to Sec. 3 in [46].

Fake Signals

The expected magnetometer response from a magnetic monopole is to plateau at a current value that corresponds to the monopole charge as seen in the previous subsections. This response is independent of the number of steps used in traversing the sample through the magnetometer and therefore a simple observable called the *persistent current* is devised to identify monopoles. This is the recorded change in the current on the pick-up coils as the sample is transported through the magnetometer i.e. the difference between the first reading and the last reading from the magnetometer.

The effect on the measurement of the persistent current is dependent on instrumental effects such as offset drifts, offset jumps and the so-called flux jumps [142]. While the first two effects have been studied using rock samples[1], the flux jumps had negligible effect on this study and were therefore not studied further.

The offset drifts caused a gradual fluctuation in the persistent current with time, typically this was equivalent to $0.1g_D$ per hour. However, since the drift has an effect at all positions in the magnetometer it has no effect on the persistent current which is a measure of the difference in current between two positions.

The offset jumps on the other hand are spurious shifts in the readings between different positions that can potentially be as large as a monopole signal. However, these offsets generally disappear with subsequent multiple measurements of the sample. In certain conditions, a small offset jump is observed consistently with multiple passes which was studied using two rock samples.

The first of these, R_1, had a magnetic moment of 4.26×10^{-5} A m^2, similar to those of the beam pipe samples (see Sec. 4.3.4); while the second, R_2, had a higher magnetic moment of 1.3×10^{-4} A m^2. Both samples were passed multiple times through the magnetometer with orientations yielding both positive and negative values of the longitudinal magnetisation. For R_1, the distribution of the persistent

1 These samples were assumed to not contain monopoles.

	Positive Magnetisation	Negative Magnetisation
Normal mode	μ = 0.024 $\pm$ 0.005	μ = -0.038 $\pm$ 0.008
	σ = 0.048 $\pm$ 0.004	σ = 0.053 $\pm$ 0.006
Abnormal mode	μ = -0.143 $\pm$ 0.004	μ = 0.005 $\pm$ 0.007
	σ = 0.050 $\pm$ 0.003	σ = 0.059 $\pm$ 0.005

Table 34: Mean and standard deviations (in units of I_{g_D}) of the persistent current distributions in various conditions using samples with magnetisation similar to the one of the beam pipe sample. Each entry is based on 45 to 160 repeated measurements [46].

current had mean values close to zero with very small standard deviations (see top row of Tab. 34). For R_2 however, the orientation yielding the positive longitudinal magnetisation consistently observed a shift by -0.149g_D relative to the empty holder measurements performed in between. This shift was not observed for the negative longitudinal magnetisation orientation (see Tab. 34). Subsequently, R_2 was passed twice through the magnetometer after being demagnetised, and it yielded a moment of 1.5×10^{-5} A m^2 followed by 4.5×10^{-6}. Similar shifts were also observed for R_1 when remeasured and it was concluded that the magnetometer had entered into an abnormal working mode, which provoked an offset jump for any sample with the positive longitudinal magnetisation of the magnitude -0.149g_D. The abnormal mode was triggered by the first pass of the R_2 which had a high longitudinal magnetisation. The magnetometer could be restored into a normal mode by manually resetting the current offset to a value near zero. After the reset, the measured persistent current for both the R_1 and (now demagnetised) R_2 were consistent with the values in the top row of the Tab. 34.

For highly magnetised samples, the resolution of the magnetometer is dominated by the offset jumps and can be considered as being the typical deviation of the persistent current from zero for samples where there is no monopole. Based on the studies with the rock samples, it was concluded that the resolution of the magnetometer in the normal mode is 0.049g_D, while in the case where the abnormal mode is triggered it is as large as 0.149g_D.

4.3.3 *MMT samples*

The MMT samples (see Sec. 2.3.3) were passed through the 2G Enterprise DC-SQUID magnetometer to measure an induced non-decaying current from a transported monopole. The passage of samples through the sensing coils is facilitated by a sample holder attached to a long carbon-fibre tube that extends the entire length of the magnetometer. The samples are placed on the holder at the maximum position of the tube and the measurements from the SQUID are recorded as the tube (with the sample) moves back to its initial position. Magnetometer measurements are made for each of the 606 aluminium rod samples from the MMT prototype detector. For offset

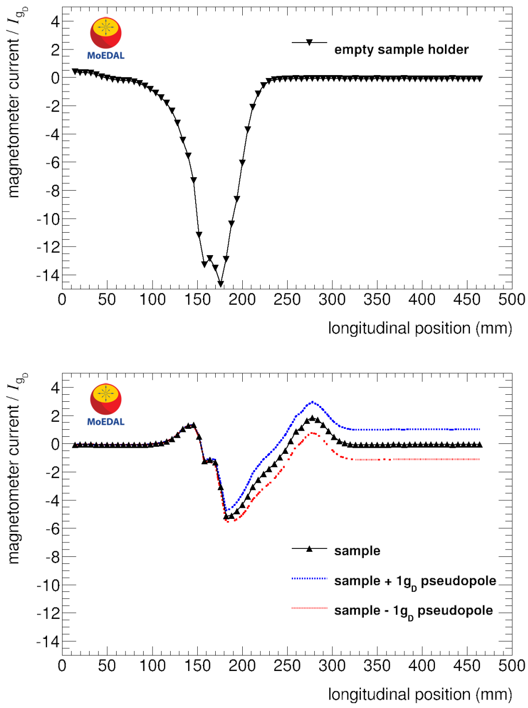

Figure 92: Magnetometer response profile along the axis of the tube for the empty sample holder (top) and a typical aluminium sample of the trapping detector after subtracting the response of the empty sample holder (bottom). The 20 cm sample is inside the sensing region for longitudinal positions between 110 mm and 310 mm. Solid lines simply connect the points. Dashed lines show the responses when the measurement from a long solenoid is added and subtracted to emulate the presence of a Dirac monopole in the sample [29].

subtraction, every tenth measurement was performed with an empty sample holder.

The measurements at 76 different positions with an empty sample holder (top) and with a 20 cm MMT sample after subtraction of the response of the empty sample holder measurements (bottom) as they traverse through the magnetometer is shown in Fig. 92. Emulations for responses from samples that would contain a positive or negative monopole are plotted and were obtained by using a long solenoid scaled to the current expected from a Dirac monopole, I_{g_D}. It is noted that the presence of a monopole substantially changes the current that is recorded at the final position. The signature of monopoles is therefore recorded by the persistent current, which is defined as the difference between the currents before and after the passage of the sample through the magnetometer sensing coil. The current values used in defining the persistent current have undergone an offset subtraction from an empty holder measurement. The magnetisation of the sample holder itself is of the same order as the typical sample magnetisation.

A sample was considered to have trapped a monopole candidate if the persistent current differed from zero by more than $0.25 g_D$. Re-

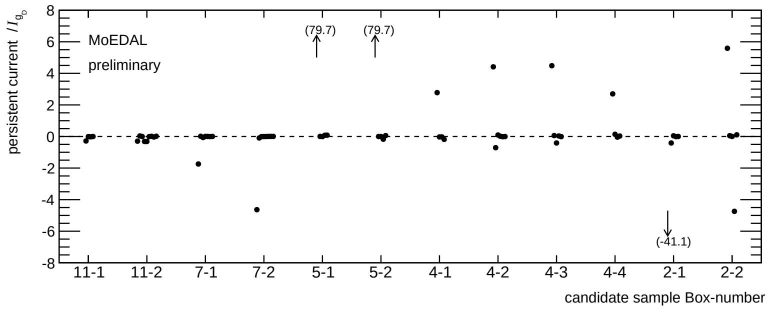

Figure 93: Results of multiple persistent current measurements (in units of Dirac charge) for the samples that yielded large ($|g|>0.25g_D$) values for the first measurement [29].

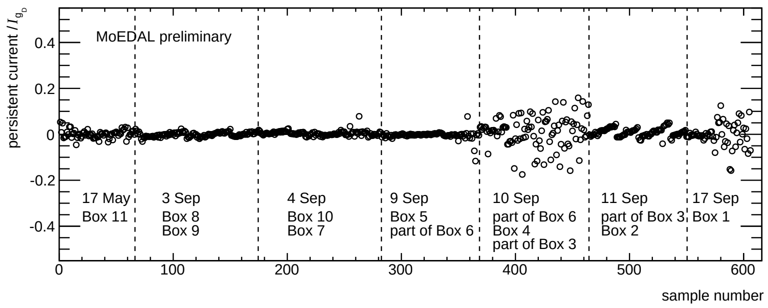

Figure 94: The persistent current (in terms of Dirac charge) measured for 606 samples from the MMT boxes during the 2013 measurement campaign [29].

peated measurements were performed for such samples to ensure the deviation from zero was in fact due to the presence of a monopole and not spurious measurements due to instability of the magnetometer. Fig. 93 shows the measured persistent current for potential candidates where additional measurements were made for the samples which showed large deviations from zero on the first pass. In all the cases, the subsequent measurements were consistent with zero. The causes of the spurious jumps and fake signals are discussed in Sec. 4.3.2

The first measurement (or the first subsequent measurement in case of spurious jumps in the first pass) for all 606 samples of the MMT prototype as a function of time is shown in Fig. 94. The measurement campaign was completed in 7 days, mostly in September of 2013. The variation in resolution over the different days can be attributed to relatively small differences in initial configurations and measurement methods - for example, how periodically an empty sample holder measurement is carried out. The measurements from the entire campaign is plotted in Fig. 94, that shows that no measurement yields a value greater than $0.18g_D$.

Limits on monopole production

No magnetically charged particles were observed in the MMT prototype detector that was exposed to 0.75 ± 0.03 fb^{-1} of 8 TeV pp colli-

DY Lower Mass Limits [GeV]	$\lvert g \rvert = 1.0 g_D$	$\lvert g \rvert = 2.0 g_D$	$\lvert g \rvert = 3.0 g_D$
spin-1/2	700	920	840
spin-0	420	600	560

Table 35: Lower mass limits (95% confidence level) in models of spin-1/2 (top) and spin-0 (bottom) DY monopole pair-production. These limits are based upon cross sections computed at leading order. These cross sections are only indicative since the monopole coupling to the photon is too large to allow for pertubative calculations [29].

sions, under the assumption that a monopole that is produced in the collisions and stop in the aluminium material would always be captured and remain bound to the nucleus. Limits on the cross sections of monopoles using various assumptions for monopole production kinematics are made based on this observation combined with the estimate of acceptance and its uncertainty. The limits are obtained using a Bayesian method with Poisson statistics described in details in [143].

Fig. 95 and 96 show the 95% confidence level upper limits on the cross section of monopoles produced via the DY production mechanism as a function of mass and charge respectively, for both spin-0 and spin-½ monopoles. The DY pair-production cross section calculations are performed at leading order and correspond to the cross sections of massive particles with a single electric charge scaled to account for the monopole charge by the factor $g^2 = (n \cdot 68.5)^2$. Since the monopole coupling to the photon is too large for pertubative calculations to converge, these DY cross sections calculations should be viewed with caution. They, however, provide a useful benchmark to compare results across different experiments.

Tab. 35 shows the corresponding mass limits for magnetic charges up to $3.0 g_D$ for both spin-0 and spin-½ DY monopoles. Compared to the mass limits obtained in Sec. 3.7 for ATLAS (for charge $\leqslant 1.5 g_D$), the MoEDAL mass limits are about a factor two lower under the same assumptions for monopole production at 8 TeV. However, for the first time at the LHC, mass limits for DY pair-produced monopoles with charge $\lvert g \rvert \geqslant 2 g_D$ are obtained.

Model-independent results are obtained for monopole production within ranges of kinetic energies and directions described by the fiducial ranges detailed in Sec. 4.2.1. A 95% confidence level upper limit on the cross section of 10 fb is set for monopoles with charges up to $6.0 g_D$ and masses up to 3500 GeV, within the fiducial regions.

4.3.4 *Accelerator material samples*

In addition to the MMT samples from the MoEDAL experiment, accelerator material from the CMS experiment that was located at 18 m from the CMS interaction point were also analysed. Seven sam-

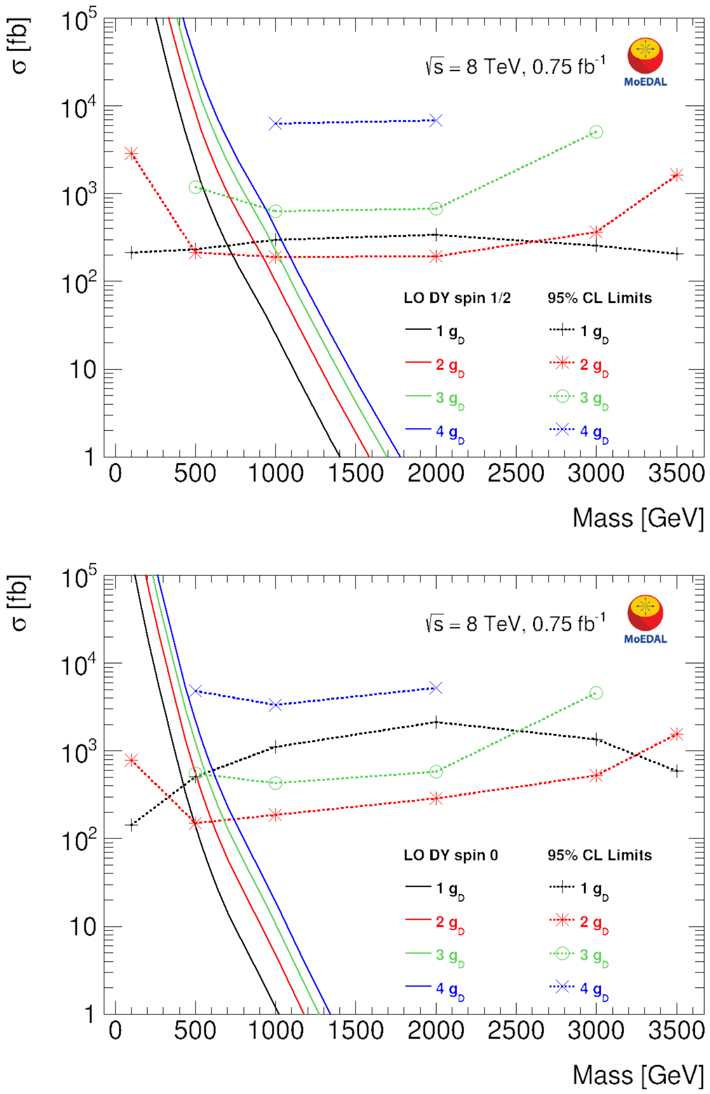

Figure 95: Cross section upper limits at 95% confidence level for DY monopole production as a function of mass for spin-½ (top) and spin-0 (bottom) monopoles. The various line styles correspond to different monopole charges. The solid lines are DY cross section calculations at leading order [29].

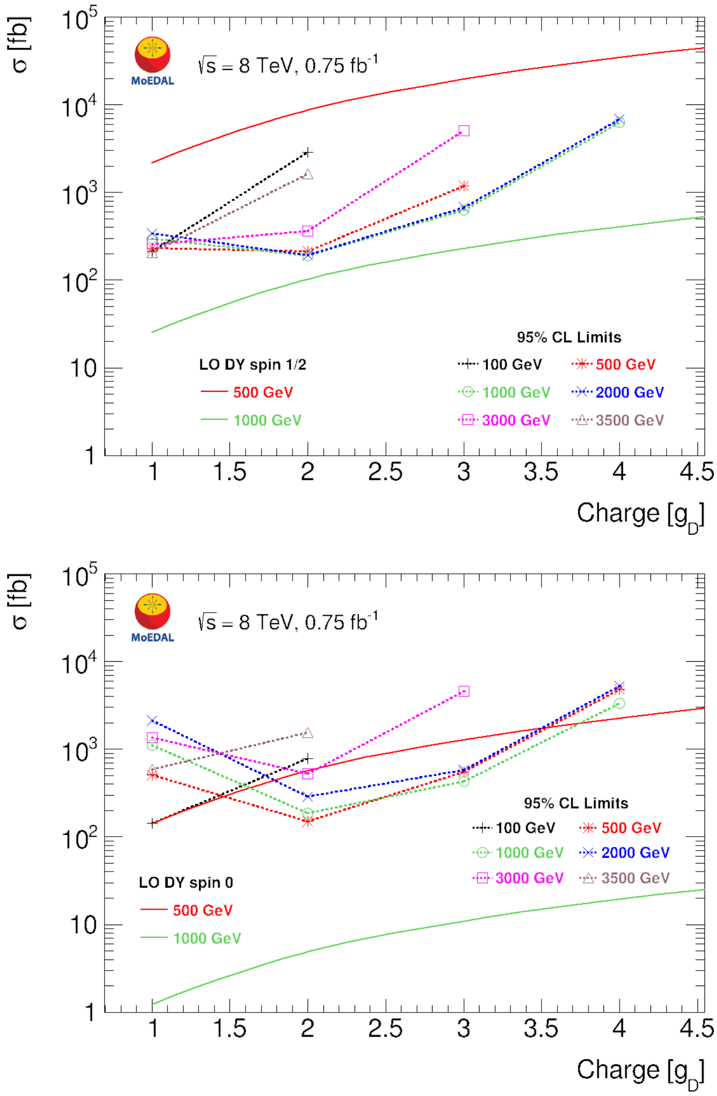

Figure 96: Cross section upper limits at 95% confidence level for DY monopole production as a function of charge for spin-½ (top) and spin-0 (bottom) monopoles. The various line styles correspond to different monopole masses. The solid lines are DY cross section calculations at leading order [29].

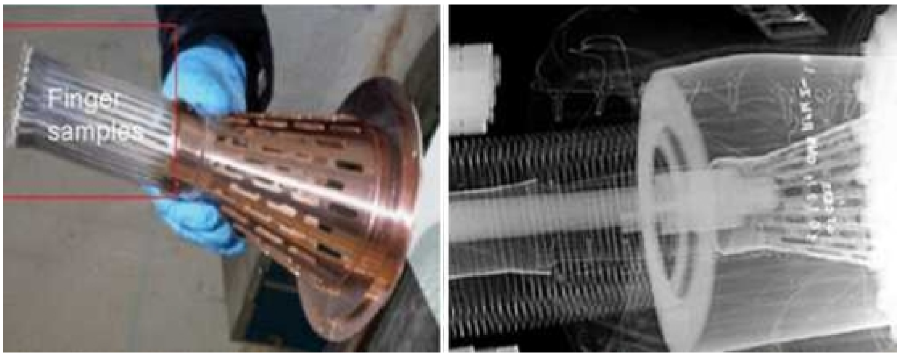

Figure 97: *Left:* a photograph of the plug-in module showing the finger samples. *Right:* an X-ray picture of the plug-in module attached to the CMS beam pipe [46].

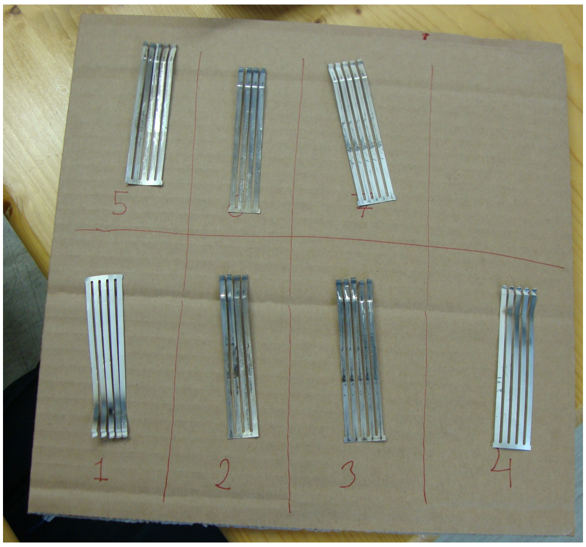

Figure 98: The finger samples after being cut to fit into the magnetometer.

ples (so-called fingers), that were part of the plug-in module attached to the CMS beam pipe and made of a copper-beryllium alloy were analysed. The plug-in module was used to maintain the beam pipe's structural integrity over changing temperatures. Fig. 97 shows the pictures of the plug-in module with the attached fingers (left) and an X-ray image of the plug-in module mounted in the beam pipe (right). The fingers on the plug-in module were replaced before the luminosity running in 2012 as they were incorrectly mounted and hung in the vacuum region. The extracted modules (and attached fingers) were deemed safe post all the safety procedures for detector material so close to the beam. The fingers were cut into seven pieces (see Fig. 98) and then passed through the magnetometer.

Each individual finger sample has a length of around 8.5 cm and is approximately 0.8 mm thick. The modules were attached at a position of 18 m along the colliding beam axis with a polar angle acceptance between 179.936 and 179.943 degrees. Given the small acceptance, monopoles that stop within the sample would possess energies below a certain punch-through energy, which is a function of its mass and charge. The energy loss of monopoles and an estimate of its

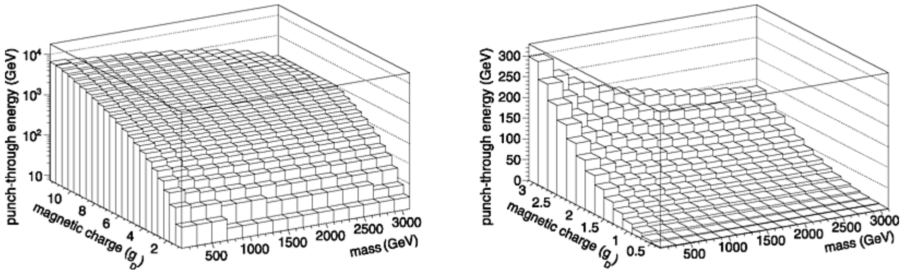

Figure 99: The kinetic energy below which a monopole incident upon the beam pipe sample would stop inside the sample, as a function of mass and magnetic charge. The figure on the right shows only the charges below $3.0g_D$ with a better precision and with a linear vertical scale [46].

range within the sample was simulated using the Bethe formula for magnetic charges [21] (see Eq. 18). Fig. 99 shows the punch-through energy range for a series of mass and charge samples. A monopole produced in collisions is expected to have a minimum kinetic energy such that the large CMS magnetic field has negligible effect on its trajectory - estimated to be of the order of 0.1 GeV for masses above several hundred GeV.

Given the limited range of the samples that were available, the analysis did not focus on producing production limits of monopoles and hence the estimates on the uncertainties of the size and positions of the samples are not considered.

Each of the seven finger samples were passed through the magnetometer (refer Sec. 4.3.1) wrapped in paper so that they would tightly fit into a slit on top of the sample holder. The procedure adopted for attaching samples to the sample holder described in 4.3.3 was implemented here as well. Given the small number of samples to be analysed, most measurements were performed in 48 steps to precisely map the magnetisation of the sample at each position - with each sample measured at least twice. In addition, frequent empty holder measurements were also made for background subtraction, similar to that described in 4.3.3. Sample number 4 was measured six times in total, of these, three measurements had different number of steps (96, 24 and 4).

Fig. 100 shows the measured induced current for sample 3 after the offset correction (subtraction of the empty sample holder measurements). The peak of this distribution helps study the magnetisation of the beam pipe sample. The dashed line provides an estimated measurement of a monopole of charge $4.0g_D$ trapped in the sample obtained from a solenoid measurement with a pseudopole equivalent to $4.14g_D$.

Fig. 101 shows the peak induced current for each of the samples, in each of its iterations. The currents are typically many orders of magnitude greater than that expected from a Dirac monopole. The offset jumps described in Sec. 4.3.2 are expected for highly magnetised samples and therefore, sample 2 is demagnetised with an oscillating magnetic field. The risk of losing a trapped monopole due to the

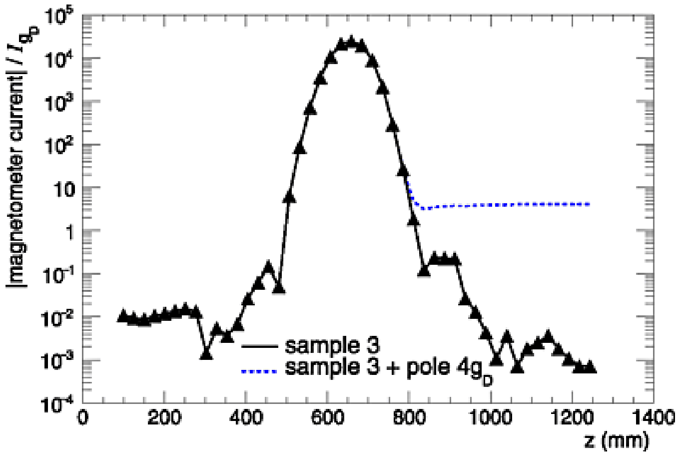

Figure 100: The measured current from the beam pipe sample 3 as a function of z in 48 steps. The dashed line indicate the expected signature of a monopole with charge 4.149_D trapped inside the sample [46].

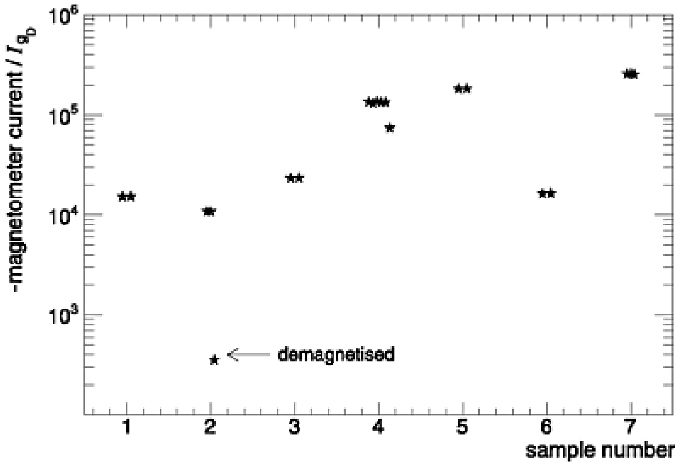

Figure 101: The peak currents associated with different beam pipe samples [46].

demagnetisation process should be minimal given the large binding energy of the monopole in material [38]. Should highly magnetised samples continually cause offset jumps in the magnetometer, the demagnetisation of the sample may be necessary and implemented.

Persistent current for all the samples after the offset subtraction are illustrated in Fig. 102. The values range from 0 to ~0.35 I_{g_D}, consistent with the rock sample calibrations shown in Tab. 34. The offset jumps during the analysis of these samples was of the order of ~$0.15g_D$, with sample 4 suffering several consecutive offset jumps which account for the higher current values, especially for first two measurements with this sample.

No monopoles with charge $\geqslant 0.3g_D$ were found in the CMS detector material.

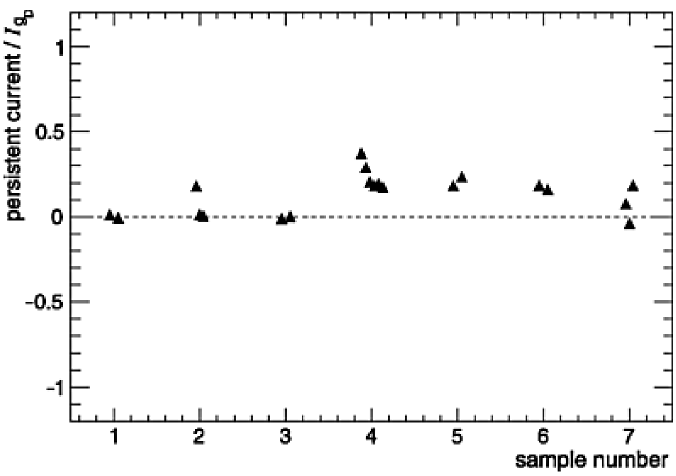

Figure 102: Persistent current left by the beam pipe samples [46].

5 CONCLUSIONS

Predictions of beyond the Standard Model particles such as magnetic monopoles and highly electrically charged objects help answer fundamental questions such as charge quantisation and the nature of dark matter. Various models, starting with Dirac's theory to Cho-Maison or electroweak models and various GUT models predict the existence of monopoles. The Dirac model makes no prediction on the mass of the monopoles, whereas electroweak models expect monopoles with masses of the order of several TeV within the LHC range.

Over the last few decades a variety of techniques have been used to search for such exotic particles (see Sec. 1.5- 1.7). The searches covered in this dissertation are simply an addition to the plethora of searches using multiple techniques to identify monopoles that could have been produced in the 8 TeV proton-proton collisions at the LHC. The highly ionising signature of these exotic particles is used to identify them in the ATLAS and MoEDAL experiments.

The ATLAS experiment uses two sub-detector systems, the TRT and the EM calorimeter to help identify monopoles and HECOs that are expected to produce regions of high ionisation. The sensitivity of the analysis was enhanced compared to previous efforts, by the development of a dedicated trigger that selected events based on the ionisation in the TRT. For the first time the ATLAS detector was sensitive to monopoles with charges greater than $1.0g_D$ with the help of this trigger. The exotic candidates were reconstructed with high efficiency using the TRT and the EM calorimeter ionisation, for events that passed the dedicated trigger.

With no events consistent with the signature of monopoles or HECOs observed in the collected 7.0 fb^{-1} of pp collision data, upper limits on the production cross section were set for two scenarios. A model-independent limit of 0.5 fb was set in fiducial regions of high and uniform selection efficiency for masses between 200-2500 GeV and charges covering the ranges 0.5-$2.0g_D$ for monopoles and 10-60e for HECOs. Limits were also set for spin-0 and spin-½ monopoles and HECOs assuming the Drell-Yan pair-production mechanism. In addition, lower mass limits were set for pair-produced particles, based on the theoretical cross section predictions.

The MoEDAL experiment uses its pioneering design to search for magnetic monopoles and highly-ionising particles. This largely passive detector, deployed in the LHCb VELO cavern at Interaction Point-8 serves multiple purposes. First, it uses nuclear track detectors to identify tracks from new particles. Second, the unique ability of the detector to trap particles using its trapping detector will help study these exotic particles in detail, if captured. In this dissertation, the results of the prototype Magnetic Monopole Trapper (MMT) detector that was exposed to 0.75 fb^{-1} of 8 TeV proton-proton collisions in late 2012 are presented. This is the first time a scalable and reusable trapping array has been deployed at an accelerator facility.

No monopole candidates were found in the trapping detector sample with magnetic charge, $g \geqslant 0.5g_D$. Assuming that monopoles are captured by aluminium nuclei, upper limits on the cross section are set at 95% confidence level in the range of 100 to 6000 fb using the Drell-Yan pair-production models for monopoles for charges up to $4.0g_D$ and masses up to 3.5 TeV. A model-independent cross section limit at 95% confidence level is set of 10 fb for monopoles with charges up to $6.0g_D$ that are produced in specific energy regimes and η regions.

While MoEDAL cannot reasonably compete with the ATLAS experiment for searches of low-charge monopoles, it has the ability to probe for much higher charges ranging up to $6.0g_D$. With its small solid angle coverage and modest luminosity, the prototype trapping detector probes ranges of charge, mass and energy which cannot be accessed by other LHC experiments. The MMT detection technique has the potential to quickly make a discovery and allow for an unambiguous background-free assessment of a signal, providing a direct measurement of a monopole magnetic charge based on its magnetic properties alone. A newer and larger version of the MMT detector was deployed in 2015 downstream of the LHCb VELO vessel as well as on its sides and was exposed to 13 TeV pp collisions.

Appendices

x

A

COMBINED w DEFINITIONS

Before the ultimate choice of the combined-w variable as described in the sub-section 3.4.4, a few alternate ways to describe the w variable were considered.

A few alternate definitions of the w variable were considered before the combined-w variable was found to be optimal choice for this analysis.

The individual components of the combined-w variable - w_{Pre}, w_{EM1} and w_{EM2} - were studied as possible discriminating variables. The w_{EM1} variable is a powerful discriminant between signal and data[1], while w_{Pre} variable has the weakest discriminating power due to the coarse segmentation of the Presampler (see Fig. 103). New discriminating variables were constructed by considering the *maximum*, *multiplicative* and *average* between the individual w variables. Due to the poor discriminating power of the w_{Pre} variable, these variables were constructed with and without w_{Pre} variable in its definition as seen in Fig. 104.

The w_{Max} variable (see Fig. 104e, 104f) and w_{EM2} variable (Fig. 103e, 103f) distributions are similar. This is attributed to the granularity of the EM layer along with the number of cells used in the construction of the w variable. For the case of the w_{Max}, Fig. 105 shows that w_{EM2} almost always has a higher value than w_{EM1}. However, the w_{Max} and individual w variables make use of only a single layer to assert their discriminating power. The variables depending on single layers run the risk of missing out on candidates that deposit more energy in either previous or latter layers and hence are considered as poorer discriminants. The $w_{\mathrm{Multiplicative}}$ variable serves as a good discriminant, however, due to its nature, the distributions tend to be broader with very long tails to lower values for signal samples. The w_{Average} on the other hand has narrower distributions for both data and signal.

The distributions of $w_{\mathrm{Multiplicative}}$ and w_{Average} show a small second peak for data as indicated in Fig. 106. The peak is due to background candidates that penetrate through the calorimeter and shower in the second layer thereby having only the w_{EM2} variable as shown in Fig. 107. To supress such background events the definition of the w variable has a cut that requires the candidate to not have energy deposited only in EM2.

The preference of w_{Average} over $w_{\mathrm{Multiplicative}}$ variable was made by considering the correlation coefficients in data in regions

1 Only 10% of the data was used to study the discriminating power of the selection variables.

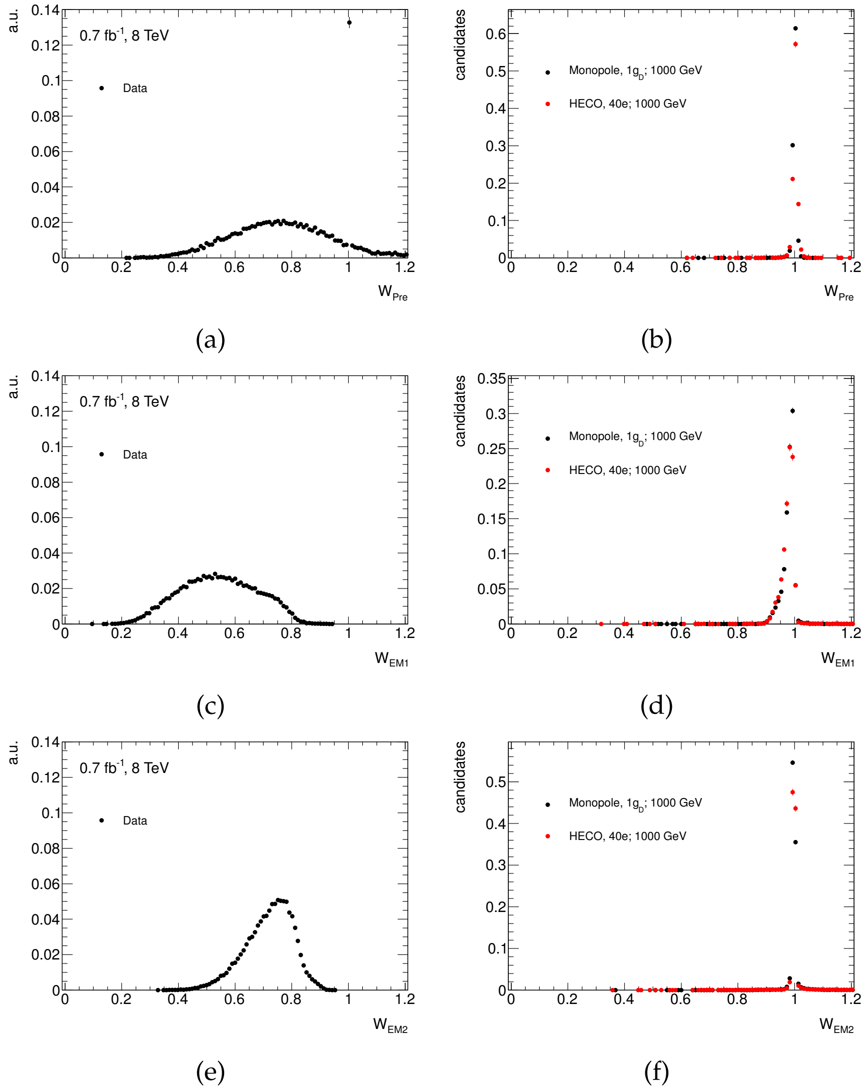

Figure 103: The w variable in each layer for data (left) and for monopole/HECO signal (right). Due to the granularity and the different number of cells used to construct the w variable in the different EM layers, the distributions in the different layers vary. The variations are more prominent in the data, which come from different processes as opposed to the signals, where HIPs are expected to have narrow distributions with a peak close to 1.

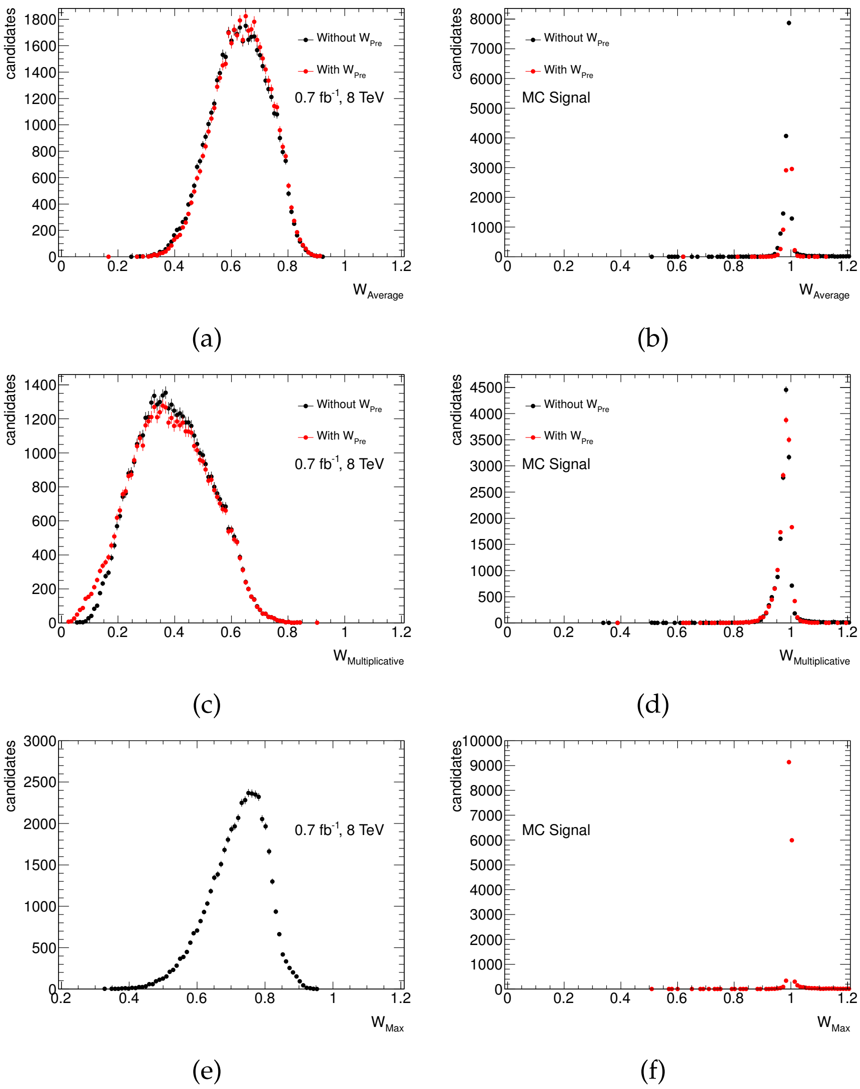

Figure 104: Distributions showing the w_{Average} (top), $w_{\mathrm{Multiplicative}}$ (middle) and w_{Maximum} (bottom) variables for data (left) and MC signal samples (right). The w_{Average} and $w_{\mathrm{Multiplicative}}$ variables are constructed with and without the w_{Pre} variable as indicated by the black and red points respectively. The addition of the w_{Pre} variable has minimal impact on the overall distribution of w_{Average} and $w_{\mathrm{Multiplicative}}$ variables.

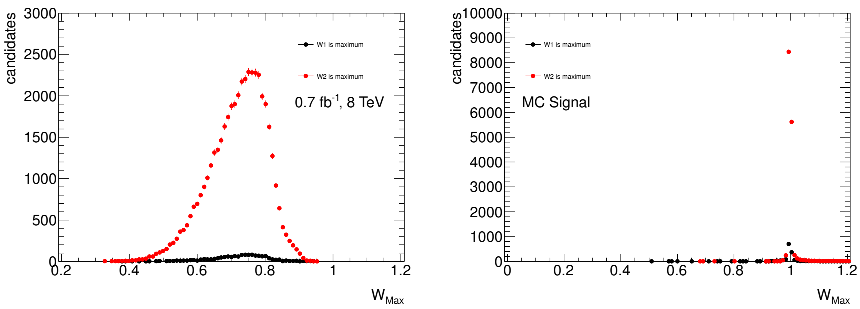

Figure 105: The distributions showing to which layer the w_{Max} value corresponds.

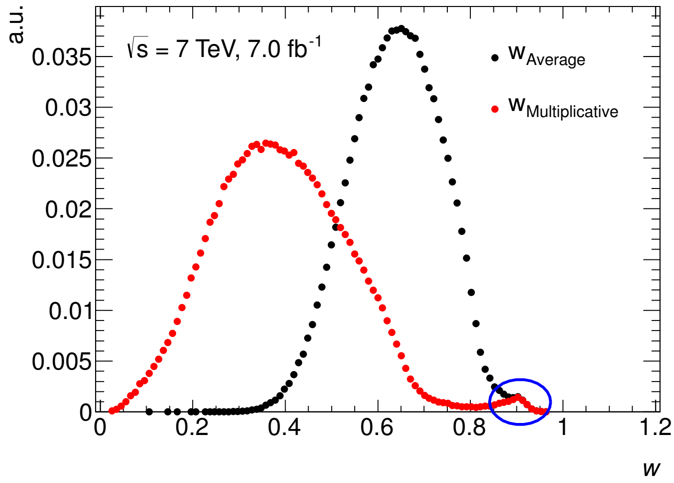

Figure 106: The distributions of the w_{Average} and $w_{\mathrm{Multiplicative}}$ variables shows a small bump in data at $w > 0.84$ as highlighted.

where the bulk of its distribution lies. The correlation coefficient in data for the w_{Average} variable computed for the region $0.5 < w_{\mathrm{Average}} < 0.8$ is 0.0505, while in the region $0.2 < w_{\mathrm{Multiplicative}} < 0.6$ is 0.1186 for the $w_{\mathrm{Multiplicative}}$ variable. The higher yielding correlation in the multiplicative case supports the choice of the w_{Average} as the final selection variable.

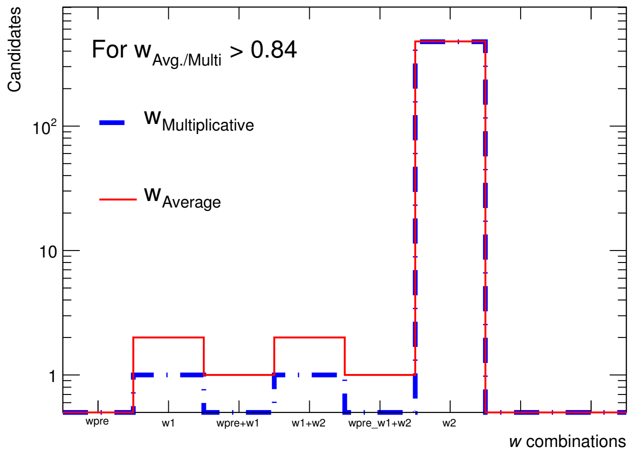

Figure 107: The plot shows the number of candidates that have $w_{Avgerage}$ and $w_{Multiplicative}$ with a value > 0.84. Each bin shows the combinations of how each of these w combination variables were constructed for these candidates.

B CORRELATIONS BETWEEN f_{HT} AND w VARIABLES

B.1 EXCLUSION OF THE TRANSITION REGION

Fig. 108 shows the profile distributions of the w and f_{HT} variables as a function of pseudo-rapidity (η). The two variables need to be uncorrelated in order to estimate the background using the data-driven ABCD method. The correlation factors (Pearson product-moment correlation coefficient) is computed for the barrel (0.034), the transition region (0.191) and the end-cap (0.154).

In Fig. 109 the profile distributions of f_{HT} as a function of the w variables are shown for data and selected simulated HIP samples. The strong correlation observed in the transition region ($1.375 < |\eta| < 1.52$) coerces the analysis to drop this region.

B.2 UNDERSTANDING THE ORIGIN OF CORRELATIONS AT HIGH-w

It is vital to understand the correlations between the two discriminating observables in the analysis. The w and the f_{HT} variables are shown to be strongly correlated in certain parts of the detector. Fig. 110 shows the ratio of the number of events with $f_{HT} \geqslant 0.7$ over those with $f_{HT} < 0.7$ for each w variable bin. The distributions in the limited η regions are fairly uniform and uncorrelated in the high w regions. The region, $2.0 \leqslant |\eta| < 2.2$, although not considered in the analysis, is also shown to illustrate the maximum values attainable by the ratio in the extreme cases.

On combining the η regions into broader ranges of barrel, end-cap and the whole detector under $|\eta| < 2.0$, as seen in Fig. 111, a correlation originating from the end-cap region is observed. In Fig. 108 the profile distributions of the two observables highlight their η-dependence.

The correlation factor between the observables in data, considering the entire detector, is 0.123. Excluding the regions $1.375 < |\eta| < 1.52$ and $|\eta| > 2.0$ reduces the correlation to 0.958. The blue curve in Fig. 111 highlights the correlation between the w and f_{HT} variables in data for the present analysis.

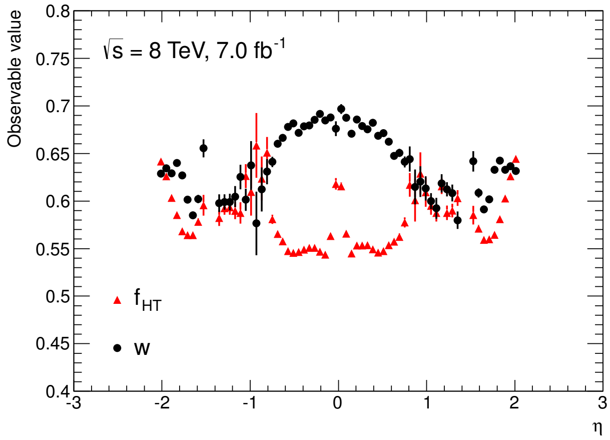

Figure 108: Profile distributions of the two observables as a function of η. The two are shown on the same canvas to highlight the correlations between the distributions in the end-cap regions.

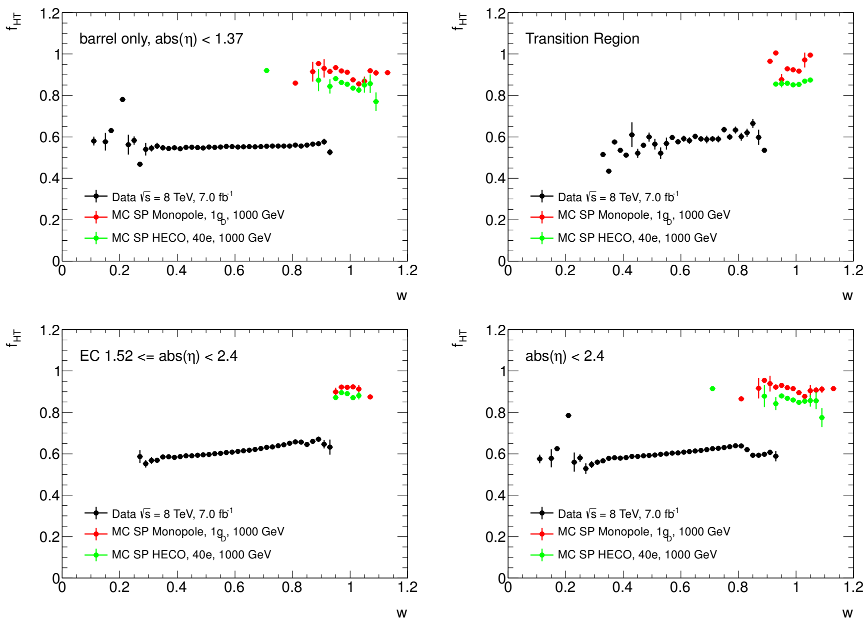

Figure 109: Profile histograms of f_{HT} as a function of the w variable in the different η regions of the detector. The region w >0.94 is blinded in data. The correlation factors are computed in the barrel (0.034), the transition region (0.191), the end-caps (0.154) and the entire detector (0.123). The correlation factor of the full detector excluding the transition region and $|\eta|$ >2.0 is 0.958.

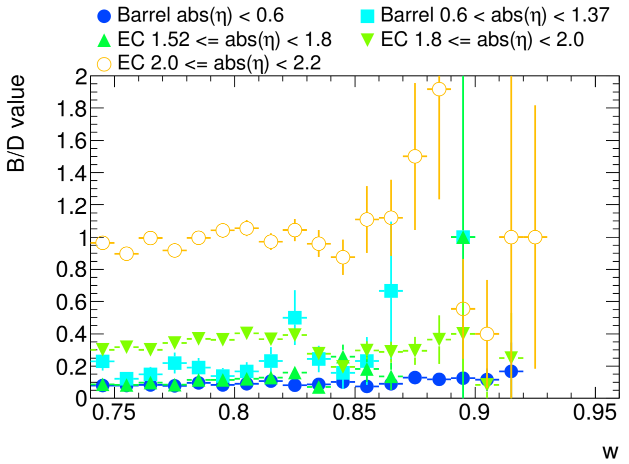

Figure 110: Ratio of the number of events in data in Region-B ($f_{HT} \geqslant 0.7$) to those in Region-D ($f_{HT} < 0.7$) in each bin of width 0.01 of w, for different η regions of the detector. The region $w > 0.94$ is blinded. Though the range $2.0 \leqslant |\eta| < 2.2$ is excluded from the analysis, it is plotted here to illustrate the maximum value the B/D ratio can attain in extreme cases.

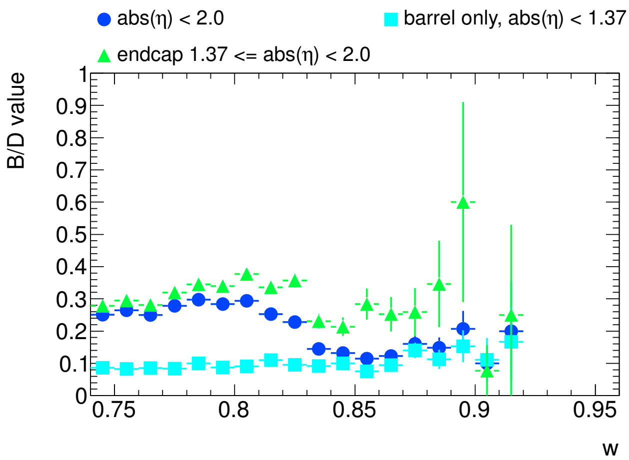

Figure 111: Ratio of the number of events in data in Region-B ($f_{HT} \geqslant 0.7$) to those in Region-D ($f_{HT} < 0.7$) in each bin of width 0.01 of w, for different η regions of the detector. The different $|\eta|$ ranges are now combined to show the behaviour of the distributions in the end-cap and barrel regions separately. The region $w > 0.94$ is blinded.

B.3 CORRELATION CORRECTION FOR THE BACKGROUND ESTIMATE

The impact of the correlation, observed in the previous section, on the background estimate should be evaluated and corrected (if needed). For completely independent variables, the ABCD method suggests that the ratio of the number of events in region-A to region-C is equal to the ratio of the number of events in region-B to region-D as explained in Sec. 3.5, for any defined range of the ABCD regions. Therefore, a correlation correction factor can be defined as shown in Eq. 44 , which in the absence of correlations should equate to unity. Using the control regions with w <0.94 for calculating ρ and extrapolating to the signal region, the background estimate can be defined as $A_{est} = \rho \cdot BC/D$.

$$\rho = \frac{A/C}{B/D} \tag{44}$$

Consider a two-dimensional plot of the ratio of the number of events with $f_{HT} \geqslant 0.7$ to that with $f_{HT} < 0.7$ against the w variable, with w <0.94 (blue curve from Fig. 111). For every i^{th} w bin (with w <0.94), a correlation correction factor can be defined as in Eq. 45, such that the i^{th} bin represents the regions-BD and every j^{th} bin (such that $j > i$) the regions-AC. As an example, an illustration of the newly created ABCD regions is presented in Fig. 112 where the i^{th} bin is $w = .80$ (constrained by the black dash and dot line) represents the region B/D, and every j^{th} bin, with $j > i$, (constrained by the red alternate small and large boxes) represents the region A/C.

$$\begin{aligned} \rho_{i,j} &= \frac{A_j/C_j}{B_i/D_i} \\ where\ \ i &< j, \end{aligned} \tag{45}$$

The correction factor ρ was defined for the i^{th} bin as the weighted average between all $\rho_{i,j}$ over all j bins, as described in Eq. 46

$$\begin{aligned} \rho_{avg,i} &= \frac{\sum w_{i,j}\rho_{i,j}}{\sum \Omega_{i,j}} \\ with\ \ \Omega_{i,j} &= \frac{1}{(\sigma\ (\rho_{i,j}))^2_{i,j}} \end{aligned} \tag{46}$$

The weight is defined as the reciprocal of the error on $\rho_{i,j}$. Fig. 113 shows the deviation from 1 to be asymmetric, with a maximum deviation of 0.45. However, in the context of this analysis with zero background events observed in the signal region, small deviations in the correction factor have negligible consequences in the background

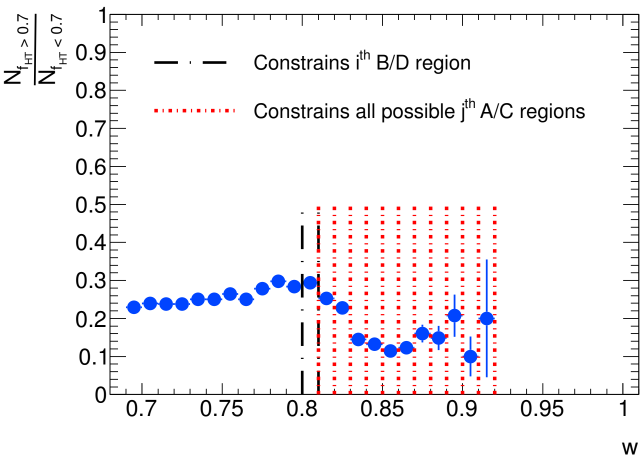

Figure 112: An illustration of the algorithm used to determine the correlation correction factor ρ. The black dash and dotted line represents the i^{th} bin which encompasses the B/D value for the B,D regions. The red alternate small and large boxes represent the j^{th} bins which encompasses the A/C value for the regions-A,C.

estimate. Thus the value and variation of $\rho = 1.0 \pm 0.4$ which constitutes a good envelope for the possible range of ρ was considered. The conclusion of this study is that the effect of correlations on the background estimate can be accounted for by taking ρ =1.4, corresponding to the largest possible background estimate and thus the most conservative limits.

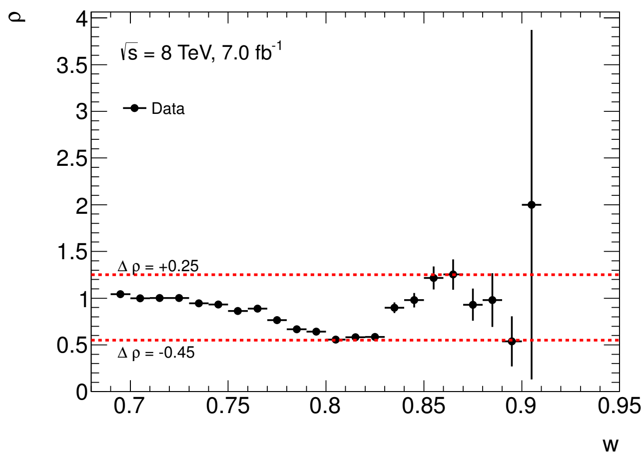

Figure 113: The correlation correction factor ρ for each i^{th} bin of w, computed as the weighted average of all possible $\rho_{i,j}$, for $j > i$, as described in the text. The red dashed lines indicated the maximum deviations from the expected value of ρ=1.

C

CAVEATS OF THE HIP TRIGGER

Sec. 3.2.5 describes the performance of the HIP trigger and briefly introduces issues concerning the efficiency bump for monopoles and efficiency drop for HECOs at higher transverse kinetic energies. This appendix provides explanation for these problems with some open ended tasks for other future enthusiasts to pursue.

C.1 EFFICIENCY BUMP FOR MONOPOLES

Fig. 114 shows the HIP trigger efficiency for a monopole of charge $g=1.0g_D$ and mass 1000 GeV as a function of a of transverse and longitudinal energy in the barrel and end-cap regions respectively. As discussed in Sec. 3.2.5 the drop in efficiency at higher energy values is due to the hadronic veto applied at Level-1. In the barrel region however, a rise in trigger efficiency for canadidates with transverse energy greater than 1700 GeV is observed. The rise in efficiency is observed only in a small region ($0.4 < |\eta| < 0.65$), and is seen to originate at the L1 trigger itself (see. Fig. 115). However the reason for such a rise in this particular region is unknown.

The source of the efficiency gain is attributed to the hardware based Level-1 system which is simulated in the ATHENA reconstruction software. The issue can be attributed to inefficiencies in the Level-1 simulations of highly ionising particles. Fig. 116 shows the energy in the hadronic Tile calorimeter in the barrel region as a function of the transverse kinetic energy for candidates that passed the HIP trigger. The plot shows that candidates with energies much greater than those permitted by the hadronic veto have passed the trigger.

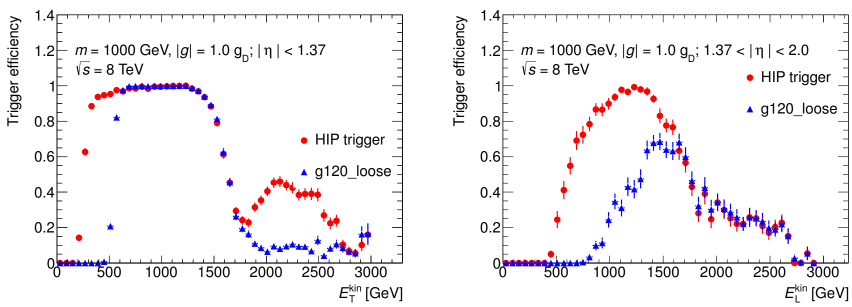

Figure 114: The HIP and photon trigger efficiency for a monopole sample of charge $1.0g_D$ and mass 1000 GeV as a function of its transverse and longitudinal energy in the barrel (left) and end-cap region (right) respectively. An increase in the efficiency is observed only for the HIP trigger in the barrel for $E_T^{kin} > 1700$ GeV.

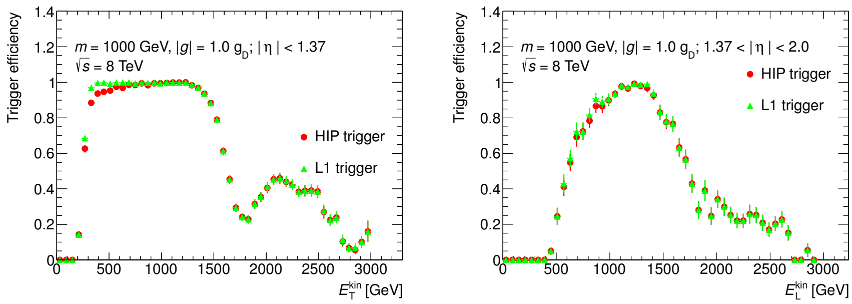

Figure 115: The HIP and L1 trigger efficiency for a monopole sample of charge $1.0g_D$ and mass 1000 GeV as a function of its transverse and longitudinal energy in the barrel (left) and end-cap region (right) respectively. An increase in the efficiency is observed for both the HIP and L1 trigger in the barrel for $E_T^{kin} > 1700$ GeV, which suggests that the phenomenon occurs already at L1.

The exact reason as to how these candidates in simulation passed the Level-1 hadronic veto is still open - perhaps simulations of highly ionising particles cause some saturation of cells in this region?

Since no physics reason can be attributed to triggering more candidates of high transverse energy in specific η regions, the excess candidates are removed. The offline hadronic veto recomputes the transverse energy of the candidates in the hadronic layers of the calorimeter (mainly the barrel and extended barrel, see Fig. 116) and applies the hadronic veto condition. This effect is shown in Fig. 117.

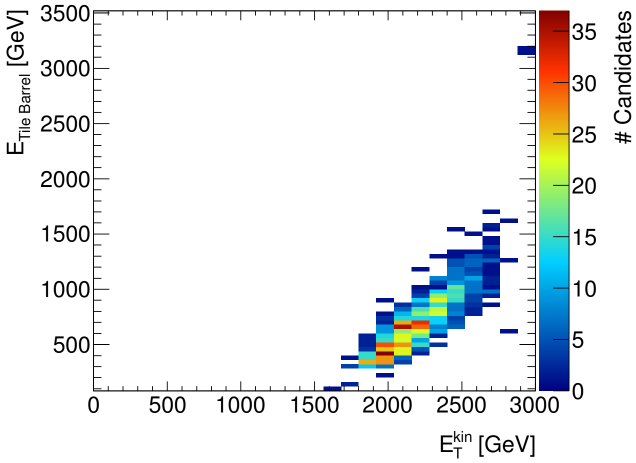

Figure 116: The energy deposited in the barrel region of the Tile calorimeter by a monopole of charge $1.0g_D$ and mass 1000 GeV, with $E_T^{kin} >$ 1700 GeV and $0.4 < |\eta| < 0.65$. Candidates deposit high energies in the barrel region of the Tile calorimeter despite the hadronic veto being applied at L1. The triggering of events with such candidates is considered an inefficiency of the L1 trigger and are corrected for in the offline selections.

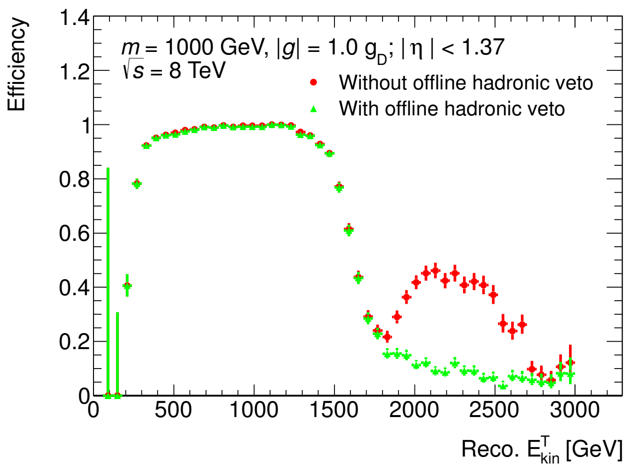

Figure 117: The trigger efficiency of the HIP trigger after the applying an offline hadronic veto to correct for the inefficiency observed from the L1 trigger.

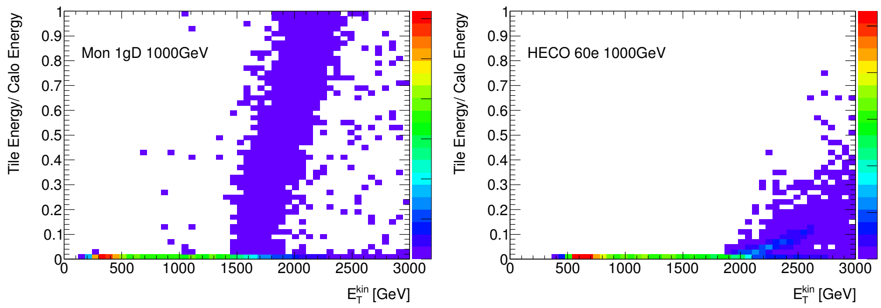

Figure 118: The ratio of the energy deposited in the Tile calorimeter to that deposited in the ECAL by a $1.0g_D$ monopole (left) and 60e HECO (right) with a mass of 1000 GeV. The ratio for HECOs is lower than expected since they lose significantly more energy as they slow down or stop.

C.2 HECO TRIGGER EFFICIENCY

Fig. 39b shows the trigger efficiency for a m = 1000 GeV HECO and charge 60e as a function of its transverse energy in the barrel. The drop in efficiency at higher transverse energies is due to the hadronic veto from the L1 trigger (for HIP trigger) and the EF-level ratio veto (for photon trigger) as described in Sec. 3.2.5. Unlike in the case of monopoles, the drop in trigger efficiency for HECOs is earlier for the HIP trigger than the photon trigger. This can be explained if the ratio based EF-veto fires at higher values of E_T^{kin} for HECOs as opposed to the Level-1 hadronic veto which is a hardware trigger that fires with 1 GeV of energy deposition in the Tile calorimeter.

The energy loss is significantly higher for HECOs as they slow down (see Fig. 2). Consequently, the ratio of the energy deposited in Tile calorimeter to that in the ECAL is expected to be high for HECOs that penetrate into Tile calorimeter and stop. However, Fig. 118 shows the ratio of energy deposited by a candidate in Tile calorimeter to that deposited in ECAL for monopoles (left) and HECOs (right) as a function of the transverse kinetic energy of the candidate. The distributions show unexpectedly low ratios for HECOs compared to those observed for monopoles. Fig. 119 shows the energy deposited by the signal candidates in Tile calorimeter, with HECOs that penetrate through to Tile calorimeter depositing considerably low energies compared to monopoles. A possible explanation for estimating such low energies in Tile calorimeter could be that the energy loss of HECOs is so high that it saturates certain layers of the Tile calorimeter and only a part of that energy is 'visible'. Hopefully, this saturation is well accounted for in simulations but unfortunately there were no studies conducted to support this claim.

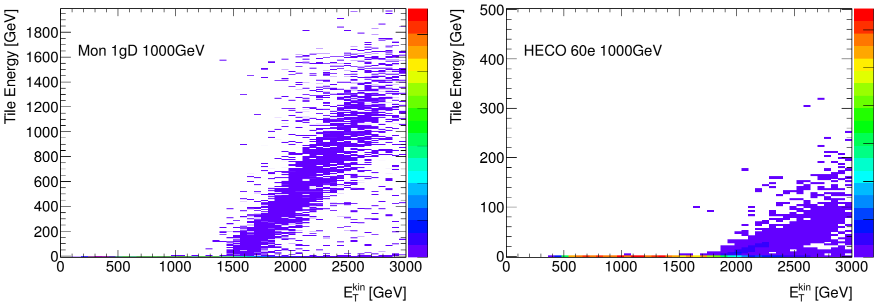

Figure 119: The energy deposited in Tile calorimeter by a $1.0g_D$ monopole (left) and $60e$ HECO (right) of mass 1000 GeV. The energy deposited by the HECO is observed to be much lower compared to the monopole and suggests a simulation issue might be present.

D ASYMMETRY IN PSEUDO-RAPIDITY

The pseudo-rapidity distributions of some signal samples showed an asymmetry, in the selected candidates. A larger asymmetry is also observed in data. Similar to Fig. 53, Fig. 120 shows that a larger number of candidates are selected at positive pseudo-rapidity values, and the asymmetry is persistent throughout the preselection and final selections. Thus, the asymmetry is not introduced by any requirements of the event selection. In data, a large asymmetry is observed at high pseudo-rapidity values, $|\eta| > 1.7$, beyond the coverage of the Tile calorimeter which is responsible for the hadronic veto at Level-1, as well as the offline selections.

The asymmetry is quantified as:

$$A = \frac{(N_F - N_B)}{(N_F + N_B)} \tag{47}$$

where $N_F(N_B)$ is the number of candidates with $\eta > 0$ ($\eta < 0$). Fig. 121 shows the observed asymmetry for each run in the dataset for both the barrel (left) and end-cap (right) regions. The outlier in the barrel region that corresponds to run number 213816 is the run that is excluded from the analysis as discussed in Sec. 3.3.1. The fact that this run, which is known to present anomalously noisy straws in some parts of the TRT, presents such a striking asymmetry strongly suggests that the inherent non-uniformity of the noise in the TRT causes the effect by affecting the trigger f_{HT} variable. While most runs show a negligible asymmetry in the barrel region, some runs tend to show a small negative asymmetry. A positive asymmetry is observed in the end-cap region for all runs suggesting a strong bias in the positive pseudo-rapidity region for the entire dataset.

Similar asymmetries were observed in the MC sample of electrons from *W* boson decays, as seen in Fig. 122. Cross-checks with an emula-

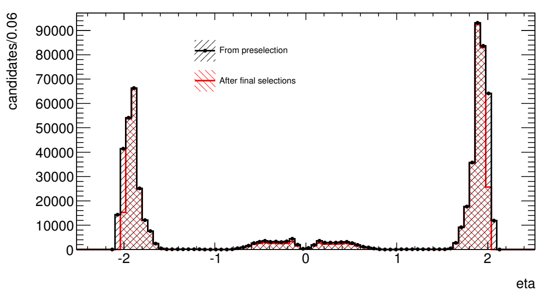

Figure 120: The pseudo-rapidity distributions of the clusters in data after applying the preselections and the final selections. No asymmetry is introduced as a consequence of the analysis selections.

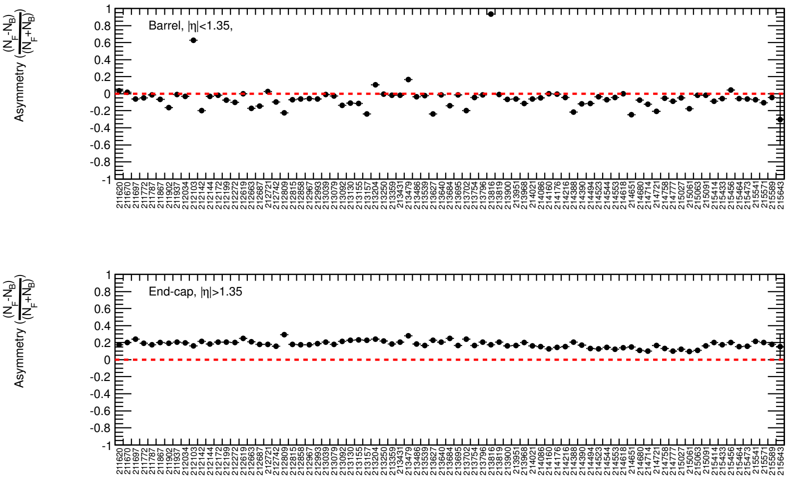

Figure 121: The asymmetry in the barrel (top) and end-cap (bottom) for each run in the ATLAS dataset. The asymmetry of approximately 20% is clearly evident in the end-caps.

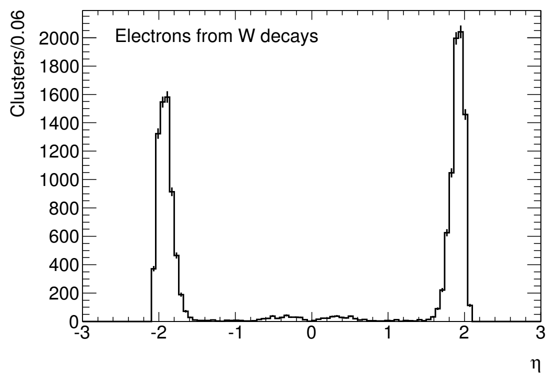

Figure 122: The pseudo-rapidity distribution of the clusters from W-decays using only the HIP trigger and no selection criteria shows an asymmetry, similar to that observed in data.

tion of the trigger suggest that the cause of the asymmetry is related to the asymmetric noise in the TRT, which seems to be adequately simulated.

Fig. 123 shows the asymmetries in the MC signal samples, where the maximum asymmetry is observed for low charge candidates that tend to penetrate through to the Tile calorimeter.

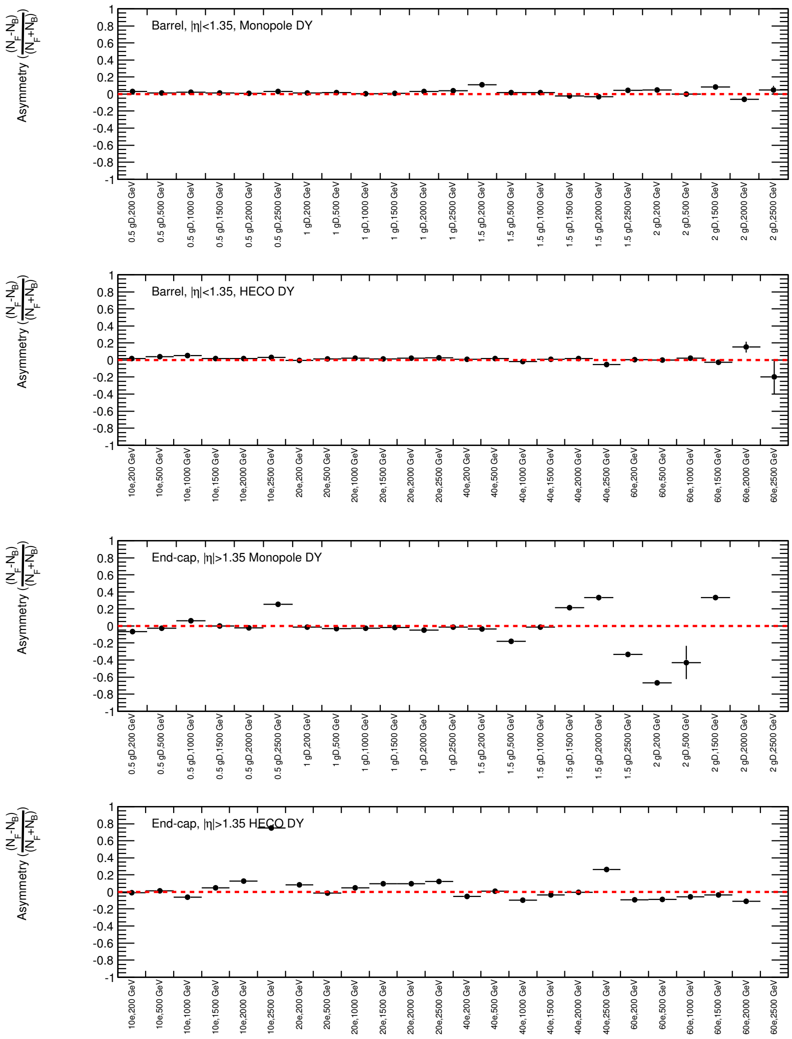

Figure 123: The asymmetry observed in the DY signal samples in the barrel (top two) and end-cap (bottom two) regions.

E

TRANSVERSE MOMENTUM (p_T) CUTS

To reach the calorimeter and create cluster candidates, particles are required to have a minimum p_T. To avoid simulating the reconstruction of particles which will not reach the calorimeter and not waste computing resources, a p_T threshold is set for each signal mass and charge point. Events with candidates that fail to cross this p_T threshold are discarded at the generator level since they have no chance to fire the HIP trigger. The thresholds are estimated by plotting the HIP trigger efficiency as a function of p_T and are conservatively chosen such that they are about 50 GeV below the turn-on in trigger efficiency. The Tab. 36 and 37 summarise the p_T cut thresholds for Drell-Yan spin-½ monopoles and HECOs respectively.

Charge	Mass	p_T cut
$0.5g_D$	200	0
	500	50
	1000	150
	1500	200
	2000	250
	2500	300
$1.0g_D$	200	150
	500	200
	1000	250
	1500	300
	2000	350
	2500	400

Charge	Mass	p_T cut
$1.5g_D$	200	250
	500	300
	1000	350
	1500	400
	2000	450
	2500	550
$2.0g_D$	200	500
	500	550
	1000	650
	1500	700
	2000	750
	2500	800

Table 36: Table summarising the p_T cuts for Drell-Yan monopoles that are applied at the generator level to reject candidates that will not fire the HIP trigger.

Charge	Mass	pt cut
10e	200	0
	500	100
	1000	200
	1500	300
	2000	450
	2500	600
20e	200	0
	500	50
	1000	150
	1500	200
	2000	250
	2500	350

Charge	Mass	pt cut
40e	200	50
	500	100
	1000	200
	1500	300
	2000	350
	2500	450
60e	200	100
	500	200
	1000	300
	1500	400
	2000	500
	2500	600

Table 37: Table summarising the p_T cuts for Drell-Yan HECOs that are applied at the generator level to reject candidates that will not fire the HIP trigger.

BIBLIOGRAPHY

[1] P. A. M. Dirac, *Quantized Singularities in the Electromagnetic Field*, Proc. Roy. Soc. Lond. **A133** (1931) 60–72.

[2] Y. Aharonov and D. Bohm, *Significance of electromagnetic potentials in the quantum theory*, Phys. Rev. **115** (1959) 485–491.

[3] P. A. M. Dirac, *The Theory of magnetic poles*, Phys. Rev. **74** (1948) 817–830.

[4] T. T. Wu and C. N. Yang, *Concept of Nonintegrable Phase Factors and Global Formulation of Gauge Fields*, Phys. Rev. **D12** (1975) 3845–3857.

[5] D. J. Griffiths, *Introduction to electrodynamics; 4th ed.* Pearson, Boston, MA, 2013. `https://cds.cern.ch/record/1492149`.

[6] R. A. Millikan, *On the elementary electrical charge and the Avogadro constant*, Phys. Rev. **2** (1913) 109.

[7] J. S. Schwinger, *Magnetic charge and quantum field theory*, Phys. Rev. **144** (1966) 1087–1093.

[8] J. S. Schwinger, *Sources and magnetic charge*, Phys. Rev. **173** (1968) 1536–1544.

[9] G. 't Hooft, *Magnetic Monopoles in Unified Gauge Theories*, Nucl. Phys. **B79** (1974) 276–284.

[10] A. M. Polyakov, *Particle Spectrum in the Quantum Field Theory*, JETP Lett. **20** (1974) 194–195.

[11] Y. Shnir, *Magnetic monopoles*. Springer-Verlag, first ed. 2005.

[12] U. Amaldi, W. de Boer, and H. Furstenau, *Comparison of grand unified theories with electroweak and strong coupling constants measured at LEP*, Phys. Lett. **B260** (1991) 447–455.

[13] T. Vachaspati and M. Barriola, *A New class of defects*, Phys. Rev. Lett. **69** (1992) 1867–1870.

[14] M. Barriola, T. Vachaspati, and M. Bucher, *Embedded defects*, Phys. Rev. **D50** (1994) 2819–2825, `arXiv:hep-th/9306120 [hep-th]`.

[15] Y. M. Cho and D. Maison, *Monopoles in Weinberg-Salam model*, Phys. Lett. **B391** (1997) 360–365, `arXiv:hep-th/9601028 [hep-th]`.

[16] Y. M. Cho, K. Kimm, and J. H. Yoon, *Mass of the Electroweak Monopole*, Mod. Phys. Lett. **A31** (2016) 1650053, `arXiv:1212.3885 [hep-ph]`.

[17] J. Ellis, N. E. Mavromatos, and T. You, *The Price of an Electroweak Monopole*, Phys. Lett. **B756** (2016) 29–35, arXiv:1602.01745 [hep-ph].

[18] S. Burdin, A. Firan, and W. Taylor, *A Search for Magnetic Monopoles at ATLAS*, Mar, 2012, https://cds.cern.ch/record/1435748.

[19] A. Firan et al., *Search for Magnetic Monopoles using the ATLAS Detector*, Oct, 2010, https://cds.cern.ch/record/1302300.

[20] Y. Kazama, C. N. Yang, and A. S. Goldhaber, *Scattering of a Dirac particle with charge* Ze *by a fixed magnetic monopole*, Phys. Rev. D **15** (1977) 2287–2299.

[21] S. P. Ahlen, *Stopping-power formula for magnetic monopoles*, Phys. Rev. D **17** (1978) 229–233.

[22] S. P. Ahlen and K. Kinoshita, *Calculation of the stopping power of very low velocity magnetic monopoles*, Phys. Rev. **D26** (1982) 2347–2363.

[23] MoEDAL Collaboration, L. Patrizii and Z. Sahnoun, *Energy Losses of Magnetic Monopoles in Aluminum, Iron and Copper*, https://cds.cern.ch/record/2140908.

[24] A. Roeck, A. Katre, P. Mermod, D. Milstead, and T. Sloan, *Sensitivity of LHC experiments to exotic highly ionising particles*, The European Physical Journal C **72** (2012) 1–18.

[25] SLIM Collaboration, D. Bakari et al., *Search for 'light' magnetic monopoles*, arXiv:hep-ex/0003028 [hep-ex].

[26] P. B. Price, E. K. Shirk, W. Z. Osborne, and L. S. Pinsky, *Further measurements and reassessment of the magnetic-monopole candidate*, Phys. Rev. D **18** (1978) 1382–1421.

[27] MACRO Collaboration, M. Ambrosio et al., *Final results of magnetic monopole searches with the MACRO experiment*, Eur. Phys. J. **C25** (2002) 511–522, arXiv:hep-ex/0207020 [hep-ex].

[28] S. Balestra et al., *Magnetic Monopole Search at high altitude with the SLIM experiment*, Eur. Phys. J. **C55** (2008) 57–63, arXiv:0801.4913 [hep-ex].

[29] MoEDAL Collaboration, B. Acharya et al., *Search for magnetic monopoles with the MoEDAL prototype trapping detector in 8 TeV proton-proton collisions at the LHC*, JHEP **08** (2016) 067, arXiv:1604.06645 [hep-ex].

[30] K. Kinoshita et al., *Search for highly ionizing particles in* e^+e^- *annihilations at* $\sqrt{s} = 91.1$ *GeV*, Phys. Rev. D **46** (1992) R881–R884.

[31] MoEDAL Collaboration. http://moedal.web.cern.ch/content/nuclear-track-detectors.

[32] CLEO Collaboration, T. Gentile et al., *Search for Magnetically Charged Particles Produced in* e^+e^- *Annihilations at* $\sqrt{s} = 10.6$*-GeV*, Phys. Rev. **D35** (1987) 1081.

[33] TASSO Collaboration, W. Braunschweig et al., *A Search for Particles With Magnetic Charge Produced in* e^+e^- *Annihilations at* $\sqrt{s} = 35$*-GeV*, Z. Phys. **C38** (1988) 543.

[34] CDF Collaboration, A. Abulencia et al., *Direct search for Dirac magnetic monopoles in* $p\bar{p}$ *collisions at* $\sqrt{s} = 1.96$ *TeV*, Phys. Rev. Lett. **96** (2006) 201801, `arXiv:hep-ex/0509015 [hep-ex]`.

[35] D. P. Hogan, D. Z. Besson, J. P. Ralston, I. Kravchenko, and D. Seckel, *Relativistic Magnetic Monopole Flux Constraints from RICE*, Phys. Rev. **D78** (2008) 075031, `arXiv:0806.2129 [astro-ph]`.

[36] ANTARES Collaboration, S. Adrian-Martinez et al., *Search for Relativistic Magnetic Monopoles with the ANTARES Neutrino Telescope*, Astropart. Phys. **35** (2012) 634–640, `arXiv:1110.2656 [astro-ph.HE]`.

[37] S. N. Anderson, J. J. Lord, S. C. Strausz, and R. J. Wilkes, *Possible evidence for magnetic monopole interacitons: Anomalous long range alpha particle tracks deep underground*, Phys. Rev. **D28** (1983) 2308.

[38] K. A. Milton, *Theoretical and experimental status of magnetic monopoles*, Rept. Prog. Phys. **69** (2006) 1637–1712, `arXiv:hep-ex/0602040 [hep-ex]`.

[39] E. Goto, H. H. Kolm, and K. W. Ford, *Search for Ferromagnetically Trapped Magnetic Monopoles of Cosmic-Ray Origin*, Phys. Rev. **132** (1963) 387.

[40] H. H. Kolm, F. Villa, and A. Odian, *Search for magnetic monopoles*, Phys. Rev. **D4** (1971) 1285.

[41] R. L. Fleischer et al., *Search for magnetic monopoles in deep ocean deposits*, Phys. Rev. **184** (1969) 1393–1397.

[42] R. L. Fleischer, I. S. Jacobs, W. M. Schwarz, P. B. Price, and H. G. Goodell, *Search for multiply charged dirac magnetic poles*, Phys. Rev. **177** (1969) 2029–2035.

[43] R. A. Carrigan, F. A. Nezrick, and B. P. Strauss, *Search for misplaced magnetic monopoles*, Phys. Rev. D **13** (1976) 1823–1825.

[44] V. A. Petukhov and M. N. Yakimenko, *Search for the Dirac Monopole*, Nucl. Phys. **49** (1963) 87.

[45] S. Burdin et al., *Non-collider searches for stable massive particles*, Phys. Rept. **582** (2015) 1–52, `arXiv:1410.1374 [hep-ph]`.

[46] A. De Roeck et al., *Development of a magnetometer-based search strategy for stopped monopoles at the Large Hadron Collider*, The European Physical Journal C **72** (2012) 1–9.

[47] P. B. Price, E. K. Shirk, W. Z. Osborne, and L. S. Pinsky, *Evidence for Detection of a Moving Magnetic Monopole*, Phys. Rev. Lett. **35** (1975) 487–490.

[48] B. Cabrera, *First Results from a Superconductive Detector for Moving Magnetic Monopoles*, Phys. Rev. Lett. **48** (1982) 1378–1381.

[49] A. D. Caplin, M. Hardiman, M. Koratzinos, and J. C. Schouten, *Observation of an Unexplained Event From a Magnetic Monopole Detector*, Nature **321** (1986) 402–406.

[50] J. Preskill, *Magnetic monopoles*, Ann. Rev. Nucl. Part. Sci. **34** (1984) 461–530.

[51] E. N. Parker, *The Origin of Magnetic Fields*, Astrophys. J. **160** (1970) 383.

[52] MACRO Collaboration, M. Ambrosio et al., *The MACRO detector at Gran Sasso*, Nucl. Instrum. Meth. **A486** (2002) 663–707.

[53] S. D. Wick, T. W. Kephart, T. J. Weiler, and P. L. Biermann, *Signatures for a cosmic flux of magnetic monopoles*, Astropart. Phys. **18** (2003) 663–687, `arXiv:astro-ph/0001233 [astro-ph]`.

[54] Detrixhe, M. et. al, *Ultrarelativistic magnetic monopole search with the ANITA-II balloon-borne radio interferometer*, Phys. Rev. D **83** (2011) 023513, `arXiv:1008.1282 [astro-ph.HE]`.

[55] ANTARES Collaboration, M. Ageron et al., *ANTARES: the first undersea neutrino telescope*, Nucl. Instrum. Meth. **A656** (2011) 11–38, `arXiv:1104.1607 [astro-ph.IM]`.

[56] BAIKAL Collaboration, K. Antipin et al., *Search for relativistic magnetic monopoles with the Baikal Neutrino Telescope*, Astropart. Phys. **29** (2008) 366–372.

[57] R. Abbasi et al., *Search for relativistic magnetic monopoles with the AMANDA-II neutrino telescope*, Eur. Phys. J. **C69** (2010) 361–378.

[58] IceCube Collaboration, A. Achterberg et al., *First Year Performance of The IceCube Neutrino Telescope*, Astropart. Phys. **26** (2006) 155–173, `arXiv:astro-ph/0604450 [astro-ph]`.

[59] Super-Kamiokande Collaboration, Y. Fukuda et al., *The Super-Kamiokande detector*, Nucl. Instrum. Meth. **A501** (2003) 418–462.

[60] Super-Kamiokande Collaboration, K. Ueno et al., *Search for GUT monopoles at Super–Kamiokande*, Astropart. Phys. **36** (2012) 131–136, arXiv:1203.0940 [hep-ex].

[61] D. F. Bartlett, D. Soo, R. L. Fleischer, H. R. Hart, Jr., and A. Mogro-Campero, *Search for Cosmic Ray Related Magnetic Monopoles at Ground Level*, Phys. Rev. **D24** (1981) 612.

[62] P. H. Eberhard, R. R. Ross, L. W. Alvarez, and R. D. Watt, *Search for magnetic monopoles in lunar material*, Phys. Rev. **D4** (1971) 3260.

[63] R. R. Ross, P. H. Eberhard, L. W. Alvarez, and R. D. Watt, *Search for magnetic monopoles in lunar material using an electromagnetic detector*, Phys. Rev. **D8** (1973) 698.

[64] K. Bendtz et al., *Search for magnetic monopoles in polar volcanic rocks*, Phys. Rev. Lett. **110** (2013) 121803, arXiv:1301.6530 [hep-ex].

[65] L3 Collaboration, M. Acciarri et al., *Search for anomalous Z –> gamma gamma gamma events at LEP*, Phys. Lett. **B345** (1995) 609–616.

[66] D0 Collaboration, B. Abbott et al., *A Search for heavy point - like Dirac monopoles*, Phys. Rev. Lett. **81** (1998) 524–529, arXiv:hep-ex/9803023 [hep-ex].

[67] I. F. Ginzburg and S. L. Panfil, *The Possibility of Observation of Heavy Dirac-schwinger Magnetic Pole*, Sov. J. Nucl. Phys. **36** (1982) 850, [Yad. Fiz.36,1461(1982)].

[68] A. De Rujula, *Effects of virtual monopoles*, Nucl. Phys. **B435** (1995) 257–276, arXiv:hep-th/9405191 [hep-th].

[69] J. L. Pinfold and others., *A Search for highly ionizing particles produced at the OPAL intersection point at LEP*, Phys. Lett. **B316** (1993) 407–411.

[70] H1 Collaboration, A. Aktas et al., *A Direct search for stable magnetic monopoles produced in positron-proton collisions at HERA*, Eur. Phys. J. **C41** (2005) 133–141, arXiv:hep-ex/0501039 [hep-ex].

[71] G. R. Kalbfleisch, W. Luo, K. A. Milton, E. H. Smith, and M. G. Strauss, *Limits on production of magnetic monopoles utilizing samples from the D0 and CDF detectors at the Tevatron*, Phys. Rev. **D69** (2004) 052002, arXiv:hep-ex/0306045 [hep-ex].

[72] ATLAS Collaboration, *Search for magnetic monopoles in* $\sqrt{s} = 7$ *TeV* pp *collisions with the ATLAS detector*, Phys. Rev. Lett. **109** (2012) 261803, arXiv:1207.6411 [hep-ex].

[73] L. Evans and P. Bryant, *LHC Machine*, Journal of Instrumentation **3** (2008) S08001.

[74] C. Lefevre, *LHC: the guide (English version). Guide du LHC (version anglaise)*, http://cds.cern.ch/record/1165534.

[75] http://cerncourier.com/cws/article/cern/54381.

[76] ATLAS Collaboration, *The ATLAS Experiment at the CERN Large Hadron Collider*, Journal of Instrumentation **3** (2008) S08003.

[77] ATLAS Collaboration, *ATLAS inner detector: Technical Design Report, 1*. Technical Design Report ATLAS. CERN, 1997. https://cds.cern.ch/record/331063.

[78] ATLAS Collaboration, *ATLAS pixel detector electronics and sensors*, JINST **3** (2008) P07007.

[79] ATLAS Collaboration, *The ATLAS Inner Detector commissioning and calibration*, Eur. Phys. J. **C70** (2010) 787–821, arXiv:1004.5293 [physics.ins-det].

[80] I. Perić et al., *The {FEI3} readout chip for the {ATLAS} pixel detector*, Nuclear Instruments and Methods in Physics Research Section A: Accelerators, Spectrometers, Detectors and Associated Equipment **565** (2006) 178 – 187.

[81] ATLAS Collaboration, *ATLAS pixel detector electronics and sensors*, Journal of Instrumentation **3** (2008) P07007.

[82] ATLAS Collaboration, dE/dx *measurement in the ATLAS Pixel Detector and its use for particle identification*, ATLAS-CONF-2011-016, 2011, http://cdsweb.cern.ch/record/1336519.

[83] ATLAS TRT Collaboration, *The ATLAS Transition Radiation Tracker (TRT) proportional drift tube: design and performance*, Journal of Instrumentation **3** (2008) P02013.

[84] ATLAS TRT Collaboration, *The ATLAS TRT electronics*, Journal of Instrumentation **3** (2008) P06007.

[85] M. Juengst, M. Schultens, and S. Zimmermann, *A time-over-threshold based approach for particle identification with the ATLAS TRT detector*, Feb, 2012, https://cds.cern.ch/record/1426267.

[86] ATLAS Collaboration, *Particle Identification Performance of the ATLAS Transition Radiation Tracker*, ATLAS-CONF-2011-128, 2011, http://cdsweb.cern.ch/record/1383793.

[87] ATLAS Collaboration, P. Wagner, *Performance of the ATLAS Transition Radiation Tracker Readout with High Energy Collisions at the LHC*, Geneva, Dec, 2011, https://cds.cern.ch/record/1403142.

[88] R. Achenbach et al., *The ATLAS Level-1 Calorimeter Trigger*, Journal of Instrumentation **3** (2008) P03001.

[89] ATLAS Collaboration, *Trigger for Dummies, Overview of the ATLAS Trigger System*, https://twiki.cern.ch/twiki/bin/view/Atlas/TriggerForDummies?rev=13, 2012.

[90] MoEDAL Collaboration, J. Pinfold et al., *Technical Design Report of the MoEDAL Experiment*, https://cds.cern.ch/record/1181486.

[91] MoEDAL Collaboration, B. Acharya et al., *The Physics Programme Of The MoEDAL Experiment At The LHC*, Int. J. Mod. Phys. **A29** (2014) 1430050, arXiv:1405.7662 [hep-ph].

[92] MoEDAL Collaboration, V. A. Mitsou, *MoEDAL: Seeking magnetic monopoles and more at the LHC*, PoS **EPS-HEP2015** (2015) 109, arXiv:1511.01745 [physics.ins-det].

[93] J. L. Pinfold, *The MoEDAL Experiment at the LHC – a New Light on the Terascale Frontier*, J. Phys. Conf. Ser. **631** (2015) 012014.

[94] ATLAS Collaboration, *ATLAS-GEO-21-02-02, ATLAS geometry database tags*, http://atlas.web.cern.ch/Atlas/GROUPS/OPERATIONS/dataBases/DDDB/show_branch_tag_comments.php?tag_name=ATLAS-GEO-21-02-02, 2013.

[95] ATLAS Collaboration, *OFLCOND-MC12-SIM-00, ATLAS COOL database tags*, https://twiki.cern.ch/twiki/bin/view/AtlasComputing/CoolProdTags, 2012.

[96] *GEANT4 Collaboration, GEANT4 physics lists*, http://geant4.cern.ch/support/proc_mod_catalog/physics_lists/useCases.shtml, 2014.

[97] M. L. Mangano, F. Piccinini, A. D. Polosa, M. Moretti, and R. Pittau, *ALPGEN, a generator for hard multiparton processes in hadronic collisions*, Journal of High Energy Physics **2003** (2003) 001, arXiv:hep-ph/0206293 [hep-ph].

[98] B. P. Kersevan and E. Richter-Was, *The Monte Carlo event generator AcerMC versions 2.0 to 3.8 with interfaces to PYTHIA 6.4, HERWIG 6.5 and ARIADNE 4.1*, Comput. Phys. Commun. **184** (2013) 919–985, arXiv:hep-ph/0405247 [hep-ph].

[99] J. Alwall et al., *The automated computation of tree-level and next-to-leading order differential cross sections, and their matching to parton shower simulations*, Journal of High Energy Physics **2014** (2014) 1–157.

[100] T. Sjostrand, S. Mrenna, and P. Z. Skands, *A Brief Introduction to PYTHIA 8.1*, Comput. Phys. Commun. **178** (2008) 852–867, arXiv:0710.3820 [hep-ph].

[101] M. Bahr et al., *Herwig++ Physics and Manual*, Eur. Phys. J. **C58** (2008) 639–707, arXiv:0803.0883 [hep-ph].

[102] T. Gleisberg et al., *Event generation with SHERPA 1.1*, JHEP **02** (2009) 007, arXiv:0811.4622 [hep-ph].

[103] A. Collaboration, *The ATLAS Simulation Infrastructure*, The European Physical Journal C **70** (2010) 823–874.

[104] J. Pumplin et al., *New Generation of Parton Distributions with Uncertainties from Global QCD Analysis*, Journal of High Energy Physics **2002** (2002) 012, arXiv:hep-ph/0201195 [hep-ph].

[105] ATLAS Collaboration, *Summary of ATLAS Pythia 8 tunes*, Aug, 2012, http://cds.cern.ch/record/1474107.

[106] P. A. M. Dirac, *Theory of Magnetic Monopoles*, 1976 Orbis Scientiae New Pathways in High Energy Physics Coral Gables, Florida, January 19-22, 1976 (1976) 1–14.

[107] E. Noordeh and W. Taylor, *Extension of the Magnetic Monopole Search to Include Scalar Monopoles*, Oct, 2014, https://cds.cern.ch/record/1966026.

[108] S. Ahlen, *Monopole-track characteristics in plastic detectors*, Phys. Rev. D **14** (1975) 2935.

[109] S. Ahlen, *Theoretical and experimental aspects of the energy loss of relativistic heavily ionizing particles*, Rev. Mod. Phys. **52** (1980) 121, [Erratum: Rev. Mod. Phys.52,653(1980)].

[110] S. Wick, T. Kephart, T. Weiler, and P. Biermann, *Signatures for a cosmic flux of magnetic monopoles*, Astropart. Phys. **18** (2003) 663, arXiv:astro-ph/0001233 [astro-ph].

[111] Geant4 Collaboration, *http://geant4.cern.ch/support/*,.

[112] Geant4 Collaboration, *Geant4 developments and applications*, IEEE Trans. Nucl. Sci. **53** (2006) 270.

[113] GEANT4 Collaboration, S. Agostinelli et al., *GEANT4: A Simulation toolkit*, Nucl.Instrum.Meth. **A506** (2003) 250–303.

[114] K. Bendtz et al., *A Search for Magnetic Monopoles and Exotic Particles with Large Electric Charge at ATLAS*, May, 2014, https://cds.cern.ch/record/1704393.

[115] J. B. Birks, *Scintillations from Organic Crystals: Specific Fluorescence and Relative Response to Different Radiations*, Proceedings of the Physical Society. Section A **64** (1951) 874.

[116] J. B. Birks and F. A. Black, *Deterioration of Anthracene under α-Particle Irradiation*, Proceedings of the Physical Society. Section A **64** (1951) 511.

[117] J. B. Birks, *Theory and Practice of Scintillation Counting*. Pergamon Press, 1964.

[118] J. B. Birks, *Theory of the Response of Organic Scintillation Crystals to Short-Range Particles*, Phys. Rev. **86** (1952) 569–569.

[119] ICARUS Collaboration, S. Amoruso et al., *Study of electron recombination in liquid argon with the ICARUS TPC*, Nucl.Instrum.Meth. **A523** (2004) 275–286.

[120] M. Aharrouche et al., *Measurement of the response of the ATLAS liquid argon barrel calorimeter to electrons at the 2004 combined test-beam*, Nucl.Instrum.Meth. **A614** (2010) 400–432.

[121] S. Burdin, M. Horbatsch, and W. Taylor, *A correction to Birks' Law in liquid argon ionization chamber simulations for highly ionizing particles*, Nuclear Instruments and Methods in Physics Research Section A: Accelerators, Spectrometers, Detectors and Associated Equipment **664** (2012) 111 – 116.

[122] ATLAS Collaboration, *Calibration of the ATLAS Transition Radiation Tracker*, ATLAS-CONF-2011-006, 2011, `http://cdsweb.cern.ch/record/1330712`.

[123] W. Lampl et al., *Calorimeter Clustering Algorithms: Description and Performance*, Apr, 2008, `https://cds.cern.ch/record/1099735`.

[124] `https://twiki.cern.ch/twiki/bin/view/AtlasProtected/ExoticHighlyIonizing2012#List_of_official_background_samp`.

[125] ATLAS Collaboration. `https://twiki.cern.ch/twiki/bin/viewauth/Atlas/TriggerGlossary`.

[126] ATLAS Collaboration. `https://twiki.cern.ch/twiki/bin/viewauth/Atlas/TriggerMenuGlossary`.

[127] ATLAS Collaboration, *Measurement of the inclusive isolated prompt photon cross section in* pp *collisions at $\sqrt{s} = 7$ TeV with the ATLAS detector*, Phys. Rev. **D83** (2011) 052005, `arXiv:1012.4389 [hep-ex]`.

[128] S. Burdin, A. Firan, and W. Taylor, *A Search for Magnetic Monopoles at ATLAS*, Mar, 2013, `https://cds.cern.ch/record/1530984`.

[129] A. Collaboration, *Search for magnetic monopoles and stable particles with high electric charges in 8 TeV* pp *collisions with the ATLAS detector*, Phys. Rev. **D93** (2016) 052009, `arXiv:1509.08059 [hep-ex]`.

[130] S. P. Ahlen, *Monopole-track characteristics in plastic detectors*, Phys. Rev. D **14** (1976) 2935–2940.

[131] S. P. Ahlen, *Theoretical and experimental aspects of the energy loss of relativistic heavily ionizing particles*, Rev. Mod. Phys. **52** (1980) 121–173.

[132] J. Labbe and R. Ishmukhametov, *Crosstalk Measurements in the Electromagnetic Calorimeter during ATLAS Final Installation*, Dec, 2008, `https://cds.cern.ch/record/1143373`.

[133] ATLAS Collaboration, *Improved luminosity determination in pp collisions at $\sqrt{s} = 7$ TeV using the ATLAS detector at the LHC*, Eur. Phys. J. C **73** (2013) 2518. 40 p, arXiv:1302.4393 [hep-ex].

[134] A. L. Read, *Presentation of search results: the CL s technique*, Journal of Physics G: Nuclear and Particle Physics **28** (2002) 2693.

[135] ROOT Collaboration, K. Cranmer, G. Lewis, L. Moneta, A. Shibata, and W. Verkerke, *HistFactory: A tool for creating statistical models for use with RooFit and RooStats*, New York, Jan, 2012, https://cds.cern.ch/record/1456844.

[136] G. Cowan, K. Cranmer, E. Gross, and O. Vitells, *Asymptotic formulae for likelihood-based tests of new physics*, Eur. Phys. J. **C71** (2011) 1554, arXiv:1007.1727 [physics.data-an], [Erratum: Eur. Phys. J.C73,2501(2013)].

[137] CDF II Collaboration. http://www-cdf.fnal.gov/physics/exotic/r2a/20140619.monopole/.

[138] J. Derkaoui et al., *Energy losses of magnetic monopoles and of dyons in the earth*, Astropart. Phys. **9** (1998) 173–183.

[139] N. S. Craigie, G. Giacomelli, W. Nahm, and Q. Shafi, eds., *Theory and detection of magnetic monopoles in gauge theories*. Singapore, Singapore: World Scientific (1986) 499p, 1986.

[140] Particle Data Group Collaboration, K. A. Olive et al., *Review of Particle Physics*, Chin. Phys. **C38** (2014) 090001.

[141] H. S. C. Chen, *Note on the Magnetic Pole*, American Journal of Physics **33** (1965) 563–565.

[142] L. P. Levy, *Magnetism and Superconductivity*. Springer, Berlin, 2004.

[143] D0 Collaboration, I. Bertram et al., *A Recipe for the construction of confidence limits*, FERMILAB-TM-2104 (2000).